UNIVERSITE DE NICE-SOPHIA ANTIPOLIS - UFR Sciences
Ecole Doctorale « Sciences Fondamentales et Appliquées »

THESE

pour obtenir le titre de Docteur en Sciences
de l'Université de Nice-Sophia Antipolis
Spécialité : Sciences de l'Univers
présentée et soutenue par :

Benoît VANDAME

TRAITEMENTS D'IMAGES A GRAND-CHAMPS ET MULTI-LONGEURS D'ONDES
Application aux relevés « ESO Imaging Survey »

Thèse co-dirigée par :
Albert BIJAOUI et Luiz DA COSTA
soutenue à Nice le 16 décembre 2004
devant le Jury composé de :

M. Albert Bijaoui	Astronome	Directeur
M. Luiz Da Costa	Senior Astronomer	Co-directeur
M. Yannick Mellier	Astronome	Rapporteur
M. Christophe Benoist	Astronome Adjoint	Examinateur
M. Emmanuel Bertin	Astronome Adjoint	Examinateur
M. Henri Lanteri	Professeur	Examinateur

Remerciements

Ce mémoire est la synthèse des travaux réalisés pour la majeure partie à l'European Southern Observatory (ESO) dans l'équipe ESO Imaging Survey (EIS) et dans le laboratoire Cassiopée de l'Observatoire de la Côte d'Azur. Au terme de ce travail je tiens à remercier mes directeurs de thèse Monsieur Albert Bijaoui directeur de laboratoire Cassiopée, et Monsieur Luiz Da Costa directeur de l'équipe EIS. Mes remerciements vont aussi pour les deux observatoires m'aillant accueilli.

Messieurs Yannick Mellier et Michel Boer pour avoir accepté la lourde tâche de rapporteur, et d'avoir effectué un rapport précis et rapide.

Messieurs Christophe Benoist, Emmanuel Bertin et Henri Lanteri pour avoir accepté de faire partie du Jury de soutenance en tant que examinateurs.

Jean Marc Miralles et Libeth Olsen pour m'avoir aidé dans les corrections du mémoire, ainsi que les autres membres de l'équipe EIS Maria Victoria Alonso, Charles Rite et Remco Slijkhuis.

Aussi, je remercie Christophe Benoist , Stéphane Arnouts, Simone Zaggia, Yazan Momany pour m'avoir aidé au cours de cette période.

Contents

Résumé français

Introduction

Depuis une dizaine d'années l'astronomie a connu une croissance sans précédent grâce à de nouveaux instruments qui ont permis de sonder l'univers à toutes les longueurs d'ondes: des rayons X aux ondes radio, et aussi à tous niveaux de résolutions: des optiques adaptatives aux caméra grand champs. Ces énormes progrès ont été atteints grâce aux avancées technologiques des détecteurs et du traitement du signal, et provoquent un flot important de données. Récemment, de large détecteurs faits de plusieurs CCDs sont construits aussi bien pour le visible et l'infrarouge. Certains (la caméra Megacam montée sur le télescope CHFT par exemple) couvrent désormais le champs de vision des plaques photographiques des décennies précédentes. De tels instruments délivrent des images au rythme de un à dix millions de pixel par seconde, et requièrent des infrastructures spéciales tant pour l'archivage que pour la réduction.

Les relevés grand-champs jouent un rôle important en astronomie. Jusqu'à récemment ils n'étaient effectués que par des observations photographiques. Ce sont ces données qui ont permis les études statistiques par comptage (Shane and Wirtanen, 1954) pour l'étude des amas de galaxies (Zwicky et al., 1968; Abell et al., 1989; Corwin et al., 1985). Une étape importante a été la numérisation des clichés pour des études plus sensibles et systématiques, comme par exemple le projet APM du groupe de Edinburgh (Maddox et al., 1990).

Avec les années 80, sont apparus les nouveaux détecteurs électroniques en même temps que de larges télescopes sont construits (Keck, Gemini et VLT par exemple). Durant les années 90, une nouvelle génération de relevés sont réalisés avec différents objectifs scientifiques (EROS (Aubourg et al., 1995), OGLE (Udalski et al., 1992), MACHO (Alcock et al., 1997)). Les premiers sont destinés à la recherche de micro-lentilles gravitationnelles et de naines brunes. En infrarouge, de large relevés couvrant tout le ciel sont réalisés (DENIS (Epchtein et al., 1994, 1997), 2MASS (Skrutskie et al., 1997)).

Aujourd'hui, les relevés sont réalisés avec des instruments multi-CCDs. Le ESO Imaging Survey (EIS) utilise le Wield Field Imager (WFI) fait de 8 CCDs monté sur le télescope de 2.2m à La Silla. Le taux nominal d'acquisition des images se fait a 0,5 MegaPixel par second. Avec le récent instrument Megacam fait de 36 CCDs, le taux nominal et de 2,5 MegaPixel par seconde.

La problématique des nouveaux relevés est de pourvoir réduire les observations avec un taux comparable a celui de l'acquisition. Aussi, les nouveaux relevés intègrent plusieurs instruments afin d'élargir les domaines d'observations (optiques et infrarouges dans le cas de EIS).

Le travail présenté propose un approche originale complète afin de traiter massivement des observations issues de divers instruments optiques ou infrarouges faits de un ou plusieurs CCDs. Ce manuscrit décrit le nouveau pipeline (nommé *alambic*) construit pour la réduction des relevés de EIS, ou de tous types d'observations en général.

Dans le chapitre 2 les outils informatiques existants sont présentés. Aussi, sont énoncées les exigences pour la création du nouveau pipeline. Le chapitre 3 décrit globalement toutes les étapes du pipeline. Le chapitre 4 détaille les principaux algorithmes dont: la détection de mauvais pixels, l'harmonisation des gains moyens pour les instruments multi-CCDs, la correction d'illumination, l'estimation des composantes larges échelles du fond de ciel, l'estimation du ciel pixel à pixel pour les images infrarouges, le calibrage des cartes de franges d'interférences, l'astrométrie à base de transformées en ondelettes, et finalement, la détection de traînées de satellites avec la transformée de Hough. le chapitre 5 illustre les applications de ce pipeline pour les relevés conduits par EIS. Enfin, le chapitre 6 liste les futurs développements, et conclut ce travail.

Prérequis pour la construction d'un nouveau pipeline

Etat de l'Art

Jusqu'à très récemment, les images numériques étaient réduites par les grands logiciels tels que IRAF (Tody, 1986) ou MIDAS (Banse et al., 1983), développés par les grands observatoires, ou bien par des logiciels commerciaux comme IDL (Research Systems Inc, 2004; Landsman, 1995). Ces systèmes sont principalement des boites à outils qui fournissent les procédures de bases pour manipuler des images. En pratique, ces logiciels sont dédiés pour une réduction manuelle de peu d'images. Aussi, ils n'ont pas été conçus pour être utilisés comme des boites indépendantes et automatiques, alors, il est difficile de les intégrer pour en faire des outils fonctionnant sans interversions manuelles. Les premières versions de ces logiciels apparaissent au début des années 80, par la suite ces outils ont étés maintenus et augmentés avec de nouvelles fonctions. Actuellement, ils restent les principaux outils utilisés pour la réductions de données. Pour IRAF, de nouveaux modules sont définis pour la réduction d'images issues d'instruments multi-CCDs: MSCRED pour le calibrage instrumentale et astrométrique, et DRIZZLE (Fruchter and Hook, 2002) pour l'alignement et la fusion d'images.

Depuis une quinzaine d'années, de nouveaux logiciels dédiés à des étapes spécifiques de la réduction ont vu le jour. Ils sont généralement écrits en langages compilés (C ou fortran) et sont entièrement automatiques. Le tableau 2.1 liste les principaux. Ces logiciels sont construits pour être utilisés manuellement, ou bien automatiquement par les programmes de plus haut niveaux.

Les principaux pipelines de réduction d'images, sont construits autour des outils mentionnés ci-dessus. Les différences majeures entre les pipelines sont, les algorithmes utilisés pour achever une étape particulière, et la façon dont les outils de bas niveaux sont gérés. En général, les pipelines sont construits en langages scripts: Perl, Python ou CL (script défini pour IRAF), afin d'encapsuler les outils externes (voir tableau 2.2). L'architecture des pipelines basée sur l'encapsulation des outils existants, impose une importante gestion des fichiers de configuration et des données temporaires. En effet, chaque module externe développé indépendamment impose sa propre convention pour la description des options ce qui impose une gestion spécifique par module utilisé. Aussi, les données progressivement transformées par l'exécution successive des modules sont transférées par écriture sur disques durs, ce qui impose plus d'administration et aussi plus de lenteur dans l'exécution.

La création du pipeline présenté, considère l'implémentation par bibliothèque informatique de tous types de tâches (algorithmes ou administration). Cette approche offre les avantages suivants: 1) meilleures communications entre les différentes tâches implementées, grâce à un environnement commun; 2) amélioration des performances grâce à l'usage de la mémoire vive pour le transfert des données en cours de réduction; 3) simplification de l'administration: tous modules intégrés à la bibliothèque informatique partagent une convention unique pour la description des options. Le pipeline nommé *Alambic* est écrit en C++.

Prérequis définis par EIS

Lors de la réduction des premiers relevés de EIS, une collection de prérequis sont apparus afin d'améliorer la qualité de la réduction: 1) problèmes spécifiques de réduction: calibrage astrométrique robuste pour l'instrument WFI, estimation du fond de ciel sans biais pour les images IR; 2) rapidité de réduction, spécialement pour les instruments multi-CCDs; 3) stratégie commune de réduction des images optiques et IR; 4) contrôle fin des options de configuration et des résultats afin de pouvoir analyser et reproduire les mêmes réductions.

Parmi les prérequis spécifiques de réduction, on note:

- *Estimation non biaisé du fond de ciel pour les observations IR* - Lorsque les premières images obtenues avec l'instrument IR SOFI furent réduites par le logiciel Jitter du projet Eclipse (Devillard, 1997), un biais des magnitudes faibles a été reporté. Ce biais a été observé en comparant les images réduites avec une réduction issue du logiciel IRAF/DIMSUM. Les sources faibles apparaissent moins brillantes de 0,15 magnitude que celles attendues, les sources brillantes apparaissant de même magnitude que celles issues de la réduction par DIMSUM. Le logiciel IRAF/DIMSUM était le seul capable de traiter correctement l'estimation et la soustraction du fond de ciel des images IR. Cette solution n'a pas été adoptée à cause de la difficulté d'intégration des outils de IRAF.

- *Calibrage astrométrique des images de WFI* - Les images issues de l'instrument WFI sont faîtes de 8 CCDs. Chaque CCD est normalement repéré grâce aux indications CRPIX1 et CRPIX2 données dans l'entête des images FITS. Dans le cas de WFI, cette information est erronée et conduit à une échec systématique du calibrage astrométrique. Une procédure robuste et automatique est nécessaire afin d'éviter des corrections manuelles.

- *Traînées de satellites visibles sur les images réduites* - Les relevés optiques de EIS intègrent beaucoup d'heures d'observations, et plusieurs images sont affectées par des satellites qui traversent entièrement le champs de vision. Jusqu'à présent, les traînées sont masquées manuellement. Certaines sont encore visible sur les images réduites, et affectent les catalogues extraits. Le besoin d'un outil robuste automatique est important pour les futurs grands instruments comme VISTA ou OMEGACAM.

- *Correction de l'erreur d'illumination* - L'erreur d'illumination est un phénomène observé récemment avec les instruments à grand champs. Le point zéro des images réduites n'est pas constant sur toute l'image, et varie de 0,15 magnitude entre le centre et le bord des images. Les premières observations de ce phénomène sont faîtes en 1995 (Andersen et al., 1995). Ce problème a été reporté à EIS lors des premières réductions du relevé stellaire Pre-FLAMES observé avec WFI.

L'instrument WFI est le plus large de l'ESO. Il est utilisé par la majorité des relevés de EIS. Une image fait 64 MegaPixel, soit 128 Moctet, le temps de pose des observations varie de une a dix minutes. Il en résulte un taux d'observation de 0,088 à 0,53 MegaPixel par seconde. Le taux maximum correspond aux observations des standards photométriques ou des observations stellaires. Le taux minimum correspond aux observations sans sources brillantes, avec des temps d'intégration plus longs. Les relevés de EIS sont des larges programmes et sont faits d'une quinzaine de nuits d'observations reparties sur plusieurs mois ou années. Un relevé typique est constitué de 300 Goctect de données incluant les observations scientifiques, les images de calibrage et les standards photométriques. Ces valeurs sont des indicateurs pour le futur instrument VST (32 CCDs, 256Moctect par image).

Le taux d'acquisition des images IR est actuellement faible de l'ordre de 0,02 megapixel par seconde. Les instruments SOFI ou ISAAC sont faits d'un seul CCD de un megapixel. Dans le cas des futurs instruments IR utilisant plusieurs larges CCDs, le taux d'acquisition tendra vers celui des instruments optiques.

Les relevés de EIS sont multi-couleurs (optique et IR) et multi-instruments. Même si les données ne sont pas traitées en temps réel, il est important de les réduire rapidement afin d'anticiper la réduction des images issues des futurs larges instruments. Aussi, afin de traiter des observations multi-instruments, un outil commun de traitement des images est nécessaire afin d'éviter la création de plusieurs pipelines.

Avec les outils précédemment utilisés dans le cadre de EIS, il était difficile voir impossible de suivre les différents paramètres et étapes car une partie des réductions était faite à la main et avec de nombreux outils indépendants. La stratégie adoptée par IRAF pour suivre l'évolution des procédures est basée sur des mots clefs écrits dans l'entête des produits réduits. Cette solution ne permet pas un contrôle fin des paramètres ni l'exploitation des résultats intermédiaires comme par exemple les points d'ancrage utilisés pour le calibrage astrométrique.

Concept de base pour le nouveau pipeline

Afin de répondre aux prérequis listés précédemment, le pipeline est construit comme une bibliothèque informatique qui fournit une base commune pour les algorithmes et les procédures d'administration requises pour transformer les images brutes en produits finis de qualité scientifique. Les avantages de cette implémentation sont multiples: 1) cette stratégie permet la transparence et le contrôle totale entre les différents algorithmes, les options de bas niveau sont alors configurable en fonction de l'instrument du filtre ou d'autres facteurs; 2) La programmation par bibliothèque informatique permet un transfert par mémoire vive des données traitées consécutivement de procédures en procédures. On évite ainsi la programmation spécifique d'interfaces nécessaires pour la connexion d'outils hétérogène, le code source s'en trouve simplifié.

Le pipeline est basé sur le notion d'instrument générique. Cette notion, utilisée par exemple par l'outil IRAF/MSCRED, est définie pour supporter divers instruments optiques multi-CCDs. Pour le pipeline, cette notion est étendue pour supporter des instruments simple-ou multi-CCDs, optiques ou infrarouges. Un instrument est défini par: la disposition des CCDs au sein de l'instrument, la configuration des électroniques de lecture de chaque CCD. Le pipeline considère différents modes d'observation qui incluent parmi d'autres: les images de calibrage instrumental, les images des standards photométriques, les champs profonds, et les champs stellaires. Une description plus détaillée est fournie section 3.3.2. Pour commencer, le pipeline reconnaît deux types d'objets: le Bloc de Réduction (nommé RB) qui consiste en une collection d'images brutes, et le Mode de Réduction (nommé RM) qui dit au système comment les images doivent être réduites avec quels paramètres. Le RM dépend de l'instrument, du filtre et du mode d'observation.

Aussi, la parallélisation du code est prise en compte de la facon la plus simple. Le pipeline dresse la liste de toutes les actions à entreprendre (RM associé à un RB), puis affecte une action par processeur libre. Les actions étant indépendantes, la parallélisation est optimum et indépendante du nombre de CCD de l'instrument.

Parmi les différents algorithmes nécessaires pour la réduction, certains sont l'adaptation de technologies utilisées dans d'autres domaines du traitement d'image. Des problèmes rencontrés dans le traitement des images astronomiques sont similaires aux traitements des images terrestres enregistrées par satellites. Par exemple, le calibrage astrométrique trouve sont équivalent dans la mise en correspondance d'images satellites. Traditionnellement, le calibrage astrométrique se fait à partir de catalogues par la méthode dite de triangulation (Deul et al., 1995). Cette approche efficace, est lente surtout dans le cas d'observations galactiques ou la densité d'étoile est grande. La méthode utilisée dans le pipeline, est basée sur la transformée en ondelettes bi-orthogonales. Cette méthode dite de multi-résolution (Mallat, 1989) a été développée pour les images satellites de la terre. La procédure définie est très efficace pour les champs très denses (voir section 5.3).

Une autre technique aussi venue de l'analyse d'images terrestres est programmée pour la détection automatique de traînées de satellites qui sont fréquemment observées par les instruments grand-champs. Il est important de les masquer sur les images brutes afin d'éviter de les observer sur les produits finis. Les traînées non masquées seront visibles sur les images réduites, et aussi sur les catalogues extraits comme des points alignés. La procédure de détection utilise la transformée de Hough (Hough, 1962), qui permet de repérer des points alignées dans un catalogue.

Finalement, des procédures ont été développées pour répondre au prérequis, tels que l'estimation du fond de ciel des images infrarouges et l'estimation de l'erreur d'illumination pour les instruments grand-champs.

Les différentes procédures sont toutes contrôlées par le protocole Extensible Mark-up Language (XML). XML est un métalangage utilisé pour décrire d'une façon standard des balises délimitées par les symboles supérieur ($<$) et inférieur ($>$) des informations de toutes natures. HTML est le plus connu des langages à balises. Le protocole XML est développé par le "World Wide Web consortium". Des balises ont été spécialement définis pour caractériser les options des procédures, les résultats, et les instruments d'observation. Ce protocole est utilisé pour les trois fonctions suivantes: 1) paramètres d'entrée des procédures; 2) la communication entre les différents modules; 3) comme une base de données interne pour sauvegarder les résultats obtenus lors de la réduction.

Le pipeline est exécuté avec un fichier XML contenant toutes les informations: instruments supportés, RMs, et les actions à entreprendre. Sachant quel instrument est utilisé le programme trouve les informations nécessaires (noeuds XML) relatives à l'instrument, RMs ... Le fichier de configuration complet est comparable à une base de données car il contient toutes les informations de tous les instruments, et les RMs supportés.

Une flexibilité du format XML est la possibilité de séparer un large fichier en plusieurs qui sont liés entre eux par l'usage du protocole XInclude (World Wide Web consortium, 2001) un dérivé de XML. En pratique, les options de configuration sont réparties en deux fichiers XML liés. Le premier est court, et contient seulement les informations sur les actions à entreprendre, l'instrument choisi, la location des données brutes sur les disques durs de l'ordinateur. Le second contient la description de tous les instruments et RMs. Ce fichier est modifié pour améliorer des paramètres lors de réductions interactives ou pour la définition d'un nouvel instrument.

En sein du source code le protocole XML est largement utilisé afin de propager les options ou résultats entre les procédures, ou, d'analyser le fichier de configuration. La lecture d'un fichier XML, afin de rechercher un noeud particulier, est facilitée grâce au protocole XPATH (World Wide Web consortium, 1999) qui permet de faire des requêtes comme pour une base de données. XPATH permet une recherche fine au travers des arborescences des noeuds XML. Pour le pipeline, toutes recherches d'information ne se font que par ce moyen. Les nécessités d'utiliser le format XML et ses dérivés sont multiples: 1) l'analyse des fichiers de configuration se font grâce à une bibliothèque informatique externe (World Wide Web consortium, 2004) où les principaux protocoles XML sont programmés. Cette stratégie évite la programmation fastidieuse de fonctions dédiées à la lecture de fichiers de configuration; 2) les options d'une procédure et des procédures de bas niveaux qui lui sont intégrées sont naturellement structurées en arbre. Le format XML correspond exactement à ces structures. Les options et celles des niveaux inférieurs sont donc administrées par une arborescence XML. Ce procédé flexible permet la modification d'options dédiées à un procédure sans affecter les autres options de bas niveaux.

Lors de la réduction des RBs, de nombreuses informations importantes émanent des procédures comme par exemple: la valeur moyenne du fond de ciel calculée pour chaque image avant la suppression du fond de ciel, les points d'ancrage utilisés pour le calibrage astrométrique. Toutes les informations issues du calcul sont écrites dans un fichier XML. Pour chaque RB réduit, un ficher XML est crée. Il contient l'identification des images brutes, et les mesures faites pour chacune. Ces informations peuvent être exploitées indépendamment par l'analyse des fichiers XML de réduction. Le format XML n'étant pas le plus facile à lire visuellement, un protocole a été défini pour convertir un fichier XML en un autre format en sélectionnant les informations désirées. Le protocole XSL est communément utilisé pour convertir des fichiers XML en pages HTML exploitables visuellement. XSL est écrit dans une langage particulier utilisant la sémantique XML. Il défini une feuille de style utilisée pour la transformation d'un fichier XML. Une feuille de style est appliquée à une collection de fichiers XML. La transformation peut avoir un but informatif visuel, comme par exemple résumer les statistiques des produits finis, ou, un transformation en vue d'une analyse automatique comme par exemple le tracé d'un graphe. Un exemple de conversion des options d'un RM au format XML en page HTML est illustré figure 3.14.

le pipeline EIS/MVM

Le développement du pipeline représente une large extension d'un travail commencé à l'Observatoire de la Côte d'Azur sous la supervision de Albert Bijaoui. Il s'agissait alors du développement d'un outil d'extraction de sources par une analyse en ondelettes: "Multi-scale Vision Model" (MVM). A l'ESO le code source a presque triplé afin de remplir les prérequis de l'équipe ESO Imaging Survey (EIS). Le code C++ est indépendant de la plate-forme utilisé. Il a été testé avec des machines telles que: PC/Linux, SUN, et Alpha Digital. Le pipeline est utilisé en mode interactif ou supervisé par le système construit par l'équipe EIS. Depuis décembre 2003, le logiciel (Vandame, 2004) est accessible au public. Il est actuellement utilisé à l'Observatoire de La Silla par l'équipe du télescope de 2.2m, et aussi dans une dizaine d'instituts en Europe.

Description succincte

Le point de départ du pipeline est une collection d'images brutes, qui dans le cas de cette thèse, sont issues de l'archive automatisée de l'ESO. Trois types d'images sont généralement requises: les images pour le calibrage instrumental, (nommées en anglais bias, dark et flat), les images des champs contenant des standards photométriques pour calculer la solution photométrique des nuits d'observation, et finalement, les images scientifiques. La collection d'images doit être choisie avec soin afin d'assurer un nombre suffisant d'images de calibrage valides. Actuellement, le pipeline ne calcule pas le calibrage photométrique.

Pour une réduction correcte, le pipeline a besoin d'images de calibrage additionnelles telles que: *bias réduit*, *dark réduit*, *flat réduit*, *carte de mauvais pixels*, *carte des pixels chauds*, *carte de poids*, *carte de franges d'interférences*, *harmonisation des gains*, *carte d'illumination*, *pixel de reference*.

Les images sont communément observées en séquence, formant ce qui est appelé à l'ESO un *Bloc d'Observation* (OB). Un OB correspond à un groupe d'images observées consécutivement ayant les mêmes caractéristiques (filtre, temps de pose, position nominal sur le ciel), et même type (calibrage, standard photométrique, science). Les images au sein d'un OB sont généralement observées avec des transitions relatives entre elles. Les translations relatives entre les images d'un OB suivent une configuration nommée motif d'observation. En pratique, le motif d'observation est destiné à remplacer les mauvais pixels d'une images par ceux valides des autres images du OB, et dans le cas des instruments multi-CCDs, de profiter des toutes les images qui permettent de compléter l'espace entre les CCDs.

Les OBs sont préparés avant les observations. Occasionnellement, un OB est incomplètement observés à cause, par exemple, des mauvaises conditions atmosphériques. Pour la réduction, la notion de groupe est aussi importante et les images sont regroupées en groupe nommé Bloc de Réduction (RB). Un RB consiste en une collection d'images et peuvent être équivalent aux OBs, ou différents pour des raisons d'optimisation de la réduction.

Dès que un RB est prêt, et un RM lui est associé, le pipeline produit une image réduite. La réduction commence avec les images de calibrage instrumental pour produire les bias, dark, et flat réduits. D'autres RBs techniques utilisés pour le calibrage instrumental sont aussi réduits par le pipeline: les cartes de mauvais pixels qui enregistrent la position des mauvais pixels; les cartes de poids qui enregistrent l'amplitude du bruit des images brutes pixel à pixel; les coefficients d'harmonization des gains moyens des CCDs pour fixer un gain unique aux images réduites; et finalement les cartes d'illumination pour corriger les variations de point zéro dans le champs de vision.

Dès que les images de calibrage instrumental sont prêtes, corrigées par les RBs techniques, et les différents catalogues et grilles de projection pour le calibrage astrométrique sont sur disque, la réduction des images scientifiques peut commencer. Ce processus est le plus complexe et dépend de la nature des observations et de l'instrument utilisé. Le but de la réduction d'un RB est de produire une image réduite avec une carte de poids associée qui caractérise la variation d'amplitude du bruit pixel à pixel. Les images au sein d'un RB sont combinées grâce à un calibrage astrométrique calculé soit pour chaque image individuelle, ou pour une image résultante qui combine toute les images brutes du RB. Aussi, durant la réduction plusieurs effets affectant globalement les images sont corrigés. Les principaux sont: 1) annulation de la signature instrumental sur les images brutes; 2) soustraction du fond de ciel; 3) estimation des franges d'interférence qui sont issues des raies d'émission du ciel observées dans certaines conditions. Aussi, trois types d'effets affectent partiellement les images brutes, et sont corrigés: 1) les satellites artificiels, qui traversent tout le champs de vision durant le temps de pose et apparaissent comme des traînées rectilignes; 2) les rayons cosmiques apparaissent répartis aléatoirement sur les images comme autant de points très compacts et brillants. 3) l'effet *cross-talk* qui est un signal fantôme produit par une étoile brillante qui apparaît sur les autres quadrant de la caméra. Ce phénomène ne concerne que les CCDs équipés de plusieurs convertisseurs électroniques. Dans le cas de l'infrarouge, ce phénomène affecte largement les images. Une étoile brillante qui dépasse le niveau de saturation du détecteur affecte les lignes ou elle se trouve. Ces lignes ayant une moyenne supérieure au fond moyen, se reproduisent sur les autres quadrants par effet "cross-talk" (voir illustration figure 3.11).

Preparation des données

Dès que les données brutes sont sur disques, et les RMs sont proprement définis (comme présenté section 3.1), la réduction peut commencer. Avant, des étapes de préparation doivent être accomplies afin de: 1) préparer les images (découpage des images brutes, filtrage des mots clefs, vérification du la précision du pointage, vérification de la position des CCDs au sein de 'instrument); 2) préparation des fichiers nécessaires pour l'astrométrie (catalogue astrométrique, grille de projection pour les produits finis).

- *Découpage des images brutes* - Les images brutes sont souvent représentées par un fichier FITS contenant plusieurs extension pour les instruments multi-CCDs. Ces fichiers sont découpés de telle sorte que chaque image soit faite de un fichier par CCD. Cette étape concerne seulement les instruments multi-CCDs.

- *Filtrage des mots clefs des entêtes des images* - Chaque instrument à sa propre convention pour désigner les informations utiles d'une image (position sur le ciel, temps de pose, date d'observation, filtre utilisé). Ces informations sont traduites dans un système unique commun aux instruments supportés.

- *Vérification du pixel de référence* - Le pixel de référence est indiqué dans l'entête des images par les deux mots clef CRPIX1 et CPRIX2. Il indique quel pixel se trouve à la position sur le ciel qui est indiquée par les mots clef CRVAL1, CRVAL2. Cette information est parfois imprécise due à l'erreur de pointage, ou tout simplement ne se trouve pas dans l'entête. Cette étape est destinée à calculer cette position par corrélation croisée entre une image brute et un catalogue astrométrique.

- *Identification des CCDs* - Pour les instruments faits de plusieurs CCDs, il est important d'identifier avec certitude leurs positions relatives. En effet, cette information n'est pas explicitée d'une façon claire et stable dans l'entête des images. L'identification se fait alors avec les pixels de référence calculés précédemment pour tous les CCDs.

- *Définition des références de projection* - Pour les images scientifiques en plus de la définition de RBs, il est important de préciser une référence de projection afin que tout les RBs réduits partages la même projection pour être combiner facilement. Un projection se définie par une position sur le ciel (CRVAL1, CRVAL2), une taille de pixel avec orientation (CD1_1, CD1_2, CD2_1, CD2_2), et un type de projection (CTYPE1, CTYPE2) souvent égal à tangente ou conique (TAN et COE).

- *Chargement des catalogues astrométriques* - Le calibrage astrométrique se fait grâce à des catalogues externes. En général, le catalogue GSC2.2 ou USNO conviennent dans la majorité des cas. Pour les instruments à petit champs de vision, ces catalogues de référence ne sont pas suffisamment dense pour les champs extragalactiques. Il convient alors d'utiliser des catalogues adaptés issus d'observations optiques du même champs prises par un autre instrument.

Réduction des RBs de calibrage, et RBs techniques

- *Création des images de calibrage réduites* - Les images de calibrage (bias, dark et flat) doivent être combinées afin de produire les images de calibrage réduites. Les images brutes sont combinées par médian afin de retirer les rayons cosmiques visibles sur les images brutes. Dans le cas des flats, les images sont d'abord divisées par leur moyenne. Les flats réduits ont donc une moyenne égale à un.

- *Détermination des mauvais pixels* - Les mauvais pixels sont toujours à la même position physique sur un CCD. Il suffit de les détecter sur des images réduites de calibrage. Une procédure est destinée à détecter des mauvais pixels par comparaison de leurs amplitudes avec la moyenne locale (voir description de la procédure section 4.1, et son application section 5.4.2).

- *Carte de franges d'interférences* - Les franges d'interférences sont observées sur les images brutes avec certains filtres. La combinaison avec un médian de plusieurs images observées avec des translations, permet de faire disparaître presque totalement les objets astronomiques des images, et alors de fournir une carte dite de franges d'interférences, qui sera utilisée lors de la réduction d'images scientifiques affectées par ce phénomène.

- *Normalisation des gains moyens des CCDs* - Chaque CCD est caractérisé par un gain moyen mesuré en électrons par Niveau numérique ($e-/ADU$). Dans le cas des instruments multi-CCDs, les gains moyens des CCDs ne sont pas identiques et varient typiquement de 10% d'un CCD à l'autre. Cette variation de gain a un impact sur le calibrage photométrique, est doit être harmonisée. La solution proposée par le pipeline est de mesurer les variations de gain moyen, et, de corriger les flat réduits afin que des images traitées par les flats réduits corrigés aient un gain unique pour tous les CCDs. La mesure de la variation de gain de fait par l'évaluation de fond de ciel entre CCDs voisins sur des images brutes réduites par un bias et flat réduits (voir description de la procédure 4.2, et son application section 5.4.2).

- *Correction des erreurs d'illuminations* - Les instruments à grand-champs utilisant un réducteur de focale placé juste au dessus de l'instrument, soufrent de l'erreur d'illumination. Cette erreur se traduit par une variation du point zéro le long des images réduites (amplitude de 0.15 magnitude en général entre le centre et le bord). Le pipeline propose une méthode pour mesurer ces erreurs. Il en résulte une carte de flux utilisée pour corriger les flats réduits. Les images scientifiques réduites avec ces flats réduits corrigés ont alors un point zéro stable (Voir description de la procédure section 4.3, et son application section 5.3.4).

Réduction des images scientifiques

Les images scientifiques sont regroupées en RBs afin d'être réduites par blocs. La notion de groupe est importante pour une réduction optimale. Par exemple, dans le cas des images infrarouges, celles-ci sont d'abord combinées en tenant compte des translations entre elles, afin de produire une image qui est ensuite calibrée astrométriquement. Les RBs sont construits et correspondent à moins de une heure d'observation. Les images groupées ont les mêmes propriétés (filtre, temps de pose, position sur le ciel). Les RBs sont associés avec un RM. Le tableau 3.8 indique les RMs crées afin de supporter la majorité des types observations scientifiques.

Un RM se caractérise par plusieurs modules optionnels: cinq sont destinés aux traitements globaux des images, et trois sont destinés aux traitements locaux. La figure 3.9 illustre les différents modules et leur ordonnancement.

- *1) traitement des effets instrumentaux* - Le premier module à être activé est utilisé pour appliquer les images de calibrage réduites (bias, dark et flat réduits) sur les images scientifiques afin de retirer les effets instrumentaux. A cette étape, une carte de franges d'interférences peut être utilisée afin de soustraire les franges observées sur les images brutes (selon la procédure décrite section 4.6).

- *2) Estimation et soustraction du fond de ciel estimé pixel à pixel* - Dans le cas ou les images ont des franges d'interférence, ou dans le cas des images infrarouges, le fond de ciel doit être estimé pixel à pixel. Il est soit soustrait par une carte de frange d'interférence, ou soit il est estimé avec les images du RB. Cette deuxième solution est nécessaire pour l'infrarouge où le fond de ciel varie avec une constante de temps typique de 10 minutes. Une procédure robuste d'estimation du fond de ciel pixel à pixel en deux passes est définie (voir section 4.5).

- *3) Estimation et soustraction du fond de ciel à larges échelles* - Pour la plupart des observations dans le domaine visible, le fond de ciel causé par l'atmosphère est une signal de basse fréquence qui peut s'estimer sur les images scientifiques n'ayant pas d'objets astronomiques étendues. Le fond de ciel est estimé par un filtrage médian itératif (voir la description de la procédure 4.4).

- *4) Calibrage astrométrique relatif* - Ce module est dédié pour le calibrage astrométrique des images d'un RB relativement à une des images prise comme référence. Ce calibrage, dit relatif, est destiné à la réduction des RBs infrarouges: la solution astrométrique relative étant plus robuste pour des cubes de données où peu de sources apparaissent. Les sources visibles sont associées par une méthode utilisant la transformée en ondelettes bi-orthogonale (voir section 4.7). La distorsion entre les images est modélisée par une fonction polynomiale d'ordre 1. Les images sont transformées par leur polynôme de distorsion, puis combinées pour produire une image associée à une carte de poids correspondante.

- *5) Calibrage astrométrique absolu* - Ce module est similaire au module (4). Le calibrage astrométrique absolu se fait avec un catalogue préalablement transformé en une image servant de référence pour toutes celles du RB. La procédure exécutée est la même que pour le module (4), les options sont adaptées au calibrage absolu, le degré du polynôme de distorsion est 2 pour les instruments à grand-champs afin de modéliser les distorsions optiques.

- *A) Détection de traînées de satellites.* - Ce module est chargé de détecter et masquer les traînées de satellites par une procédure utilisant la transformée de Hough (voir la description complète section 4.8). Cette procédure est exécutée avant de fusionner les images lors de l'exécution du module (4) ou (5).

- *B) Rejet des rayons cosmiques et autres défauts.* - Une procédure est dédiée pour détecter et masquer les mauvais pixels résiduels ou ceux affectés par des rayons cosmiques. Cette procédure est basée sur un rejet des pixels comparés à ceux des autres images du RB et à la même position sur le ciel. Il faut donc un minimum de trois images pour exécuter cette procédure, et aussi la connaissance de la distorsion astrométrique de chacune. Ce module est exécuté juste avant que les images soient combinées lors de l'exécution des module (4) ou (5).

- *C) Estimation de l'effet "cross-talk"* - Dans le cas des instruments infrarouges, la saturation des étoiles et l'effet "cross-talk" sont estimés sur les RBs réduits. Ce module est exécuté à la suite du module (4) ou (5).

Creation des produits finis

Dans le cas de relevés profonds observés durant plusieurs nuits, une position sur le ciel peut être observées plusieurs fois avec la même configuration (temps de pause, filtre). Chaque groupe d'images observées continûment est regroupée en RB. L image finale réduite, ou produit fini, est construite en combinant chaque image issue de la réduction d'un RB. Cette fusion se fait en tenant compte de: 1) la variation de transparence de l'atmosphère qui est calculée par le calibrage photométrique des nuits d'observations; 2) la variation de l'amplitude du bruit enregistrée par les cartes de poids associées aux images. La co-addition pondérées permet de fournir le meilleur rapport signal sur bruit des produits finis. Si plus de trois RBs réduits sont combinés, alors une seconde passe de suppression de rayons cosmiques est appliquée.

Algorithmes et procédures

Détection de mauvais pixels

Les mauvais pixels sont ceux qui ne réagissent pas de façon linéaire lors de l'exposition à un flux de lumière. On note parmi eux: 1) les pixel froids, qui n'intègrent aucun électrons; 2) les pixels chauds, qui accumulent très vite des électrons et tendent vers la saturation. La détection de ces mauvais pixels est importante, car sinon, ils restent visible sur les produits finis. La procédure utilisée pour détecter les rayons cosmiques sera capable de retirer quelques mauvais pixels mais la majorité d'entre eux ne seront pas masqués.

La détection se fait avec les images de calibrage réduites telles que le bias, dark et flat réduits. Un mauvais pixel est supposé avoir une amplitude différente de ses voisins. Une image de calibrage réduite est soustraite par sa version lissée par des filtrages médians successifs. Il résulte une image ou seuls les fins détails sont visibles. Ceux-ci, assimilés à de mauvais pixels, sont détectés par seuilage à plusieurs fois l'amplitude du bruit mesuré.

Le dark réduit et la meilleure des images de calibrage capable de détecter les pixels qui affecte la matrice CCD seulement lors de longs temps de pose. Malheureusement, dans le cas des observations optiques, ces images sont peut ou pas observées. De nombreux mauvais pixels invisibles sur les autres images de calibrage réduites ne sont pas détectés. La solution consiste à utiliser les image scientifiques où les mauvais pixels sont visibles. Afin de retirer les sources astronomiques deux filtrages médians, l'un sur les images individuelles l'autre pour la fusion d'un groupe d'image, sont appliqués sur un groupe d'images scientifiques. L'image résultante est utilisée pour la détection de pixels chauds. L'impact de cette procédure est illustré section 5.4.4.

Harmonisation des gains moyens pour les instruments multi-CCDs

L'harmonisation des gains est une étape obligatoire pour les instruments multi-CCDs, chaque détecteur ayant sont propre gain moyen. La procédure proposée utilise le fond de ciel d'une observation comme référence. Le ciel est supposé constant ou à faible variation. Chaque image CCD d'une observation est traitée avec un bias et un flat réduit. Le fond de ciel est mesuré sur les quatre bords d'un CCD. La valeur moyenne d'un bord de CCD est connectée au bord voisin d'un CCD contiguë. Le rapport des deux fonds de ciel renseigne sur le rapport des gains moyens des deux CCDs. Une étude de la variation de gain moyen mesuré par cette procédure sur l'instrument WFI est illustrée section 5.4.2.

Correction d'illumination

L'erreur d'illumination est due aux réflexions secondaires entre le détecteur et le correcteur de champs. Ces réflexions s'additionnent aux images brutes. Les flats observés puis réduits sont, comme toutes images, affectés par ce phénomène. Pour les images scientifiques traitées avec les flats réduits l'erreur d'illumination devient une erreur multiplicative qui affecte le points zéro des images réduites. Celui-ci évolue au long de l'image réduite suivant une fonction nommée erreur d'illumination.

Cette fonction est dépendante du filtre, mais stable dans le temps. L'estimation de cette fonction peut se faire par association de sources extraites d'un image réduite avec un catalogue photométrique. En pratique, cette solution n'est pas toujours applicable pour les grands champs, car les catalogues photométriques disponibles ne couvrent que de petite surface.

La méthode adoptée dans ce travail, est basée sur une approche relative. L'estimation de la fonction d'illumination se fait avec des images consécutives observées avec des translations entre elles. Les magnitudes relatives entre les différentes mesures de brillance de l'étoile observée sur les différentes images donnent une estimation du gradient de la fonction d'illumination en ces points. En intégrant cette mesure pour toutes les étoiles, la fonction d'illumination est modélisée par une fonction polynomiale d'ordre 4. Les flats réduits sont alors multipliés par la fonction d'illumination. L'application de cette méthode est illustrée section 5.3.

Estimation du fond de ciel large échelle

Sur les images scientifiques, sont visibles les sources observées et aussi le fond de ciel constant ou à faible variations. Le fond de ciel peut être estimé sur les images brutes si les objets astronomiques étudiés sont de petites tailles.

Le fond de ciel est estimé par un version lissée par des filtrages médians successifs. Cette procédure définie une transformation pyramidale à base de médian.

Estimation du fond de ciel pixel à pixel

Dans le cas des images infrarouges affectées par des franges d'interférences ou par un fond de ciel de nature haute fréquence, le fond de ciel doit être estimé pixel à pixel.

Cette estimation peut se faire au sein d'un RB qui contient un nombre significatif d'images. Dans ce cas, une carte de fond de ciel est construite en fusionnant le cube d'images formée par le RB avec un filtre médian. Il résulte une carte de fond de ciel qui est appliquée à toute les images du RB.

Cette estimation est rendue plus robuste en rejetant les pixels significatifs des images du RB. Un masque est préalablement formé à partir des images astrométriquement calibrées, puis combinées. Cette méthode en deux passes permet l'estimation non-biaisé du fond de ciel au sein d'un RB.

Calibrage astrométrique avec transformée en ondelettes

Le calibrage astrométrique se calcul en trois étapes: 1) Association entre un catalogue de référence, et les sources extraites d'une image à calibrer; 2) Calcul d'un modèle de distorsion à base de polynômes par la méthode des moindres carrés; 3) Distorsion de l'image calibrée pixel par pixel suivant le modèle de distorsion.

La première étape est primordiale est doit être robuste afin de rejeter les sources ayant bougées significativement entre l'intervalle de temps qui sépare le catalogue de référence et l'image à calibrer, et aussi pour associer avec certitude des sources très denses. La méthode proposée dans ce travail est basée sur la transformée en ondelettes bi-orthogonal. Cette transformation décompose un image en différentes résolutions de plus fins détails aux larges composantes. La décomposition en résolution permet de contraindre la distance minimale entre les maxima locaux d'une image. Pour associer un catalogue de référence avec les sources extraites d'une image, le catalogue est transformé en image où chaque point est représenté par un fonction de Gauss à deux dimensions. L'image de référence et l'image à calibrer sont transformées dans l'espace en ondelettes. Les maxima locaux significatifs de chaque plan en ondelettes sont extraits. A l'échelle de plus large résolution, les maxima locaux des deux images sont associés avec une fenêtre de recherche de taille donnée par la longueur d'onde de la plus haute fréquence représentée à ce plan. Les points associés sont utilisés pour calculer un distorsion polynomiale d'ordre un. L'association des points est alors déduite aux plans inférieurs en tenant compte de la première distorsion calculée.

Cette méthode itérative est robuste car la fenêtre de recherche utilisée au plan de résolution maximale est égale à plus ou moins un pixel correspondant a plus ou moins 0.25 arcsec pour les instruments optiques typiques.

Détection de traînées de satellites avec la transformée de Hough

Les satellites traversent le champs d'observation rapidement et sont observés comme des traînées. Pour chaque image brute un catalogue de maxima locaux, dont la valeur est plus grande que trois fois l'amplitude du bruit, est extrait. Les points rigoureusement alignés sont la signature d'une traînées de satellites. Chaque point du catalogue est transformé dans l'espace de Hough en une droite. Des points alignés sont transformés en une famille de droites qui se coupent toutes en un même point dont les coordonnées dans l'espace de Hough sont la pente et l'abscisse à l'origine de la droite passant parmi les ponts alignés catalogués.

La procédure consiste en l'extraction d'un catalogue de maxima locaux et de la transformée de Hough du catalogue. Les points de condensation significatifs détectés dans l'espace de Hough traduisent la présence de points alignés dans l'espace direct. Un masque est crée pour encadrer chaque droite détectée.

Application

Relevé Chandra Deep Field South

Le relevé Chandra Deep Field South (CDFS) est centré sur le relevé profond observé par le télescope rayons X. Le relevé est observé par l'instrument WFI pour les bandes U, B, V, R et I, et avec l'instrument SOFI pour les bandes J et Ks.

Les deux articles décrivant la réduction sont présentés en annexe A et B.

Relevé GOODS/ISAAC

Le projet GOODS regroupe les observations très profondes du champs CDFS observés par une grande variété d'instruments basés sur terre ou dans l'espace. Le relevé GOODS/ISAAC est observé par l'instrument infrarouge ISAAC. plus de 250 heures d'observation sont intégrées par les mosaïques finales des filtres J, H et Ks. L'image finale est constituée de 24 champs de vision de l'instrument ISAAC.

Relevé Pre-FLAMES

Le relevé Pre-FLAMES est destiné à fournir des cibles pour le nouveau spectroscope FLAMES. La position astrométrique doit avoir une précision minimale de 0.2 arcsec. Les champs sélectionnés pour ce relevés sont des champs galactiques comme par exemple des amas ouverts, des amas globulaires, des nébuleuses, le petit et grand nuages de Magellan. Les champs sont observés avec l'instrument WFI avec les filtres B, V et I. l 'article présenté en annexe C illustre la réduction des premières images observées. Lors de la dernière réduction de ces observations, la correction d'illumination a été activée.

Relevé XSSS/WFI

Le relevé XSSS est l'observation optiques de 15 champs profonds observés par l'instrument rayon X XMM. Ces champs sont observés par l'instrument WFI avec les filtres B, V, R et I. Le temps d'intégration des 15 champs et de 90 heures réparties sur un an et demi.

Conclusion

Le pipeline a atteint un niveau de fonctionnement quasi automatique. Il est maintenant distribué, et utilisé par de nombreux utilisateurs. Lors du travail de thèse, plus de 40 nuits de l'instrument WFI et ISAAC ont été réduites. Cela correspond à la réduction de 3% des observations scientifiques de ces instruments.

Le futur de ce pipeline, est l'intégration ou l'amélioration de procédures. En particulier pour le calcul astrométriques des instruments multi-CCDs. La méthode actuelle calcule une solution astrométrique par CCD, au lieu d'un calibrage globale en tenant compte de la position relative des CCDs.

Ce projet tend naturellement vers la notion d'Observatoire Virtuel (VO), car le pipeline est capable de traiter des images issues de différents instruments. Pour tendre vers cette notion, des outils de gestion et requête des archives d'images doivent être développés pour utiliser automatiquement le pipeline.

Chapter 1

Introduction

Over the past decade Astronomy has witness an unprecedented growth - never before have so many and so powerful facilities become available to astronomers at the same time. These facilities have allowed astronomers to probe the very large red-shift Universe, to map the microwave background, to carry out large red-shift surveys probing large volumes of space over a broad range of red-shifts from the nearby Universe to z>3. Combined a host of exciting new results to discover new types of rare objects such as very cold stars and quasars at red-shift as large as 6.

This incredible progress has been achieved thanks to the enormous technological advances in detector and information technology of recent years. An important side effect of these developments has been to provoke a flood of data to be stored and processed. And still more is in store for the next decade with new ground- and space- facilities being currently built to cover the entire wavelength domain.

Among these new facilities, particularly challenging has been the development of large-format CCD detectors, both in optical and more recently in infrared, with modern instrument having field-of-views approaching the size of large photographic plates (degree scale) of yesteryears but with a performance many times larger. These instruments, mounted on dedicated telescopes, lead to rates of gathering image data of tens of million of pixels per second that need to be efficiently processed to avoid a glut of data and enable the effective compression of the large amounts of raw data into significantly smaller volumes of science grade products.

Wide-angle imaging surveys have had an important role in Astronomy but until recently they relied primarily on photographic plates. Still surveys such as Palomar and those carried out in the UK Schmidt have served as an essential foundation for all the work done in observation astronomy until the end of last century. It was from these data that statistical studies involving counts were conducted (Shane and Wirtanen, 1954), clusters of galaxies identified (Zwicky et al., 1968; Abell et al., 1989; Corwin et al., 1985). A major step forward was possible with the systematic digitalization of the photographic plates using densitometers as done by the british teams APM (Maddox et al., 1990) and Edinburgh group. The resulting data have been used for a variety of statistical studies (Efstathiou et al., 1988) as well as to provide samples for a variety of follow-up work (*e.g.*, SSRS2, 2dF) including large spectroscopic surveys conducted in 4-meter class telescopes, which were the basis of great advances in observational cosmology.

In the meantime, starting in early 80's a steady progress was achieved in the technology of

CCD as well as infrared detectors, with improving quality (cosmetic, lower dark current and readout noise) and increasing size. This progress led at the end to a many-fold increase in the sensitivity of the detectors and a leap in the depth to which imaging surveys could reach in reasonable integration times. This came at particularly important time, namely at the time new, large-aperture telescopes (*e.g.*, Keck, Gemini, VLT) were being commissioned, with the spectroscopic limit greatly exceeding the depth of available catalogues extracted from photographic plates.

In the 90s the progress of the past decade led to a new generation of digital surveys with diverse scientific goals. These included time-domain surveys (*e.g.*, EROS (Aubourg et al., 1995), OGLE (Udalski et al., 1992), MACHO (Alcock et al., 1997)) primarily seeking to detect micro-lensing events associated with brown dwarfs and the determine their contribution to the mass budget of the halo of our Galaxy; wide-angle near-infrared surveys (*e.g.*, DENIS (Epchtein et al., 1994, 1997), 2MASS (Skrutskie et al., 1997)), and the more ambitious wide-angle, multicolor optical SDSS photometric survey over the entire northern sky. Most of these surveys were self-contained in the sense that main science results were to be extracted from the surveys themselves or of existing facilities

Nowadays, the surveys are achieved with large multi-chip instruments. The EIS surveys are using among others the Wield Field Imager (WFI) made of 8 CCDs and mounted at the 2.2 meter telescope at La Silla. The acquisition rate of images quoted in megapixel per second, is now an unique estimator that imposes a scale in the development of the archive system connected to them, and also imposes the processing software to be fully automatized and fast. In case of the WFI, the mean acquisition rate is 0.25 megapixel per second. With the current new instrument such as Megacam mounted at the CFHT telescope, the mean acquisition rate is roughly 1.3 megapixel per second. For the time being, this instrument is the largest available, it is made of 36 CCDS.

Also, with the IR surveys, the data rate are in practice higher due to the short exposure time made at those wavelengths. The processing of the IR domain is also more complicated as one needs to deal with the complex patterns of the IR sky background. This implies more complete procedures, that must be concatenated within a complete pipeline to massively reduced such data.

It is important to emphasize that while most softwares available when used properly can yield equally good results, most have been designed to handle small data sets and the challenge is to be able to handle large optical/infrared data sets robustly and in an unsupervised way. In addition, if the system is supposed to be used to handle survey data from different instruments and different observing strategies for distribution some of the top requirements are that it should be instrument independent, capable of handling single- and multi-chip optical and infrared instruments (coping with effects characteristic of different wavelength domains), have a high-throughput and be able to generate extensive and comprehensible logs thus providing users of the survey data the required information about the process. Given the degree of sophistication it is clear that more than a history in the FITS header is required.

The primary goal of this work has been to develop a modern software system that would respond to the challenges outlined above. In chapter 2 the basic requirements for building such a modern software reduction system are presented. This is followed by a brief discussion of the previously available packages and how they fail to meet the requirements. In chapter 3, an overview of the system developed is presented, including some background information on the C++ library that underpins the entire development. Details about some of the key algorithms used by the pipeline are presented in Chapter 4, including de-fringing, large- and small-scale background estimation, automatic identification and masking of satellite tracks, a common feature in wide-field imagers, bad pixel rejection and astrometry. In addition, techniques to handle specific issues of wide-field, multi-chip instruments are also discussed, including illumination correction. In Chapter 5, the pipeline is used to deal with real data from a variety of imaging surveys being conducted at ESO by the ESO Imaging Survey (hereafter, EIS). These surveys involve different optical and infrared imagers, different strategies and extended time baseline. In this chapter, the results of the reductions obtained using the pipeline are compared, whenever possible, to those obtained by other authors using different tools. Not only is the quality of data compared but also the speed at which the reductions are carried out. The latter is essential to meet the requirement for the software to be the data reduction engine in a mass production environment. Finally, In chapter 6, conclusions are presented with a brief discussion of some of the areas that can be further developed in the future and their importance.

Chapter 2

Requirements for a modern image pipeline

2.1 State-of-the-Art

Until very recently the reduction of CCD images were carried out mostly using standard packages such as IRAF (Tody, 1986) and MIDAS (Banse et al., 1983) developed by the main astronomical centers in the US and Europe, and commercial packages such as IDL (Research Systems Inc, 2004; Landsman, 1995). These systems are essentially tool boxes which provide the basic functionalities to operate on images, well-defined procedures to carry out a specific task such as: creation of master calibration frame or to flat field a set of science frames. The primary objective of these packages was to enable individual users to carry out the reduction of a finite amount of data in a semi-automatic way. It was never envisioned to used them to built high-throughput image processing system for unsupervised operation over long stretches of time as required today.

Even though possible building a pipeline from these tasks is neither desirable nor does it lead to the construction of efficient systems. There are several reasons for that. First, because the basic algorithms have either to be used as they stand, or must to be adapted to conform with the existing environment. Second, because the communication between modules needs to be done via read/write. Third, some of the important modules were developed by individual users and may not have the required support. Fourth, the development of new modules may have to be done in less than universal language as is the case of SPP which underpins IRAF. This is the case of older systems such as IRAF and MIDAS, the first being more popular with astronomers. It is important to emphasize that the first pipeline built by the ESO Imaging Survey (EIS) project was made to handle optical instruments including multi-chips and wide-field imagers. It made extensive use of IRAF tasks such as MSCCDRED (an extension of CCDRED) and DRIZZLE (Fruchter and Hook, 2002) developed for HST images and later adapted for the EIS pipeline.

Nowadays there has been a paradigm shift from this type of development toward a new one based on the use of libraries, consisting of not only basic image operations but also more complex tasks. The main difference with the previous implementation is that the libraries are written in for instance C or C++ therefore being more efficient and enabling the code base to be easily expandable and providing the required infrastructure for building a pipeline. This was the philosophy of ECLIPSE (Devillard, 2001) developed at ESO, FLIPS developed by Kaiser's group in Hawaii.

Modern image processing pipelines are, nowadays, built around one of these libraries. The difference between these pipelines are: the algorithms provided by the underlying library, the use or not of "external" modules, and the manner by which the different modules communicate with each other and are wrapped together in an end-to-end system. These choices also depend on the mode of operation of the pipeline. To a large extent, the implementation is dictated by the volume of data to be processed, and the scope of the pipeline, for instance, if it is dedicated to one or several instruments. The different library/wrapping combinations lead to major differences in the degree of automatization of the system, the quality of the reports obtained, the cosmetic quality of the products and above all the throughput of the system as measured by the ratio of the number of pixels that can be processed per unit of time for sustainable operation. Normally, the convention of mega-pixels per second (Mpix/sec) will be adopted in the present work. It is important to emphasize that while the quality of the final science grade products may be the same the data rate may vary significantly from one implementation to another, impacting on the required resources.

For those with available descriptions such as Terapix, Bonn and OmegaCam; Terapix has developed their own algorithms to deal with astrometric calibration: Astrometrix (Radovich, 2002) and to correct the distortions: SWARP (Bertin, 2002) as well as LDAC tools developed by the DENIS project (Deul, 1990) and expanded by the EIS project for the manipulation of catalogs, all wrapped by Perl scripts. The group in Bonn utilizes the FLIP library (Cuillandre, 1999) for image processing, routines such as LDAC tools, Astrometrix and SWARP for advanced processing, all wrapped by shell scripts. Similarly, the OmegaCam pipeline developed for regular operations of VLT utilizes the Eclipse library (Devillard, 1997), the routines mentioned above and Python as a wrapper.

While the approach outlined above gives developers more flexibility and enables the plug-in of different algorithms an alternative implementation adopted by the EIS project, is to consider the pipeline proper simply as another level of building library tasks, moving up in the hierarchy of complexity. This solution yields several advantages among which: 1) it facilitates the interface and communication between different tasks as they share the same environment; 2) one can obtain a significant increase in performance both in terms of sheer speed as well as facilitating the unsupervised processing by by-passing read/write operations needed by the use of stand-alone modules and using memory most of the time; 3) there is no need for a external wrapper while processing images, which in the case of EIS is done exclusively using the so-called *Alambic* which is the pipeline routine.

In addition, to these advantages which depend on the way the pipeline is implemented, the EIS/MVM library incorporates a host of new algorithms. Most of these new algorithms, described in more detail in chapter 4, have been developed for remote sensing which provide great improvements using wavelet decomposition and a multi-resolution approach.

Finally, it is also important to distinguish between a image processing pipeline, which is the main focus of the present work, from a survey system such as the one developed by the EIS team which uses the image pipeline described here as an image processing engine with an administrative wrapper written in Python as described elsewhere (da Costa et al., 2004). It is

Packages	Typical pipeline steps						CCD
	Calibration	IR background	Background	Stacking	Astrometry	Warping	
Eclipse/Jitter (Devillard, 1997)	*	*		*			IR/All
IRDR (Sabbey et al., 2001)	*	*		*			IR
IRAF/Dimsum (Eisenhardt et al., 1999)	*	*		*			IR
LDAC (Eisenhardt et al., 1999)					*		Optical/All
Astrometrix (Radovich, 2002)					*		Optical/All
Drizzle (Fruchter and Hook, 2002)						*	All
Swarp (Bertin, 2002)			*			*	All

Table 2.1: The available tools (first column) are evaluated within a typical pipeline made of the following steps: 1/ calibration step to remove the electronic signature, 2/ IR background estimation for IR CCDs, 3/ Sky background estimation for optical CCD, 4/ stacking of large IR data cube, 5/ astrometric solution, 6/ warping of images to final products. The packages are specialized for one or couple of reduction steps, some are dedicated for IR or optical detectors (indicated in the last column).

important to emphasize that the image pipeline proper involves no scripting language being all written in C++.

From other large ongoing surveys, IRAF is used as the main pipeline architecture. The UKIDS survey is using 80% of the total observed time. The full pipeline is developed in common with the VISTA instrument under the name of VISTA Data Flow System (VDFS) . The image processing pipeline is based on C routines (IRDR) (Sabbey et al., 2001) that are used encapsulated in IRAF (CIRDR) (Lewis, 2003). The image pipeline has to cope with the complex estimation of the sky background with IR instruments. A two pass technique is developed and similar to the IRAF/DIMSUM task. The Wide Field Survey WFS is using the Isaac Newton Telescope INT (McMahon et al., 2001) has been reduced with IRAF (Lewis and Irwin, 1999). The Gemini NOAO data are reduced with IRAF (Lewis, 2004). One Gemini is mounted the IR instrument (Hodapp et al., 2000) also IRAF based.

The observed images named *raw* must go through several reduction steps to be transformed into final products of science grade. The classical schema of reduction is a sequence of independent algorithms. Nowadays all sort of specialized tools are available carrying out part of the full sequence. Table 2.1 gives a general overview of the common tools with their main goals within a typical pipeline.

The packages are mainly written in compiled languages (C or fortran) to provide efficient computation. The softwares are used stand alone with their local configuration files for fine tuning. Note that none of them automatically transforms a group of raw images into final products. Some tools are redundant, they correspond to different approaches with algorithm improvements (IRAF/DIMSUM offers better photometric stability than the Eclipse/Jitter), or efficiently improvements (IRDR is made for faster computation than the IRAF/DIMSUM).

PACKAGES	FACILITIES			COMPUTER			CCD
	Reduction	Photometry	Extraction	GUI	Langage	Database	
Eclipse (Devillard, 1997)	*				C		IR/All
Elixir (Magnier and Cuillandre, 1997)	*	*			C		Opt/All
MIDAS	*	*					All
IRAF/MSCRED (Tody, 1986)	*	*			C,F,CL		Optical
Omegacam	*	*	*	*	C,Py	*	VST/opt
Terapix	*	*			C,Pe	*	Megacam/opt
ESO Imaging Survey	*	*	*	*	C,F,Py	*	All

Table 2.2: The listed packages are arranged in 2 level of complexity. First, the toolboxes, Second the automated solution. Also mentioned are the facilities of the pipeline, and an indication of its implementation and manipulations. Some of them offers Graphical User Interface (GUI) to control the administration. The packages are implemented using different compiled languages: C, or F for Fortran, and also scripting languages: Pe for Perl, Py for Python and CL (IRAF script language) Professional database dependency is given.

An *image pipeline* is the generic word characterizing the sequence of steps needed to transform groups of raw images into final products of science grade. Over the years numerous implementations have been assembled but most often they are dedicated to one instrument, or to a well defined scientific project. Most of them are build on existing tools (as listed in table 2.1), which are encapsulated with scripts of different languages (Shell, IRAF/CL, Perl, or more recently Python). From the main available pipelines (listed figure: table 2.2), one distinguishes two level of complexity. *First level*: the toolbox implementation that provides all necessary procedures to achieve all steps of reduction, one needs to manually administrate the reduction (data, sequence of procedures). *Second level*: A complete toolbox plus automated scenario that executes all steps of the image pipeline.

All the listed pipelines are organized in two levels. First: the algorithms, they are written in a compiled language (mainly C or Fortran) dealing with a single step of the image reduction, some have been developed before the corresponding pipeline (as the one listed in table 2.1). Second, the procedures managing the algorithms. The administration of data and their progressive transformations are managed by procedures that encapsulate the low level algorithms. This development is often done is script languages that try to harmonize the different local conventions of the heterogene configuration files of the algorithms. For instance the Omegacam consortium (dedicated for the coming VLT Survey Telescope VST) used variety of low level tools: the casual image manipulations are done with the Eclipse C package, the astrometric solutions are computed with the LDAC tools, and the warping/stacking is achieved with the Swarp software. IRAF is a complete set of tools defined in an integrated environment. All IRAF tasks (single algorithms) are generally written in a compiled language and executed in a common environment where the numerous parameters and logs are in a standard format. Another important implementation is IRAF. It is an open toolbox that let the user defining its own sequence. Lots of administration are required to build a successful pipeline. It is important to emphasize that some implementations are developed closely to large databases (public or commercial). This construction offers lots of flexibility to keep trace of events, but also makes the pipelines difficult to export to different sites as it relies on the connected database.

2.2 Requirements for a new system

From the early experiences of the ESO Imaging Survey, a set of requirements emerged: 1) Among others, the need to address specific problems such as frequent failures in the astrometric calibration (mainly WFI), biased sky subtraction of IR images, poor cosmetics. 2) High Throughput to deal with the ever increasing volume of data especially from wide field cameras. 3) A *c*ommon strategy to handle both optical and IR, single/multi chips detectors. 4) The need to trace and associate the different options and results as for instance the number of associated stars during the astrometric calibration. Those informations are necessary to fine tune the input options, and assign a quantitative quality to the reduced images.

As reduced data from the first surveys became available several issues emerged:

1. Unbias background estimation of IR observations - When the first SOFI IR observations of the EIS Deep Survey reduced using the Jitter program of the Eclipse package (Devillard, 1997) were released, a magnitude bias of the faint sources was reported. This bias was noticed from the comparison between the released images with external reduction carried out using the IRAF/DIMSUM package. The faint sources appeared shallower than expected by 0.15 magnitude whereas the bright sources agreed with the external reduction. This bias of magnitude was due to the background estimator used. The procedure used was over-estimating the background at location of faint sources. An unbias estimator was needed to properly reduce the IR images. The IRAF/DIMSUM was the only procedure able to carry out a good reduction. This solution was not adopted due to its difficult integration within a larger framework.

2. Astrometric calibration of the Wide-Field Imagers - Especially for the Wide-Field Imager (WFI), the location of the individual chips as expressed by the keywords CRPIX1 and CRPIX2 available in each FITS extension have been either not provided or inadequate, leading to systematic failure of the astrometric calibration. A robust and systematic procedure was needed to avoid manual recovery.

3. Remaining satellite tracks - The large optical EIS surveys (couple of degrees) integrate lots of hours of observations. A lot of images are affected by satellite tracks crossing the field of view. Most of them were processed by manual interventions to mask out the affected pixels. Unfortunately some tracks remain, and affect locally the image and the extracted catalogues. The need for an automated and efficient tool appears more and more important with the future large instruments (WFI, MEGACAM) associated with large surveys.

4. Illumination error correction - The illumination error is a phenomena observed recently with instruments using a focal reducer. The Zero-Point of the reduced images

is not constant throughout the field-of-view and varies up to 0.15 magnitude in case of instruments of large field of view (WFI for instance). The first observations of this phenomena were done in 1995 (Andersen et al., 1995). This problem was first reported to EIS when the Pre-FLAMES stellar survey observed with the WFI instrument was released. The photometric comparison of the extracted sources with an external photometric catalogue shows clearly the variation of Zero-Point as a function of the position within the instrument.

The WFI imager is the largest instrument, made of 8 chips (64 MegaPixel in total), used for various EIS surveys. The acquisition rate quoted in MegaPixel per second depends on the exposure time. With exposure times between 1 to 10 minutes, the maximum number of images observed ranges from 5 to 30 per hour (including the over-head time). The acquisition rate is therefore between 0.088 to 0.53 MegaPixel per second. The high rate corresponds to observations of photometric standards or to stellar fields (short exposure time). The slow rate corresponds to observations where no bright sources appear in the field-of-view thus allowing longer exposure time. Considering a night made of 8 hours of scientific observations and 2 hours of electronic calibration (bias and flat images observed at a rate of 30 images per hour), the instrument provides 12 to 38 Gbyte of data per night. The EIS surveys are large proposals spread over several nights of observations, typically 15 nights spread over one year. A complete survey is then made of 300 Gb of data. The acquisition rate defined for WFI is an indication for coming instruments such as the VLT Survey Telescope (VST: 32 CCDs, 256 MegaPixels in total) which will deliver images at 2.12 MegaPixel per second (short exposure time).

The acquisition rate of the near IR data is currently much smaller due to the small size of the detectors. SOFI or ISAAC instrument are single-chip instrument of 1 MegaPixel each. The acquisition rate is around 0.017 MegaPixel per second (the exposure time of archived images is typically one minute). The new IR instruments will compete with the optical detectors for high acquisition rates. For instance, WFCAM made of 4 IR square detector of 2k pixels each will provide an estimated 0.26 MegaPixel per second. The future VISTA instrument 4 times larger than the WFCAM will deliver theoretically images up to 2 MegaPixel per second.

EIS surveys are multi-color (mixing optic and IR), and multi-instruments and are using routinely the WFI for the optical part. Even if the operations are not in real time, and the reductions conducted offline, the need for a fast reduction is mandatory. Also the long term goal of the EIS project has been to cope with the data volume expected from ESO's survey telescopes such as VST and VISTA.

The earlier EIS image pipeline was built with a wide variety of tools (including most of the one listed in table 2.1) that were encapsulated in Shell, IRAF or Python scripts. Also the administration was quasi duplicated as optical and IR imagers were used. Therefore the need for an unique tool to handle the different imagers IR or optical domain, single/multi chips emerged. The adopted solution was to have a complete stand-alone image processing library. This integrated solution offers a more simple integration as for instance, options of different procedures sharing an unique convention. By contrast, a pipeline built on top of several low-level tools of different types depends on a variety of conventions which impose more administration/filtering to connect them.

With the tools previously used within the EIS survey, it was not possible to trace the different procedures applied to the the raw images up to the final science grade products. The reproducibility was not possible as some processing steps were executed by hand with settings that were lost/forgotten. Also the variety of packages makes the trace for logs more complicated (numerous format conventions). The solution adopted by the IRAF package to trace the different procedures is based on keywords written on the manipulated images. This header manipulation is made complex or impossible when images are combined for instance in case of multi-chip instruments. A more adequate solution is based on separate logs that follow the processing steps. Then a process can be reproduced identically (same data and options), but also several options can be tested.

2.3 The New Pipeline: Basic Concepts

In order to address the requirements mentioned above, the image processing library presented here has been built around the following concepts: The pipeline is built as an homogeneous library which provides a common framework to all algorithms as well as administration procedures required to transform raw images into science grade quality images. The advantages of this common environment approach is manifolded: 1) it provides transparency and control of all algorithms involved, and of their respective input parameters, thereby enabling their fine tuning to different instruments and filters as appropriate; 2) the seamless concatenation of different processes making it possible the execution of all processes in-memory thus avoiding additional interfaces between different codes which normally imply significant time losses both in I/O as well as requiring human intervention either in operation and/or coding.

The pipeline is based on the notion of a generic instrument. This notion used for instance by the IRAF/MSCRED task, is designed to support diverse optical multi-chip instruments. Here, this notion has been further expanded to encompass single/multi-chip, and IR/optical instruments. An instrument defined by the chip geometry and electronic layout is characterized by a set of input parameters to the pipeline. The pipeline also considers different modes of observation which include among others: calibrations, standards, deep or stellar. More detailed descriptions are provided in section 3.3.2. For the time being, it suffices to say that the pipeline recognizes two types of objects: the reduction block (RB) which consists in a collection of raw images, and a reduction mode (RM) which tells the system how the images should be reduced and which parameters to use. The RM depends on the instrument, filter and the observation mode. The exact details for defining a RM are discussed in section 3.3.2, and chapter 5.

Since the pipeline is meant to deal with generic instruments (single or multi-chip), instead of implementing solutions such as Beowulf systems requiring the parallelization of the code and an additional layer of data management, the solution adopted is to launch one RB per processor available within a machine. This lead to a full utilization of the CPUs, as all RBs are first organized within a list, which is submitted to the machine. A four CPUS machines is therefore providing reductions four times faster than single CPU, even with single-chip instruments. To further increase the overall throughput one just requires adding different machines which can be managed independently as developed in the context of the EIS team. This solution is instrument independent and provides maximum flexibility allowing both reduction and post-processing operation using the same hardware.

In building the library, an effort has been made to incorporate technologies developed in other areas of image processing. Many of the problems encountered in the reduction of astronomical images, are common to other fields such as remote sensing. For instance, in both cases images have to be "calibrated" a procedure known as astrometric calibration in astronomy or image registration in other fields. However, until recently the methods developed for one field were not readily available for the other. In particular, in astronomy, the procedure commonly used utilizes "catalogues" of point-like objects, and uses triangulation techniques (Deul et al., 1995) to make associations between the image being processed and some reference catalogue. While this classic method normally leads to robust results it tends to be extremely slow with process scaling as $\sim O(N^2) - O(N^3)$, in addition to other limitations discussed in more detail below. In remote sensing, even though much more difficult, because of the nature of the images (shades) one method normally adopted is image based and utilizes multi-resolution techniques (Mallat, 1989) using, for instance, the bi-orthogonal wavelet transform. In contrast to the classical approach mentioned above, this method yields extremely accurate solutions and equally importantly scales as $O(NlogN)$. In addition, the latter method is especially suitable in dealing with extremely crowded fields where the number of sources is very large and the separation between them correspondingly small. In this case, the ability of the method to work at different resolutions, scales the search radius accordingly, as well as the speed make an enormous difference. In section 5.3, a good example of the performance of the algorithm is shown using images from the Small Magellanic Cloud (SMC).

Another procedure of great interest, especially in wide-field imaging, is the ability to automatically identify linear tracks on the image left behind by orbiting satellites. While they are small blemishes on the image, they create havoc when extracting catalogues for scientific applications. Again resorting to remote sensing applications, one can make use of the Hough mathematical space (Hough, 1962) which is commonly applied to recognize roads, buildings, or more generally any sharp, locally linear features. The technique of Hough transform is an important tool able of detecting satellite tracks as faint as eyes can do (see Chapter 4) has been incorporated into the library. The specific implementation is particularly fast. To the best of our knowledge this is the first attempt to automatically detect and mask the satellite tracks on astronomical images.

Finally, techniques were developed to address some of the specific problems mentioned before such as: an unbias estimator for the background on infrared (IR) images, and, for computing corrections for the well known illumination-error presents especially with wide field imagers.

The various processes are bound together by employing the Extensible Mark-up Language (XML) technology. XML itself is a metalanguage to design markup languages, i.e. text language where semantic and structure are added to the content using extra "markup" information enclosed between angle brackets. HTML is the most well-known markup language. The XML protocol is developed by World Wide Web consortium. Some XML tags have been defined for the pipeline to characterize local options and logs. The protocol is used in three distinct ways of the pipeline: 1) for the input parameters, 2) as a way of communicating between different modules, 3) as an internal database and to store the history of the process.

The pipeline is executed with an XML file containing all information about instruments, RMs, and actions to be achieved. Knowing which instrument is being used, the software finds the proper informations (XML nodes) related to that instrument, RMs ... The complete configuration file, similar to a database, is large and contains all supported instruments. Another advantage of the XML is the possibility to split this large file into several ones linked together according to the XML based protocol named XInclude (World Wide Web consortium, 2001). To the pipeline is given the master configuration file, the other ones being linked during the parsing. By default, the parameters are organized in two files: a short one where main actions are specified, and a long one containing all low level descriptions that in practice are not modified. Driving the pipeline is made by interacting mainly with the short XML file which activates the main steps described in chapter 3. The long file, is modified to define new instruments or RMs.

Within the source code the XML protocol is used intensively to propagate options/results through procedures, or to parse the configuration file. The parsing is made easy thanks to complementary protocols such as the XPATH (World Wide Web consortium, 1999). This one defines a standardize way to query nodes/contents of an XML tree. It is comparable to a database query, but oriented for a structured tree. The advantages of including XML within the source codes are multiple: 1) The parsing of the configuration files is administrated with a standalone library implementing the XML protocol and lots of derivatives products (as for instance the publicly available libxml2 World Wide Web consortium (2004)). This implementation prevents the library to develop codes dedicated for the parsing. This is made possible thanks to the universality of the XML protocol. 2) The XML protocol was seen as the unique way to propagate and control options through encapsulated procedures. Options are given from one procedure to a low level one, as a dedicated branch of an XML tree. Again, this strategy prevents dedicated coding for administration. Now, the image library is based on the available libxml2 library, and does not include any administration codes relative to parsing or propagating options. Note that historically, a very preliminary version of the pipeline was built by encapsulating C++ procedures with PERL scripts. Half of the PERL source code was dedicated to parse the local ASCII configuration files. Latter, when the XML was integrated to the image library, all related low level administration coding disappear as well as PERL scripts.

While the procedure are computed, lots of information occurs. For instance, the background value when it is subtracted, the location of the detected satellite tracks, the anchors used for the astrometric solution, the distortion model... Those information are kept and written in XML format taking advantage of its hierarchical description. Furthermore, the associated XML files can be translated to any format and make their content available in a human-readable HTML or text form using suitable style-sheets. Those ones are written in a specific language name XSL also written in XML format. This language offers a standard way to transform XML content into something else as describe in the style-sheet. It worth emphasize the numerous flexibilities of this approach: 1) the conversion of XML logs to HTML or text forms is executed on the fly with all type of defined style-sheets. The filtering is very fast, and therefore, one needs to keep only reduction logs. The human-readable forms are then produced dynamically on demands, and are deleted after human inspection. 2) Numerous style-sheets can be created to produce human-readable logs of different purposes. For instance, one can built its own very specialized style-sheet to drag information about detected satellite tracks. Other logs can focus on astrometric solutions. 3) A style-sheet is compatible with the reduction logs, as far their internal structure is not modified. Therefore, a style-sheet is compatible with all reduction logs. This compatibility offers the possibility to analyze archived reduction logs, and then to make long term analysis as for instance the stability of the mean harmonization gain chip to chip.

Chapter 3

The EIS/MVM pipeline

This chapter presents a detailed description of the EIS/MVM image processing library. It represents an extension of the work initiated several years ago at the "Observatoire de la Cote d'Azur" (OCA) under the supervision of Albert Bijaoui. This was part of the so-called "Multi-scale Vision Model (MVM)" project, which is still underway. At ESO, it has been significantly expanded to fulfill the requirements set by the ESO Imaging Survey (EIS) project, and described in the previous chapter. The C++-based library (using standard ANSI C++) is platform independent and has been tested in machines such as Linux (Red-hat, Suze), SUN, and Alpha Digital. It is being used both in a stand-alone mode and as the image processing engine of an end-to-end, integrated data-reduction (survey) system (da Costa et al., 2004). In the former format it has been publicly available since mid-December 2003 (Vandame, 2004), and is currently being used at La Silla by the 2.2m telescope team, and in at least nine institutes across Europe.

This chapter gives a brief description of the concepts used in building the library, followed by a discussion of the different steps required for the preparation and reduction of the data. Finally, a short introduction is made of how the XML technology is used by the system as both a user-interface, as well as an internal wrapper connecting the different algorithms within the library.

3.1 A Brief Description

The starting point of the pipeline is a set of images which in the cases presented here (see chapter 5: Applications) are downloaded from the ESO science archive. Three types of images are normally requested: calibration images used to remove signatures associated to the electronic properties of the instrument (bias, dark and flat observations); images of fields containing photometric standards to be used to compute photometric night solutions; and finally, the science images. The set of data must be selected with care to ensure that sufficient valid calibration images are requested with the science frames. Note that the pipeline does not include modules for the absolute photometric calibration of the final science images.

It is important to emphasize that for the proper reduction of science images, a number of additional calibration images and ancillary files are necessary among which: *master-bias*; *master-dark*; *master-flat*; *bad-pixel-map*; *hot-pixel-map*; *weight-map*; *fringing-map*; *gain-harmonization*;

illumination-map; *reference-pixel*. The ones actually used depend on the instrument being considered as described below.

All images are commonly observed in a sequence, forming what at ESO is called an *Observation Block* (OB). An OB corresponds to a group of images observed consecutively, with the same characteristics (filter, exposure time, nominal pointing), and same "type" such as calibration, photometric standards, and science. The images in a science OB are normally shifted in position by a few percent (typically 5%) of the detector size relative to each other, as described by the dithering-pattern defined as part of the OB.

The reasons to make shifts between different exposures are manifolded: 1) to fill-in regions that have been masked out because of bad pixels/columns, when combining different exposures; 2) to remove cosmic rays with a sigma-clipping rejection algorithm applied to OBs containing three or more exposures; 3) to fill-in the imprint of the inter-chip gaps of multi-CCD instruments; 4) to benefit from overlaps of neighboring chips between shifted images, which provide the required constraints for algorithms (*e.g.*, relative mean-gain computation, global multi-chip astrometric calibration), note that no algorithms implemented in the pipeline currently use these overlaps; 5) to improve the quality of the fringing-map estimation within an OB (see section 4.5).

On the other hand, there are good reasons to make these shifts as small as possible: 1) to avoid a dilution of the Point Spread Function (PSF) anisotropy of the merged images. In case of cosmic shear or micro-lensing detection, the PSF anisotropy must be computed and corrected precisely on deep reduced images made of several raw observations, in order to improve the signal to noise of the lensing. To prevent a smoothing of the PSF anisotropy, the observed images should be shifted by tens of pixels, sufficient to fill-in bad-pixels; 2) to produce sharp exposure-time maps. Note that adopting a 5% dithering pattern typically implies a 10% decrease of image size with the total exposure time given by the sum of the integration time of each individual exposure. In summary, the amplitude of the dithering pattern must be a compromise between technical constraints and scientific goals. For most applications, however, large shifts of the order of 5% are adequate especially for estimating/removing fringes for IR and optical imagers.

The OBs are prepared before the observations, and are commonly planned to last less than one hour, although there are exceptions. Occasionally, an OB is observed incompletely due, for instance, to bad weather or to sunrise. During the reduction, the notion of group is also important, and images are grouped in so-called *Reduction Blocks* (RB). One RB consists of a single OB or a group of OBs. In addition, it also possible to reject individual images in the group, based for instance on background noise, seeing, and other observational parameters (*e.g.*, airmass, time-interval relative to twilight). The ideal RB depends very much on the RM, as will be explained in more detail below. In addition to these RBs, the system can also be used to prepare the so-called "technical" RBs, which are used to compute the several derived maps mentioned above, depending on the RM chosen. Note that the same RB can be used to produce different results depending on the RM associated with it.

Once an RB is prepared and an RM associated to it, the pipeline produces a final reduced image. The reduction starts with the calibration RBs to produce the master flat, dark, and bias calibration frames. Other technical calibration RBs are also processed by the pipeline such as: the bad-pixel-maps which registers the location of bad-pixels; the weight-map which registers the noise amplitude variation of the raw images; the mean-gain harmonization coefficients which are computed to ensure a unique electronic gain of the different chips of the instrument; and finally, the illumination-map which registers the Zero Point variation throughout the field-of-view (as detailed latter). When the master calibrations are ready, corrected by the technical calibration RBs, and the different catalogues and reference grid projections for the astrometric calibration are on disk, the reduction of science RBs starts. This process is the most complex part of the pipeline where lots of procedures are executed depending on the nature of observations and the instrument being used. The main goal of reducing a science RB is to produce a unique image associated with a weight-map that characterizes the inhomogeneity of the noise amplitude. The images within the RB are combined with an astrometric calibration computed either for each individual image, or for a resulting image which combines all the raw images of the RB. Also, during the reduction, several effects affecting globally all the raw images are estimated and removed. The main ones are: 1) removal of the electronic instrumental signatures; 2) subtraction of the sky background; 3) estimation of the fringing effect that are issued from sky emission lines and are observed in special conditions (as described latter). Also three types of local defects affecting partially the raw images are processed: 1) the artificial satellites that cross the field-of-view and are observed as tracks on the raw exposures; 2) the cosmic rays which appear as randomly spread small bright spots and affecting all exposures; 3) The cross-talk which is a ghost phenomenon produced by the saturation of bright stars that appear on the other read-out ports. This phenomenon concerns only the CCDs having two or more electronic converters. In IR this phenomenon is affecting greatly images where bright stars are observed (as detailed below), whereas with optical CCDs, this effect is considered negligible.

Note that frequently in astronomical applications a given position on the sky is observed using several similar OBs (*e.g.*, integration-time, filter and number of exposures), either on the same night or on different nights. The ultimate goal is to combine all of these reduced images sharing the same filter of observation into a single image. This is done by constructing a stacking block (SB), which consists of a group of reduced images taken with the same filter and at the same sky position.

Like in the case of the RBs, individual images can be removed from the SB based on some image attribute such as seeing on the images and PSF distortion. Finally, the SB must be validated which means that all images share the same reference grid (center, pixel size, orientation and projection type) and that each contributing reduced image was produced from unique raw exposures. The co-addition of an SB to produce a final science product, is also done by the pipeline (see section 3.4). The same principles apply to the construction of an image mosaic with a mosaic bloc (MB) replacing the SB as the survey system is handling thanks to the absolute photometric calibration.

The RM first of all selects the modules to be executed during the processing of the associated RB. Second, it provides all the input parameters required by the various procedures, including the full characterization of the detector and telescope used. The basic categories of RMs are: calibration, technical, and science. In each case, several options are available. For science RMs a number of options and procedures are available to handle observations of: photometric standard (standard), crowded (stellar) and high galactic latitude fields (deep) as well as fields containing extended objects (stellar), where in parenthesis the adopted internal name of the RM is given.

One of the important features of the image pipeline presented here, is that it can be used

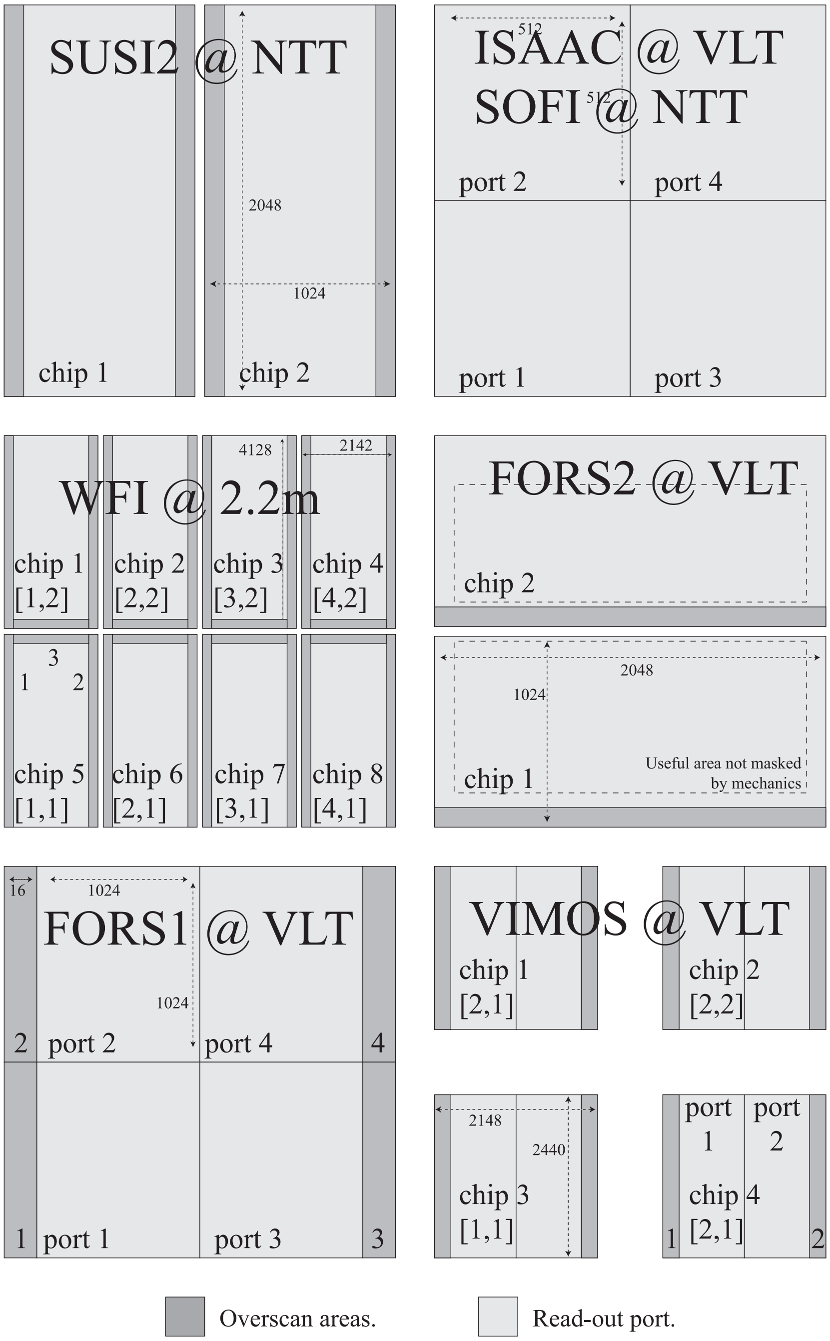

Figure 3.1: The figure shows the layout of various ESO imagers such as: 1) SUSI2 (top-left); 2) ISAAC/SOFI (top-right); 3) WFI (middle-left); 4) FORS1 (middle-right); 5) FORS2 (bottom-left); 6) VIMOS (bottom-right). Also shown are the number of CCDs, their size in pixel, the number of read-out ports and the number and location of the over-scan regions when applicable. Note in particular in the case of WFI, the electronic layout (one of the over-scan areas) of the top CCDs differs from those on the bottom. In the case of FORS2, the CCDs are not fully illuminated by the sky due to the masking created by the mechanical structure of the instrument. Therefore, a fraction of the second CCD has to be discarded.

to handle a large variety of imagers including single- or multi-CCD instruments, and in both optical and IR domains. Therefore, the RMs must also provide a full description of the physical layout of the detector (number of CCDs, size, location), of its electronic layout per chip (*overscan areas*, *read-out ports*), and other characteristics such as projected pixel-size and orientation, gain and read-out noise per port. It is important to note that the instrument description can be quite complex. This is illustrated in figure 3.1, where nearly all imagers of ESO are presented. The top-left shows the layout of SUSI2, the first multi-chip detector used by the EIS project, mounted on the NTT at the La Silla observatory. The light grey represents the active area (corresponding to a read-out port) of the detector, while the dark-grey represents the over-scan areas. For the particular case of SUSI2, there are two over-scan regions, and one read-out port per chip. Another example of relevance to EIS is the top-right panel where the layout for the SOFI and ISAAC IR detectors are shown. In this case there are four read-out ports, which define four quadrants. Taking into account this geometry is particularly important in defining the reduction procedure for these instruments as encoded by the RM. For multi-chip instruments such as the WFI, the description becomes even more complex. From figure 3.1 one can see, that the electronic layout (over-scan areas in between the top and bottom CCDs) of the top CCDs are different from those at the bottom. This may differ from instrument to instrument as, for instance, is the case for the 12k camera at CFHT which adopts a different scheme. The relevance of this point is that if not properly described it leads to an unnecessary increase in the inter-chip gap as was the case for first release of WFI images taken as part of the Pre-FLAMES survey (see section 5.3). In addition to the points mentioned above, the complete characterization of the instrument also depend on other instrumental such as vignetting. The details are instrument dependent and will be discussed in the appropriate sections of chapter 5.

Another complicating factor in creating a pipeline capable of handling a generic instrument is the fact that even within the same observatory different conventions to write the image into a FITS file are adopted. For instance, SUSI2 is represented by a single pixel-map merging the images from the two CCDs, while, for WFI each CCD is represented by a FITS extension, which is the most commonly adopted format. Still other conventions exist such as FORS2 and VIMOS, for which a single exposure is represented by multiple FITS files.

Also important is the location of each individual chip and where they appear in the FITS extension because the order in which they appear in the file may change (has changed) with time.

Finally, in order to make the system as general as possible, does allowing the processing of images coming from different ESO imagers as well as different observatory (*e.g.*, CFHT), the instrument specification requires a dictionary that defines the convention encounters in the raw images for the name and unit of the FITS keywords.

3.2 Data preparation

Once the raw data are on disk, and the RMs are properly defined (as discussed in sub-section 3.1), the process can start. Before the actual reduction of the data, some preparation steps are required in order to: 1) prepare the images (splitting, keyword filtering, check of pointing precision, check of the chip position within the matrix of chip); and 2) prepare the ancillary information (astrometric catalogues, reference grid of the final products).

Splitting of images

The first step is to check the number of fits extensions in the raw images. If this number corresponds to the number of CCD chips expected for the instrument, the original raw image is split into individual ones. A graphical representation is given by the top part of figure 3.2.

Unfortunately, currently there is no uniform way of representing an image of a multi-chip instrument. In fact, SUSI2 with two-chips is represented by a single image in the same FITS extension, FORS2 is organized into two FITS files, while WFI is represented with one FITS file made of one extension per chip (height in total). This latter format seems to be commonly used as a world-wide convention (*e.g.*, CFHT), and is the one that the pipeline handles automatically. Therefore for other formats, the splitting requires external intervention.

FITS header keyword

A list of basic keywords (seven in total as given in the bottom part of figure 3.2) in the FITS header of the raw image must be translated (name and unit) into those recognized by the system and defined for the generic instrument. All others are re-computed as required to conform to the internal convention and ensure consistency throughout the processing phase. A set of word recognition patterns must be specified to automatically recognize: calibration images (bias, dark, dome or twilight flats) from the contents of the object-name and filter-name keywords. This is important in order to cope with changes in the filter-name convention adopted which has evolved in time. The word recognition patterns are very efficient to cope with evolving convention of the archive system over time. It is important to emphasize, that only those images properly identified by the pattern recognition algorithm are subsequently used, the rest being discarded. The following gives the list of keywords that are either computed, or read from the part of the RM describing the instrument. For each one, also the name convention adopted internally by the pipeline is given.

- Number of sub-integrations (SUB-IMAG) - With IR detectors, the images saved in an archive system are the average of several ones of same exposure time. Each image is made of sub-integrations. With the ESO IR imagers one speaks about NDIT sub-integrations with exposure time DIT each. The notion of Gain, Exposure time, Total exposure time are updated. For the other instruments (mainly optical) where each image is directly saved in an archive system, the number of sub-integrations is not used and therefore considered to be equal to one.

- Exposure time (EXPTIME) - Is set to the exposure time of a single sub-integration. In case of an optical instrument, this information is taken directly from the FITS header. The unit adopted is seconds.

- Total exposure time (TOT-EXPT) - It is computed as the exposure time multiplied by the number of sub-integrations. For an optical detector, this value is equal to the exposure time as the number of sub-integrations is one.

- Total number of images (TOT-IMAG) - This indicates the number of raw images stacked. Therefore this number is equal to one for the raw images, and then increases while the images are reduced/stacked.

- Electronic Gain (GAIN) - It is set by the default electronic gain multiplied by the number of sub-integrations. For an IR detector, the sub-images are combined by taking the counts to be given by the mean, and therefore the effective electronic gain is modified (increases). The unit adopted is electron per ADU.

- Read out noise (RON) - The read-out noise is a noise produced by the electronic converter during the process of reading the chips. Since this is typically small compared to the sky background noise, the pipeline does not update at the different stages of processing. In principle, the amplitude of the RON of the raw image, should be equal to the original value divided the square root of the number of sub-integrations.

- Julian Date (JDAY) - Often the Julian date of a raw image is given at the beginning of the exposure time. The Julian date is updated to correspond the the middle of the exposure, by adding half of the total-exposure-time of the image. The unit adopted is the true Julian date.

- Airmass (AIRMASS) - The airmass of one image is computed using the location of the pointing (α, δ), the Julian date of the observation and the longitude of the telescope. The definition adopted is the inverse of the cosinus of the zenith distance.

- Pixel scale and rotation - Normally the coordinate system of raw images is described by the keywords *CDELT1, CDELT2, CROTA1* and *CROTA2*, which are then converted to the recent WCS recommendation using the CD-matrix convention which consists of four keywords: *CD1_1, CD1_2, CD2_1* and *CD2_2* that describes the size (degree) and orientation of a pixel projected on the sky. In addition, the keywords *CTYPE1, CTYPE2* indicate the type of projection (TAN or COE). Their values are respectively: *RA—TAN*, and *DEC–TAN* or *RA—COE*, and *DEC–COE*.

It is important to emphasize that in order to be able to deal with a generic instrument mounted on an arbitrary telescope it is vital to adopt the CD-matrix convention described above. In fact, one of the cumbersome aspects of dealing with instruments such as SUSI2 and WFI was the fact that no information about the pixel-scale or orientation was available neither explicitly nor implicitly in the header (CDELTs were set to one, and CROTAs to zero) For those instruments, the pipeline introduces these keywords in the splitted images.

Reference pixel check

Given the importance, for the astrometric calibration of an image, of being able to locate the raw science images on the sky with an accuracy in pixels of roughly 10% of the field-of-view, a procedure has been developed to compute a reference pixel. This proved to be particularly important in the case of ESO's multi-chip instruments (*e.g.*, SUSI2, WFI) since either they had inadequate values for the CRPIXs (set both to one for all chips) in the FITS extension corresponding to each chip, or the pointing model was too inaccurate with shifts larger than one chip (2000 pixels). In addition, for those imagers the orientation and pixel-scale were also unknown as the values for CDELTs and CROTAs where not correct (see above).

This check is carried out using a cross-correlation technique between two images. The first is a low-resolution (under-sampling by a factor of 8 the original pixel scale of the CCD considered)

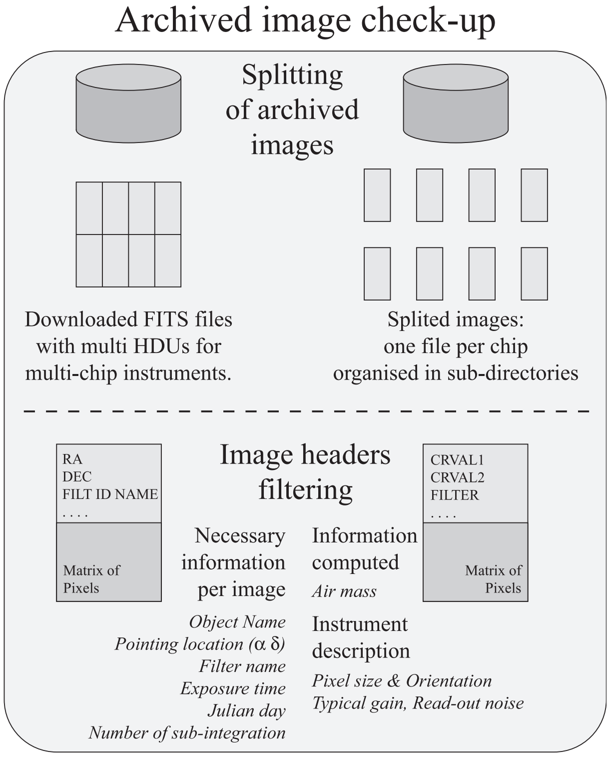

Figure 3.2: Pipeline preparation part. These steps are executed to filter the raw images with their local description issued from an archive systems. First, the raw images are splitted such that one image is made of several FITS files, one per chip. While splitting the images, the size and number of chips is checked. Second, the information describing each image is tested and convert to a constant system convention. From each image, seven distinct information must be found as written in the figure. Some redundant information is recomputed using the instrument characteristic (airmass, pixel size and orientation, mean electronic properties).

version of a mock image created from a reference astrometric catalogue drawn from a much larger area than one CCD (ranging from 4 to 36 times the original field-of-view). The other is constructed from the science image to the same resolution as the one adopted earlier using wavelet transform, padded with zeros to match the mock image size (imposed by the cross-correlation computation). In preparing the low-resolution science image, care must be taken to: remove cosmic rays, subtract the sky background, and discard bright stars, since otherwise the cross-correlation peak of the two images may be invisible. Section 4.7.2 gives a more detailed description of the method. The peak of the cross-correlation yields the value that must be written to the CRPIX keywords in the header of the chip being used, to correspond to the position on the sky given by CRVAL1 and CRVAL2. This correction is then applied to all frames (individual chips) belonging to the same night or an arbitrary period of validity specified by the user. This procedure is possible thanks to the speed of the algorithm which works with low-resolution images and benefits from the Fast Fourier Transform (FFT). A graphical representation is given by the top part of figure 3.3. One advantage of carrying out this reference pixel check at the preparation phase is to assure that during reduction only a refinement of the astrometric solution is required. Note, however, that the method is only valid for correcting translations. Rare cases of unknown orientation of the WFI instrument have been encountered. The orientation is rotated by 4 degree of the expected one (North up) and may fail the Reference-pixel check up, or latter on the astrometric solution of some RBs. The success of the astrometric solutions of a large set of WFI images is 99% as quoted in sub-section 5.4.

In order to carry out the procedure described above, a technical RB referred to as *reference-pixel* has to be created. The RB should contain only one image, which preferably consists of homogeneous stellar field to ensure good results. The period of validity of the reference-pixel solution, as explained above, is typically of the order of a month. However, this depends on how often the pointing model is revised (including instrument changes). Previous experience has shown that occasionally a nightly reference-pixel check may be required, especially for the first year of operation of the WFI imager.

It is worth noting that when reducing data spanning a long time interval, one reference-pixel RB should be created in validity time intervals. Otherwise, some data will stay uncorrected which in turn may cause the failing of the astrometric calibration. In practice reference-pixel RBs are typically defined every half validity time interval to ensure that all data will be corrected at least one (if two corrections occur for the same data, the CRPIX values will be the same within couple of pixels).

Chip identification

When dealing with multi-chip instruments some algorithms (such as the mean gain harmonization as described in section 4.2) require information about the exact location of each chip and this must be checked by the system. Since it is not advisable to rely in the order in which they appear in the FITS file, which may (have) change in time, this must be computed. Once new CRPIX values are available these are used to cross-check if the computed CRPIXs are consistent by verifying that the location of each chip reproduces the real array. In case of an inconsistency is detected there are two possibilities: the first is that an error as occurs with the cross-correlation procedure. This is possible, for instance, for small field of view instruments without sufficient sources; The second may be caused by the re-ordering of the chip in the FITS file. In this case the chip are relabeled to match the geometry of the detector as defined in the configuration file. See figure 3.3 for illustration.

Reference grid creation

For science frames, besides the RBs, one also has to provide the definition of a reference grid onto which the final reduced images will be mapped (astrometric solution followed by a warping procedure). This reference grid is defined by a reference sky position (α and δ), a pixel scale and orientation given by the WCS CD-matrix, and a projection such as which can be tangential (TAN), conical equal area (COE), etc... The use of a reference grid is not mandatory but it is recommended for deep observations and mosaics since it is easier to co-add reduced images sharing the same grid convention. A unique projection grid is defined for all observations made at the same sky location (dithering or mosaic). If a reference grid is not specified, each image will be warped to its local WCS information. This is the case with photometric standard fields that are reduced but never merged.

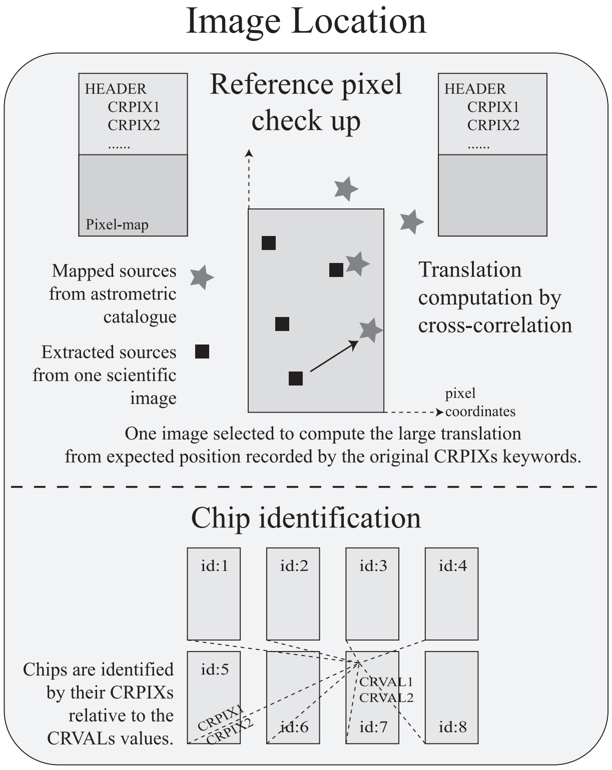

Figure 3.3: Pipeline preparation part. The two steps shown in the figure are executed in order to compute adequate values for CRPIXs for each chip, which can also be used to identify the chips within the array.

The images corresponding to reduced RBs, sharing the same grid, can later be easily co-added to provide final products which may be even larger than the original field of view (*e.g.*, mosaic) (see top part of figure 3.4).

One can extend the notion of reference-grid as to enable one to compare data from different instruments, useful in the case of multi-wavelength surveys such as GOODS, described in chapter 5.2. This strategy facilitates the use of image-based algorithms such as: image subtraction, multi-band source-extraction, extraction of objects using chi-square image as reference, and the simple production of color images.

Astrometric catalogue retrieval

The astrometric calibration of the images depends on an external astrometric catalogue. For wide-field instruments (FOV $\sim$ 30'), the common catalogues used are the USNO (Monet et al., 1998) or GSC2 (Bucciarelli et al., 2001), while the recent very accurate UCAC2 (Zacharias et al., 2000) can be used for stellar field observations. For instruments with small field-of-view ($\lesssim$ 5'), as it is the case for current IR imagers, the common astrometric catalogues are often too sparse especially for high galactic latitude fields. For these cases, one must resort to denser catalogues provided by the user as illustrated in section 5.1 and 5.2.

The pipeline offers an automatic retrieval of the GSC2.2 catalogue. Only one catalogue is requested per distinct sky region (see bottom part of figure 3.4). For other types of astrometric catalogues, an external intervention is required to set them in a proper directory, and they will be used automatically by the pipeline.

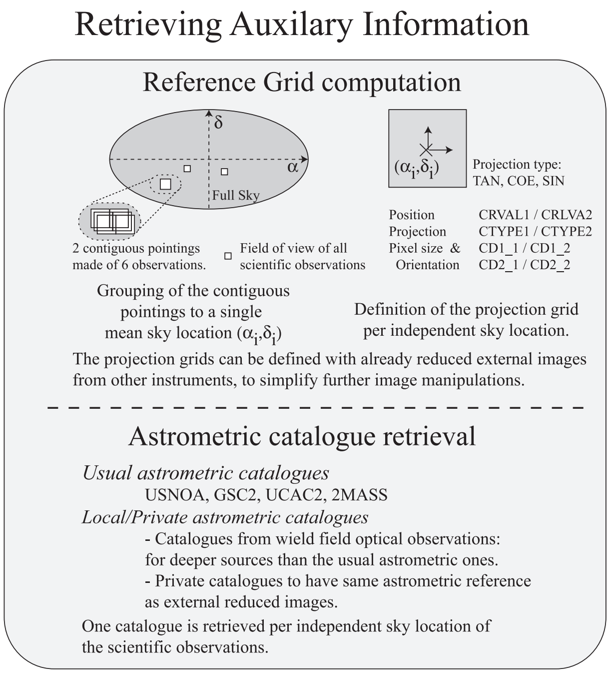

Figure 3.4: Pipeline preparation part. These steps are executed to prepare the needed external material for the astrometric solution and warping of the scientific RBs. First, scientific RBs are automatically grouped in distinct pointings, and then a reference grid per region is created. A sky location is commonly covered with several images observed with dithering pattern, and sometimes with several contiguous pointings to enlarge the final sky coverage of the final reduced products. In both cases, a unique grid is defined to ensure grid-compatible reduced RBs. Second, the astrometric catalogues are retrieved. The nature of the catalogues depend on the sky coverage of the instrument, and the depth of the observations. One catalogue is retrieved for each distinct region.

3.3 Reduction

3.3.1 Master calibration and technical RBs

Master dark, bias and flat

The first RBs to be reduced are those associated with the calibration frames. However, it is also possible to assign external master calibrations, in which case this step is skipped. To produce the master calibrations, the exposure frames are first grouped in RBs by their type namely *bias*, *dark*, *dome-flats* and *twilight-flats*. Flats taken with the same filter, and dark observations of same integration time over a pre-defined period of time (see below) are grouped together into distinct RBs. In the case of flats, the group must share the same filter, while for darks, which are primarily used in the IR, they must share the same integration time. The latter condition is because the dark current in IR detectors varies significantly with the exposure time. Hence, it is necessary to have dark RBs with the same integration time as those of the calibration (flat) and the science RBs to be processed. By contrast, current optical detectors have negligible dark current and dark exposures are rarely taken, even though as discussed below, they are useful for other purposes.

The next calibration frame to be considered is the bias, which is only important for optical detectors. In the IR the amplitude of the bias is not a constant, because its value in a line is a function of the mean counts of the line in question. Therefore, the bias depends on the sky brightness, on the number of sources, and more importantly on the contribution of very bright sources that may be present within the frame. In practice this bias is not computed/subtracted, and only the strongest effects of it, are tentatively removed when dealing with the cross-talk effect (as described later).

The pipeline can use both dome-flats (namely those obtained by illuminating a screen inside the dome), and sky-flats (exposures of the sky taken close to twilight). However, as discussed in chapter 4.3, dome-flats are, in general, a poor approximation of the true sky background pattern. Therefore, typically sky-flats are preferred in the reduction of data from optical imagers. In the case of IR, (as detailed in chapter 5.2) both have been used successfully – the so-called special flats in the case of SOFI and sky-flat in the case of ISAAC. It is important to emphasize that the type of flat to be used in the reduction can be selected by the user. However, one must make sure that the illumination correction map (see below) applied to the data is consistent, i.e. the RB used for estimating the illumination correction must have been reduced with the same type of flat as the science RB.

The period of validity of a calibration RB, which depends on the instrument and type can also be specified by the user via a configuration file to be presented later in this chapter. This allows the pipeline to cope with very large sets of observations spread in non-continuous nights over a year or more. Typically, for optical imagers, master flats are considered valid for a period of 10 days. This period is based on accumulated experience and represents a compromise between two extreme conditions. Ideally, the validity time should be equal to one night. However, this choice becomes very restrictive because it imposes all requiring sky-flats (*e.g.*, 5 valid flats) to be observed for each night for all filters (*e.g.*, 5 passbands), which is in practice not feasible for all instruments. In practice using the WFI archive, for instance, it is not possible to find a significant number of sky-flats per night and filter. On the other hand, the variations of CCD gain monitored at the telescope, show that during a period of ten days the response of the electronic is stable and normally it is possible to find sky-flats in all filters. In case of IR detectors, the validity period of the flat observations is very long as the gain is very stable. Tests of master flat images made on a year basis, show a very good stability within 1% (NTT Team, 1997). A final test for the flat RBs is to make sure that each contributing image has an adequate mean count, avoiding exposures with low counts and consequently poor *signal-to-noise* (S/N), and those with counts close to saturation (typically equal to two third of the saturation level). For CCDs, with 16 bits quantification between 0 to 65536 ADU, the typical low and high cut criteria are 10000 and 40000 ADU. For the bias, the validity period is set to five days as numerous bias images are usually available (up to sixty per night). The dark calibrations for IR are valid for a week or less.

Finally, only RBs with a minimum number of raw images are considered, leading to a proper cosmic rays or other random defects rejection when combining the grouped raw images of an RB into a master calibration frame. Typically, five raw images are mandatory for flat RBs, and three for the bias/dark RBs. When three or more images are combined by computing a median value per pixel, the contribution of cosmic rays and remaining visible bright stars, is minimized. It is important to emphasize that during the observation of sky-flats, the telescope must be shifted from one exposure to the next, to avoid bright stars propagating into the master flat calibration, and thus leading to holes on the science images reduced with this master flat. This problem has been frequently seen in tests with FORS mounted on the VLT, and less frequently with WFI. Nevertheless, it suggests that the pointing of consecutive exposures in a sky-flat RB should be checked to ensure that only exposures with shifts significant larger than the PSF are used. During the observations, care should also been taken to avoid regions with large density of bright objects.

After applying all the above tests, one must check that valid calibration RBs exist for all filters (flat RBs), and exposure times (dark RBs). Only rarely, one must resort to dome-flat RBs because not enough sky-flats are valid over the desired period. Alternatively, one can change the selection parameters in such a way as to relax the conditions leading to an increase in the number of valid sky-flat RBs. Finally, a maximum number of twelve exposures per RB is imposed in order to optimize the cost/benefit ratio as more than that are typically redundant. All the tests described above are carried out automatically by the EIS/MVM pipeline.

After bias, dark and flat RBs are prepared, and input parameters for the various algorithms are read from the proper configuration file, the pipeline produces the master calibration images automatically. For multi-chip instruments an additional step is required, namely that the chip to chip variation in the mean electronic gain must be corrected for as described below. For bias and dark RBs, the processing steps include: first the mean of the over-scan area associated to one read-out port (if available) is computed and then, the counts within the area of the chip corresponding to that read-out port is subtracted by this value. The corrected images are then combined by computing the median for each pixel with the resulting pixel-map of the corresponding master bias/dark being saved.

For the flat RBs, the images are again corrected for the over-scan, as described above, and then subtracted by the master bias (optical detectors) or master dark with the same integration time (IR detectors), closest in date to the flat RB being considered (using the first exposure as reference). Then, the resulting images are normalized by their mean, computed with a sigma-clipping procedure, combined by computing the median to produce the master flat which is then saved. The header of the master calibration images is used to store information such as: the filter (set to "closed" for bias and darks), the exposure time (critical for darks, and set to one for flat), the mean Julian date of the contributing images (used in the assignment of a master calibration image to a science RB), and finally the number of images combined. For multi-chip instruments, these procedures are carried out chip by chip, allowing the process to be multiplexed.

It is worth pointing out, that for SOFI, external master calibration flats, produced by the telescope team, are used. These are based on the so-called *special-flats*, that requires a special reduction procedure (see section 5.2) which has not been implemented in the pipeline described here.

Bad-pixel (cold/hot) and Weight-map

Most CCDs have numerous bad-pixels which must be identified and masked out, to ensure that the reduced science images have a good cosmetic quality, leading to the extraction of high-quality science grade catalogues. The most common are: *cold-pixels* which do not convert photons into electrons, and are characterized by very low counts; *hot-pixels* characterized by very high counts including saturated ones caused by random variations of the quantum efficiency of the detector. Fortunately, those are stable and always appear at the same location. A hot-pixel that reaches the saturation level during an exposure, also affects the part of the column corresponding to the direction in which the charges are transferred during the read-out of the CCD. This part appears brighter than the local mean by several ADU. The number of hot-pixels reaching saturation is a function of the intrinsic characteristic of the detector and of the exposure time. In the bias exposures, most hot-pixels appear as Dirac functions, few reach saturation and therefore normally do not impact the columns where they lie. By contrast, in longer exposures, most hot-pixels reach saturation, causing many more bright columns to be seen (see section 5.4.2). In the first case, the detection can be made using the master bias, but in the second case, only master darks (or long science exposures) can be used to detect them and their impact to the columns. From this discussion while bias images can be used to detect hot-pixels and few bright columns, a much better detection can be done by using long exposures (dark or science) to detect more hot-pixels and more of the bright columns making a significant improvement of the final reduced images.

Finally, it is worth emphasizing that the effect of bad-pixels must be masked out, at the calibration level. While it is possible to remove a significant fraction of bad-pixels/columns by a sigma-clipping procedure during the reduction of an RB, another fraction will not be removed because by then the images would already have been warped, and the sharp nature of the original features would have been lost. This implies that traces of the original bad-pixels/columns will be seen not as sharp features but rather convolved by the kernel utilized by the warping procedure (as illustrated in section 5.4.4).

In addition, to the electronic bad-pixels, other locations of the CCDs are affected by other defects such as dust particles reducing part of the photon flux, and the vignetting which sharply reduces the flux to zero at the border of the camera. Even though in principle this decreasing flux would be corrected by the flat-correction it is preferable to mask these regions out in order to improve the cosmetic of the reduced science images.

While the defects mentioned above may have different origins they share the same geometrical characteristics of being small and having sharp edges. Given the importance of identifying these features automatically, a special procedure has been developed and is applied to every master calibration image (dark, bias and flat) created by the pipeline. Basically, bad-pixels whatever their origin, are detected by thresholding a master calibration image subtracted by its own smoothed version (see chapter 4.1 for description and justifications), in order to keep pixels with values outside plus or minus ten times the noise amplitude of the subtracted image. The thresholded images is then converted into a bad-pixel map, setting to zero the value of the amplitude of the count at the location of the detected bad-pixels/columns or any other features that need to be masked out, while the other pixels are set to one. This procedure when applied to master flat efficiently detects the cold and hot-pixel, while when applied to master bias or dark calibration images detects residual faint bad-pixels usually forming bad columns. A refinement is made by thresholding master flat images to reject areas where the flat efficiency is lower than 80% (strong vignetting). This area is set to zero on the bad-pixel map associated with the master flat. Since the creation of the bad-pixel maps is efficient, this is done on-the-fly each time a calibration is produced, thus avoiding to save bad-pixel maps to be used for different observation sets. This is especially important for wide-field imagers for which saving intermediate calibration images is costly in time and space.

As mentioned earlier, current optical imagers have stable electronic and darks are rarely observed. Indeed, those calibrations indicate the time dependent dark current, which is now negligible. Nevertheless, as mentioned above, those observations are the only one with the science to have long exposure time, and therefore suffering from numerous hot-pixels getting saturated. The lack of dark observations makes the detection of those special bad-pixels and their corresponding bad columns impossible. A dedicated procedure is designed to detect the hot-pixels from a *hot-pixel-map* RB made of several scientific images of the longest exposure time whatever is the filter (the hot-pixels are independent of the filter used), and sky location. This procedure is used to compute a bad-pixel map that is later combined with the one mentioned above. A precise description is given in the algorithms chapter section 4.1, the main idea is to benefit from several science observation to remove the astronomical sources, and then focus on the hot-pixels and their affected columns. It is worth emphasizing that the hot-pixels are always at the same location and one hot-pixel-map RB is sufficient for proper detections even for raw images observed during nights spread over a year or more (see statistics with the WFI imager at section 5.4.2 made with observations spread over six months). Note that with IR detectors, this notion is useless as darks are always observed, and the hot-pixels are already registered by analyzing the master dark calibrations.

The created bad-pixel maps are combined with the master flats to produce a so-called *weight-map*. The later is produced by multiplying the master flat by the bad-pixel map computed from it, and the bad-pixel map created from the master bias and dark as described above. If avaialble, the resulting image is also multiplied by the bad-pixel map computed from the hot-pixel-map RBs, based on long science exposures. The resulting image is a weight-map saved with the same name of the master flat but with another extension (".weight.fits") to differentiate the flat from the weight-map.

Therefore, all master flats are associated with a weight-map, which is used to produce final science images by a weighted co-addition procedure described latter and to enable the proper extraction of science catalogues from reduced images with varying exposure-time maps. The weight-map produced by the pipeline is equivalent to an exposure map that is characterizing the inverse of the noise amplitude pixel per pixel. Therefore by multiplying a reduced image by the square root of the associated weight-map, one obtains an image with a constant noise amplitude, as required for a proper signal to noise thresholding (see the sextractor manual Bertin (2003))

Note that during the creation of the master calibrations, their corresponding bad-pixel maps and finally the weight-maps are all produced in memory by the same procedure thus avoiding unnecessary I/O operations, thereby ensuring a very high throughput. In practice the amount of memory used is accessible to most of machines, and is typically 15 times the size of one raw image.

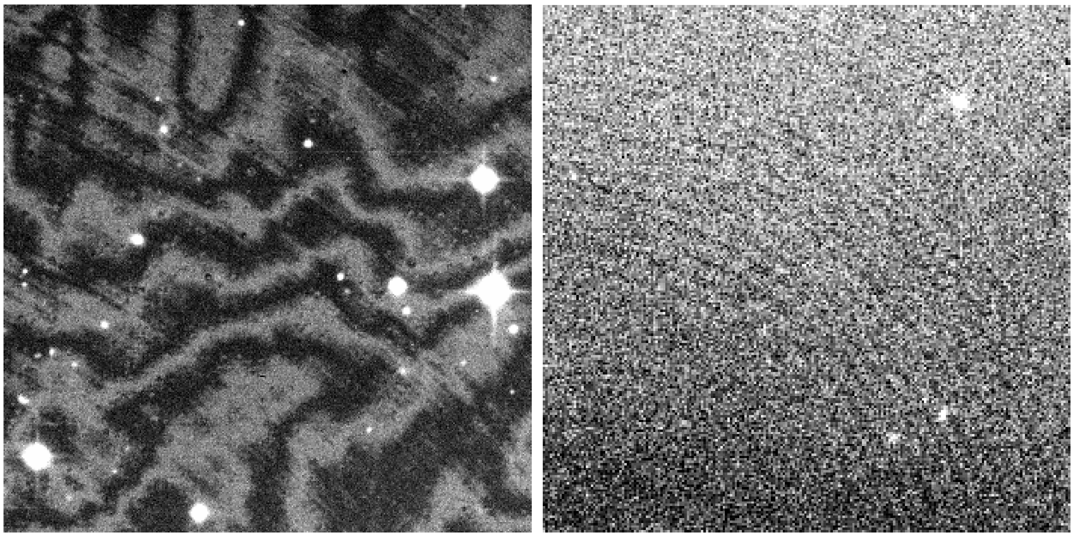

Figure 3.5: Different type of fringes observed with optical (left panel) and IR imagers (right panel). The left panel shows the fringe pattern observed in a red optical passband (filter I) of the WFI imager. The image is a section of 500 pixels on the side of a field observed for 10 minutes. The pattern appears very sharp (small gray circles are visible), or elongated (waves crossing all the CCD). The right panel shows the fringe pattern observed in a one-minute J-exposure taken with SOFI. The pattern is well represented by a Bessel function.

Fringes and Background-maps

The groundbased instruments suffer from interferences caused by atmospheric emission lines, depending on the filter used. This effect occurs especially with optical imagers in red passbands (filter I) or with IR detectors with the J passband (see figure 3.5 for illustration). The other IR passband also suffer from a complex background pattern. Those defaults are independent of the pointing location, and quite stable in time (at least for the optical detectors). One way to remove this additive signal is to get an estimate, here after *fringing-map*, computed from several science frames set in a fringing-map RB. The latter contains several images observed with a large pattern, or from distinct pointings. Each RB is proceeded with corresponding master bias/dark and flat calibrations, the images are normalized to one, and then combined with by a median. The computed fringing-map is a calibration image used to remove the instrumental effect on science images observed with the same filter. It is important to emphasize that the fringing-map RBs must contain field of view with no extended sources such that the astronomical sources vanish with the median stacking of the images. One should dissociate this technique, from a second one used to estimate fringes from the scientific RBs themselves during their reduction (as described later, and in section 4.5).

Gain Harmonization (Multi-chip Cameras)

For multi-chip instruments, variations in the mean electronic gain of each chip in the array must be corrected for. Otherwise, the sky background of the reduced images will vary as

Figure 3.6: The sky background variation observed on a reduced WFI image corrected only for instrumental signature (bias and flat correction). The image illustrates the amplitude of the chip to chip gain variation.

illustrated in figure 3.6. The amplitude of the peak-to-peak variation in the gain is about 20%. Therefore, this is a critical step for a reliable photometric calibration. As noted above, for multi-chip instruments, a correction factor must be applied to all master flat calibration images and associated weight-map before their use in the reduction of science RBs.

For each master flat produced by the pipeline, an estimate of the correction factor for each chip to bring them to a uniform gain level is computed. This is done by creating a technical RB, referred *mean-gain-normalization* RB by selecting an image with as high background counts as possible to improve the statistics, and with a Julian date as close as possible to the master flat being considered.

The selected image is then split in individual chips and each chip is corrected for instrumental effects (bias or dark, and then flat). Under the assumption that the sky background of neighboring chips should be constant, the ratio between the mean values of the background estimated within thin strips taken near the closest border between two chips is taken as the correction factor, hereafter referred to as *flux-scale*. A more detailed description of the procedure is presented in section 4.2.

This procedure is a robust alternative to the photometric calibration of individual chips. This is an important point considering the difficulties of obtaining enough photometric standards uniformly distributed across the field of view of a wide-field imager, and to a large extend independent of the illumination effect across the detector (see discussion below) since, the scale in which the chip to chip comparison is made, is much smaller than the scale of the variation of the amplitude of the illumination effect. The long term stability, which defines the validity period of the gain correction is presented is section 5.4.2.

Note that for each reduced master flat, fluxscales must be computed. Therefore, a *mean-gain-normalization* RB must be created per flat RB. Such RB contains only one image used for the procedure. Two types of raw images can be used for this procedure: a raw flat, or a long exposure image of an empty field. The first choice yields the most robust results, as the sky background counts are large. The second choice should only be considered, if one suspects the gain correction evolves over a period of few nights. Then a reduced master flat that integrate raw flat images observed too far from the scientific ones, should be corrected using an RB based on a science image. In practice, for the WFI instrument, currently the only multi-chip instrument being monitored, no evolution of mean gain over a period of 10 days has been observed, and therefore the mean gain normalization RBs are made with raw flat observations.

In summary, this procedure should always be executed for multi-chip instruments, and is regulated by the image selected for the gain-harmonization RB (raw flat or raw science), the percentage of the linear size of the chip to use to define the strip and the parameters defining the sigma-clipping always applied by the pipeline when computing the count statistics.

Illumination-error correction

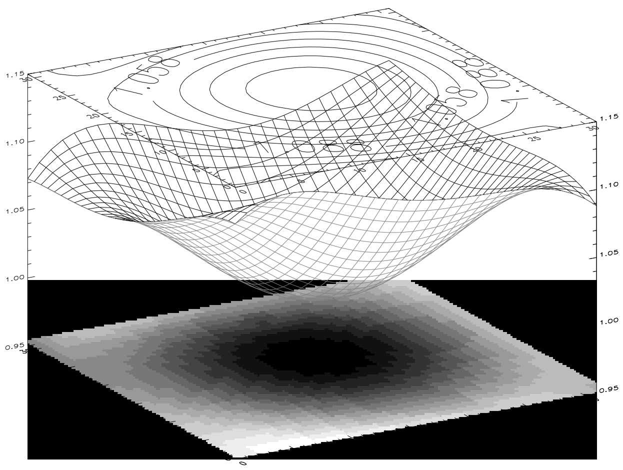

Figure 3.7: Illumination-map computed for the V-843 filter of the WFI instrument. This flux unit map gives the correction to be applied on V-843 master flats in order to fix a constant ZP on the science reduced images using this corrected flat. The flux convention is fix to one in the middle of the field-of-view.

Most of the instruments using a focal reducer are affected by the so called *illumination error*, which implies that the photometric zeropoint will not be a constant across the camera. This variation is represented by the so-called *illumination-map* which must be determined. This correction is more important for large field-of-view telescopes such as the 2.2 meter telescope at La Silla than for instruments with smaller field-of-view. For WFI images, the variations have a typical sigma of 0.05 magnitude, and a peak to peak amplitude of up to 0.2 magnitudes. Figure 3.7 illustrates the illumination error computed for the V filter. This map is in unit of relative flux, with the center of the image being the reference (flux equal to one). This phenomenon is due to an additive light emanating from reflections within the camera/focal-reducer system. An out of focus additive ghost image affect all observations. The master flats are therefore biased, and the reduced images using biased master flats have not a constant

ZP. It is worth emphasizing that this phenomenon is the main source of photometric error as pointed out by (Manfroid, 1996).

One way to compute an illumination-map (see section 4.3) is achieved by measuring and modeling the magnitude variations from the same stars observed on different reduced images taken with a dithering pattern. The corresponding master flats, sharing the same filter, are then corrected to decrease the illumination-error to a couple of percent. This procedure is executed on the dedicated *illumination-map RB*, good candidates for this computation contain five or more images observed with a large dithering pattern (10% the size of a chip). Also, the field of view shall contain bright stars that have large signal-to-noise.

The illumination-maps are globally a constant phenomenon and depend on the filter used (see long term stability in section 4.3.6). Previous models of illumination-map (polynomial functions) are saved as an instrument characteristic. To prevent this complex computation relying on special observations (good image candidates are not always available within the raw images) the previously computed models saved in the instrument description are applied directly to the master flats.

The high quality of the reduction of the calibration images is very critical for two distinct properties characterising the reduced scientific images. First, the stability of the Zero Point depends on the mean gain normalization, and the illumination correction, without this the ZP is varying within 5 to 10% between chips, and throughout the full field of view. Second, the local defaults are a function of the robustness of the procedure used to mask them during the reduction of the calibration images. If a bad pixel is not detected at the calibration reduction level, it will remain on the reduced science frames, and eventually it will be removed with a sigma clipping rejection used to mask out cosmic rays, if it is bright enough. It is common with large imagers to have some CCDs with lots of bad pixels and columns. The hot-pixel RBs and the dedicated procedure have proved to be very efficient and aims to a good image quality (see the study about bad pixels stability of the WFI instrument in section 5.4.2).

3.3.2 Photometric Standard and Science

In order to reduce science exposures taken consecutively in time and having the same characteristics such as filter and location on the sky are grouped into RBs. Additional constraints such as on the integration time of each exposure (*e.g.*, exposures should have same integration time within a factor of two), and the total elapsed time between the first and last exposure (*e.g.*, ≤ 1 hour) can also be applied to organize the exposures into different RBs. While, in principle, each individual raw exposure could be reduced one by one (RBs made of one image), and final products (see below) built by combining all these individual reduced images, there are many reasons for building RBs with a larger number of exposures.

First of all, from a practical point of view, using large RBs (≥ 4 exposures) yield a significant reduction in volume of data, which is a fundamental importance when dealing with wide-field imagers. In addition, there are other important technical reasons. For instance, in case of IR observations, several short exposures are required due to the high amplitude of the sky-background at those wavelengths. Typical IR science RB contains several one- to two-minutes exposures over a period of one- to two-hours of observation. This implies that objects detected in these frames have very low S/N making them harder to associate with an external reference catalogue, occasionally leading either to a failure of the astrometric calibration, or a poorly determined solution. To overcome this problem, it is preferable to carry out a relative astrometry first, i.e. using a catalogue extracted from one image to register the other images in the RB. Even though the number of reference points maybe small, they are much better determined than using an external catalogue as would be the case for an "absolute astrometric calibration" because they are better defined (same depth and wavelength, and have no proper motion). The same arguments apply when reducing U-band, or any other shallow images such as those obtained using narrow-band filters.

On the other hand, RBs cannot be arbitrarily large, covering long time intervals. In fact, they are typically restricted to be one hour long to avoid large variations of airmass and the uncertainty of assigning an airmass to the resulting reduced image, since no corrections to the flux due to airmass variations are applied at this stage of the reduction (but see section 3.4).

Another reason for making smaller RBs is in the case when the final images is the result of the combination of a relatively small total number of exposures (≤ 8). In this case, to improve the cosmetic quality of the final image, it is preferable to make a large number of reduced images and then co-add them later so as to benefit from the overlap of the neighboring chip. It is worth emphasizing that this is an optimal strategy for the final image. By contrast, the reduced images are left with most of the original cosmic rays especially in the inter-chip gaps (see section 5.4). This argument of course is only valid when cosmic rays are rejected using a sigma-clipping procedure described in next chapter. Alternatively, one could use other techniques (*e.g.*, Bertin (2001)), to identify and remove cosmic rays, currently not available in the pipeline described here.

In the case of deep observations, involving a large number of exposures (≥ 9) per filter per pointing, it is preferable to have at least three RBs with three or more images. For instance, if RBs are made of five images corresponding to less than one hour of continuous observation, the cosmic rays are removed with a sigma-clipping applied on the five images registered. The reduced image resulting from an RB has a S/N improved at best by $\sqrt{5}$ in comparison with the raw image. A final product is built with an SB made of all reduced RBs of this pointing observed with the same filter. If the SB contains three or more images, then a second pass of cosmic rejection based on sigma-clipping is possible. The first pass of cosmic rays is made at three times the noise amplitude of the raw images, and then the second pass applied on the reduced images, is made at three times the noise of the reduced RB roughly equal to $3/\sqrt{5}$ of the noise amplitude of the raw images, thus removing lower amplitude cosmic rays as well as other defects. The two passes of cosmic ray rejection is possible only with the notion of RB.

Based on the discussion presented above, the process of creating science RBs has been automatized and it is regulated by the following parameters; 1) the ratio between the integration time of a long and short exposure typically taken to be two; 2) the minimum number of images per RB, which in turn depends on the RMs to be associated within; 3) the minimum number of RBs (three by default) per pointing and filter for a second cosmic ray rejection using sigma-clipping; 4) the maximum elapsed time between the first and the last image of the RB.

It is important to emphasize that the pipeline is not aware of the OB notion, which means that it has total flexibility to group images into an RB in an optimal way by imposing a variety of rules which can improve the quality of the final products. Occasionally it may reflect the original OBs but this is not a requirement.

After an RB is created and an RM such as those given in table 3.8 are assigned, one must also link the RB with the proper master calibrations, reference grid, and a default or user-selected astrometric reference catalogue (if so required by the RM) as described in the preparation section 3.2. Unless otherwise specified, the pipeline will use the master calibrations as required by the RM closest to the date of the RB (first image). Of particular importance is for the user to decide which reference-grid to adopt as that may depend on the overall goal of the project. Once all the above steps are defined the combination RB/RM is submitted to the pipeline which at the end produces a reduced image and its associated weight-map, which as mentioned above, is critical for the proper extraction of catalogues.

A critical step is the selection of the proper RM to be used since this depends on the instrument filter and observing strategy. Table 3.8 summarizes the currently available science RMs. The table gives: in column (1) a sequence number; in column (2) the RM type; in column (3) the instrument; in column (4) the passbands to which this RM is optimized; in column (5)-(9) the processes that this RM activates (see figure 3.9); in column (10)-(16) the master calibration images and ancillary files required by this RM; and finally in column (17)-(18) the background scale resolution, S, (representing 2^{s+1} pixels) (see description of the associated procedure in section 4.4), the wavelet scale, W represented the scale of the bi-orthogonal wavelet transform used for the astrometric calibration as described in more detail in section 4.7.

The three RMs named *standard*, *deep* and *stellar* are defined for all instruments and cover most of the observation types. The only distinction between them is how the sky background (the large scale component) is considered. The *deep* mode is dedicated for extra-galactic fields or pointings with objects much smaller than the field of view (10 times smaller). For this RM the estimation of the large scale sky background is unaffected by extended astronomical sources, thereby being unbiased, and during the reduction, the images have their large scale background removed. On the other hand, using the *stellar* RM no background is estimated nor removed. This RM is adequate for fields containing large extended sources such as nebulae, globular clusters, Milky-Way, as well as nearby galaxies. The other parameters relative to the astrometric solution are similar as they do not depend on the density of the sources nor on the depth of the astrometric catalogue being used.

From a reduction point of view, the reduction of standards and science are equivalent, except that they are driven by different RMs. The main difference is the choice of parameters used in the astrometric calibration of the frame which is first order polynomial distortion mode in the case of photometric standards. A more detailed discussion on the RMs will be presented below.

An important difference between the optical and IR domains, is the nature of the observed sky background. In the case of the optical domain, the main contribution comes from large scale variations, except in the I-band, where fringing becomes an issue. In many ways, dealing with an I-band image is similar to those obtained by IR observations. However, in the I-band, it is possible to estimate the fringing pattern from separate observations, in other words the fringing pattern is stable at least over a period of hours. In the extreme case of the IR (J through K), this is no longer true requiring the small-scale background or fringing-map to be estimated from the RB itself as long as the observations does not contain extended sources larger than the size of the dithering pattern of observation.

In the latter case, one must resort to chop-mode observations that is a sequence of on-off target exposures. In this case, the off-target exposures can be used to estimated the background, and then subtracted from the on-target exposures.

Id	RM	INS	FILT	REDUCTION STEPS					DEPENDENCIES							SCALE	
				1 Calib	2 Fringing-est	3 Background	4 Relat-Astro	5 Astrometry	Bias	Dark	Flat	Wheight	Fr-map	Cat	Grid	Smoothing	Wavelet
1	deep	WFI	U	*		*	*	*	*		*	*		*	*	9	7
2	deep	WFI	BVR	*		*		*	*		*	*		*	*	9	7
3	deep	WFI	I	*	*	*	*	*	*		*	*		*	*	9	7
4	deep-fr	WFI	I	*		*	*	*	*		*	*	*	*	*	9	7
5	stellar	WFI	all-I	*				*	*		*	*		*	*	-	7
6	stellar	WFI	I	*				*	*		*	*	*	*	*	-	7
7	standard	WFI	all	*			*	*	*		*	*		*		-	7
8	deep	ISAAC	all	*	*	*	*	*		*	*	*		*	*	7	5
9	standard	ISAAC	all	*	*	*	*			*	*	*				7	5
10	deep	SOFI	all	*	*	*	*	*		*	*	*		*	*	7	5
11	stellar	SOFI	all	*		*	*	*		*	*	*		*	*	7	5
12	standard	SOFI	all	*	*	*	*	*		*	*	*		*		7	5

Figure 3.8: Typical example of Reduction Modes for the main instruments used for the EIS surveys. Three type of RMs are defined: the deep mode for the extra-galactic images, the stellar mode for the large extended objects or very dense star areas. The standard mode is similar to the stellar mode but differs in low level parameters and does not use a reference grid. The modules used are indicated with the Reduction steps column. The dependencies are given with the following short name: Fr-map for fringing-map, Cat for astronomical catalogue, and Grid if a reference grid must be used. The Scale columns gives the two main parameters of the reduction (scale to estimate the smooth component of the background, and scale for the wavelet transform used for the astrometric solution).

Typical examples of RMs are given in table 3.8, and their main characteristics are described below:

1. This *deep* mode defined for the shallow U-band filter of WFI, is made for extra galactic fields where the smooth sky background can be estimated with no interferences with the astronomical sources. The master calibrations used are: bias, flat, and weight-map. The smooth sky background is estimated at large scale as the CCD is large. The raw images of the RB are stacked after the computation of the relative astrometry, and the resulting image with improved S/N is astrometrically calibrated with a catalogue and a reference grid. As justified above, the absolute astrometry is computed with the stacked image where sources have better S/N than on the raw images. Of course, this is true if the RB contains more than one image.

2. The *deep* mode strategy of B, V or R filter is dedicated to extra-galactic fields observed with large band filters. The smooth sky background can be estimated with no interferences with the astronomical sources. The master calibrations used are: bias, flat, and

weight-map. The smooth sky background is estimated at large scale as the CCD is large. The raw images of the RB are astrometrically calibrated one by one, with a catalogue and a reference grid, and then are warped and stacked.

3. The *deep* mode for the I passband is distinct from the other passband as fringes are estimated/subtracted within the images of the RB. With this mode, all steps are executed. The master calibration used are: bias, flat and weight-map. The pixel-based background is estimated from the RB which therefore must contain at least five images observed with a consistent dithering pattern. The large-scale structure sky background is estimated/subtracted even though it should have been removed completely by the pixel-based background, some residuals may occur with unstable sky transparencies. The relative astrometric solution is also activated because I-band images are quite shallow for the WFI instrument in comparison to R-band for instance.

4. The *deep-fr* mode is dedicated for I passband images only. With this mode, the fringes are subtracted using an external fringing-map, and therefore is suitable for RBs containing few images (less than five). Also after removing the instrumental effect with a master bias, flat and fringing-map, the images are firstly stacked with a relative astrometric solution, and then the resulting image is astrometrically calibrated with a catalogue and a reference grid. Note that this mode has a different name, as the pipeline is not able to decide if fringes should be removed locally or, by using an external fringing-map. This choice is given to the user who has to connect the proper RM to the I passband RBs.

5. The *stellar* mode is assigned to RBs consisting of images which include large extended sources, or very crowded star fields (*e.g.*, large nearby galaxies, the Magellanic clouds). This mode is similar to the deep mode (2) but without estimation and removing of a large scale sky background. The master calibration images used are bias and flat. No distinction is made for the U-band since by definition in this case the field must contain bright sources.

6. The *stellar* mode for the I-band is the same as the one before (5), but with a master fringing-map. This map is used when removing the instrumental effect. Note that in some case of non-photometric night, this mode should be also applied to R-band images as fringes may be visible also for this filter. The only difference with the mode (4) *deep-fr*, is that the sky background is not estimated nor removed.

7. The *standard* mode described is designed to handle photometric standard fields. This mode enable the use of the relative astrometry and stacking, as the images are normally shallow, and the sky background is not removed, as it is not necessary. Since the astrometric accuracy is not required, and may not even be possible with some fields due to the typical shallowness of the exposures, a first order, with a large window search (see 4.7), is used. Since, there are individual observations, which will not be combined, a reference grid is also not needed. It is worth emphasizing that while in principle the sky background could be removed experience has shown that it is a good way of checking that the gain harmonization has been successfully applied.

8. This *deep* mode is made for extra-galactic fields observed with the IR ISAAC instrument. The pixel-based sky background must be estimated within the RB, and the raw images are too shallow for a direct absolute astrometric calibration. Therefore all steps are

activated. The master calibration used are dark and flat. This imposes that all the raw images within the RB have the same exposure time. An input RB must contain at least ten or more images to ensure good pixel-based background estimation. Also the smooth scale background is estimated from the RB, as some residuals may occur during non-photometric nights. The astrometric calibration is made with a reference grid to facilitate the creation of final products. It is important to emphasize that the astrometric catalogue used must be dense or the calibration will be weak. In practice, the commonly used GSC2.2 or USNOA are not suitable for a good calibration, one should first deal with optical observations taken with wide-field imagers in order to produce a deep catalogue. Note, that the scale parameters are two level lower than the one for the WFI instrument as the CCD size is four times smaller.

9. The *standard* mode of the ISAAC instrument is made to reduce the photometric standard RBs. Typically with ISAAC, five images with large dithering pattern are observed. Taking advantage of this strategy, the pixel-based sky background is estimated from the RBs themselves, thus ensuring that photometric standards and the science exposures are reduced in the same way. Note that no absolute astrometric calibration is computed as the field of view is too small (2.5 arcmin, four times smaller than the SOFI one) and astrometric failures may occur as very few astronomical sources are visible. Fortunately the pointing precision for the VLT telescope is so accurate (couple of arcsec) that the astrometric registration is not mandatory, and the standard stars are reliably associated.

10. Same parameters and dependencies as mode (8) before but for the SOFI instrument.

11. The *stellar* mode for IR has not been intensively tested. It concerns the reduction of extended sources larger than the dithering pattern of observation. This mode is dedicated for chop-mode observations, where observations are made consecutively around the scientific target, and an off-pointing far enough to benefit from an empty sky location. For this case, the off-observations are used to build a fringing-map (by feeding the pipeline with a fringing-map RB) that is then used to subtract fringes for the scientific observations.

12. The *standard* mode of SOFI is dedicated to photometric standard RBs. It is similar to mode (9) but with an absolute astrometric calibration made possible thanks to the size of the field of view (5 arcmin).

As briefly mentioned before, the EIS/MVM pipeline consists of five main modules, and three auxiliary modules, dealing with the cosmetic quality of the final image products. A schematic view of the pipeline structure and its dependencies on external information is shown in figure 3.9. Hereafter, the number of the modules will be used throughout the text. These modules are described below.

Instrumental effect removal

This module is represented in figure 3.9 as block one. For each optical image of the RB the master bias is overscan corrected with a constant for each read-out port associated with one or more over-scan areas. Then the science images are divided by the master flat. A similar

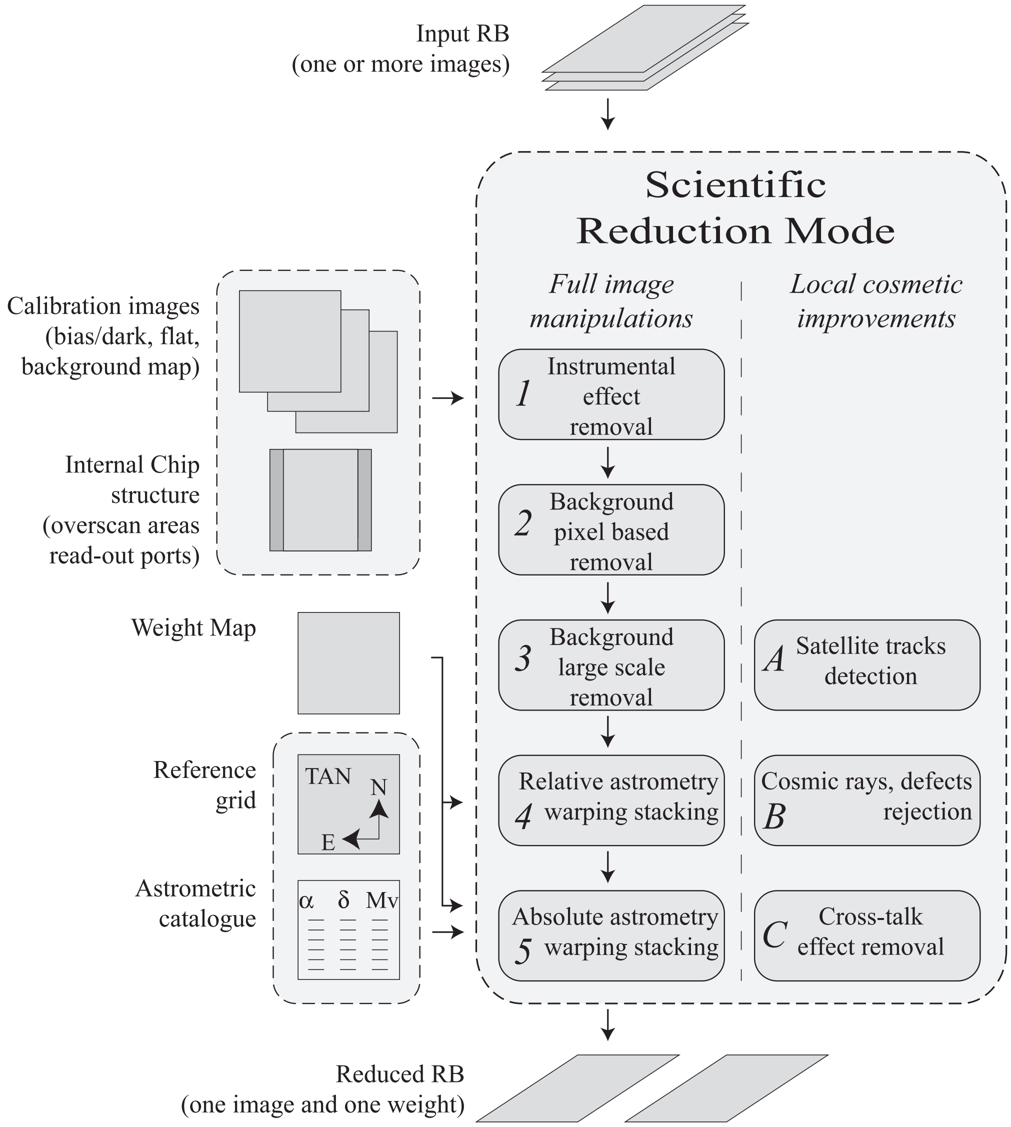

Figure 3.9: Main steps of a Reduction Mode used to reduce a scientific RB containing one or several images into a reduced image with its corresponding weight-map. Steps 1 to 5 are activated depending on the observation type and the instrument. Steps A and B are cosmetic procedures that are executed after the astrometric solution during step 4 or during step 5 if step 4 is not activated. Note that step 2, depending on local options may execute locally the step 4.

procedure is adopted for the IR images except that instead of the master bias, the master dark with the appropriate exposure time is used.

If an external background/fringing-map is used (required by the RM) to remove the fringes of the input images, a correlation factor is computed to match the amplitude of the fringes in the fringing-map and that in the science image. The input images are then subtracted by the scaled fringing-map (see section 4.6 for a complete description of the procedure).

The bad pixels pointed by the weight-map (pixel equal to zero) are set to a special value that indicates to the next modules that those must be discarded. It is worth emphasizing that they are not replaced by interpolated values of their neighboring pixels, they will be filled-in during the stacking of the RB, or later when building the final products.

Small-scale Background removal

This module is normally used to deal with images observed in passbands where both low and high-frequency features such as fringes are present in the background. This is typically the case for the red passbands in the optical (R and more conspicuously in I for EEV CCDs such as the ones mounted in WFI, SUSI2) and in all infrared domains. The procedure is made of two steps:

1. Background removal first step - A first crude attempt to estimate the local background is done by assuming that the observed features are stable in pixel coordinates. A first estimate of the local background level is computed as the median of the intensity of all images in the RB at that pixel. Next, all images in the RB are subtracted by this estimated background. However, as shown in sub-section 4.5.1 this estimate is biased and greatly affects the flux of faint objects. In some cases, this quality is enough and then the module stops, and the reduction continue with the other ones.

2. Mask estimation for the second step - To improve the background estimate it is necessary to mask out objects. In order to do that the images of the data cube are registered, warped and stacked by module 4. The stacking of the images is needed to estimate a mask obtained from the deeper image cumulating all observations. Objects are extracted from the stacked image. Each one is evaluated in size and position. A mask is created by plotting each detected objects by a circle enlarged by a typical factor of two. This refinement offers a better masking of the faint wings of the objects that have not been detected (an evaluation of the enlargement factor on IR extra-galactic images is given in sub-section 4.5.3).

3. Background removal second step - The mask is then applied to the original images in the RB at their original pixel coordinates. Pixels inside the masks are then discarded in the calculation of the mean for a second estimate of the background. This second estimate is used to subtract the background of each image. The resulting RB is then used by the next module. The stacked weight-map issued by this procedure and the following stacking must be checked to validate the parameters: Is the two steps option possible? Is the enlargement for the mask not too large and produce lots of holes in the weight-maps? The success of this procedure relies on a large dithering pattern, faint density of the sources of the field, a proper number of images, and short exposure time to map

properly the background evolution (especially in IR). Note that this module cannot be applied in cases where there are not enough exposures or for very crowded fields, another Reduction Mode using an external fringing-map is used instead, as discussed above and further described in sub-section 4.5.1.

Large-scale Background removal

This module computes and removes the smooth large scale of the background of each image. This procedure assumes that the images have a smooth background and that the smoothing scale is larger than the largest object in the image. For each image a mini-background is computed with a pyramidal median transform according to the *smoothing scale* adopted. This scale S defines the size in pixel (2^{S+1}) of the window size of an equivalent median filtering (see section 4.4 for a complete description of the median pyramidal transform). An estimate of the background, for each read-out port, is computed merging a user specified number of mini-backgrounds. Once this estimate is available the mini-backgrounds are re-sampled back to the original read-out port scale and subtracted from all images in the RB. In the case of IR observations carried out in nights of variable conditions, it is recommended to deal with each image separately. At this point any residual imprint of the read-out port structure in the CCD is removed.

Imprints of read-out ports, theoretically should be removed when the instrumental effect signature is removed using a master bias/dark and a master flat. Nevertheless, in case of IR detectors, master flats may suffer from the unstable IR bias (as described above) and implies small non-linearities that are visible (background steps) from one read-out port to the others of a processed image. Experiences show that with the special flat strategy applied for the SOFI instrument, imprints of read-out ports are negligible. By contrast, with the ISAAC instrument, larger background steps are visible using normal master flat-sky calibration where no IR bias are estimated/subtracted.

Relative astrometry, warping and stacking

The relative astrometry, warping and stacking module is responsible for producing a single image, combining all the images in the RB after they are relatively astrometrically calibrated and warped into a grid defined by a reference image (see below).

This module is used for both optical and IR images, which are individually very shallow (*e.g.*, U-band filter, or narrow band filters). In this case, the images in the RB, are first stacked, to increase the S/N of sources in the image, before an absolute astrometric calibration is attempted. Of course, this module is skipped if the data cube contains only one image. Otherwise the following steps are executed:

1. Selection of best reference image - By default, the first image of the RB is used as the reference image for the relative astrometric calibration. A test is made to select the reference image which has the maximum number of significant local maxima estimated on the last scale of the wavelet transform (see below). This test is made in order to select among the images in the RB, the one with the largest number of sources and best S/N.

2. Check/rejection of images with relatively high noise amplitude - This step is made to ensure uniformity of the final reduced image by rejecting images with larger than normal noise amplitude. This test is especially important for IR observations where the sky brightness can evolve rapidly.

   In order to reject images with high noise amplitude, the criteria is defined by the three following steps: 1) the median m of the noise amplitude of the individual images is computed; 2) the variation σ_v is computed such as $\sigma_v = median|\sigma_i - m|$, where σ_i is the noise amplitude of the i^{th} image; 3) the criteria t is defined as $t = 5 \times \sigma_v + m$. Images with noise amplitude greater than t are rejected from the RB.

   This criterion is equivalent to a sigma-clipping but using a median estimator which is more robust when dealing with small number statistics (*e.g.*, RB $\leq$ 10 images). It is important to emphasize that this test can only be performed when the background contribution is removed. It is important to note that strong residual fringes will also contribute to the noise. Therefore, images either with varying sky brightness, or high residual fringes will be rejected by this procedure. As a final remark, it is important to point out, that the procedure described can only be applied after the small-scale background estimated is subtracted.

   In practice 10% of the images are rejected during non-photometric nights, and none during nights with stable conditions. An illustration of this procedure with ISAAC IR images is detailed section 5.2.1.

3. Relative astrometric solution - The astrometric solution is referred to as relative when the distortion computed for each image is done using an image in the RB itself as reference. The user can select the reference image to be either the first or the one with the largest number of extracted objects in the RB. This is important when the transparency of the atmosphere varies significantly during the time interval corresponding to the RB under consideration. This is the case for the IR observations in general, and in particular, for the H-band.

   The association between extracted objects of one image and the reference image is carried out using the multi-resolution wavelet approach described in section 4.7, which combines high-throughput and robustness. The main parameter is the *wavelet scale* W used to decompose each image in different resolutions up to the scale W corresponding to low resolution details (smooth components). The other parameter known as the *window search* by other algorithms (*e.g.*, triangulation), used as a tolerance error, is naturally set by the resolution of the wavelet plane being iteratively used from scale W to scale 1 or 2 of highest resolution (sharp components). From the associated points, a distortion model of first second or fourth order is computed by a least-square estimator. If the number of associated sources is less than 5% (optionally 10% depending on the RM) of the number of objects from the reference image, the associations are assumed to be wrong and the image is discarded. This happens when the sky condition changes leading to a sudden decrease in the number of extracted sources.

4. Computation of the mean background variation - With images of extended sources the sky background cannot be estimated with module (3) because the extended sources will be partially subtracted. The sky background is kept and visible on the reduced RB. The sky brightness may evolve in time if the observations are done during

twilight, or if the sky conditions vary. One must check the evolution of the mean sky brightness measured by the mean background of the images. To eliminate this component all images are required to have the same mean sky background count as the reference image. This is accomplished by subtracting the difference between the mean background of an image and that of the reference.

For an RM which do not remove the background, when this procedure is not done, it may lead to the presence of sharp steps at the border of the stacked images, being an indication of a rapid evolution of the background of the raw images.

5. Satellite track detection - The satellite tracks are detected/masked by re-setting the affected pixels of the image to a "special value", thus forcing these pixels to be discarded in any further computation. The satellite tracks are searched for on an image by image basis, using the Hough space (see below).

6. Cosmic rays and other local defects removal - In order to be able to reject cosmic rays using a sigma clipping technique, the images concerned must first be astrometrically calibrated, to guess the mean pixel translation between them. But before warping, so as not to distort the characteristic of the cosmic rays, by convolving them by the interpolation kernel used in the warping procedure. If less than three images are aligned, the procedure described below is not executed.

7. Warping of images - Each image of the RB is warped using the distortion model computed for it. The same is applied to the master weight-map to create an image specific weight-map. The warping procedure properly ignores pixels that have been assigned a "special value", either from the pixel of the image due to image dependent effect such as track cosmic rays, as well as, special pixels in the master weight-map, which originally applies to all images in the RB registering common defect (*e.g.*, bad-pixels columns etc. as computed during the creation of the master calibration). It is worth pointing out, that after warping, each image has its own weight-map. Finally, each warped image is divided by its own exposure time in order to normalize the staked image to one second integration time. The warped weight-map are not normalized because weight-map indicates ratio of noise amplitude of the associated image which is insensitive to normalization.

8. Stacking of the warped images - All warped images and weights now share the grid of the reference image they can be combined by computing the mean value of the counts pixel by pixel. The corresponding warped weight-maps are simply added and reflect relative exposure-time map. By definition, the inverse of the weight-map corresponds to the variance of the noise amplitude defined per pixel. The final stacked image is trimmed according to a user specified minimum number of contributing images.

   Note that to avoid large use of memory, the final image and weight-map are built iteratively by warping and processing the input image one by one.

9. IR Cross talk effect removal - For IR images, the procedure to remove the cross-talk effect is executed on the final image produced by the above procedure.

The final image and its corresponding weight-map produced by this module is fed into module (5) if so required by the RM.

Absolute astrometry, warping and stacking

The absolute astrometry, warping and stacking module is responsible for producing a single image with a corresponding weight-map combining all the images in the RB that have been aligned to the reference grid, using an astrometric catalogue. If the module 4 was executed, then the RB contains only one image corresponding to the stack of the raw images, with a corresponding weight-map. This module is the same as module 4 (relative astrometric calibration, warping and stacking as illustrated in figure 3.9), but with a reference grid and an astrometric catalogue. The two modules have been separated for clarity.

A preliminary step is executed before module (4) to create an astrometric reference image. This reference image is a mock image defined as large as the expected size of the stacked image given by the dithering pattern of observation. A rough approximation is obtained from the different image location given their reference pixels and sky location. This value is enlarged by 10% to ensure the full-coverage of the area of interest being considered in order to cover the residual translations. Also, this image is built with the same projection, pixel-size and orientation as defined by the chosen reference grid. The astrometric catalogue is converted into pixel coordinates according to the mock image reference system, and the magnitudes are converted into flux with an arbitrary zero-point (30) to prevent infinite amplitude values. The converted catalogue is then included into the mock image, where each source is represented by a two-dimensional symmetric Gaussian function set at the location given by the catalogue, and with the amplitude given by the flux. This mock image is given to module (4) as the reference image. All further steps are similar to those described for this module.

Satellite track removal

Figure 3.10: Satellite track observed with the WFI instrument. Close artificial satellites, have high velocity and cross the full field of view in a couple of seconds. The track appears with a constant amplitude along a line. The track has the thickness of the seeing. Some very bright satellites can saturate the detector.

The artificial satellites due to their large number (several thousands in operation, and other thousands space debris) are often observed on raw exposures. Their proper motion is high, one arcmin per minute for the geocentric satellites, which have the slowest sky apparent motion. Therefore, they are observed as tracks crossing the full field-of-view (see figure 3.10). If catalogues are extracted from images containing tracks, these appear as a series of aligned sources greatly compromising the scientific value of the catalogue. This characteristic makes the Hough transform, which converts a set of aligned points into a Dirac function, an ideal algorithm to identify and remove these features from an image. When a track is detected, pixels along a strip of a width, specified by the user, surrounding the locus of the detected track are set to a "special value" and discarded for any further processing as already mentioned. For information the "special value" chosen is the maximum value for a float always named FLT_MAX for all compilers (roughly equal to $1e37$). The procedure is described in section 4.8, and the results of extensive tests carried out with a large set of WFI images are reported in section 5.4.3.

Cosmic rays and other defect rejection

The cosmic rays on an image are rejected for RBs containing a minimum of three images that have been properly registered (either by the relative or the absolute astrometric calibration modules). This procedure detects the cosmic rays or other defects before the warping of the individual images of the RB. From the astrometric calibration, the shifts between the images are computed. When the translations between images are known, and the noise amplitude of the images computed, the detection starts. It consists of a loop for all pixels of the estimated final size of the stacked image, as if the individual images were combined applying only the translations computed above. For each of them, the pixels from the individual images contributing to the stacked one, given by the translations known between the images, are copied in a list. Note that rejected pixels flagged to a special value (the one masked out by the weight-map or by the satellite tracks procedure for instance) are not included in that list. If this list contains less than three points, no cosmic ray detection can be made for this final pixel. If three or more are found, then the median of the listed pixels is computed. Pixel with values outside the median plus or minus three times the noise amplitude of the individual images are rejected, and the pixel on the corresponding image is set to the "special value", which indicates to the system, as before, that it should be ignored for further processing.

This procedure assumes that between two raw images, an integer shift is sufficient to describe the distortion between them. Note that the translation is computed for the middle of the CCD, from the astrometric calibration. This assumption is not exact, but sufficient even for strong optical distortion as the dithering pattern represents only few percent of the CCD size, and the optical distortions from one image to another are within a pixel. Of course, this procedure is only valid if the images grouped in an RB have been observed with the same orientation of the instrument.

It is worth emphasizing that after applying this procedure, cosmic rays are still visible at the border of the reduced image where less than three individual images contribute. For larger dithering pattern larger regions at the borders are affected. In case of multi-chip instruments, where RBs are reduced chip by chip individually and then assembled to a final image, this leads to residual cosmic rays or other defects visible at the inter-chip gaps. These are removed later when creating the final products, if the corresponding SB contains three or more reduced images.

One advantage of removing the cosmic rays and other defects before warping the images, is that their properties are not affected by the convolution with the Lanczos function or the bi-cubic interpolation applied during the warping procedure. Otherwise, since the Lanczos function has negative wings, this will transform cosmic rays into mexican-hat like features whit negative rings surrounding bright spots. These features are then difficult to remove completely by the sigma-clipping algorithm.

An important point to make is that the cosmic ray rejection is carried out when the images are relatively homogenous in noise amplitude, and therefore the sigma-clipping can be applied without having to take into consideration the corresponding weight-maps. This makes the procedure more efficient. By contrast, this can not be done when removing cosmic rays from an SB, where each image has its own complex weight-map. Therefore, for the second cosmic rays rejection applied at the level of the SB, the weight-maps must be used slowing somewhat the entire procedure (as detailed in section 3.4).

IR cross-talk effect removal

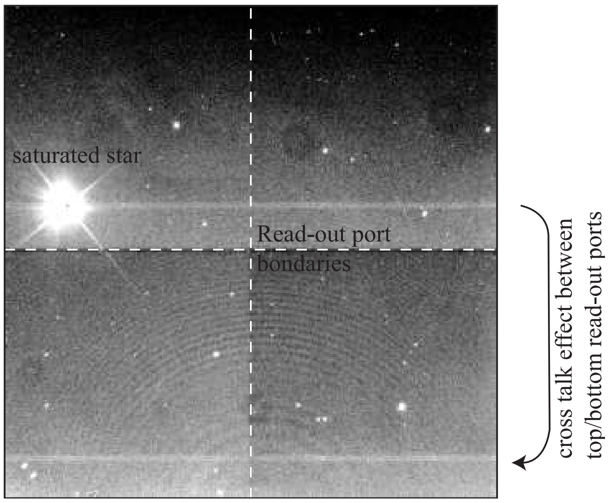

Figure 3.11: Cross-talk effect observed with the IR instrument SOFI. The image shown has been processed with a dark and a flat to improve the signal to noise of the cross-talk effect. Also visible are the typical fringe patterns observed in J passband (large rings at the bottom of the image). The CCD has 4 electronic converters reading a quarter of the full image (1k by 1k pixel). The bright stars (top left quadrant) saturates the detector, and the lines where pixels saturate are affected. This effect is propagated to the three other quadrants by the cross-talk effect.

Another pernicious defect which affects primarily IR detectors is illustrated in figure 3.11 by the two visible bright lines (in fact four given that there are four read-out ports), one crossing the bright star, and the other in the lower part of the detector caused by the cross-talk effect.

To remove this effect, the procedure is applied to the image produced by modules (4) or (5) depending on the RM utilized. This phenomenon is estimated by computing the mean of each line after masking out and enlarging the detected sources on this image. The masking of the sources is mandatory to prevent an over-estimation of the mean computed on a line where sources are visible. The computed mean is then subtracted from each corresponding line.

The current version of this procedure applies only on images where the sky background has been previously removed, and therefore cannot be used with stellar mode for SOFI or ISAAC. The impact of this procedure does not affect the photometry as illustrated for ISAAC final products (see section 5.2.2).

While in principle it could be done at the level of instrumental effect removal (module 1), in practice it suffers from the same effect of over-estimating the background, and therefore, it leads to an over-correction producing a dark line.

3.4 Final product

In the case of multi-chip instruments at the end of the reduction process for each RB, one reduced images is created per chip. These are merged together into the final image as specified by the reference grid. This assumes that flux scaling correction of the flats described earlier is adequate (see validation with section 5.3.2). This step is integrated into the pipeline to produce automatically one final image per RB for multi-chip instruments.

Often the observations are carried out as a sequence of OBs. Therefore, at the end of the reductions several reduced RBs (one image plus one weight each) are available all sharing the same reference grid. At this point these intermediate images can be combined using the weight-maps and the noise, as weight.

The merging of different reduced RBs in case of lots of images have been observed at different time or nights, a relative ZP between the images must be computed by an external module. The relative ZP are mandatory to stack reduced RBs that have been observed at different sky transparencies (due to the airmass and general weather conditions). The relative ZP can be deduced also from absolute photometric calibration. An ultimate procedure is able to assemble reduced images of the same grid, using a weighted co-addition taking into consideration relative fluxscale between them (computed from relative ZP, or from the photometric calibration). Note this procedure is the same as detailed in the Swarp documentation (Bertin, 2002) At this stage a second rejection of cosmic rays is applied when three or more RBs are merged, leading to the removal of lower S/N features not detected in the original frames.

3.5 XML interfaces

Instrument configuration

The generic instrument defined by the pipeline as explained above, offers lots of flexibility to handle a variety of instruments. To be supported, an instrument is described in a pre-defined node named *observatory*. Within this root node, the various descriptions are grouped in seven sub-nodes, each one is dedicated to a specific description. The name in brackets is indicated the sub-node name adopted for the XML:

1. Telescope location - <telescope> - Location on Earth and name of the telescope where the instrument is mounted.

2. Instrument properties - <instrument> - Main electronic and pixel size characteristics of the instrument.

3. Chip Geometry - <chip-geometry> - Description of the matrix of CCDs.

4. Quadrant Geometry - <quadran-chip> - Description the read-out ports and the over-scan areas for each chip.

5. FITS raw keywords - <raw-fits-keyword> - Name and unit conventions of the raw FITS keywords to be converted to standard pipeline keywords.

6. FITS alias keywords - <alias-fits-keyword> - Name of the FITS keyword adopted within the pipeline.

7. Calibration images recognition - <calib-recognition> - Word pattern-recognition used to identify calibration images from the native object-name FITS keyword of the raw images.

A description of each sub-node with their contents, and examples using ESO imagers are illustrated in appendix D.

Science RM configuration

The RMs controlling the reduction of the science RBs are complex because they describe the procedures used, and also their corresponding options. The XML protocol, used to describe a science RM, offers a great readability by using sub-nodes for each of the procedures used. Figure 3.12 lists the deep RM defined for the WFI instrument. All informations are within a node named *mvm-stack-option*. It is worth emphasizing, that each RM defined for a specific science RB and instrument is described within this node, and all are contained within a large configuration file. The pipeline recognizes them according to their properties described in the sub-node named *properties*, where three properties are given; 1) the name of the science RM is given by the node *reduction-mode* (deep in the example); 2) the name of the instruments valid for by this RM is indicated by node *pattern-instrument-name* (set to WFI in the example). Note that several instruments may share the same options for the same type of scientific RM; 3) the name of filters for which the RM is made. Several filters share the same options, in the example, the RM is defined for filter B, V and R. The given RM is the deep mode for the WFI instrument as described by the table 3.8 line number (2).

The five main modules (figure 3.9) defined for a science RM, are activated by the XML nodes set to yes, respectively: *flag-deflat*, *flag-fringing*, *flag-miniback*, *flag-jitter* and *flag-astrometry*. The options related to the modules, are organized in sub-nodes named respectively: *deflat*, *fringing*, *background*, *jitter* and *astrometry*.

In each sub-node associated with one of the five main modules, a special node, named *xinc:include* followed by several properties, indicates the unique location of some low level options common to all RMs. The factorization of those options avoids redundancy and is a robust way of ensuring that all RMs share the same ones which typically defined the sigma-clipping parameters, or some obvious informations such as the activation of the normalization of the image to one second. Note that those options could have been fixed within the source

```
<mvm-stack-option>
    <properties>
        <reduction-mode>deep</reduction-mode>                                        Name of the RM
        <pattern-instrument-name>wfi</pattern-instrument-name>              selected Instrument
        <pattern-filter>^B|^V|^R</pattern-filter>                                 selected Filter
    </properties>

    <flag-deflat>yes</flag-deflat>                                   Instrumental effect removal
    <flag-fringing>no</flag-fringing>                                Fringe estimation within RB
    <flag-miniback>yes</flag-miniback>                            Large scale background removal
    <flag-jitter>no</flag-jitter>                                Relative astrometry and stacking
    <flag-astrometry>yes</flag-astrometry>                       Absolute astrometry and stacking

    <deflat>
        <xinc:include parse="xml" href="#xpointer(/mvm-stack/defs/def[@name='deflat-base']/*)"/>

        <flag-use-flat>yes</flag-use-flat>                                                A master flat is used
        <flag-use-bias>yes</flag-use-bias>                                      A master bias (or dark) is used
        <flag-use-fringing>no</flag-use-fringing>                              No external fringing map is used
        <flag-use-mask>yes</flag-use-mask>                               A mask (from the master-weight) is used
    </deflat>

    <background>
        <xinc:include parse="xml" href="#xpointer(/mvm-stack/defs/def[@name='mini-back-base']/*)"/>

        <scale>9</scale>                                     The sky background is estimated at scale 9
        <merge-step>1</merge-step>                  The background is estimated image per image independently
        <flag-force-zero>yes</flag-force-zero>                              The mean of each image is removed
        <flag-calc-threshold>yes</flag-calc-threshold>         Bright sources are removed before estimation
    </background>

    <astrometry>
        <xinc:include parse="xml" href="#xpointer(/mvm-stack/defs/def[@name='jitter-base']/*)"/>

        <flag-fft-search>yes</flag-fft-search>                A FFT is used to compute residual translation
        <flag-read-wcs-translation>no</flag-read-wcs-translation>    Translation read from headers (CRVALs)
        <fft-scale>5</fft-scale>                                           Input wavelet scale for the FFT search

        <stat-coef-threshold>12.0</stat-coef-threshold>           Detection level of anchors in wave space
        <amer-scale>7</amer-scale>                            Number of scale for the wavelet transform
        <amer-median>1</amer-median>                Removal of cosmic before wavelet transform with median
        <scale-last-match>2</scale-last-match>                                    Scale of best resolution
        <distortion-order>2</distortion-order>                                            Distortion order
        <swarp-kernel>LANCZOS3</swarp-kernel>                                               Warping kernel
        <swarp-resample>1.0</swarp-resample>                       Zooming factor applied for the warping

        <flag-rejection>yes</flag-rejection>                                              Cosmic rejection
        <stat-rejection-coef>2.5</stat-rejection-coef>                             Cosmic rejection factor

        <flag-trim>yes</flag-trim>                                                   Trim stacked final image
        <trim-min-image>1</trim-min-image>              Trim parameter (minimum number of stacked images)

        <flag-remove-mean-axes>no</flag-remove-mean-axes>                   Cross-talk effect removal
        <flag-compute-bias-scale>no</flag-compute-bias-scale>  Compute mean background offset between images
        <flag-hough>yes</flag-hough>                                             Search for satellite tracks

        <flag-use-mosaic-ref>yes</flag-use-mosaic-ref>         Enable the use of an external reference grid

        <hough>
            <xinc:include parse="xml" href="#xpointer(/mvm-stack/defs/def[@name='hough-base']/*)"/>

            <stat-detect-coef-threshold>20.0</stat-detect-coef-threshold>            Detection coefficient
            <stat-detect-deep-coef-threshold>15.0</stat-detect-deep-coef-threshold>          Fine detection
        </hough>
    </astrometry>
</mvm-stack-option>
```

Figure 3.12: Example of an input parameter file using the XML protocol. The portion shown describes the RM deep for the WFI instrument for filter B, V and R. Some low level options are described externally to this node, and are linked by the *include* statement. Those low level options are common to several RMs, and to prevent redundancies, each RM link to those stable options.

code of the pipeline, but if one of those options appear to be important, one has the flexibility to move them within each RM, with a distinct value. It is worth emphasizing that the inclusions within the configuration file can be organized freely, and are transparent to the software because all inclusions are first resolved by the XML library before being parsed for the pipeline.

Within the node *deflat* related to the module controlling the instrumental effect removal, the XML nodes specify which master calibrations are necessary to reduce the RB: *flag-use-bias* indicates the need for a master bias or dark, *flag-use-flat* indicates the need for a master flat, *flag-use-fringing* indicates the need for a fringing-map, and finally, *flag-use-mask* indicates the need for a weight-map which is used by this module to set the rejected pixels to a special value such that the next modules discarded them.

The node *background* gives the options for module (3). The main options are: 1) the background scale *scale* used to estimate the smooth component of the sky background with the median pyramidal transform; 2) the number of sky background computed by the median pyramidal transform merged together *merge-step* such as several images of the RB are subtracted by the same estimation of the sky background; 3) an option *flag-calc-threshold* used to mask out the bright sources before the computation of the pyramidal median transform. This option is made to decrease the residual influence of bright stars in the pyramidal median transform.

The nodes *jitter* and *fringing* are not present in the XML because these two modules are not used by the RM.

The node *astrometry* contains the options used to compute the absolute astrometric calibration. This module is made of several steps, executed in the following order: Each image of the RB is filtered temporarily to reject very sharp details, cosmic rays or other electronic defects, detected on the raw image subtracted by its median convolved version The median convolution made with a mask of 3×3 pixels is executed *amer-median* times. The processed images within the RBs are transformed with the bi-orthogonal wavelet transform up to scale indicated by option *amer-scale*. The significant local maxima of each wavelet plane are detected at *stat-coef-threshold* times the sigma amplitude of the plane.

The option *flat-fft-search* is activated to search the residual translation using the Fast Fourier Transform between the mock image where the astrometric sources are mapped, and the raw images one by one. The *fft-scale* indicates which scale of the wavelet transform is used to perform the translation search. The mock image is built according to an external reference grid as specified by the option *flag-use-mosaic-ref* set to yes in the example. The associations of reference points is made iteratively in the wavelet plane from scale *amer-scale* to scale *scale-last-match*. The latter is chosen in general to scale 2 corresponding to the resolution of the typical seeing. The distortion model computed from the associated points is a second order polynomial function as indicated by the option *distortion-order*.

The satellite tracks are detected in the option *flag-hough* is set to yes. The option for the Hough procedure are set in the XML node name *hough* where the two detection threshold coefficient of the Hough space are given by the options *stat-detect-coef-threshold* and *stat-detect-deep-coef-threshold*. The second one corresponds to a second pass made on the images where the bright sources are masked out to improve the S/N of faint tracks observed in the Hough space.

After each image has been astrometrically calibrated, the sigma-clipping procedure is applied on the RB to reject cosmic rays and other defects. The rejection is activated by the option *flag-rejection* set to yes, and the rejection coefficient is indicated by the option *stat-rejection-coef* (here set to 2.5 times the noise amplitude).

Before being warped and stacked, the mean sky background shift between the images is first computed if the option *flag-compute-bias-scale* is set to yes. This option is not needed for deep observations, as the sky background has been removed by the module (3). The warping is made with the interpolation function specified by the option *swarp-kernel* set to Lanczos order 3 in the example. The option can be set to Lanczos2, Lanczos3, Lanczos4 or Lanczos5. The option *swarp-resample* indicates the zoom factor applied on the image during the warping. This re-scaling is used to decrease the pixel-size of the raw images to conform with the one of another instrument if desired.

When the images are stacked into a reduced image, and the corresponding weight-map is created, the user can specify to reject final pixels that does not originate from a minimum of *trim-min-image* raw pixels. This option is suitable for IR imagers where the RBs contain lots of images. In this example, the option is activated, to trim the image such as the size of the reduced image is not larger than the valid reduced pixels.

Finally, the last option available concern the IR cross-talk effect activated by the option *flag-remove-mean-axes* set to yes.

With the RM presented here, the module in charge of the fringing estimation and the relative astrometric solution are not activated. The main options available for the fringing estimation module are the activation of the two step procedure, and the enlargement size to build the mask (as described in section 4.5). The main options of the relative astrometric calibration are similar to the one of the absolute astrometric solution, as those two modules share the same procedure but has a different node name (jitter).

RM source code

In order to illustrate the numerous options and procedures that a science RM needs, figure 3.13, shows schematically the structures implemented in the source code for dealing with the numerous modules. Here, the reader is invited to see: the main modules (1) to (5), the two user options described above (smooth scale and the wavelet scale) surrounded with a gray rectangle, and the numerous internal options handled by the pipeline (beyond the scope of this manuscript). This illustration emphasizes the impact of the XML that was critical to help the encapsulation of the modules in a systematic way.

XML node visualization

One XML configuration file may contains all the RMs for the different instruments, the description of the all supported instruments, and other information relative to the process. Therefore one XML is in practice a long file in ASCII format. To simplify the reading or parsing of the options from an user point of view, the XML configuration file can be converted in whatever format such as convenient HTML pages. The protocol in charge of describing the transformation is named XSL. The program or *style sheet* is charge of the filtering is also in XML format.

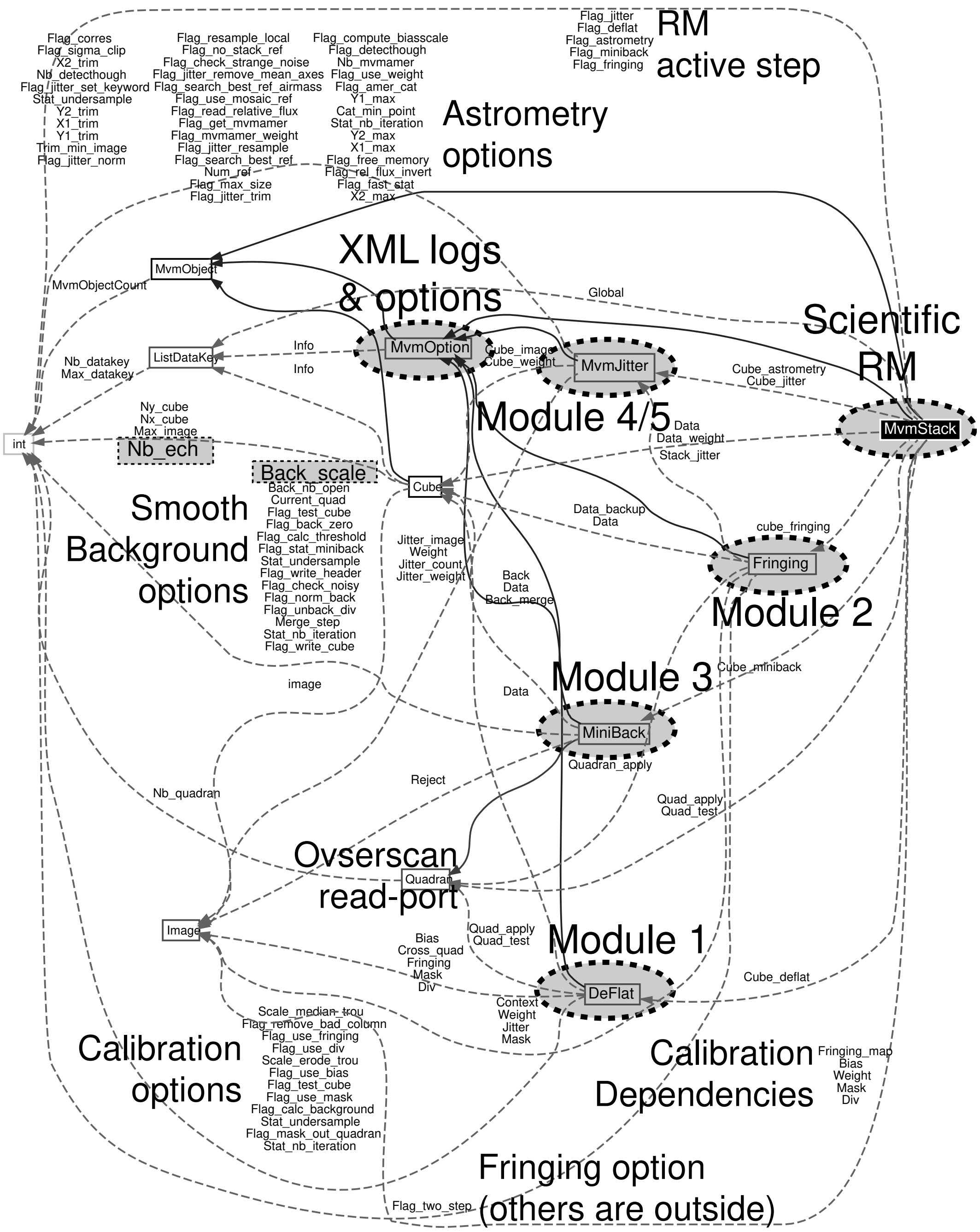

Figure 3.13: Visualization of the structure of the source code handling the reduction of a scientific RB. This figure focus on the module encapsulations, and not their chronological execution as shown in figure 3.9.

<table>
<tr><th>deep</th><th>isaac-sw</th><th>h|k</th><th></th></tr>
<tr><th colspan="2">Properties</th><th colspan="2">Dependencies</th></tr>
<tr><td>pattern-catalog</td><td>.</td><td>Flat</td><td>yes</td></tr>
<tr><td>pattern-mosaic-ref</td><td>.</td><td>Bias/Dark</td><td>yes</td></tr>
<tr><td>pattern-chip-id</td><td>.</td><td>Fringing-map</td><td>no</td></tr>
<tr><td>pattern-nb-image</td><td>^[5-9]$|^[1-9]\d</td><td>Weight-map</td><td>yes</td></tr>
<tr><td>pattern-jitter-size</td><td>^[0]?.0[7-9]|^[0]?.[12]</td><td>Extern mosaic ref</td><td>yes</td></tr>
</table>

Deflat		Fringing		Background	
Active	yes	Active	yes	Active	yes
Scale	0	2 steps	yes	Merge	1
Stat border	yes	Enlarge	2.1	Zero	yes
Strip relative	0.1	Merge 1 & 2	13 & 13	Scale	7
		Size min/max	28 & 250	Divide	no

MVM	Fringing/Jitter	Jitter	Astrometry
Active	yes	yes	yes
Scale & Fft	5 & 4	5 & 4	5 & 5
Flag fft & Amer median	yes & 1	yes & 1	yes & 1
Order & Last scale	1 & 2	1 & 2	1 & 2
Kernel Type	LANCZOS2	LANCZOS3	LANCZOS3
Norm expt & Bias	no & no	yes & no	yes & no
No Stack First	no	no	no
Rejection @ sigma	yes @ 3.0	yes @ 3.0	yes @ 3.0
Hough @ sensitive	yes @ 1.0	yes @ 1.0	yes @ 0.33
Check Noisy @ sigma	yes @ 8.0	yes @ 8.0	no @ 10.0
Trim @ nb images	no	yes @ 4	yes @ 1

Figure 3.14: An illustration of an HTML page created from the XML log produced by the system. It displays the main parameters which define the RM used for the IR camera ISAAC, mounted on one of the ESO VLT telescopes.

The style-sheet that transforms an XML into HTML pages can be built graphically thanks to several commercial software that produce automatically a style-sheet designed graphically.

Figure 3.14 illustrates an example of a compact HTML page built by a style-sheet applied on an XML file containing the description of the deep science RM for the ISAAC instrument. The reduction mode shown is used for processing images observed with the filters H and K. The field properties, for instance, lists the minimum number of images in the RB and the minimum amplitude of the jitter pattern required for the execution of this RM. Dependencies lists the master calibration images needed for reduction. In this example all the five main modules of the reduction mode are active. The absolute astrometric calibration is made using a reference grid specified. Also shown are possible settings for the various modules such as: noisy image rejection, cosmic rays removal and track detection using Hough transform. It is worth emphasizing, that several style-sheets can be built, each one dedicated for a specific purpose. The one presented, is made for a power user who wants to follow the main options of all modules.

Reduction log

Another usage of the XML is made to describe the process log of the reduced images, built during the execution of the science RM. In each log, the first node records all relevant information to reproduce the processing, such as: the full description of the RM used, the name of

```
<mvm-stack>
  ...
  <astrometry-stack>                                  Absolute astrometric calbration log
    ...
    <anchor-match   image-id="2"              Astrometric calibration image #2 of the RB
                    reference-id="catalog"
                    action="search">
      <matrix-match>            Rotation and scale between reference grid and raw image
        <polynom axis="x" order="1">
          <coeficient exp-x="0" exp-y="0" value="0"/>
          <coeficient exp-x="1" exp-y="0" value="1.000"/>
          <coeficient exp-x="0" exp-y="1" value="0.000"/>
        </polynom>
        <polynom axis="y" order="1">
          <coeficient exp-x="0" exp-y="0" value="0"/>
          <coeficient exp-x="1" exp-y="0" value="-0.000"/>
          <coeficient exp-x="0" exp-y="1" value="1.000"/>
        </polynom>
      </matrix-match>

      <shift-match  scale-id="5"              Shift between mock image and raw image #2
                    shift-x="248"
                    shift-y="312"/>
      <regression scale-id="2">                                 Distorsion model order 2
        <residual unit="pixel" value="0.89272" nb-match="540"/>
        <polynom axis="x" order="2">
          <coeficient exp-x="0" exp-y="0" value="250.86548"/>
          <coeficient exp-x="1" exp-y="0" value="0.9976910"/>
          <coeficient exp-x="2" exp-y="0" value="3.1617834e-07"/>
          <coeficient exp-x="0" exp-y="1" value="-0.001635"/>
          <coeficient exp-x="1" exp-y="1" value="1.5405879e-07"/>
          <coeficient exp-x="0" exp-y="2" value="7.7474197e-08"/>
        </polynom>
        <polynom axis="y" order="2">
          <coeficient exp-x="0" exp-y="0" value="310.65882"/>
          <coeficient exp-x="1" exp-y="0" value="4.5939643e-05"/>
          <coeficient exp-x="2" exp-y="0" value="3.3712287e-07"/>
          <coeficient exp-x="0" exp-y="1" value="0.9978517"/>
          <coeficient exp-x="1" exp-y="1" value="-1.452402e-07"/>
          <coeficient exp-x="0" exp-y="2" value="3.7171930e-07"/>
        </polynom>
      </regression>

      <list-match>                                           List of all the associations
        <match    x-init="609.0344"          y-init="35.262"
                  x-convert="858.556"        y-convert="345.995"
                  x-ref="858.915"            y-ref="345.991"/>
        <match    x-init="328.874"           y-init="37.024"
                  x-convert="578.956"        y-convert="347.653"
                  x-ref="578.974"            y-ref="348.003"/>
        <match    x-init="737.114"           y-init="37.868"
                  x-convert="986.391"        y-convert="348.659"
                  x-ref="985.913"            y-ref="347.074"/>
        ...
      </list-match>
    ...
    <track-search image-id="1">                         Satellite track search on image #1
      <hough-transformation nb-point="2695"/>
      <hough-detection nb-track="1">
        <track track-id="1">                                      Equation of the track found
          <slope>0.806</slope>             <offset>314.3</offset>
          <nb-point>268</nb-point>
        </track>
      </hough-detection>
    </track-search>
    ...
  </astrometry-stack>
</mvm-stack>
```

Figure 3.15: Portion of a log produced by the pipeline during the execution of a science RM on a RB containing two images. The portions shows

the raw images being processed, the master calibrations used, and ancillary informations for the astrometric calibration (reference grid, name of the astrometric catalogue). The following XML nodes of the process log gives the results of the modules applied.

Figure 3.15 illustrates a portion of a log produced during the reduction of a science RB made of two WFI exposures reduced with a science RM of type deep. The portion selected illustrate the results related to the absolute astrometric calibration, and the satellite tracks detection.

The node *anchor-match* gives the results of the associations between the astrometric catalogue and extracted sources, and the polynomial distortion model. The options of this node specify: the image being processed with option *image-id*; the reference used for the astrometric calibration, in this case the option *reference-id* is set to catalogue, for the relative astrometric computation, this option is set to the number of the reference image (the first by default).

The information under the node *matrix-match* refers to the distortion between the matrix element of the projection grid, and the matrix element of the raw images. This computation is made to have a first approximation of the rotation and scaling factor between the reference grid and the raw image. In this case, the grids has the same orientation as the raw images, and the distortion is equal to identity.

The node *shift-match*, gives the translation computed between the reference image and the image: options *shift-x* and *shift-y*. Option *scale-id* is set to the input parameter *fft-scale*.

The distortion model is saved under the XML name *regression*. The option *scale-id* is set to the input parameter *scale-last-match*. The sub-nodes *residual* give the residual value in pixel unit, between the associated points after applying the distortion model and the extracted sources. Option *nb-natch* gives the number of associations.

The two following nodes *polynom* gives the two dimensional distortion model. Then all the associations are saved under the node *list-match*. Each one is saved in a node *match* where the options *x-init* and *y-init* give the location of extracted sources; the options *x-convert* and *y-convert* give the location of the converted position of the extracted source when applying the distortion model; the option *x-ref* and *y-ref* are the pixel coordinate of the catalogued sources. With this list containing all the associations, one can built the residual diagram.

The information regarding the satellite tracks are given by the node *track-search*, where the option *image-id* gives the image number. Within the node *hough-transformation* the option *nb-point* indicates how many local maxima have been extracted and converted into the Hough space. Within the node *hough-detection*, option *nb-track* indicates how many tracks have been detected. For each track, a sub-node is created, and one find the node *slope* and *offset* that gives the equation of the lines. The node *nb-point* indicates how many points are aligned. In the example, one track was found.

Chapter 4

Advanced Algorithms & Techniques

4.1 Bad pixel Map

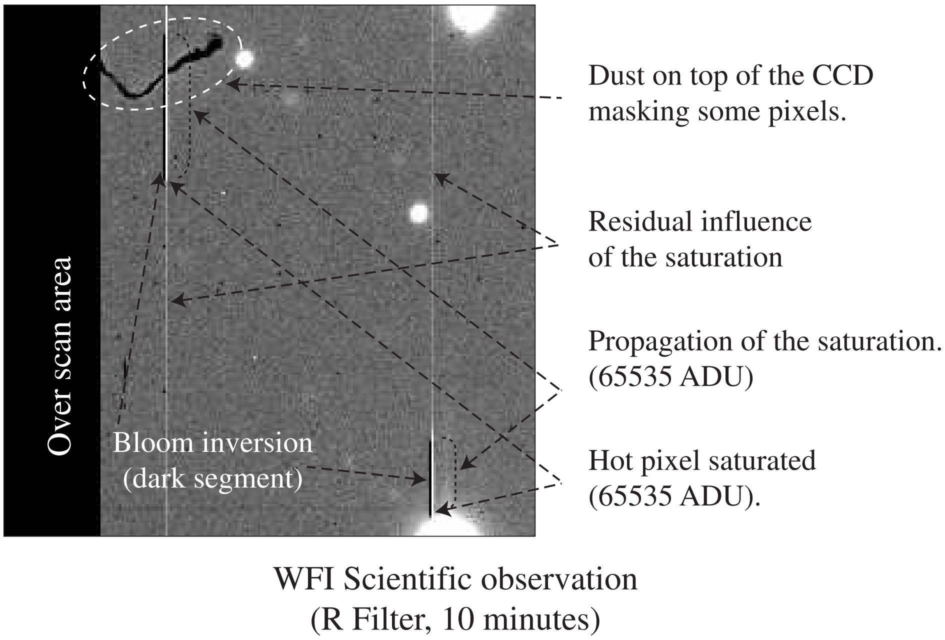

Figure 4.1: Bloom inversion observed with CCDs. The figure illustrates a raw image of 10 minutes observed with the WFI instrument (portion of chip 7). This portion shows two vertical segments reaching the saturation level. In the left column of the two segments, one notices darker segments of same size. This effect is named bloom inversion.

A large variety of bad pixels exists and are not all easy to identify. One could distinguish three main categories. Firstly, the dead pixels which do not collect electrons and appear with a very low ADU in all cases. Secondly, the hot-pixels which collect electrons very fast. If the exposure time is long enough, they get saturated, and may impact the rest of the columns during the read-out time. Some hot-pixels will saturate only with long exposure time (10 minutes for instance) and therefore appear only on dark or scientific images. Thirdly and last category is made of all other bad-pixels that are issued from complex electronic events beyond this study.

In this last category, one finds the case of pixels affected by saturated pixels of the neighboring column. With the WFI instrument, one notices that if a portion of a column gets saturated, on the next (or previous) column the corresponding portion of pixels has a low level compared to the expected mean of the nearby non-affected pixels. This phenomenon may be due to the high potential between the two portions that implies a transfer of electrons from the non-saturated column to the bloomed portion. This portion is then losing electrons, and appear fainter than the other unaffected pixels. Figure 4.1 illustrates two cases of such bloom inversion caused by saturated hot-pixels and their propagation to the column. Those two segments of 100 pixels each, reach the saturation level of 36536 ADU. One can observe two segments of low count on the left columns of the saturated segments. Those two affected segments are 100 ADU lower than the mean sky background equal to 1200 ADU. Quick inspection of the images produced by the 12k camera mounted at the CFHT telescope has shown no bloom effect visible. This effect might depend on the electronics in charge of reading the camera.

It is important to emphasize that those low level portions are often visible on final product images if they have not been preliminary detected/masked-out using dark observations for instance. Even when combining lots of scientific images with a sigma-clipping procedure, the low level segments may keep unmasked for two reasons: Firstly, the amplitude of the bloom inversion effect is comparable to the noise amplitude of the raw images, and the sigma-clipping procedure may not detect all segments. Secondly, if the sigma-clipping procedure is executed after the warping of the images (and this occurs with most of the available softwares), then the affected segments (bad columns) are dissolved by the warping kernel. Indeed a segment is not well sample in according to the Shannon sampling, and a warped segment appears as a larger one of smaller amplitude. An illustration of this effect observed in a reduced WFI image is illustrated in section 5.4.4.

This section details how bad-pixels are detected and recorded from the master calibration images. Also, to complete the lack of dark observations, an original procedure is defined to detect bad-pixels from scientific observations.

4.1.1 From master calibrations

The bad pixels are problematic and affect the reduced images. The strategy is too detect them from the master calibration images (bias, flat and dark), and then create a mask to indicate which pixels will not contribute to the final reduced images. This mask is multiplied with the master flat, to produce a weight-map, which characterizes the relative noise amplitude of the pixels.

From the master calibrations, different types of bad pixels are isolated. From the master bias, one detects a few hot-pixels that saturate during the read-out time and then produce hot columns. With the master flat, one identifies the pixels with low efficiency (cold pixels) and the location of dust that masks partially some connected pixels. From the master dark, one finds the location of the hot-pixels and their corresponding hot columns if they saturate during the exposure time. This last calibration is very important to isolate all bad columns or hot

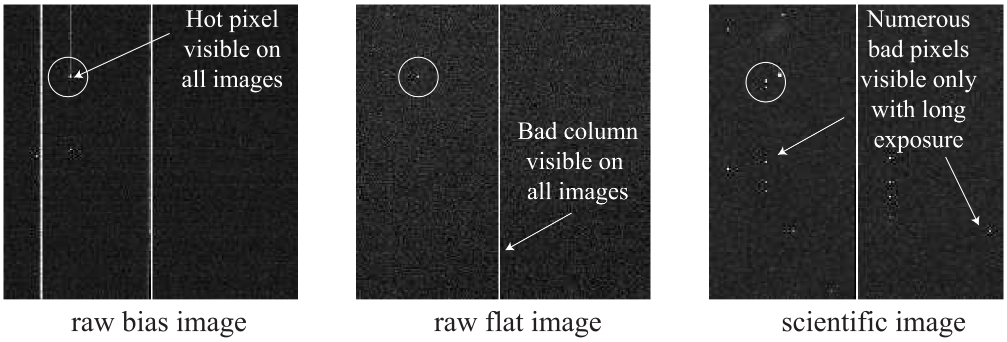

Figure 4.2: Hot pixel observed on different calibration images from the WFI imager. The three images illustrate the same portion of the chip 7 from the WFI instrument. The left image is a raw bias image where a couple of hot-pixels are visible. The middle image is a flat image of 1 second in filter R. Few hot-pixel appear, and some appearing on the bias image are invisible on the flat image. The right image is a scientific exposure of 600 seconds in filter R. Many more hot-pixels are visible in comparison to the bias or flat.

pixels that appear only with long exposure time (and therefore invisible in bias or flat images), figure 4.2 gives an illustration of hot-pixels visible only in the image with long exposure time.

The bad pixels are assumed to have a strange behavior in comparison to their local neighborhood pixels. The detection is made by comparing the amplitude of a pixel versus the median amplitude of the nearby pixels. A master calibration image is smoothed by a median pyramidal transform. The bad pixels are quickly dissolved as they are not extended. In practice a scale of 4 is used for the pyramidal transform (equivalent to a median filtering with a size of 12×12 pixels). The last scale is re-sampled to the original master image size using a bspline interpolation (see figure 4.26). The master calibration is subtracted by its smooth version to produce a detection image. The bad pixels are detected by thresholding the detection image to keep pixels greater or smaller than $n.\sigma$ the noise amplitude of the image. This approach is very efficient and a typical threshold is set to 10σ. This sensitive method detects: the cold-pixels, the saturated hot-pixels, and also the pixels affected by the bloom inversion.

4.1.2 From scientific images

Unfortunately for optical instruments, observations of darks are not made systematically because the dark current is now negligible, and no measurement is needed. The master dark is thus often missing when reducing a set of nights, and numerous hot-pixels and their corresponding hot columns are not masked-out on the weight-maps. To solve this lack of observations, the bad pixels detection from master dark is replaced by a special procedure using a cube of scientific images of long exposure time.

On all raw images the hot-pixels are always at the same physical location. To isolate them from the astronomical sources two steps of median filtering are used (the procedure is illustrated in figure 4.3). The first one is applied on the images independently. One assumes the hot-pixels and other bad-pixels to be sharp and isolated incidents in comparison to the mean sky background. On an image subtracted by its convolved version with a median (3×3 pixels),

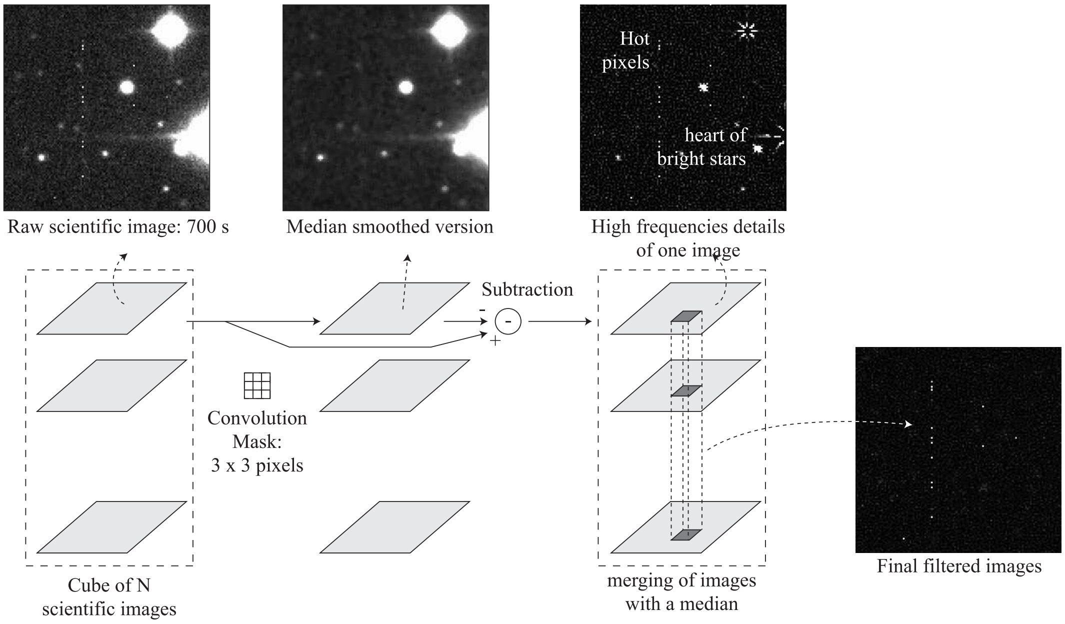

Figure 4.3: Schematic illustration of the procedure used to detect bad-pixels from a cube of scientific images. The top left image is a portion of one of the N input images of the cube. The top center image is a portion of one input image smoothed with a median filter (kernel 3×3 pixels). The top left image is a portion of one input image subtracted by its median smoothed version. On this image, one observes the initial bad-pixels, and also some strange cross like patterns issued from the heart of the bright stars. The final filtered image is issued from the merging of the residual images with a median. The signatures of the astronomical sources are dissolved. The bad pixels are detected by threshold.

only the very high frequency details appear. On this residual image, the mean is equal to zero, and only the bad pixels and also the heart of the bright astronomical sources are visible within a homogenous noise. In order to separate the hot-pixels or other detector defaults from the heart of the bright stars observed on the residual images, a second filtering step is needed. It is applied to the cube of residuals. The cube is combined with a median to produce one image where the astronomical sources have disappeared. Note that the original images of the cube must be at least 5 for good statistics, and observed with a dithering pattern or from different sky locations for a good filtering of the astronomical sources. The final filtered image is then used to detect bad-pixels as it is made for a bias, dark or flat master image. The detection of bad pixels from this procedure is very sensitive and stable. All the hot-pixels are detected, and also the pixels affected by the negative bloom. Indeed, has the cube is made of several images, the final images used for detection as a noise amplitude smaller than the original images. The detection of all bad pixels is then more sensitive. In practice the hot pixels are very stable, and such a mask can be used for several years of observations whatever is the filter of observation.

It worth emphasize that this procedure takes advantage of two distinct properties: first, the bad-pixels are sharp and affect a small amount of pixels, and second, the projected pixel-size of the detector is supposed to properly sample the nominal seeing of the observations. If this second assumption is not true, the stars are under-sampled and appear very sharp, therefore, one runs the risk to detect the heart of bright stars as bad-pixels. Note that, when using a RB of 5 or more images observed with a dithering pattern, the probability of assigning the heart of bright stars as bad-pixels is very small. In general of optical detectors have a good sampling, and this procedure is adequate. In the case of the SOFI imager, the pixel size is similar than the best seeing available and this procedure should be avoided. Fortunately, in practice, with SOFI or IR imagers darks are always observed, and bad-pixels are detected from master-darks.

The cube of data made of images to be used for this procedure must be made of the longest exposure time whatever is the filter. One must avoid very crowded stellar fields, and must provide images observed with a dithering pattern or from different sky region. For the pipeline the Reduction Block is named *hot-pixel-map* (See the special RB creation in the Data preparation sub-section 3.2). Actually the procedure is automatically executed, but the RBs must be created by the user. The bad-pixels are very stable and one RB of this type is enough. The resulting mask is then applied to all master weight-maps for all filters. A study of time stability over a period of one year of the detected hot-pixels from the scientific images is presented in section 5.4.2.

4.2 Gain harmonization for multi-chip detectors

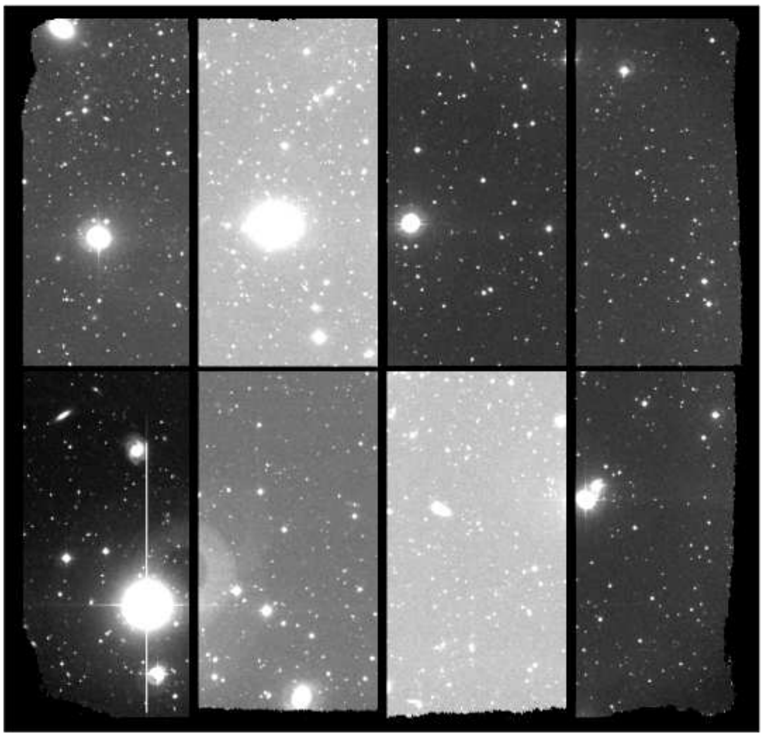

Figure 4.4: Mean gain variation on the multi-chip instrument WFI with filter V. The illustration is the assemblage of the 8 chips reduced independently. The reduction steps activated are; 1) instrumental effect removal (using normalized flats), 2) astrometric solution and warping of the chips to facilitate the final assemblage. The sky background of the raw chips is kept, and the ZP variations appear clearly with the sky background jumps from one chip to another.

A procedure is designed to calibrate the master flats to fix a unique effective gain for all the chips. The electronic converters of a multi-chip instrument are not identical, and give different mean gain. Therefore each chip has its own efficiency, and by consequence its own Zero Point (which varies within 10% compared to the other chips for the WFI instrument). This phenomenon is highlighted when reducing an image and keeping the smooth sky background component. In this case, the mean sky background values are not identical from one chip to another, and steps appear at the chip borders. Note that this effect is different to the illumination-error, which is a smooth error of the ZP throughout the full field-of-view. Nevertheless, the mean harmonization can be achieved whatever is the ZP illumination-error, and is even mandatory before computing an illumination-map.

Figure 4.4 shows the impact of the mean gain variations on a single WFI reduced image. The real sky background is almost a constant with smooth variations. No abrupt discontinuities would appear if all the mean gains were harmonized. Taking advantage of this observation, a fluxscale is computed per chip such that the sky background jumps disappear. The master flats are then divided by the fluxscales to have equal mean gains for future reductions. The advantage of this procedure is to offer a relative calibration (same mean gain on all chips) with no photometric computation nor matches with photometric catalogues.

Procedure description

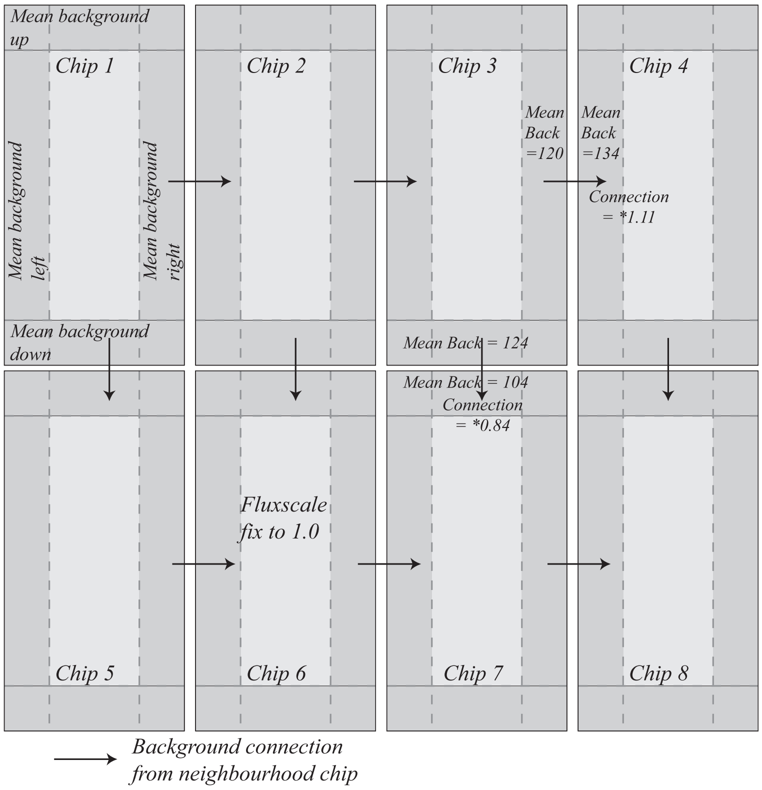

Figure 4.5: Chip connections to compute the mean gain variations with the WFI instrument. The background values are computed on the 4 borders of each chip. The borders are connected to the adjacent one of a neighboring chip. Each connection gives a fluxscale between one chip mean gain to another chip. Here, on chip 3, the background of the right border value 120, is connected with the chip 4 left border value 134. The fluxscale is the ratio of the background values equal to 1.11. Other connections are established between chip 3 and chip 7. In total 10 connections are done. The fluxscale of chip 5 is chosen as reference. The 7 other fluxscales are computed with a least square estimator using the 10 connections.

The mean gain from one chip to another is compared in a relative way by dividing the background value of a chip by the background value of a neighboring chip. One gets the fluxscale between the 2 associated chips, or in other words, the mean gain variation of the 2 chips. Note that the "real" sky background is not assimilated to a constant but suffers from various events such as: smooth variations due to faint clouds, gradients due to the moon halo, smooth illumination correction. The chip background comparisons are therefore affected by the sky variations. To be variation independent, the sky backgrounds are computed at the 4 borders of each chip. The mean gain comparison, is done by dividing the sky background computed in one border, versus the adjacent one of the neighboring chip. One establishes connections between neighboring chips. Each connection gives a fluxscale from one chip to another. Figure 4.5 illustrates the connections done with the chip borders of the WFI instrument (4 by 2 CCDs). For chips arranged in matrix of size (X, Y), the number of connections is equal to: $(X-1)Y + X(Y-1)$. The unknown parameters are the fluxscale f_i with $i \in [1, X*Y]$ that must be applied on the $X*Y$ chips. As it is a relative correction, one chip is chosen as reference, and the unknown parameters are $X*Y-1$. The number of connections is greater or equal to the number of unknown fluxscales. The system is solved by a least square estimator. The flats used to remove the instrumental effect, are corrected chip by chip by dividing by the corresponding fluxscale f_i. The correction is also applied to the corresponding weight-map.

This procedure depends on one image given by the special Reduction Blocks named *Mean gain normalization* (as described in sub-section 3.2 step number 4). Two types of images are good candidates to build those RBs: either a raw flat, or a raw scientific image of long integration time. In case of scientific observations, empty fields are recommended as they do not contain bright and extended sources that could affect the background statistics. Very dense star fields, or very short exposure time should be avoided. In practice, raw flats offer stable candidates because of their high background counts leading to better signal to noise of the statistics.

Comparison with other approaches

The main motivation for the procedure is to avoid a chip-based absolute photometric calibration, and also to harmonize the mean gain before the illumination correction. It is important to emphasize that the procedure is insensitive to the illumination-error. This error imposes a smooth variation of the ZP throughout the field of view. It affects the sky background that keeps a continuous shape. The procedure is robust as it uses a local computation on a single image. By comparison two other methods exist:

1. Mean Gain harmonization using photometric catalogues - This procedure relies on an absolute photometric calibration computed chip by chip. This method is subject to two important limitations. Firstly, in case of photometric catalogues like the Landolt one, the number of catalogued stars is not very dense, and the field of view of the catalogue may cover poorly the sky coverage of the instrument. Secondly, the photometric calibration is affected by two effects: the mean gain variations chip to chip, and the illumination-error. The ZP computed for a chip, corresponds to the ZP of the barycenter of the observed stars associated with the catalogued ones (in the middle of a chip in case of numerous randomly dispersed associations). Within a chip, the illumination-error can affect a ZP up to 0.10 magnitude. Therefore, the photometric calibration chip to chip will not correct the mean gain variations, but will compute a mixed solution limiting the variation of the two coupled effects.

2. Mean gain computation with consecutive shifted observations - Another strategy is to take advantage of consecutive images of the same field observed with a generous dithering pattern. With such observations, a star observed in the border of one chip, is observed in another chip on another image. One computes the photometry of the sources chip by chip, and associate stars from one chip to the next one in the other images. The multitude of associations helps to find a ZP shift chip to chip which is converted in fluxscale. This procedure is efficient as one computes the mean gain

variations using the same stars observed on different chips, and does not rely on absolute ZP. Nevertheless, this method is limited by the transparency variations. This latter is rarely smaller than one percent in optical wavelengths, and is subject to large variations with non-photometric nights. The transparency evolution is a complex phenomenon, and the numerous tests done to compute the illumination-map shows the rare case where the transparency variation is smaller than half a percent (as shown in figure 4.15).

Validation

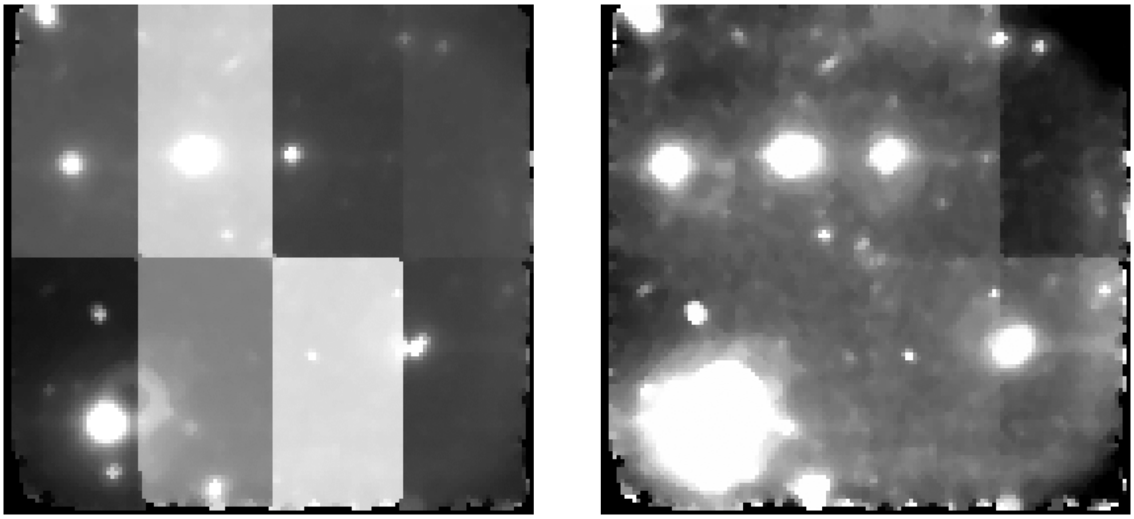

Figure 4.6: Background comparison. LEFT: image reduced with native master flat. The background jumps are typically 12%. RIGHT: image reduced with corrected master flat. No background jumps are visible, except at the top right chip, where the jump variation is 1% of the background value of the right adjacent chip. Note the gaps between the chips are not visible because the median filtering is done by excluding pixel equal to 0.0 (as the gaps), and dissolves details smaller than the equivalent mask size (64 pixels). The color scale of the 2 images are not compatible: the background jump of the corrected image represents only 1% variation.

To validate the result of the gain harmonization, the WFI image displayed at figure 4.4 is reduced a second time with the harmonized master flats. The 2 images are smoothed with a pyramidal median transform up to scale 7 (64 pixels). The filtering is made to dissolve small objects and remove inter-chip gaps. The median smoothing decreases the image resolution and the noise amplitude for a more significant background step measurement. Figure 4.6 shows the 2 smoothed images. The sigma of corrected background (computed with rejection) is 9 times smaller than the uncorrected one. The background jumps vary within 10% in the uncorrected data. No significant jumps are visible on the corrected image with the exception of the top-right chip where the background decreases by 1% relative to the neighboring chips. Note that the image used for the harmonization procedure was another scientific image observed 2 nights before. The mean gain variations are stable for a couple of days if the electronic of the instrument is not reset. A study of the WFI mean gain stability is made over one year with four filters (see sub-section 5.3.2).

4.3 Illumination correction, accurate ZP

Recent studies (Andersen et al., 1995; Manfroid and Selman, 2001; Manfroid, 1996) using different telescopes show that the amplitude of the flat-filed error over the camera area can be of the order of 0.1 magnitude. The zero-point is not constant among a reduced image, and varies according to a specific shape named the illumination error, the variations have a typical sigma of 0.1 magnitude, and a peak to peak up to 0.2 magnitude, in the case of the WFI instrument. The calibration error must be considered as one of the major sources of uncertainty in CCD photometry. This phenomenon should not be mixed with the well know vignetting effect of most instrument. This latter is due to the occultation of the pupils of the telescope when observations are done far from the central optical path. This effect is properly handled by the flat.

The main causes of photometric errors, are parasite light added in a non-uniform way on the detector. It is issued from lenses (instrument may have one just on top of the CCD to flatten the focal plane), or from internal reflections inside the telescope. All images from the sky (flat and science exposures) are affected. Therefore the master flats used to correct the pixel to pixel variation (multiplicative effect correction) are also affected, and provide a *fluxscale* error for the reduced scientific images.

This typical error makes the same star appearing fainter than if measured near the edge. To correct this effect, an illumination map measuring the relative flux error is computed, and then used to correct the master flats, so that future reductions using the corrected flat provide reduced images without illumination error. The correction is only relative, the goal is to remove the ZP variations over the field-of-view. In other words, the illumination correction, is an auto-control of the flat. Two general approaches allow the computation of the illumination map:

1. The illumination map is computed comparing the magnitude of the extracted objects from a reduced image, versus the matched objects from an external dense photometric catalogue of the same field. The differences give the delta magnitude at different locations in the image. Using a least square estimator with rejection, one can measure an approximation of the illumination map with a 2D polynomial function.

2. The illumination map is computed using at least 3 consecutive images observed with a dithering pattern. By comparing the magnitude of the associated astronomical objects observed in the consecutive reduced images, one gets the differential of the illumination map at certain location inside the image. Also using a least square estimator with rejection, the illumination map can be approximated by a 2D polynomial function (cf. 4.3.2 for all the details).

The first method is robust and easy to implement, but it will provide an auto-control of the flat based on an external catalogue assuming it perfect or at least with an internal relative accuracy greater than the typical illumination error. Also for wide field imagers, it is rare to find a catalogue covering the full field-of-view with an adequate density. The second method is a pure internal relative approach dealing only with observations. The main difficulty is to find a proper set of images with a large enough dithering pattern of observation, and enough stars with a very high signal to noise ($\gtrsim 100$) for an accurate relative photometry.

An illumination map is computed for a filter by comparing a reduced image with an external photometric catalogue, or by comparing dithering reduced images with themselves. It results in an illumination map showing the fluxscale error over the field-of-view. The illumination map is independent of the pointing, and the same map can be shared among other reduced images. The idea is to correct the master flat (by dividing with the computed illumination map), then future reductions of raw images using the corrected flat do not suffer from the illumination error.

The following sub-sections detail the 2 approaches. The second one using several images is explained and tested more precisely than the first because it provides more stable results.

4.3.1 Illumination map computed using an external catalogue

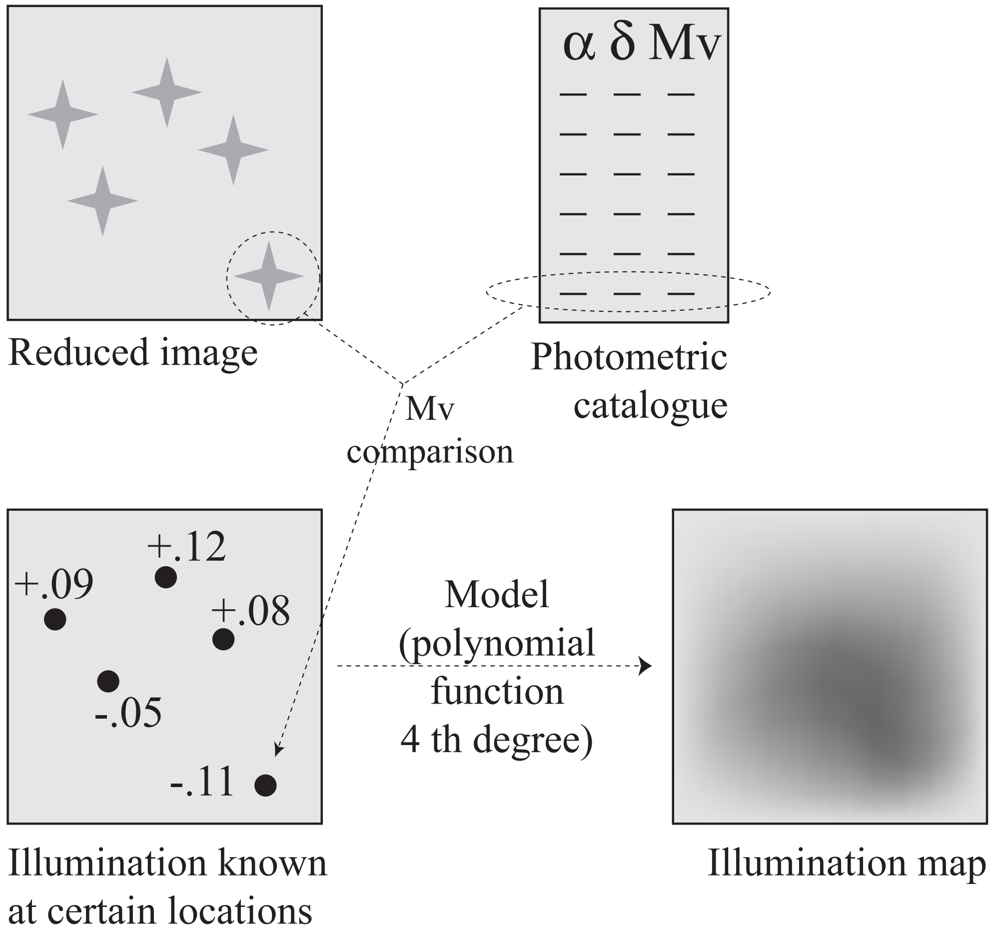

Figure 4.7: Illumination map computation with external photometric catalogue.

The computation of the illumination-map is done with an external photometric catalogue. The procedure defined is illustrated in figure 4.7. The corresponding steps are detailed below:

1. Image reduction. A raw image is chosen with a corresponding external photometric

catalogue. The image is reduced with the following steps activated: instrumental effect removal, astrometric solution.

2. Source extraction. The sources from the reduced image are extracted. One gets a catalogue of position and magnitude.
3. Source and catalogue association. The photometric catalogue is converted in pixel coordinate using the World Coordinate System of the reduced image. The extracted sources are associated with the converted catalogue with a classical window search.
4. Illumination computation. The new catalogue provides for associated sources the pixel coordinates (x and y) and a magnitude comparison with the photometric catalogue. The illumination-map is known at the location of the associated points. The illumination-map is computed by modeling the solution with a polynomial function of degree 4. The unknown parameters are solved for with a least square estimator.

The illumination map is computed from the associated catalogue. Let $F(x, y)$ be the illumination-map at location (x, y). The catalogue of the N associations gives the magnitudes of the extracted sources M_i and the corresponding photometric reference P_i at location (x_i, y_i). One establishes a system of N equations:

$$F(x_i, y_i) = M_i - P_i \tag{4.1}$$

F is approximated by a 2 dimensional polynomial function of order O:

$$F \approx \sum_{p=0}^{O} \sum_{q=0}^{O-p} a_{pq}\, x^p\, y^q \tag{4.2}$$

Where a_{pq} are the unknown parameters of the illumination map. The model of F has $(O+1)(O+2)/2$ unknown parameters. The typical order of the polynomial function is 4. The order should be an even number because the shape of the illumination-map is center symmetric. The system is solved with a least square estimator. The solution is iterated several times to reject points of bad photometry that have large discrepancies with the model. The iterated least square solution is more robust and reject typically 10% of the sources.

4.3.2 Illumination-map computation: the relative photometry approach

This approach relies on several consecutive reduced images, with no need of an absolute photometric calibration. The magnitude comparison of the same star observed two times, at two different locations on the detector is not null, and gives the differential value of F the illumination-map for these two locations.

The illumination correction is computed using an illumination-map RB containing at least 3 images observed with a generous dithering pattern (random translations in different directions). The absolute astrometric calibration of the images is made with the World Coordinate System (WCS) of the first one used as reference. The images are reduced (instrumental effect removal, absolute astrometric calibration, warping) but not stacked. A catalogue is then

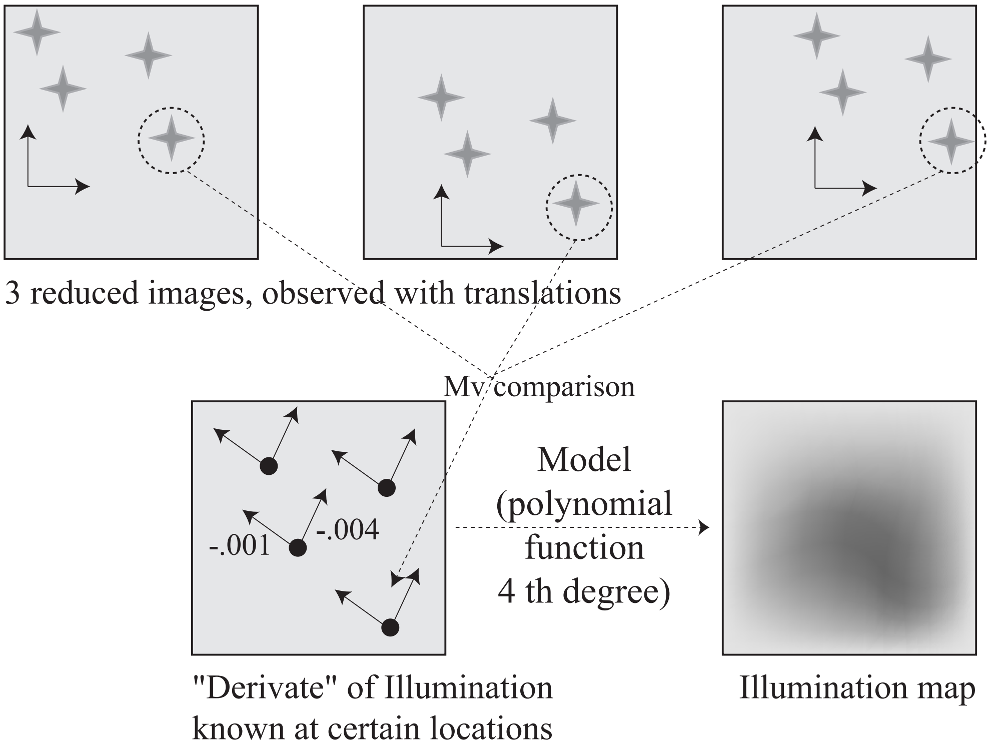

Figure 4.8: Illumination map correction from several reduced images observed with translations.

extracted per reduced image. To have very small RMS of the measurement, only the bright sources with signal to noise greater than 100 are considered. Let N be the number of images used, and ($\Delta x_{n,m}$, $\Delta y_{n,m}$) the translation between image n versus m in the x and y direction. Note that the translations are given by comparing the reference-pixel (CRPIXs) of the reduced images (all share the same reference grid given by the WCS). $M_{n,i}$ is the relative magnitude of $S_{n,i}$ the i^{th} star from the n^{th} catalogue located at $(x_{n,i}, y_{n,i})$. The absolute zero-point is varying from one image to another, only the variation are important in a relative context, let $\Delta m_{n,m}$ be the zero-point shift from image n to m. The variation in time of the zero-point is important to consider, because its typical amplitude is comparable to the illumination-error applied on a source observed on two distinct image shifted according to the dithering pattern (see section 4.3.5 for illustration).

Each i^{th} catalogued star $S_{n,i}$ observed in the n^{th} image is associated with one j^{th} star $S_{m,j}$ observed from the m^{th} image ($m \neq n$), by using a window search. Each $S_{n,i}$ has a maximum of $N-1$ associations with the other catalogues. Less associations occur for stars observed in the border of a chip and therefore those are invisible on another image due to the inter-chip gaps or the shifted field-of-view. Using the known translation between two images n and m, F the illumination correction has the following relation between a matched star $S_{n,i}$ and $S_{m,j}$:

$$\begin{gathered} F(x_{n,i}, y_{n,i}) - F(x_{n,i} + \Delta x_{n,m}, y_{n,i} + \Delta y_{n,m}) = \\ M_{n,i} - M_{m,j} + \Delta m_{n,m} \end{gathered} \tag{4.3}$$

Equation 4.3 is not equivalent to a derivative because the translations between images are not infinitesimal, so the system is solved by modeling the illumination map, without using direct integration of the observed differential values. Replacing F in equation 4.3, by its approximation from equation 4.2, shows the simple relation:

$$\sum_{p=0}^{O}\sum_{q=0}^{O-p} a_{pq}\left(x_{n,i}^{p}-(x_{n,i}+\Delta x_{n,m})^{p}\right).$$
$$\left(y_{n,i}^{q}-(y_{n,i}+\Delta y_{n,m})^{q}\right)=M_{n,i}-M_{m,j}+\Delta m_{n,m} \tag{4.4}$$

The N catalogues are cross-identified 2 by 2 providing $N_{tot}=N(N-1)/2$ distinct set of associations. Each couple of associated stars from all the different cross-identifications generates a new equation (4.4). The unknown coefficients a_{pq} are solved by a least square estimator with rejection. Only the parameter a_{00}, the constant term of F cannot be computed. Indeed the illumination correction is deduced from a differential approach, and the constant term disappears in the equation (4.4). In a relative photometry context this term is not mandatory and is set to 0.

The zero-point shifts between the images ($\Delta m_{n,m}$) must be known more precisely than the typical amplitude of $M_{n,i}-M_{m,j}$ ($\simeq 0.01$). The zero-point is varying in time with airmass, but also randomly with the transparency of the sky. Measurements made with WFI images show that typical variations of the transparency is about a few percents. These variations must be taken into consideration, or the resulting illumination will be affected by large gradients in the direction of the shifts ($\Delta x_{n,m}$, $\Delta y_{n,m}$).

The $\Delta m_{n,m}$ are in a total of N_{tot}, but depend only on $N-1$ independent values $\Delta m_{1,n}$ because the magnitude shifts evolve with the zero-point function of time, and not with the combination of images. The $\Delta m_{1,n}$ are computed while cross-identifying catalogs. The two magnitudes of each couple of associated stars from two catalogues are compared, and all theses differences are averaged with rejection. Let the resulting mean be $\Delta' m_{n,m}$ the zero-point shift between image n and m. Those N_{tot} shifts are expressed as a linear combination of the $N-1$ independent values $\Delta m_{1,n}$ such as:

$$-\Delta m_{1,n}+\Delta m_{1,m}=\Delta' m_{n,m} \tag{4.5}$$

The $\Delta m_{1,n}$ are solved also with a least square estimator. The experimentation has shown zero-point shifts must be computed using the data, because the transparency is evolving randomly and cannot be modeled (as the airmass for instance). This strategy determining the shifts imposes a symmetric shape to the illumination map F, or more precisely the minimum efficiency of the map is exactly in the middle of the camera. This assumption is compatible to the optic design of a telescope and prove to be efficient (see section 4.3.4 for WFI tests).

It is important to emphasize that the $\Delta m_{n,m}$ should be computed before the resolution of F. With equation 4.4, one could chose to compute the $\Delta m_{n,m}$ parameters as well as the a_{pq} parameters within the same least square estimator. The computation will be impossible because the matrix built for the least square estimator is not invertible: for each value of $\Delta m_{n,m}$ a distinct stable solution F exists. Also, if one decides to neglect them be setting all $\Delta m_{n,m}$ to zero, the illumination-map computed will be valid only for very stable photometric night (ZP variations within 0.2%).

4.3.3 Procedure description

The complete procedure from the choice of the images for the computation, to the correction of the master flats and weight-maps is made of the following steps:

1. Creation of the illumination-map RBs - A set of consecutive images (at least 3) observed with a consistent dithering pattern (at least 5% of a chip) are grouped in an RB. As the *illumination-map* is filter dependent, one must create one illumination-map per filter used.

2. Reduction of the images - The images defined in an *illumination-map* RB are reduced according to the special RMs named also illumination-map. Those RMs commonly include: the instrumental effect removal, a background pixel scale estimation if needed (with the I optical passband, and for IR images in general), an absolute astrometric solution and warping. Note that the warped images are not stacked but saved on disk. For each image of the input RB, it yields a reduced image per chip with a corresponding weight map. After the warping procedure, all the reduced images share the same reference grid defined by the first image of the RB as an external reference grid is not mandatory.

3. Extraction of sources and filtering - For each reduced image, the astronomical sources are extracted in three steps. Firstly, a smooth background is estimated and subtracted with a pyramidal median transform. Secondly, the noise amplitude is estimated with a sigma-clipping. Thirdly and lastly, the sources are extracted with a threshold done at typically 4 times the noise amplitude. The flux of the extracted sources is measured with an aperture magnitude of 8 arcsecs. The photo-centers are converted into sky position. It is important to emphasize that during the reduction, the images are not trimmed to remove the masked over-scan areas for instance and the reduced images have the size of the corresponding chip (within a couple of pixels due to the warping of the images). The non-trimmed image keep the chip geometry and gives a proper positioning of the sources relatively to the full detector facilitating the correction of the master flats.

4. Catalogue associations - The catalogues of the same reduced images (in case of multi-chip instrument) are merged and then converted to pixel coordinate relatively to the full detector (as it is described in the option XML file). One gets the shifts between the images from the pixel coordinate of the reference pixels (CRPIXs information of the WCS). The N catalogues are filtered to keep only sources 5 magnitudes brighter than the limiting magnitude, and not affected by the saturation. The N pixel coordinate catalogues from the N input images are then associated taking into consideration the different shifts.

5. Estimation of the delta ZP - The relative zero points $\triangle m_{n,m}$ of the N catalogues (a total of $N(N-1)/2$ values) are computed by a median of the differential magnitude of the associated sources. The $\triangle m_{1,n}$ (see equation 4.5) are solved with a least square estimator and one gets the estimated $\triangle' m_{n,m}$. Each catalogue is then shifted with its corresponding relative ZP.

6. Model computation - Each object of each association is giving an new equation (see 4.4). The unknown parameters are solved with a least square estimator. The computation with the least square estimator is iterated by rejecting objects that have residuals larger than 3 times the sigma value of all the residuals. Note that the polynomial model is computed in pixel space relative to the full instrument.

7. Master calibration correction - For each chip of the instrument, the polynomial model is plotted on an image of the size of the chip taking into consideration the location of the chip within the detector. The created image is in delta magnitude unit, and is converted into fluxscale. The fluxscale 1.0 is set to the middle of the detector. This image I_{zp} is the illumination-map for the chip considered, and for the filter of the raw images used for the computation. The master flats and weight-maps sharing the same filter than I_{zp} are multiplied by I_{zp}. One gets illumination corrected master flats and weight-maps. For visual inspection, the illumination-map created from the polynomial model is plotted for the full detector and then saved.

A valid illumination map is difficult to obtain and depends on a lot of parameters. The following sub-sections give a method to validate a model, establish the impact of the photometric conditions on the computation, and study the long term stability. Nevertheless, the illumination-error are independent sky position, and quite stable in time (on a year base for instance). When working on a run of observations, one may use a default polynomial model computed from other runs and saved into the XML input file. The pipeline chooses a corresponding model to correct the master flats and weight-maps depending on the filter.

4.3.4 Validation method

To validate an illumination correction map, one must compute the flatness of the zero-point on a reduced image. Either this test is done with an external catalogue (for instance the Landolt catalogue used to compute the absolute zero-point), or is done relatively using special astronomical objects where the color diagram is well known. The globular clusters far from the Milky Way, with a very small reddening effect are good candidates to check the flatness of the zero-point if of course they are large enough to cover a large part of the instrument field of view. They show a typical Color Magnitude Diagram (CMD, for instance V magnitude versus color B-V) with a very thin main sequence with a typical turn-off point. This point must be as thin as possible, and its position in the color diagram must be uncorrelated with the location on the image. The validation of the illumination map with the globular cluster is chosen because it does not depend on external catalogues, and provide a pure relative internal test – matching the application of "only" relative correction.

It is important to emphasize that if the illumination-errors for filter B and V were similar, and if the B and V images are observed exactly at the same sky position, then the color B-V of the turn over will not be correlated with the sky position. In conclusion, for images observed at the same sky location (no shifts), with different filters sharing the same illumination-error, no error in color vs the sky position are perceptible. The test mentioned is relative as it relies on the color and not on the magnitude. In other word, this test is valid to establish that two illumination-maps from two distinct filters are relatively consistent. An absolute validation of an illumination-map is made by comparing the magnitude versus the sky position of two catalogues extracted from two observations shifted by the half the size of the detector for instance.

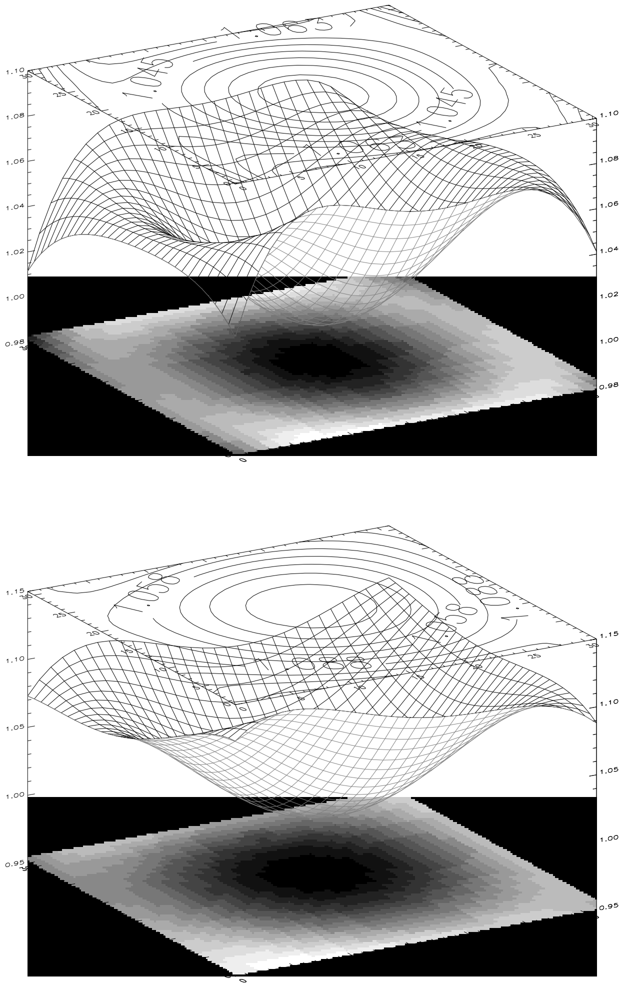

Figure 4.9: Illumination maps computed for the instrument WFI with filter B-842 (top) and V-843 (bottom). The map are in fluxscale unit. The global shape of the maps looks similar with a minimum efficiency in the center of the detector (set to 1.0 as it is a relative correction). The V illumination correction appears very symmetric, whereas the illumination-map in B has a more complex shape. The sigmas of the illumination-map are 2% for filter B, and 3.3% for filter V. The peak-to-peak variation is up to of 13% for the V filter.

A set of several consecutive nights sharing observations of a deep field, and globular clusters is used. They are part of the Pilot Stellar/Deep Survey handled by the ESO Imaging Survey team. The deep field is located at $\alpha : 9h57' \, \delta : -20\infty15'$ and contains enough bright stars to compute a proper illumination map: 300 stars with magnitudes at least 6 magnitudes brighter than the limiting magnitude of the individual images. Two times five consecutive images with a consistent dithering pattern of observation (within a box of 15% of the detector size) are reduced one by one and then cross-compared to compute the illumination map in V and B with a forth order polynomial function (see Figure 4.9). The two illumination maps are not identical, this can be due to the illumination error implied by the different filters (B and V).

The master flats and weight-maps are corrected using these maps (multiplication by the illumination-map), therefore all further reduced images are corrected. The standard fields used to compute the absolute zero-point have to be reduced with the same corrected flats as the scientific frames, to provide the true and constant zero-points.

To test the robustness of the results and quantify the internal accuracy of the procedure, secondary illumination-maps are computed from the corrected data. The previous images (5 deep images with filter B and V) used to compute the illumination map in B and V are reduced once more with the corrected master flat. Then two new illumination maps are derived. The new maps are "theoretically" expected to be constant and equal to one, because the illumination error have been removed by the corrected flats. The variations of the new maps give the internal stability of the procedure. The two new illumination-maps obtained for filter B and V are now equal to $1 \pm 0.35\%$. The larger peak-to-peak amplitudes are observed in the corners of the new maps, and are always smaller than 2.5%. The very small variations of the secondary illumination maps have to be compared to the variations of the first illumination-maps (see figure 4.9). The comparison prove the internal stability of the procedure.

The tests are also carried out using two globular clusters NGC6752 and NGC6397. Two observations are made per filter B and V per target, with an integration time of 240 seconds each. The images are reduced (the two observations per filter and target are stacked to fill-in the inter-chip gaps), one using the native master flat, and a second time with the master flat corrected by the illumination-maps extracted from the deep observations as described above. The sources are extracted with Sextractor (Bertin and Arnouts, 1996) using the MAG_APER magnitude estimator. The CMD V versus (B-V) is plotted for the two targets based on catalogues from without and then with the illumination correction (see the CMD of NGC6397 on figures: 4.10 and 4.11, see the CMD of NGC6752 on figures: 4.12 and 4.13). The main sequences of the two globular clusters appear much thinner in the CMD after illumination correction, the turn over of the main sequence is also smaller and do not appear double as in the uncorrected CMD. With each CMD is also plotted the color (B-V) versus the right ascension (bottom-left), and versus the declination (bottom-right).

To quantify the photometric precision, the color of the turn-off is studied at different locations of the image. For globular clusters with no differential reddening, the color of the turn-off is constant over the field. Therefore a map showing the values of the color of the turn-off as a function of the location in the image is a good estimator of the stability of the relative zero-point. This estimator is very robust and depend only on the physics of the globular cluster. Here the test is made on the observations of NGC6752.

The color of the turn-off is computed on the CMD using a first order moment in color direction of points inside the selected window with the following borders: [0.03 : 0.12] for the (B-V) color, and [-5 : -6.5] for the V magnitude. This method is used with stars located at different locations of the WFI field within a 10×10 grid, where each cell has a projected size in the sky of 3×3 arc-minutes. The result is a 10×10 pixels image showing the color of the turn per cell. This low level sample is enough to characterize the smooth illumination error. A finer resampling cannot be used (splitting the WFI image in smaller cells) because the number of stars per cell decreases, and the uncertainty of the measurement increases.

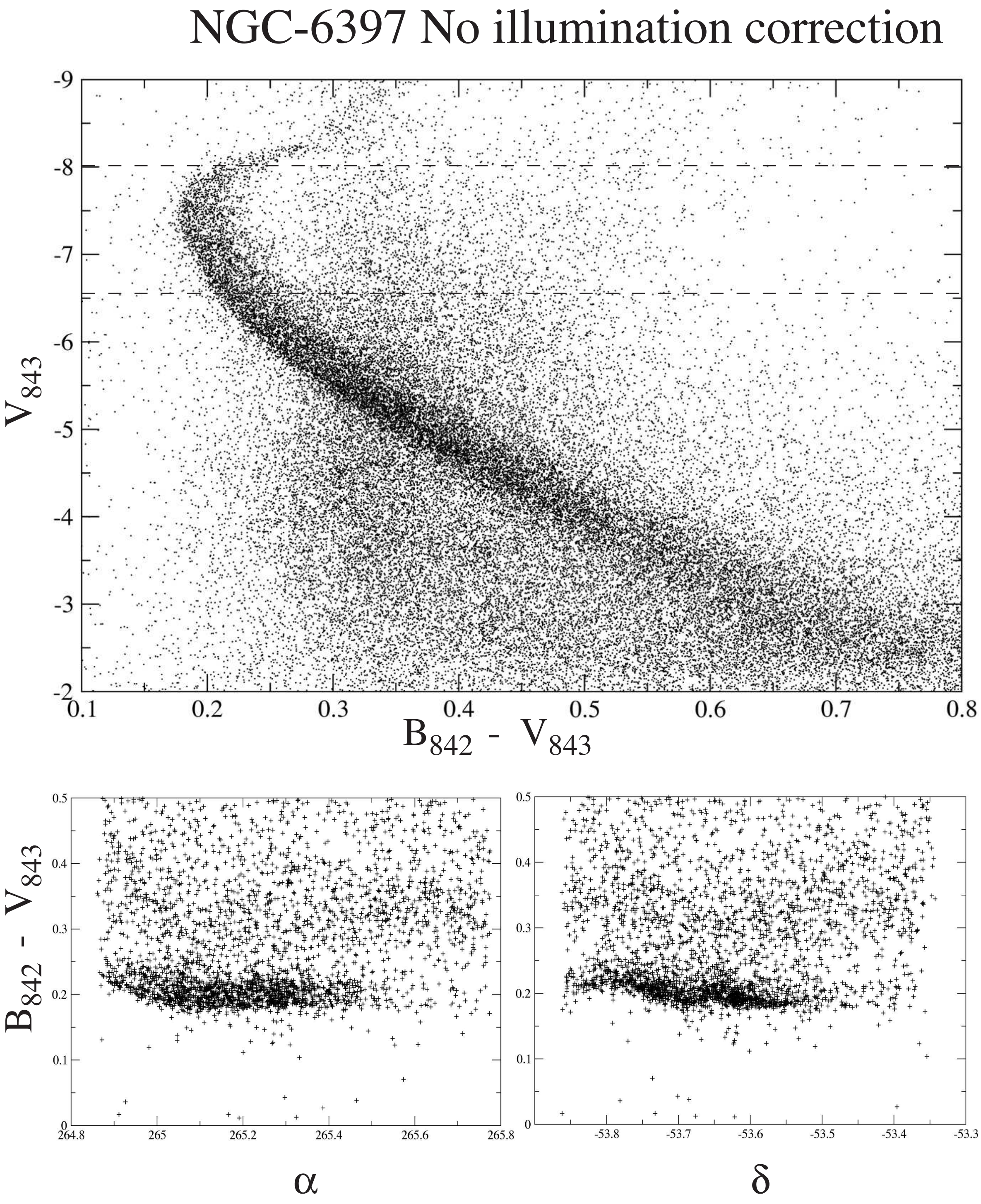

Figure 4.10: The upper panel illustrates the CMD V-843 versus (B-842 - V-843) of the globular cluster NGC6397, with no illumination correction. The absolute zero-point has not been set, and the filter system is the native WFI one (the number associate with the passband name is a unique identifier for the ESO filters). The bottom panels illustrate the color B - V of the sources with a V magnitude between $[-8, -6.5]$ corresponding to the turn-off region (the magnitude selection is represented by the dashed lines on the upper panel) as a function of the declination (left panel), and right ascension (right panel).

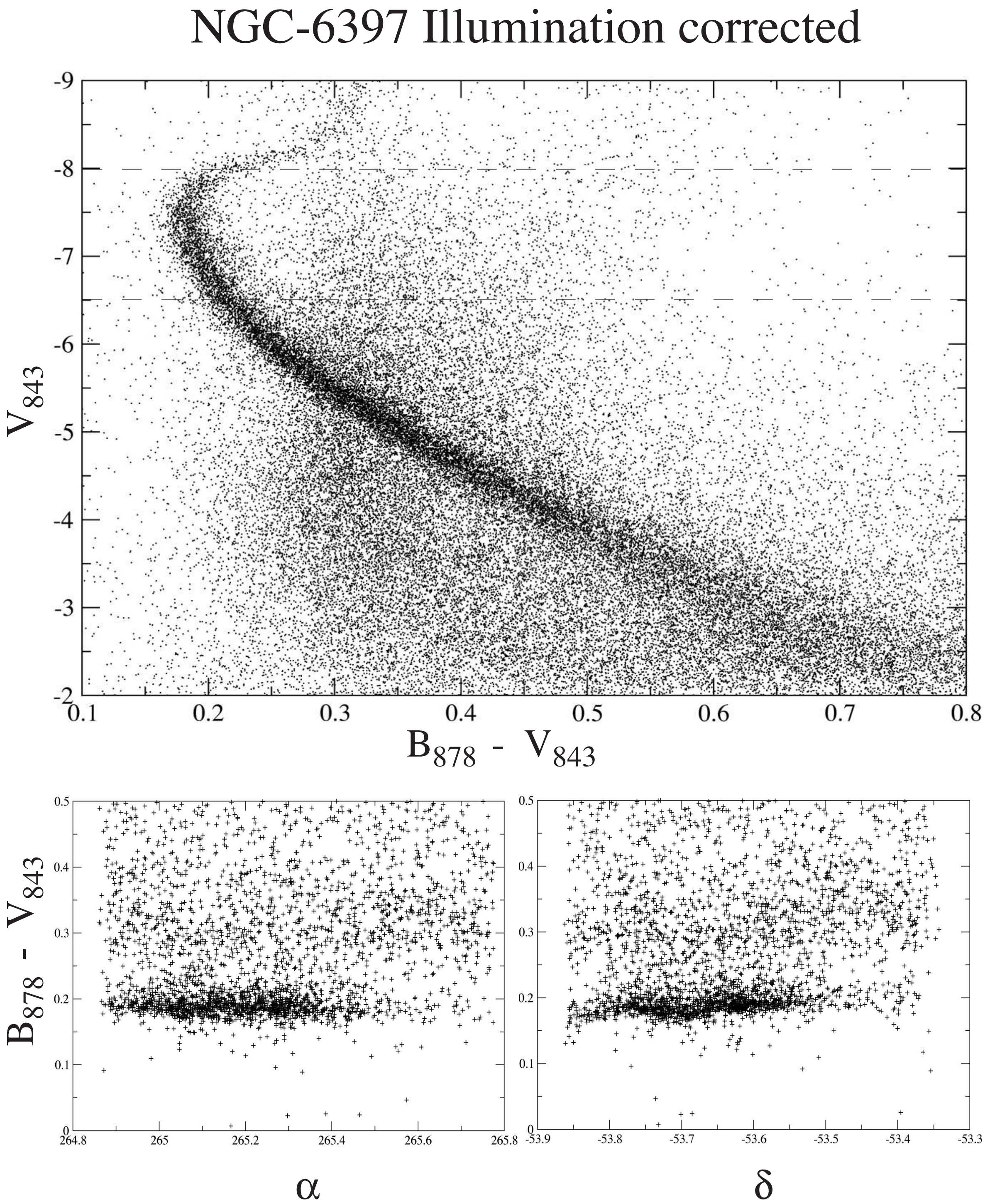

Figure 4.11: Same illustration as figure 4.10 but with the images corrected for the illumination-error.

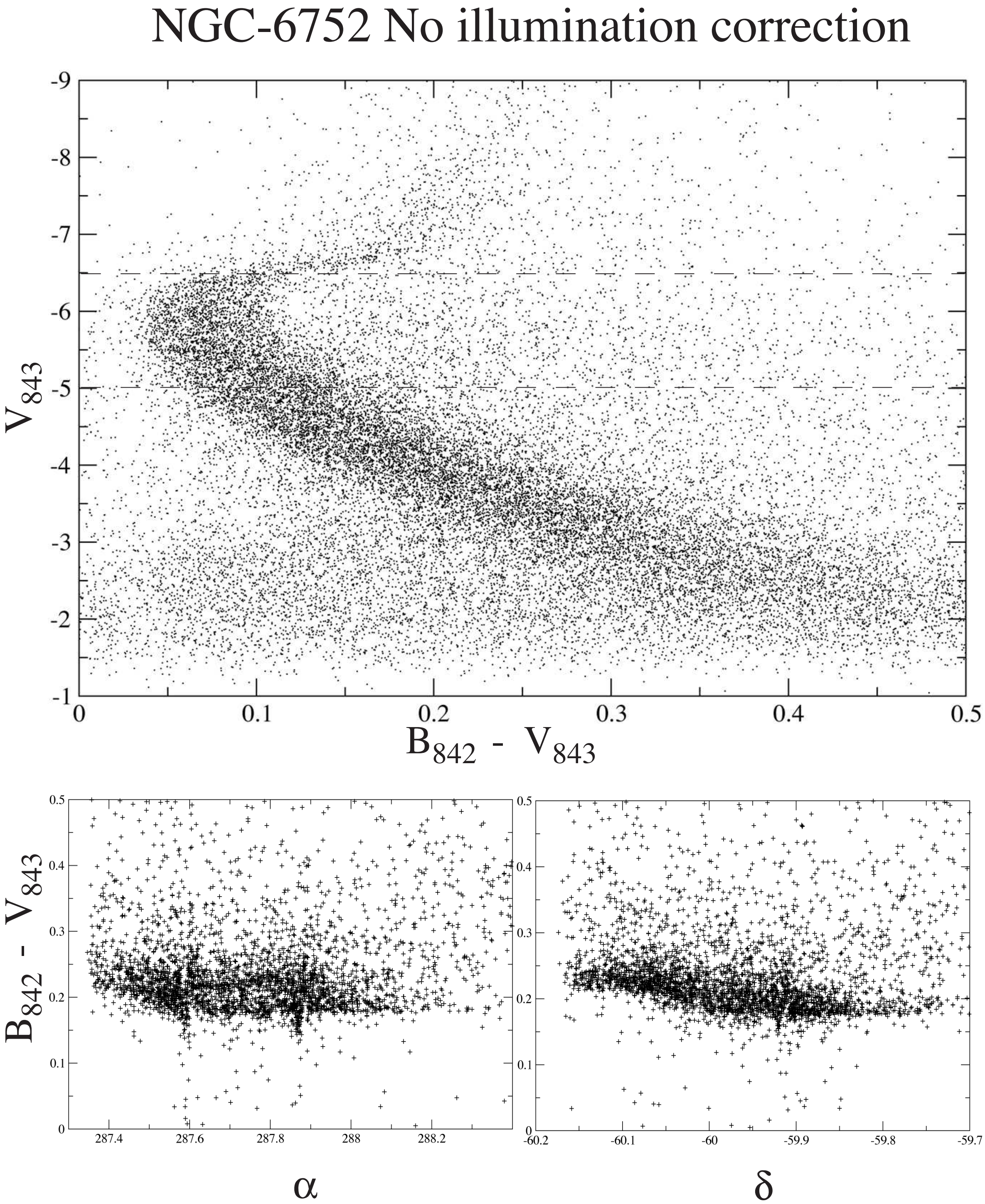

Figure 4.12: Same illustration as figure 4.10 but for the target NGC6752 not corrected for the illumination-error.

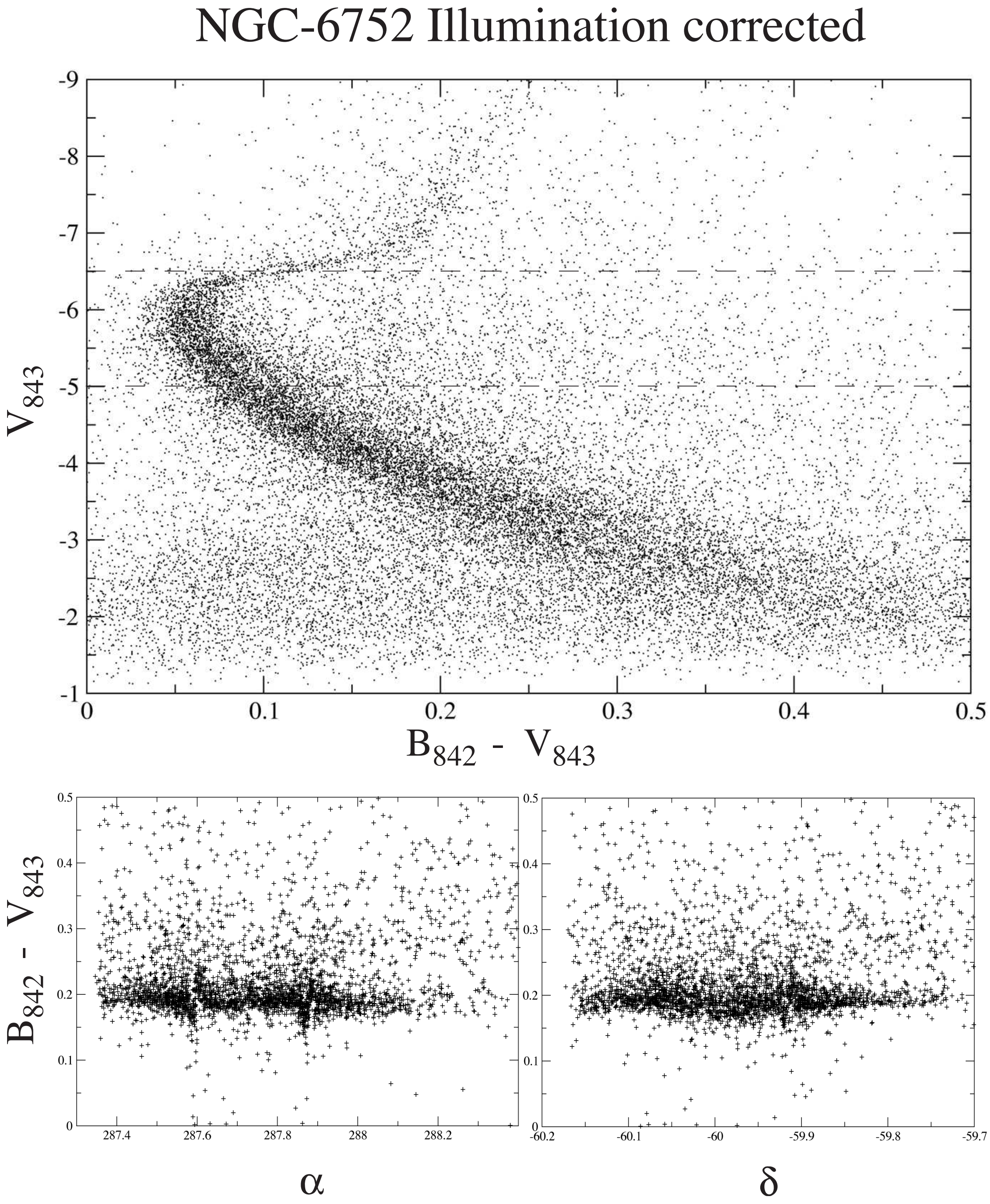

Figure 4.13: Same illustration as figure 4.10 but for the target NGC6752 corrected for the illumination-error.

Also the measurements done in the cells far from the center of the globular cluster are more noisy, because the density of stars from the globular cluster is low, and also nearby stars pollute the expected CMD. Figure 4.14 illustrates the color map obtained with and without the illumination correction applied.

The color map figure 4.14-B is the illumination error for the color B-V derived from the deep observations (subtraction of image 4.9-bottom from image 4.9-top). This map has to be compared with figure 4.14-C, which is the same map but computed from the color of the turn-off point of the globular cluster. Both maps are relative fluxscale correction values. They are difficult to compare because of the different sampling of the two maps, and also the divergence at the border of the computed illumination map for filter B (see figure 4.9-top), nevertheless the global shape and amplitudes are comparable. The comparison of these two maps is a validation of the computation of the illumination maps, also the flat corrected map of the turn-off point figure 4.14-D is another proof.

The amplitudes of the illumination error for color B-V (figure 4.14-B/C) are small (with a sigma of 4%) compared to the amplitude observed from the illumination map per filter, this means that the illumination maps are quite similar from on filter to another, but not equivalent.

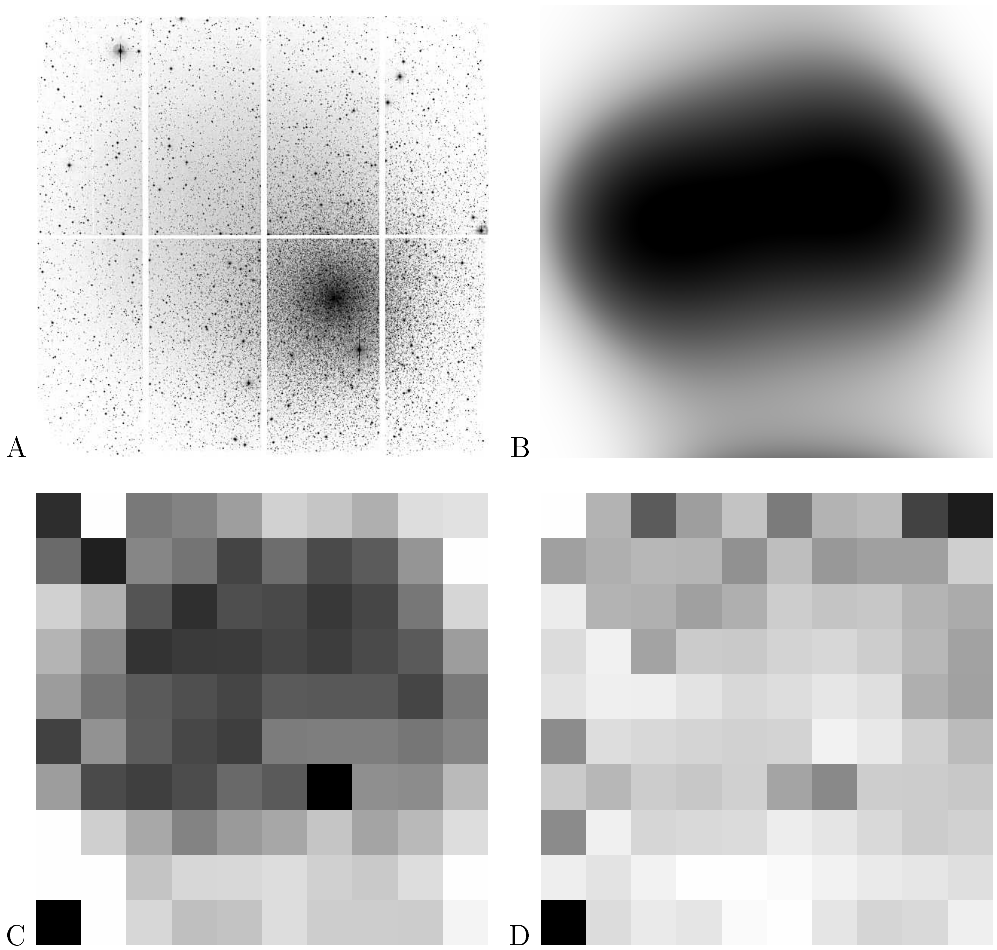

Figure 4.14: B-V Color of the turn-off of the main sequence as a function of the location. ***A:*** reduced V image of the globular cluster (negative intensity), the 8 chips of the WFI detector appears thanks to the gap. ***B:*** Difference between illumination-maps for filter B and V. ***C:*** Color of the turn-off computed on a 10 by 10 grid covering the entire image. The color of the turn-off is more difficult to compute on the top and left of the reduced image, because at these locations stars from the globular cluster are mixed with nearby stars. Nevertheless, the global shape gives the color error when the image is not corrected from the illumination. This map has the same shape and comparable amplitude to the computed color illumination (B). ***D:*** Color of the turn-off computed on a 10×10 grid, after illumination correction. The correlation with the position is now negligible. The sigma of this map is a factor of 2.5 smaller than the sigma of the map obtained from the uncorrected data. Note that the grey-scales of (C) and (D) are compatible.

4.3.5 Impact of the photometric stability

The instrumental illumination-map depends on the instrument and the optical system. In case of poor photometric conditions, the sky also provides its own "sky illumination-map". This one is assumed flat for good photometric conditions, and modeled by the airmass absorption. In case of a non-photometric night, the "sky illumination map" is an unpredictable signal. As the computation of instrumental illumination-map includes also the atmospheric effects, one must select images where the photometric conditions are stable.

The following tests are made to evaluate the stability of computed illumination-maps from numerous images observed during 3 nights where photometric conditions are evolving from stable to cloudy. A total of 90 images have been observed with filter B and V. They are grouped into 18 RBs of 5 images each. For each RB an illumination map is computed. The photometric conditions are evaluated from the variation of the relative ZPs from the first image to the 4 other ones of each RB. It corresponds to the term: $\Delta_{1,m}$ of equation 4.5. Figure 4.15 illustrates the 18 illumination-maps with their corresponding relative ZPs ($\Delta_{1,m}$). The similarity of the illumination-maps per filter is evaluated by subtracting them and flagging (grey circle) the ones that are similar within 0.5% (the sigma of the difference is smaller than 0.5%).

One notices that only 11 of the 18 illumination maps are similar, the other ones are varying and some present very different shapes. One goal of those tests is to define a criterion that could be used to validate an illumination map. From the tests one notices that the valid illumination-maps (highlighted by a grey circle) are derived from consecutive images where the variations of ZP are within 1%. The criterion of the ZP variations smaller than 1% is now used to validate if a computed illumination-map is valid. Experiences show that this criterion is a robust validation.

4.3.6 Long term stability

An important aspect of an illumination-map is its stability during a long period (month or year as it will be established below). The previous tests have established that an illumination-map is independent of the pointing and the airmass. If it is stable during several years, then the polynomial function modeling the illumination-error is computed one time for one filter, and then used to correct all master flats during the period of stability.

The following tests are made to evaluate the long term stability the illumination-maps computed from the run of May 1999 (as describe in sub-section 4.3.4). Again the two globular clusters are used. For different projects, they have been observed two times. They were observed for the EIS project on May 1999 (results previously shown), and a second time in June 2002 for NGC6397, and in July 2000 for NGC6752. Same filters were used, except for the 2002 observation where a new B filter (B_{978}) was installed at the WFI instrument to complement the B_{842} (used previously since the creation of the instrument: 1999 - 2002).

The July 2000 observations of NGC6752

The July 2000 observations of NGC6752 are made of short exposures. For filter B_{842} a total of 7 images of 5 and 10 seconds are observed, the reduced image cumulate 55 seconds of

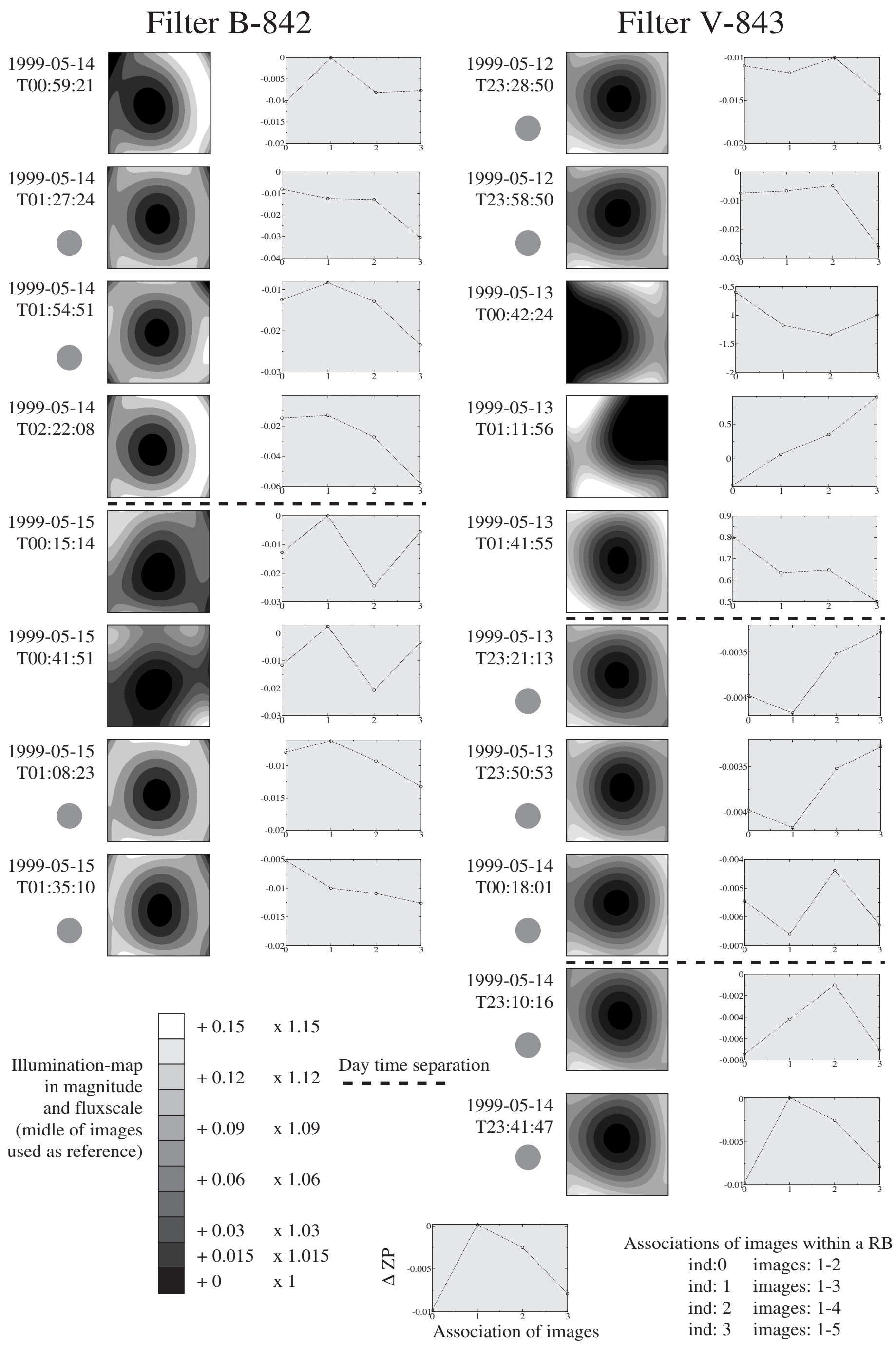

Figure 4.15: Stability of the illumination map with variable photometric conditions. The figure shows 18 illumination-maps computed from RBs of 5 images with filters B and V. The images have been observed consecutively during 3 nights. The illumination-map are shown in grey scale with 0.015 magnitude per interval. On the right of each map is given the relative ZP from the first images to the four ones of each RB. The date of observation is given, and a grey circle is drawn for the maps that are similar within an error of 0.5% (largest difference of subtraction of 2 maps).

Figure 4.16: Reduced images of the globular cluster NGC6752 observed with the WFI instrument filter B_{842} in May 1999 (left panel) and July 2000 (right panel). The center of the globular cluster is in chip 7 for the first observations, and in chip 2 for the latter observations. One notices the difference of depth of the 2 reduced images.

integration. For filter V_{843} a total of 8 images of 3 and 7 seconds are observed, the reduced image cumulates 20 seconds of integration. The dithering pattern of the observations is small and similar for the 2 filters. The center of the globular cluster is located in chip 2, whereas for the May 1999 observations the center of the target is located in chip 7 (See figure 4.16 for illustration).

The pointing offset between the 2 set of data, ensures that a star observed on both reduced images does not have the same position within the instrument (in pixel coordinate) and therefore is not affected by the same ZP offset due to the illumination error. Therefore, if two catalogues extracted from the two periods are in sync (no bias in photometric comparison versus the sky location), this proves that the illumination-map is correct. The integration time of the July 2000 observations are shorter than the May 1999 ones (made of 480 seconds for each filter), the limiting magnitudes of the 2000 reduced images are 3.5 magnitudes and 2.4 magnitudes shallower for respectively filters V and B. Due to the depth difference the magnitude comparisons are noisy. The turn-off of the main sequence observed from the latest reduced images is close to the limiting magnitude. Therefore the color B-V of the turn-off is noisy and is not a good estimator to determine if the illumination correction is adequate. Instead, simple photometric comparisons are done with the catalogues extracted from the May 1999 observations.

The July 2000 observations of NGC6752 are reduced twice, one with a native master flat-sky only corrected to have a constant mean gain, and a second time with a the master flat-sky corrected by the illumination-map computed from the deep images of May 1999 (figures 4.9). The stability of the illumination-map is deduced from the magnitude comparison per filter of the extracted catalogues as a function of the α and δ sky position. The catalogues used as reference are extracted from the May 1999 reduced and illumination-corrected images filter B and V. The catalogues to be compared with are extracted from the 2000 data set, firstly: from the reduced image, and secondly: from the reduced illumination-corrected images. Figures

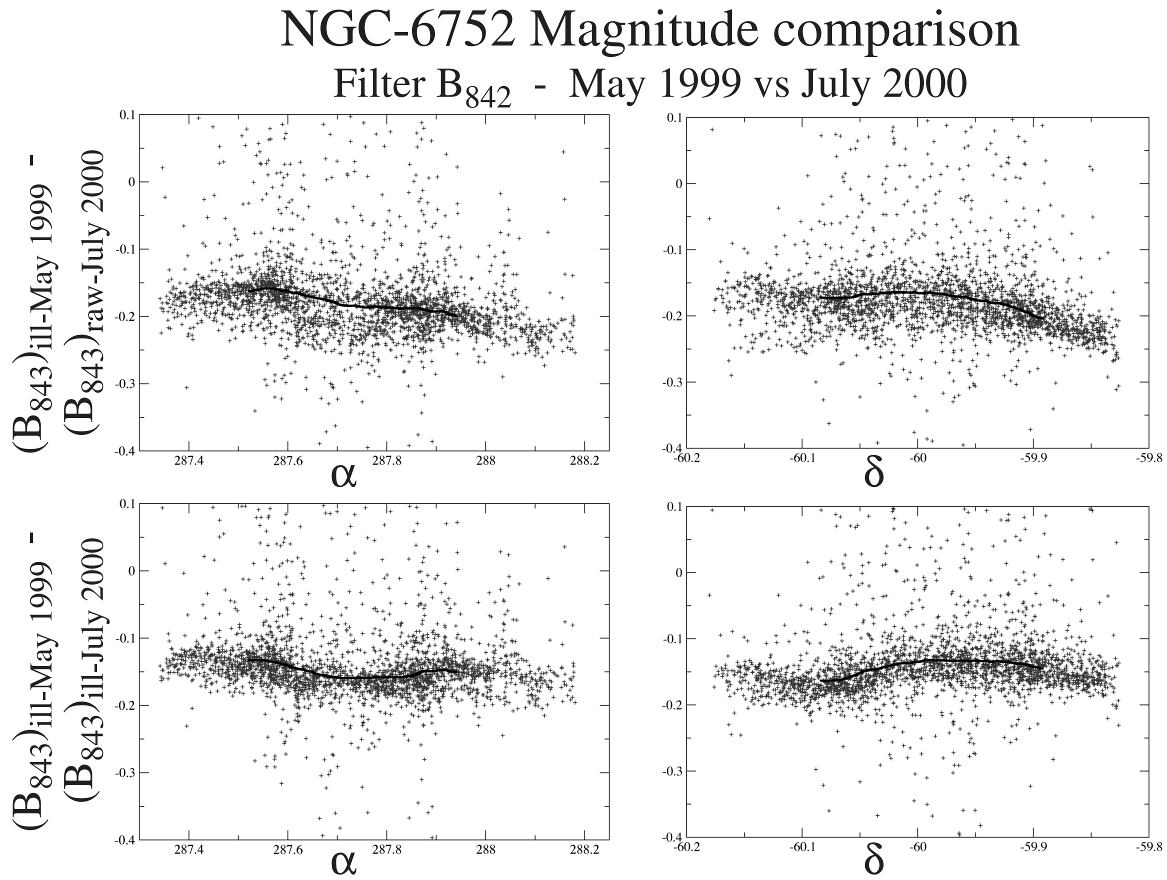

Figure 4.17: Magnitude comparison of the extracted catalogues of the globular cluster NGC6752 observed in May 1999 and July 2000 with the WFI instrument filter B_{842}. The catalogue of the May 1999 observation is computed from illumination-corrected reduced image and it is used as reference. A catalogue of the July 2000 observations is extracted from the native reduced image and compared with the reference (top panels), an illumination corrected one is extracted and compared with the reference (bottom panels). The magnitude comparison is made as a function of α (left panels) and δ (right panels).

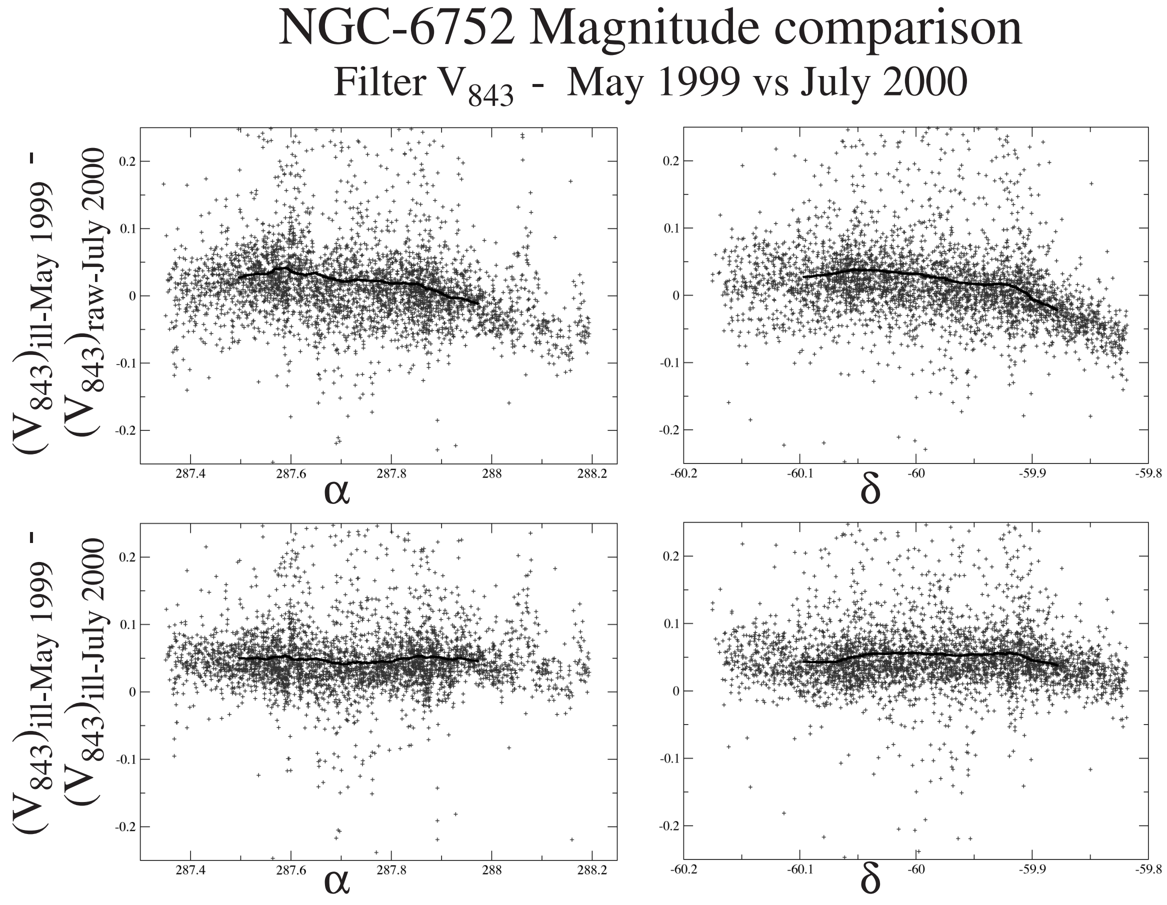

Figure 4.18: Same illustration as figure 4.17 but for the V-843 WFI filter.

4.17 and 4.18 illustrates the magnitude comparison for filter B and V. On each figure, the top panels show the comparison with the reduced 2000 images with no illumination-correction, on the bottom panels the comparison is done with the illumination-corrected reduced image. One notices the large dispersion of the magnitude differences. In V the dispersion is larger than in B as the depth of the catalogue is 3.5 mag shallower and only 2.4 for B filter. Nevertheless, the running median shows that the 1999 and 2000 illumination-corrected catalogues agreed well for the V filter whereas the uncorrected data show a gradient. It is important to emphasize that despite the large pointing offset of the 2 set of data, the catalogues are in sync within 1.5%. This proves that the illumination correction computed from deep observations of May 1999 for filter V_{843} is valid and can be used one year later. This statement is not as sharp for the magnitude comparison achieved with the B filter. The illumination correction corrects poorly the data. This indicates that the B_{842} illumination correction has evolved in shape from 1999 to 2000. Historically, in 1999 the electronic of the WFI instrument was suffering from contamination of the dewar, the shape of the master flats were unusual with a large ring. This problem has been corrected in the beginning of 2000, the latter master flats appear with no strange shape. This event may explain the evolution of the illumination-map for the bluer filters. The CCD transmission is decreasing to 60% for the B wavelength.

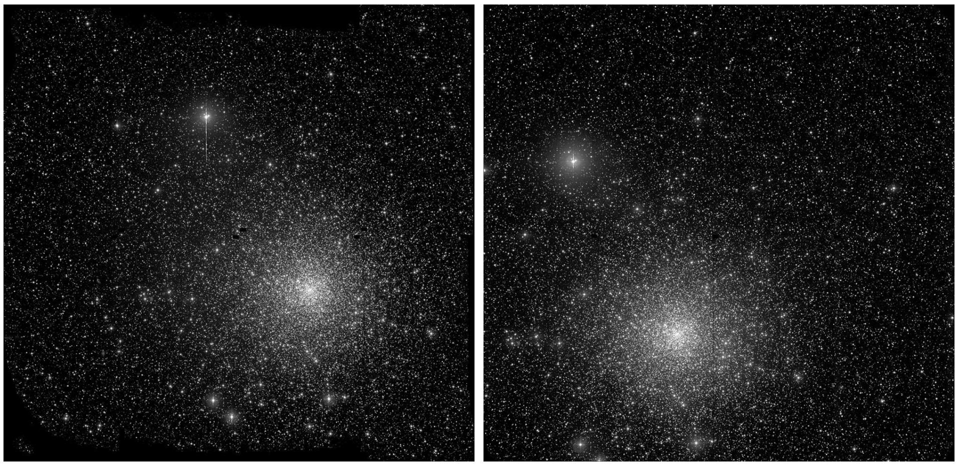

Figure 4.19: Reduced image of the globular cluster NGC-6752 with the WFI instrument and the B_{842} filter made in May 1999 (left panel) and the B_{878} June 2002 (right panel). The center of the globular cluster is in chip 7 for the first observations, and in chip 6 for the latter observations. One notices the difference of deepness of the 2 reduced images.

The June 2002 observations of NGC6397

The NGC6397 observations of June 2002 are made of short exposures. For filter B_{878} a total of 3 images of 90 seconds are observed, the reduced image cumulate 270 seconds of integration. For filter V_{843} a total of 3 images of 70 seconds are observed, the reduced image cumulates 210 seconds of integration. The dithering pattern of observation is small and similar for the 2 filters. The center of the globular cluster is located in chip 6, whereas for the May 1999 observations the center of the target is located in chip 7 (see figure 4.16 for illustration). Also, the integration time of the June 2002 observations are shorter than the May 1999 ones, therefore the limiting magnitudes of the 2002 reduced images are 0.9 mag and 0.6 mag shallower for filters V and B respectively. The limiting magnitudes are comparable and provide consistent magnitude comparison for the 2 set of data. Note that the new B filter (B_{878}) has a larger and bluer passband than the first B filter (B_{842}) used in 1999 and 2000. As the filters are different, the magnitude comparison with the 1999 B_{878} catalogue is expected more noisy. Also the illumination-map of this new filter is unknown, and the illumination-map of filter V_{843} is used by default.

The images are reduced with the native master flats with no illumination correction. The B-V color plotted as a function of α and δ position shows that the color of the turn-off is independent of the pointing location. This prove that the illumination-map for the filters V_{843} and B_{878} are similar. Therefore all the master flats are corrected by the V illumination map computed from the May 1999 observations (figures 4.9). The images are reduced again with the corrected master flat. The B and V catalogues are extracted from the 2 reductions. The magnitude comparison with the 1999 catalogues are illustrated in figures 4.20 and 4.21. The V filter shows the best results: the dispersion of the magnitude comparisons is small, and the illumination-corrected data are in sync within 1.5% with the 1999 corrected catalogue (one can notice a small bias incompletely corrected in α direction). This comparison proves that the illumination-map stayed constant within 1.5% over a period of 3 years from 1999 to 2002.

For the B filter, the dispersion is larger due to the color term of the two different B filters used. The illumination correction is quite good even if some remaining bias are visible especially in Delta direction. Therefore the illumination maps of the new B and V filters seems similar even if more precise computation could isolate some differences.

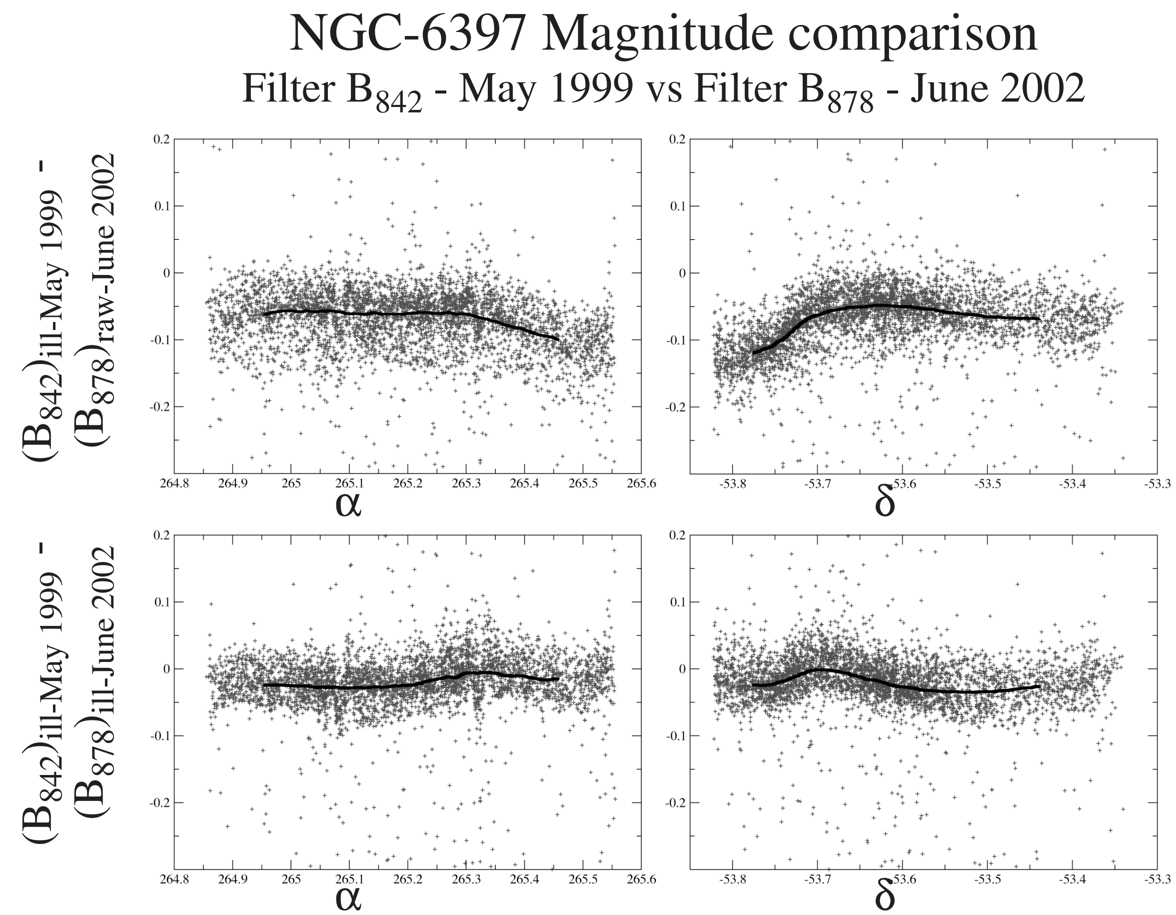

Figure 4.20: Magnitude comparison of the extracted catalogues of the globular cluster NGC6752 observed with the WFI, in May 1999 with filter B_{842}, and in June 2002 filter B_{878}. The catalogue of the 1999 observation is computed from illumination-corrected reduced image, and is used as reference. A catalogue of the 2002 observations is extracted from the native reduced image and compared (top panels), an illumination corrected one is extracted and compared (bottom panels). The magnitude comparison is made as a function of α (left panels) and δ (right panels).

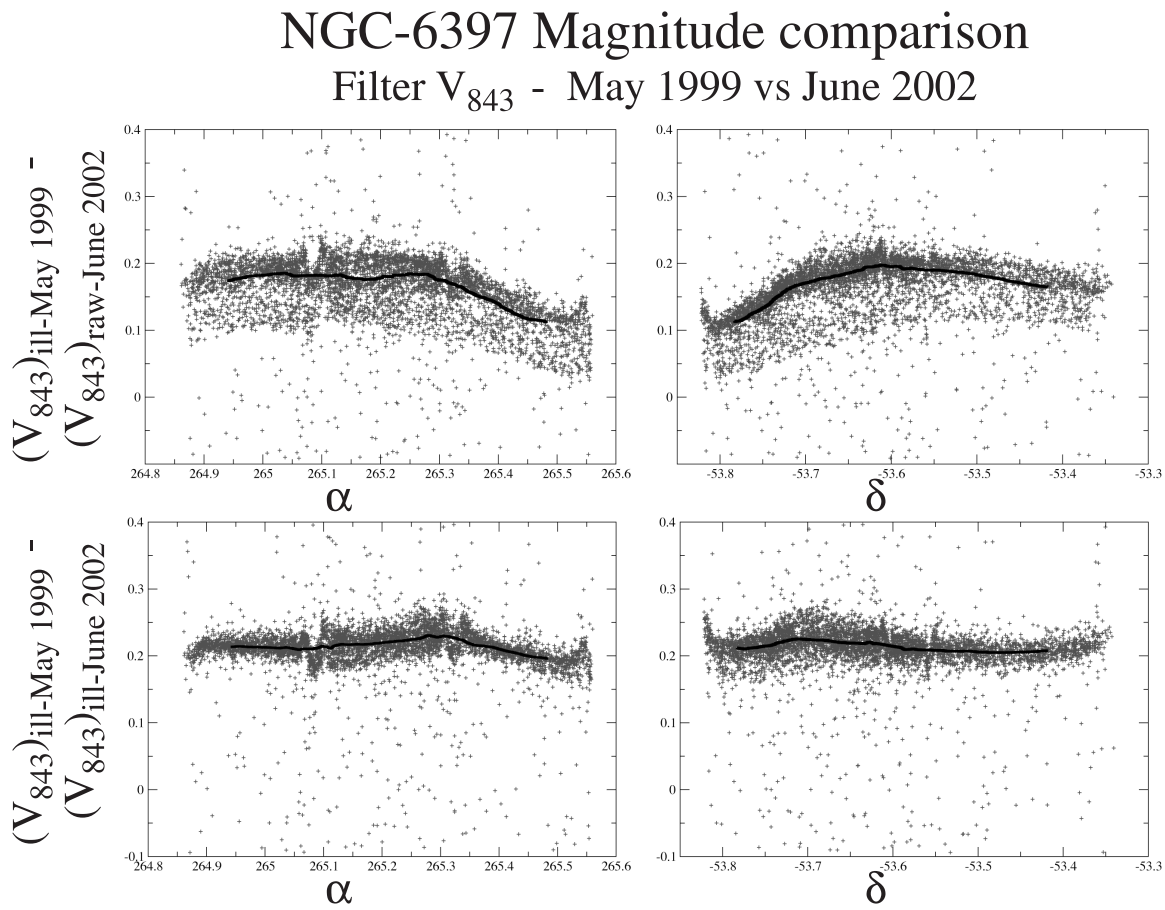

Figure 4.21: Illustration similar to figure 4.20 but for the filter V_{843}.

Deduction of illumination-maps for other filters

The illumination-map of the B_{878} filter was unknown, and successfully estimated using the illumination-map computed from images observed in 1999 for the V_{843} filter. To verify if the V illumination-map is also adequate for the other filters not yet calibrated, all the June 2002 observations of NGC6397 are tested. The filter are: U_{877}, I_{875}, and the already tested B_{878}, and V_{843}. The different CMDs will are computed.

The U observations are made of 3 images of 240 seconds, the I observations are made of 4 images of 50 seconds. The master flats of the different filters have all been corrected by the V_{843} illumination map computed from the deep images observed in May 1999. The U and I images are reduced, and the different CMD are constructed. Figure 4.22 shows the V versus (B-V) CMD, as complementary plot of the previous test. Figure 4.23 illustrates the B versus (U-B) CMD. Finally, figure 4.24 gives the I versus V-I CMD. Unfortunately the globular cluster has not been observed with the R filter. Also given are the color of the two filters as a function of the α position (bottom left), and the color versus the δ position (bottom, right). On these bottom plots, a running median is computed and plotted as the dark line. It is computed to get the trend of the color of the turn-off as a function of the sky position. In all cases, the running median as a peak-to-peak variation smaller than 0.015 Magnitude. The dispersions of the colors around the running median are larger than the one observed from the 1999 extracted catalogues. This is due to shallower observations. For the U and I filter the magnitude are more noisy because of the depth of the data. Also the I magnitudes are more noisy due to the fringe patterns. The different CMDs show no illumination effect, and one can conclude that filters: U_{877}, B_{878}, V_{843} and I_{875}, have the same illumination-map similar to the one computed in from 1999 observations with filter V_{843}.

From the various tests, one may conclude the following points: Firstly, the illumination-error are independent of the pointing location and airmass. Secondly, the illumination-error is stable in time if the instrument is not modified. The 1999 - 2000 period seems to be affected by a technical problems that affects the filter B_{842} (contamination of the dewar during the year 1999). The computed model decrease the illumination-error by a factor of 2 to 3. The different models are now saved in the configuration file, and can be applied to master flats of any observation. One expects the models to be stable at least up to October 2002 where the telescope has been upgraded to decrease the light diffusion in the telescope tube. The illumination-maps are certainly affected, and must be computed again for recent observations.

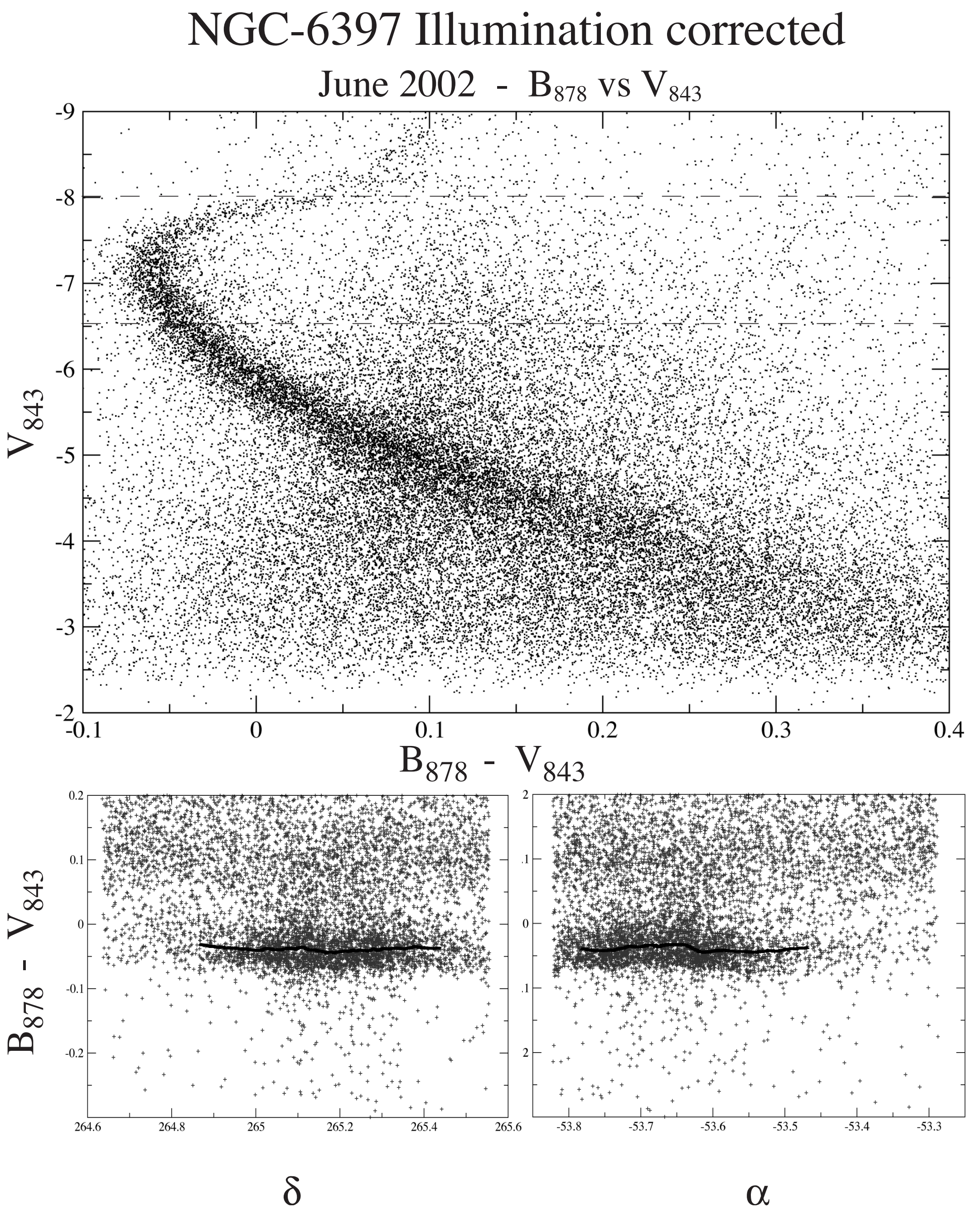

Figure 4.22: CMD of the globular cluster observed with the WFI instrument in June 2002. The filters used are the B_{878} and V_{843}. The reduced images are illumination-corrected. The top panel shows the V filter versus the color B-V. The bottom panels illustrate the color B-V of the source brighter than magnitude -6, as a function of the α (left) and δ (right panel) sky position. For the two panels, a running median gives the tendency of the color of the turn-off. The largest variations of the running average are within 1.5%.

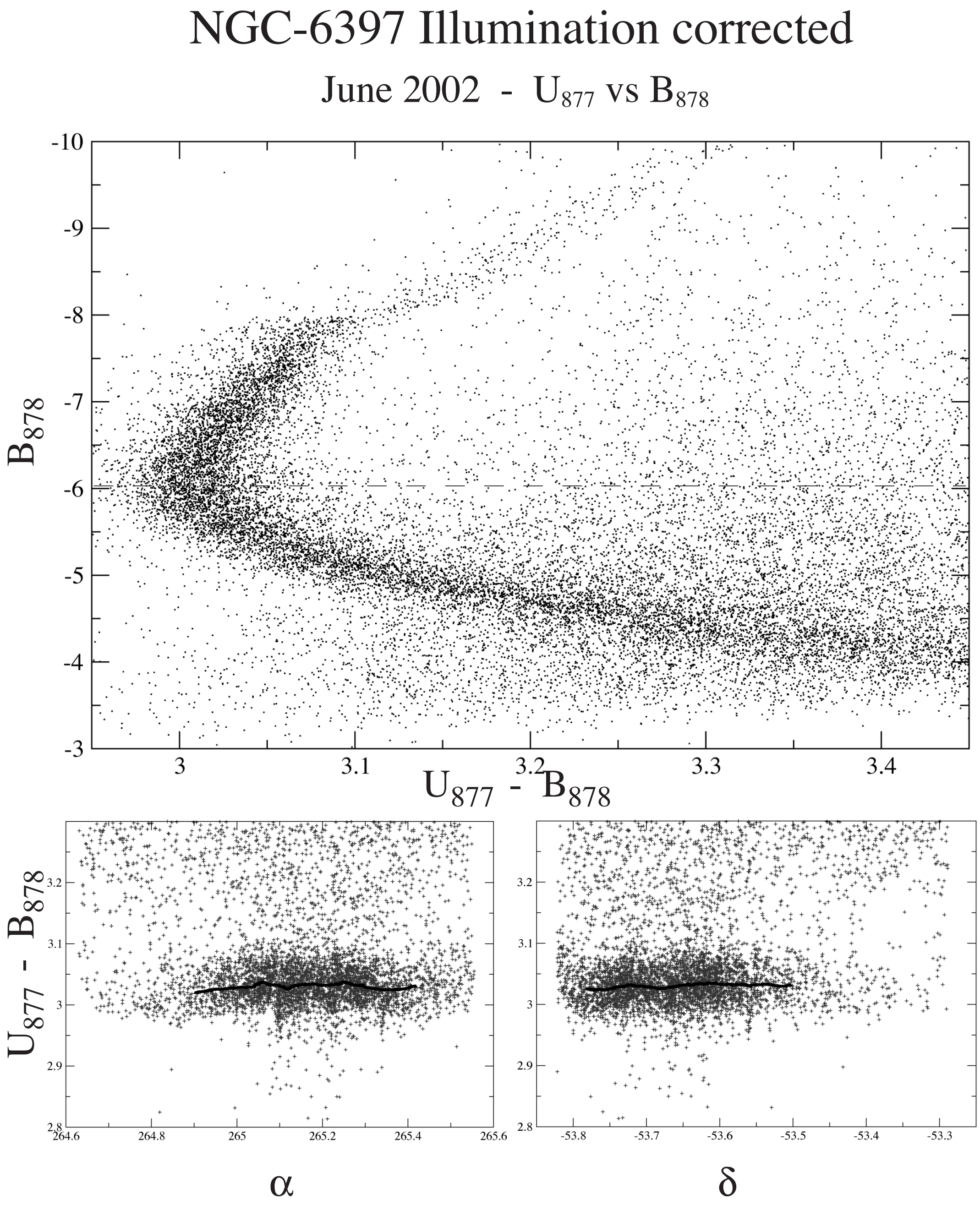

Figure 4.23: Illustration similar to figure 4.22 but for filters U_{877} and B_{878}.

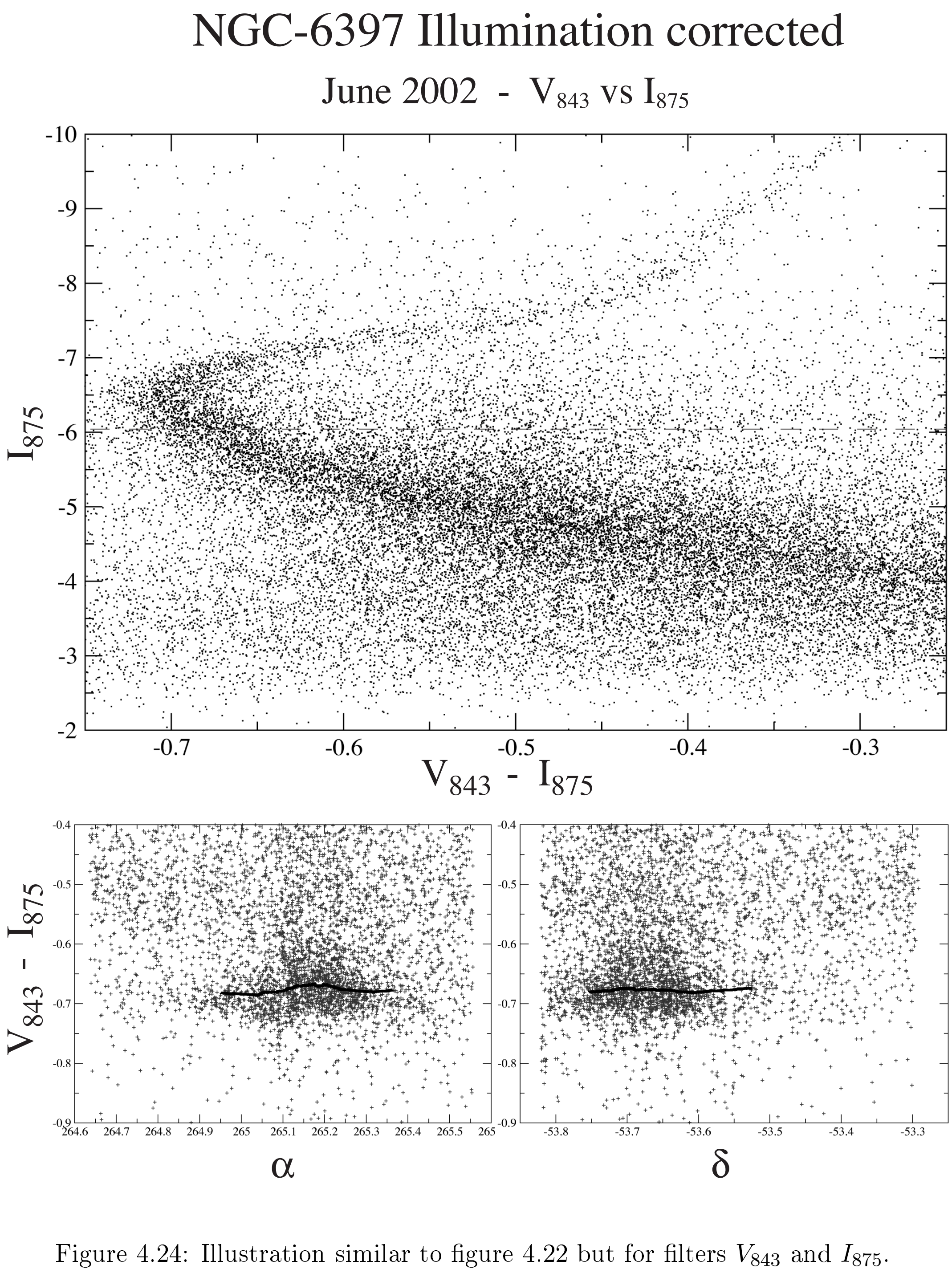

Figure 4.24: Illustration similar to figure 4.22 but for filters V_{843} and I_{875}.

4.4 Background large-scale structure estimator

The atmosphere adds a component quasi constant with smooth variations in the optical wavelength domain due to sky light diffusion (here the fringes caused by to interferences are not considered). This additive signal should be removed during the image reduction. This signal is characterized by low spatial frequencies. One speaks about the *large scale structure background*. The task is to define a robust estimation of the sky background insensitive to the astronomical objects. In the case of deep observations with no extended sources, it is easy to separate astronomical sources from the background, because the sources are middle or small scale structures. In the case of extended sources covering a large fraction of the image (nebulae, globular clusters), the dissociation is difficult or impossible. The dissociation cannot be done without prior knowledge (shape of the astronomical sources for instance).

This section presents an estimator based on median filtering used in multi-resolution. This estimator is a generic tool used for different purposes. The procedure dedicated to the sky background estimation and subtraction is described.

Multi-resolution Median estimator

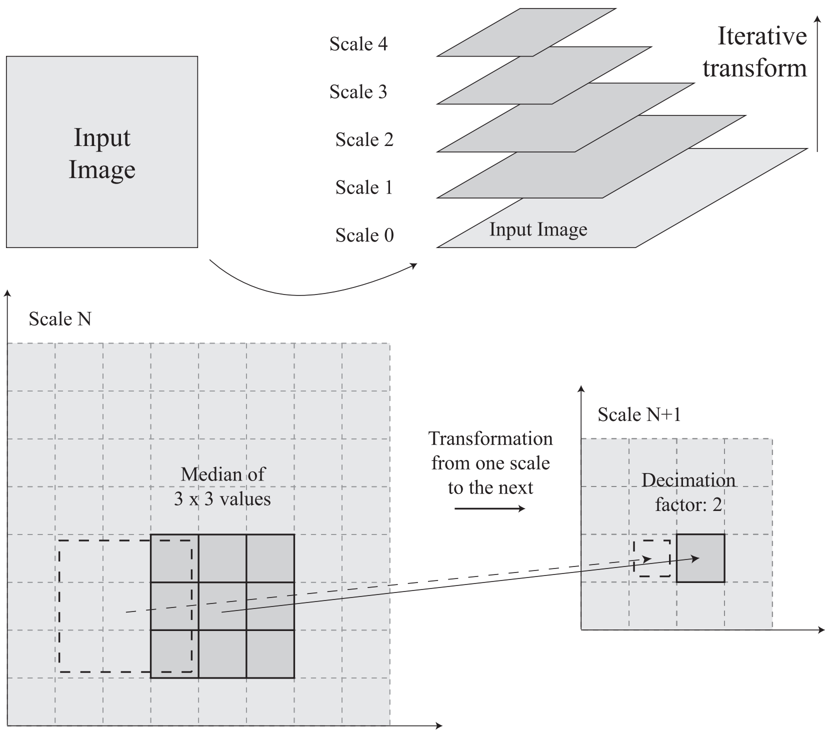

Figure 4.25: PYRAMIDAL MEDIAN TRANSFORM. Iterative algorithm using a median filter estimated with a kernel of 3×3 pixels. From one scale to the next one, the image is smoothed and decimated by a scale factor of 2.

This algorithm isolates the different structures of the image using an iterative smoothing with a median filter. Figure 4.25 illustrates the smoothing process.

1. The input image to be transformed is considered as scale 0 of the pyramid.
2. From scale N to scale N+1, the transformation is done as follows:
   (a) The image at scale N is smoothed with a median filter of size 3×3 pixels.
   (b) The median smoothed image is decimated by a factor of 2. It produces the image at scale N+1.
3. The pyramid grows up to the last scale S corresponding to the large scale structure of the background.

At the last scale S, the image is named the *mini-background*. S is chosen to correspond to the large scale structure of the typical background of the input image, table 3.8 illustrates the values adopted for the different supported instruments. The mini-background is smaller than the original image by a scale factor of 2^{S-1}, the details smaller than this scale factor are "dissolved", and give negligible contributions into the mini-background. The pyramidal smoothing is similar to a direct median smoothing with a square kernel of size 2^S pixels. This approach offers fast computation because the kernel size is small (3×3 pixels), and the intermediate images are decimated.

Sky background subtraction

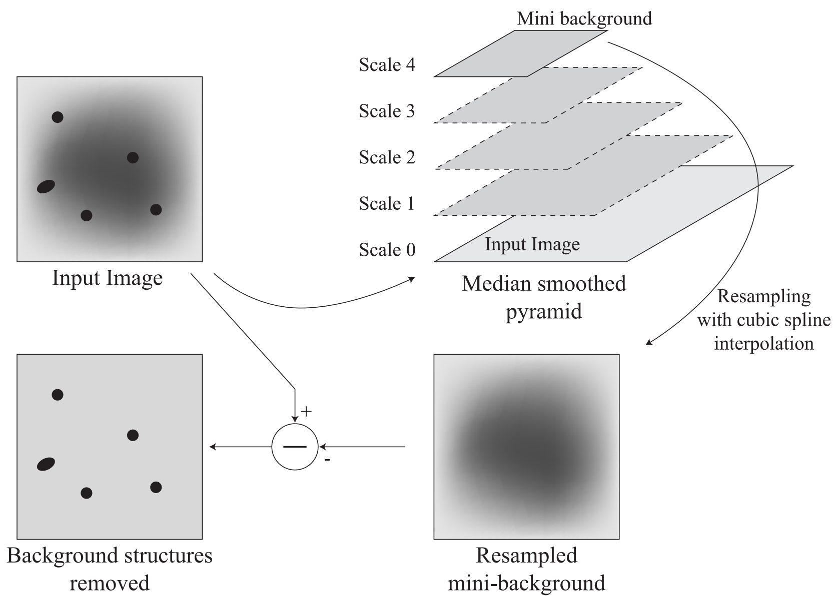

Figure 4.26: Illustration of the procedure defined to estimate and subtract the sky background of an image using the multi-resolution median estimator.

Figure 4.26 illustrates the process of sky estimation and subtraction. The sky background is estimated by the pyramidal median transform up to typically scale 8 or 9 (corresponding to details of 256 and 512 pixels respectively). Note that if the detector is small, as for instance, SOFI or ISAAC (1024 pixel large), the scale used to estimate the sky background must be smaller than 9, as the image size at this scale is only 4×4 pixels large. In practice, a scale of 7 is used to estimate the sky background (as illustrated in table 3.8). The small image of the scale chosen is then resampled to the original image size using a bi-cubic resampling. The original image is subtracted by the resampled one. The resulting image, is image zero centered as the mean as been subtracted as well as the smooth variation of the background. This procedure is used within the pipeline for the module (2) of the Reduction Mode (see figure 3.9). The procedure is also applied to detect bad pixels from master flats that are subtracted by their smoothed version taken at scale 4 (as described in section 4.1).

The procedure is very efficient and fast. Similar approaches are used by source extraction softwares to remove sky background before extracting the sources. For instance, the Sextractor tool is using a median/mean estimator within a matrix typically equal to 64 pixels. The specific option named *BACK_SIZE* defines this matrix size. A value of 64 corresponds to scale 7 of the procedure defined in this section.

For input images with large extended sources (globular clusters, nebulae) the sky background cannot be estimated by the median smoothing because the extended objects will contribute to the smoothed images at any scale and till thus be partially subtracted. In that case it is not simple to remove the sky background. A model of the extended sources must be computed first. Such technique depends on the sources and have not been investigated in this work.

4.5 Unbiased background small/pixel-scale estimator

Fringes are a common phenomenon present on near-infrared images. Fringes are an additive signal stemming from sky emission lines, making a non-negligible contribution to the total signal, typically of the order of 10% of the background level. Hence, subtracting its contribution is essential for a proper reduction of the image. While in the optical, the fringing pattern is relatively stable (but exceptions exist) over the time scale of a night, in the infrared the fringes vary very quickly. Fortunately, the fringing pattern is largely independent of the pointing and consecutive images share the same pattern. This allows them to be separated from the astronomical objects by shifting the pointing of the observations. While the objects will fall in different pixel locations the fringes will not.

Note that more generically one speaks about background pixel-based estimation. Indeed some IR passband such as K has no fringes but a complex sky background with details as small as couple of pixels. The problematic of estimating pixel-based background within a data cube, is to isolate sky background from the astronomical sources. By contrast, the sky background observed with common optical filters (with the exceptions of I) is very smooth and its estimation is much simpler as described in section 4.4. Of course, when using the pixel-scale background estimator, all components of the background are estimated, whatever are their size.

The following sub-sections presents: Firstly, a recent two-pass procedure technique now available with different packages. Secondly, the procedure implemented in the pipeline. Thirdly, an internal comparison to illustrate the impact on the photometry of the two-pass method versus the one step procedure. And finally, an original refinement of the procedure is illustrated.

4.5.1 Two-pass technique

Figure 4.27 the initial crude background estimation of the fringing pattern computed at every pixel using the estimator E given by:

$$B_{i,j} = E\left(P_{n_{i,j}} - \mu_n, \forall n\right) \tag{4.6}$$

where $B_{i,j}$ is the computed background at the location $(i,\, j)$, $P_{n_{i,j}}$ is the counts of the pixel (i, j) of the n^{th} image, and, μ_n is the mean of the n^{th} image. Subtraction of μ_n is important because it may vary from one image to another in the case of non-photometric nights. The estimator E can be a median, a mean, a mean computed with a sigma clipping, or whatever estimator converging to the mean.

Unfortunately, whatever the E estimator, it is biased due to the presence of faint astronomical objects which cannot be detected in the individual images due to their low S/N. However, if all images are combined these objects can have a significant contribution. For instance, for an RB with 60 images objects detected in the final image with a S/N $\sim$ 2 have a S/N $\sim$ 0.25 on the individual images. Neglecting their contribution in estimating the background leads to an overestimate of the background, and consequently to an underestimate of the flux of the objects in the final stacked image. This effect can be as large as 0.2 mag near the limiting magnitude.

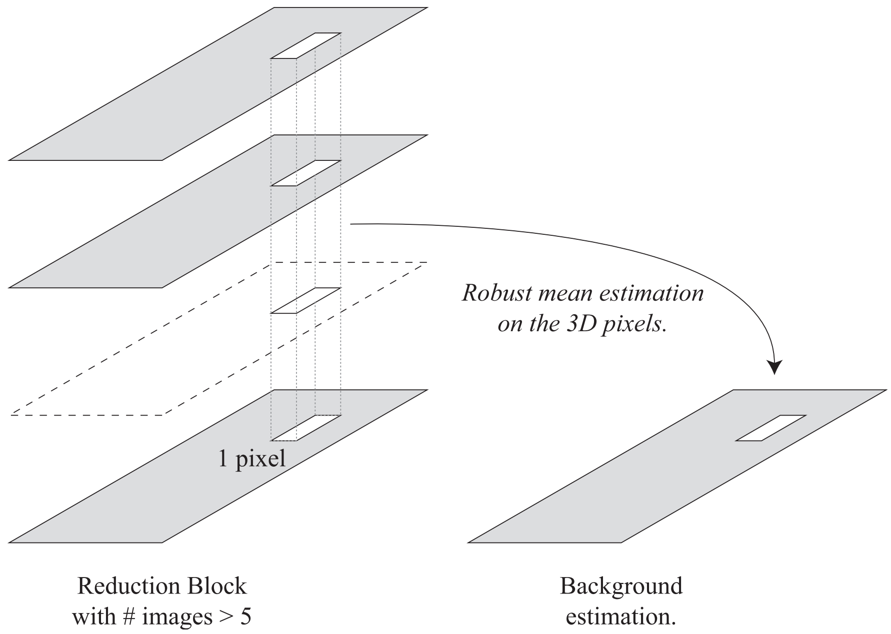

Figure 4.27: Illustration of the first pass used to estimate a background-map from a cube of images with a simple median filtering.

In order to improve the estimator E in equation (4.6) it is necessary to distinguish pixels which have the "*background value*" from those contaminated by the light of objects as illustrated in Figure 4.28. In order to do that one has to use the first estimate of the background, combine the sky-subtracted images, detect objects, and create masks which encompass surrounding pixels containing the object. The masks are then mapped back to the individual images and used to discard pixels in a second estimate of the background. Typically, the mask size is taken to be about twice the estimated size of the objects. An illustration of the second pass is given in Figure 4.28.

If the background is evolving during the total exposure time, it can be estimated from a fraction of the images observed consecutively. The algorithm allows to specify a range of images to be used to estimate the background. In the IR the background is evolving faster, and a range of typically 15 images is used to compute the background, corresponding to 30 minutes of observation.

One limitation of the method is that, for large objects and very dense regions it may be impossible to "see" the sky, in which case holes will appear in the final image. In order to avoid this case a proper choice of the amplitude of the jitter pattern is critical. If the astronomical objects studied are too large, this procedure (one or two passes) cannot be used, the only way is to get a fringing map by mixing the observations of other empty fields with a median. This is a typical case to deal with optical observations of globular clusters, nebulae, or other very large objects. In that case one needs to collect all the images empty enough to build a fringing map, thus assuming stability of the fringe patterns. The observation strategy for large astronomical objects has to use specific Observation Blocks to get one or more fringing maps observed from empty fields.

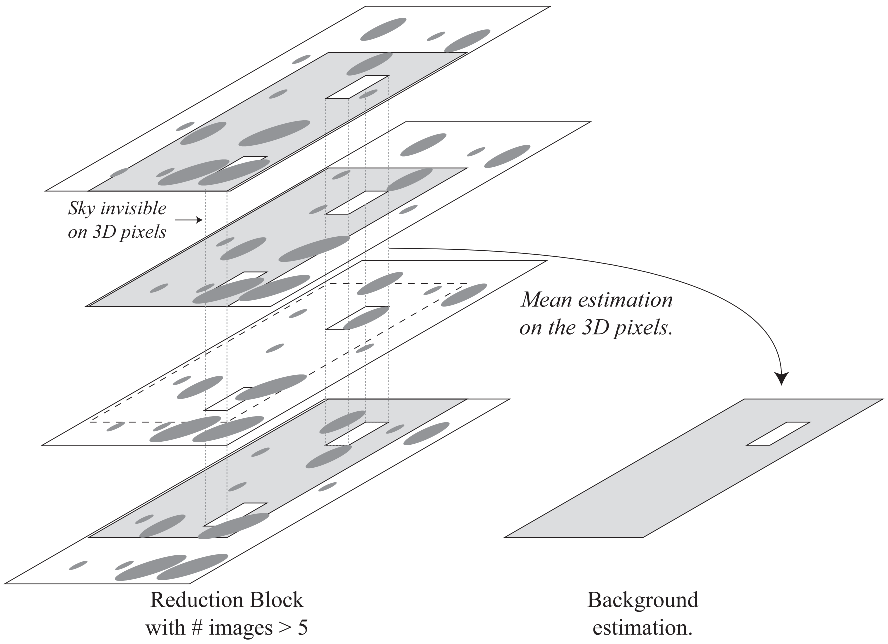

Figure 4.28: Illustration of the second pass used to estimate a background-map from a cube of images with median filtering after masking objects in the final stacked image, as described in the text.

4.5.2 Procedure description

The complete two background estimation with two steps is a complex procedure as it relies on: a relative astrometric calibration, a warping/stacking procedure to stack a cube of images, a rough detection procedure to detect objects to create the mask. The complete two-pass estimation is made of the following steps:

1. Fringing pattern estimation first step. A fringing-map is formed for the *merge-step* consecutive images. This parameter offers flexibility to estimate sky background within a sub-block of the full RB. The fringing-map is computed with a sigma-clipping. One fringing-map is computed per sub-block of size *merge-step*.

2. Fringing pattern subtraction. Each image of the RB is subtracted by the computed fringing-map corresponding to the *merge-step* sub-block. The fringing-map used for image number i is a linear combination of the fringing-map of the 2 closest *merge-step* sub-blocks. The goal of combining fringing-maps of consecutive sub-blocks of merge-step images is to follow the smooth evolution of the fringe patterns. This refinement provides less fringe residuals on the processed images, than if it is not applied.

3. RB stacking. The RB needs to be stacked to estimate the mask for the second step background estimation. The procedure used is described in full detail in sub-section 4.7

4. Mask Creation

(a) The stacked image S is multiplied by the square root of its corresponding weight-map (issued from the stacking of the RB). The noise amplitude is therefore homogeneous throughout the full stacked image.

(b) S is smoothed by a cubic bspline of the same size as the typical seeing. The smoothing is used to improve the signal to noise of the PSF like objects.

(c) The large scale structure background is removed following the same procedure as described in sub-section 4.4. Note, that the background is quasi flat, but for a proper estimation of the objects the residual smooth variations of the background are removed.

(d) The images is smoothed by a Gaussian function with sigma equal to the nominal seeing. The smoothing is made to improve the S/N of the astronomical sources.

(e) The noise amplitude is computed with a sigma clipping. Then the image is thresholded at 3 times the noise amplitude computed (this correspond to 1.25 times the noise amplitude before smoothing the image). The image is the astronomical object are extracted.

(f) The diameter of each object is computed by the minimum circle containing all the segmented pixels. The diameters are then multiplied by the *enlarge-mask* parameter. The enlargement is justified to mask-out the extracted portion of the objects plus their faint extended wings not detected at the applied threshold.

(g) The minimum diameter is imposed to be equal to the size of the nominal seeing times the enlarge-mask option. This criterion is motivated by the fact that a detected source and its faint extended wings must be at least as large as the nominal seeing. Also, the maximum diameter is set to a quarter of the detector size. This second criterion, is chosen to avoid large holes in the mask leading to holes on the reduced RB. Note that, if lots of sources are larger than this criterion, this procedure is probably not a good choice to estimate the pixel-based sky background.

(h) A mask as large as the stacked image S is built, and all pixels are set to one. Each catalogued source is drawn by setting to zero the pixels belonging to a disks centered on the photocenter of the source, and with the diameter computed above.

5. Fringing pattern estimation with mask. The fringe pattern is estimated as in the first step. In addition, the mask is temporally applied to each image of the RB knowing the shifts between them (see figure 4.28 for illustration). If for a 3D pixel, the sky is visible (non-masked) less than 4 times within the merge-step images of a sub-block, then the affected pixel of the fringing-map of this sub-block is flagged as *non-visible*.

6. Fringing subtraction. The fringing-map computed is removed as in step 2. In addition to this step, the pixels of the fringing-map set to non-visible, are set to rejected on the corresponding images of the sub-block. These pixels will be discarded when the images will be stacked during the execution of module (4) or (5) (as illustrated by figure 3.9).

The 2 important parameters of this procedure are the *merge-step* (size of a sub-block) and the *enlarge-mask* (enlargement of the detected objects). The merge-step parameter is used to fit as close as possible the background variation. With H band observations, the background is evolving quickly within 5 or 10 images (of one minute each). Here the merge-step parameter is set to 10 or 15 to follow as close as possible the background variations. In case of J filter, the background is more stable and the background variations time constant is larger. The merge-step is set to 30 images (of one minute each) for instance. The *enlarge-mask* is an important parameter having a great impact on the photometry. It is used to mask a greater area than the detected pixels of each object, but a larger masking means larger risk of not being able to determine the sky background.

It is worth emphasizing, that this procedure is unbiassed for a reduced image computed from one RB. But, in case of final product that combines several reduced RBs (SB made of several images), this procedure is biassed. Indeed, the mask built to prevent an over-estimation of the sky background around faint sources, is computed per RB and not from a stacked SB. Therefore, the mask does not include sources fainter than 1.25 times the noise amplitude of the stacked RB. Nevertheless, the sources affected on a reduced SB, have a $S/N \leq 1.25 \times \sqrt(n)$, where n the number of images in a SB. For SB containing 9 or less images, the bias starts for sources fainter than 3.75 times the noise amplitude of the stacked SB. For this amplitude, the photometric error is larger than the bias imposed by the procedure, therefore the final product is valid. Note that in practice, only very deep observations have SB with more than 3 reduced images. A photometric comparison with another procedure applied on the very deep observations of the ISAAC/GOODS survey shows a good agreement for a final product computed from a SB made of 6 images (see sub-section 5.2.3).

In conclusion, an ideal procedure would be a 3 steps estimation in order to built masks from final products. This implementation, would decrease the photometric bias of faint sources for very deep observations. Note that this improvement would imply a more sophisticated administration, and the mask computed from a final product, should be properly applied on each raw images of the contributing RBs, taking in consideration, possible complex distortions (rotation, scale).

4.5.3 Validation of the method

Internal comparisons two-pass procedure versus one pass

In order to benchmark the two steps approach versus the one step approach, a test is done on IR observations. The data cube used, comes from the ISAAC instrument located on a VLT telescope. The images are part of the ISAAC/GOODS survey, a very deep survey located in the Chandra Deep Field South. It contains 60 images observed with the J filter. Each image has an exposure time of 120 seconds (which is effectively observed with 4 sub-integrations of 30 seconds). The data cube is reduced (all the modules of the Reduction Mode are activated) two times. Firstly with the one-pass background pixel based removal, and secondly with the two-pass background pixel based removal. The sources are extracted and measured on both reduced images using an aperture measurement of 2 arcsecs using the Sextractor software. Figure 4.29 shows the difference in magnitude of the extracted objects detected on both images. The objects from the first reduction are fainter and biased up to 0.08 magnitude. The bias in magnitude appears already for the brightest objects and increases for the faint objects. The value of the bias is also a function of the object density of the observed field.

A comparison of the two-pass procedure with an external author showing similar photometric

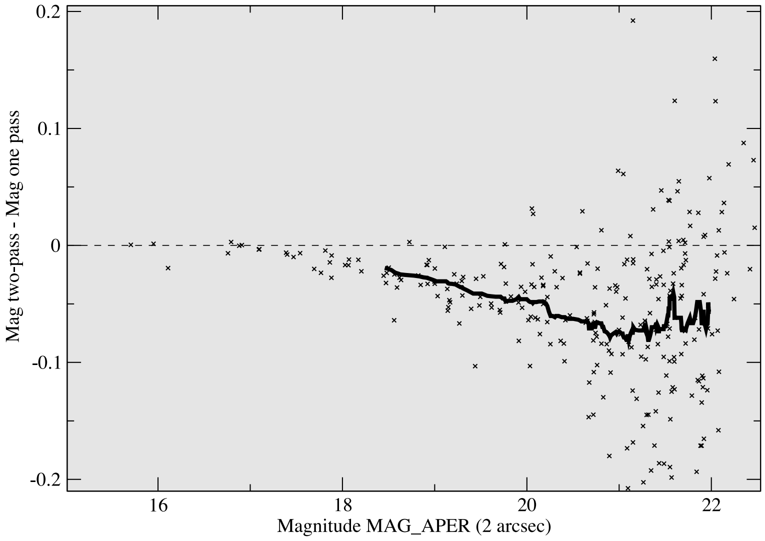

Figure 4.29: Magnitude comparison between catalogues issued from reduction with one pass versus reduction with two pass to estimate the fringes. The first pass estimation of the background, leads to a bias in photometry of faint objects up to 0.08. The continuous line build with a running median indicates the trend of the photometric points.

results is illustrated with the large GOODS project made with the ISAAC instrument (see section 5.2).

Internal comparison with different enlarge-mask option

The following test is done to compare the impact of the option mask-enlarge. An RB of 60 images (1 minute each) observed with the SOFI instrument in filter J is reduced 2 times. The 2 reductions are similar except for the option *enlarge-mask*. In the first case the option is set to 1.0 and then to 2.0. A portion of the stacked image from the first step background estimation and the 2 versions of the mask are shown in figure 4.30.

The impact of this option is not visible on the reduced images. Figure 4.31 shows a comparison of the photometry of the extracted objects where a small bias in magnitude is noticed. The objects are extracted with the Sextractor software using the MAG_AUTO estimator. From the small bias one concludes that the enlarge-mask option of 1.0, leads to a small over-estimation of the sky background. The very faint sources below the noise amplitude are not detected when creating the mask. Therefore whatever is the enlarge-mask option, the sources have the same magnitude. This effect is visible on the running median. Experiences show that beyond *enlarge-mask* of 2, the impact in photometry is not visible The optimal value is therefore 2.0. Note, that for some reductions the *enlarge-mask* option is chosen smaller to prevent too much masking in case of dense fields with many small objects. In some cases it could be impossible to estimate the background if the field is too crowded. In this case, one has to use an external background-map.

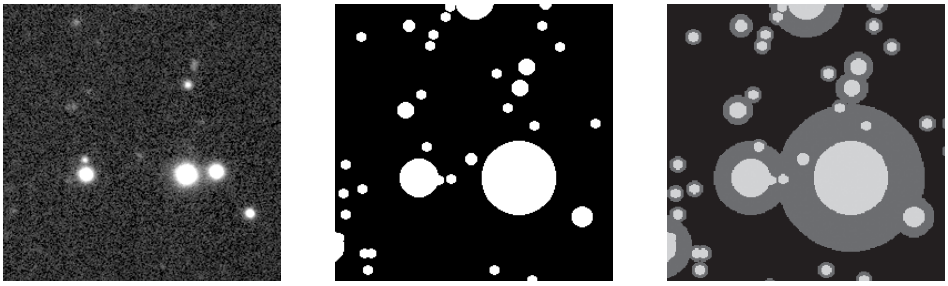

Figure 4.30: Mask creation for the second step estimation of the background. LEFT: stacked image (portion only) from an RB containing 60 images (one minute each) observed in J band with the SOFI instrument. This stacked image is used to compute the mask used for the second step. CENTER: Computed mask with the *enlarge-mask* parameter set to 1.0. RIGHT: Computed mask with the *enlarge-mask* set to 2.0. (On top of this mask is represented the mask of the enlarge-mask 1.0 case).

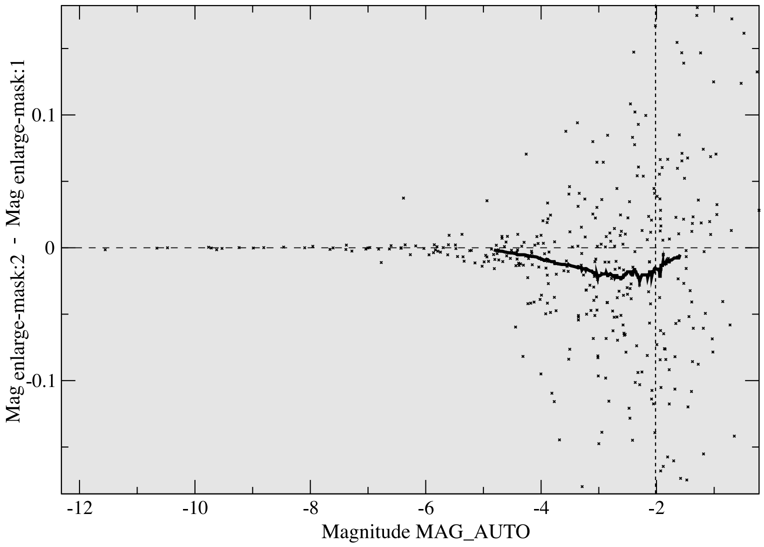

Figure 4.31: Impact of the mask for the two-pass background estimation. This plot compares the magnitude of the objects extracted from the reduced images using 2 different reductions of the same RB. In the first case, the *enlarge-mask* is set to 1.0, in the second reduction the parameter is set to 2.0. The bias is increasing for faint objects, and finally is negligible to the very faint end objects. The difference of magnitude is in favor of the reduction achieved with *enlarge-mask* set to 2.0 (the objects are brighter up to 0.02 magnitude). The continuous line is a running median of the plotted points.

4.6 Fringing removal with external fringing-maps

The unbiased background small scale estimator described in section 4.5 requires special properties of the input images. The procedure does not apply for three cases of RBs: Firstly, the ones containing too few images (less than 5) for the two steps fringe estimation procedure. Secondly, the ones with a dithering pattern of observation smaller than the largest astronomical sources. Thirdly, for observations of large extended sources or very crowded stellar fields. For those cases, an external fringing-map is necessary to subtract the fringes of the input images of the RB. The external fringing-maps are computed with several scientific observations made of one or more targets observed with the same filter (as described in sub-section 3.2). In practice this concerns mainly the redder optical passband (filter I) where fringes are very strong. With IR observations the small scale background is generally estimated within the RB or from special observation strategies. This sub-section details the procedure used to scale an external fringing-map to fit the fringe amplitudes of the scientific images.

Scale factor computation for external fringing-maps

The fringes are globally constant in shape, but may evolve in amplitude depending on the strength of the night sky emission lines. Therefore a fringing-map must be scaled before being applied a scientific image. Let F be the fringing-map, and I a bias and flat corrected image. The scale f is computed by:

$$f = \frac{\langle F\ ,\ I \rangle}{\langle F\ ,\ F \rangle}$$

Where $< F, I >$ is the cross-correlation of $F$with I. $< F, F >$ is the auto-correlation of the fringing-map. The correlation between two images of same size $[X, Y]$ is computed by the simple integration:

$$\langle F, I \rangle = \frac{1}{X \cdot Y} \sum_{i=1}^{X} \sum_{j=1}^{Y} (F(i, j).I(i, j))$$

The image I is then subtracted by $f.F$ to remove the fringes. The cross-correlation is a common method to compute a scale factor between two similar signals. Nevertheless, one must take care to remove the differences between the two signals such as: the noise, the large scale-structure background, the astronomical sources. For those three points, a filter step is applied temporally on I and F before the computation of f:

1. LOW-PASS BAND FILTERING - The images are smoothed with a Gaussian of 1 pixel wide. This smoothing decreases the noise amplitude by a factor of 2.0. Only the high frequencies of the fringes will be affected. In practice it improves the signal-to-noise of the fringes without modifying their shape.

2. BACKGROUND SUBTRACTION - The background of the images is estimated with a Pyramidal median transform (as described in section 4.4). Scale 4 or 5 are typically used.

The images are then subtracted by this smoothed version in order to remove constant and large scale structure details. This filtering step will also remove the smooth component of the fringes. The portion removed is not significant as fringes are made of high-frequency details.

3. REMOVAL OF ASTRONOMICAL SOURCES - The sigma of the images is computed. One assumes that the sigma of the images is due in part: to the photon noise previously suppressed by the Gaussian smoothing, and mainly, to the fringes themselves. Note that the large scale structure background has been removed and do not contribute to the computed sigma. In order to keep only the fringes with the remaining noise before computing the cross-correlation, the images are thresholded to keep signal within $[-4\sigma, +4\sigma]$. This high and low cuts remove the astronomical sources and remaining bad pixels.

This improved procedure is mandatory to compute a proper scale factor in the following cases: I has a short integration time and the fringes are not very bright, I has lots of bright stars or very extended sources.

Application to WFI images

The following illustration is based on WFI observations. A fringing-map is computed from 10 images made of 2 distinct pointings observed with a dithering pattern of 5 images. The 2 pointings have been observed during 2 consecutive nights. The procedure is tested with an image rich of stars (field XMM-12 part of the XMM project presented in section 5.4) taken 56 nights after. The fringing-map used is the closest available in time within the downloaded data. Figure 4.32 illustrates 4 images: *top-left*: The raw image processed by a master bias and flat (I), *top-right*: the fringing-map F, *bottom-left*: the processed image with the fringing-map $I_p = I - f.F$, and, *bottom-right*: a smoothed version of I_p named I_s. In order to highlight its fringe residuals, this image is smoothed with a pyramidal median transform up to scale 3 (I_s). Some residuals are visible with a maximum amplitude of 12 ADU corresponding: to 1% of the mean sky background, and 30% of the noise variation of I_p. The following table summarizes the different fringe amplitudes before and after the procedure. Also mentioned is the S/N of the fringes.

	Image I	processed image I_p
Amplitude of fringes	98 ADU	12 ADU
Noise of the image	41 ADU	41 ADU
Fringe S/N	2.4	0.3

With this single image, the fringe residuals are 0.3 times the noise amplitude. In practice, several images are stacked (RBs contain several images, final products integrate several RBs) and the fringe residuals are a combination of the ones observed on the individual processed images. If no dithering pattern of observation is made, one run the risk to have the same residuals at the same sky location, and therefore the final stacked image may have brighter fringe residuals as the noise amplitude decreases, and the signal-to-noise of the residuals

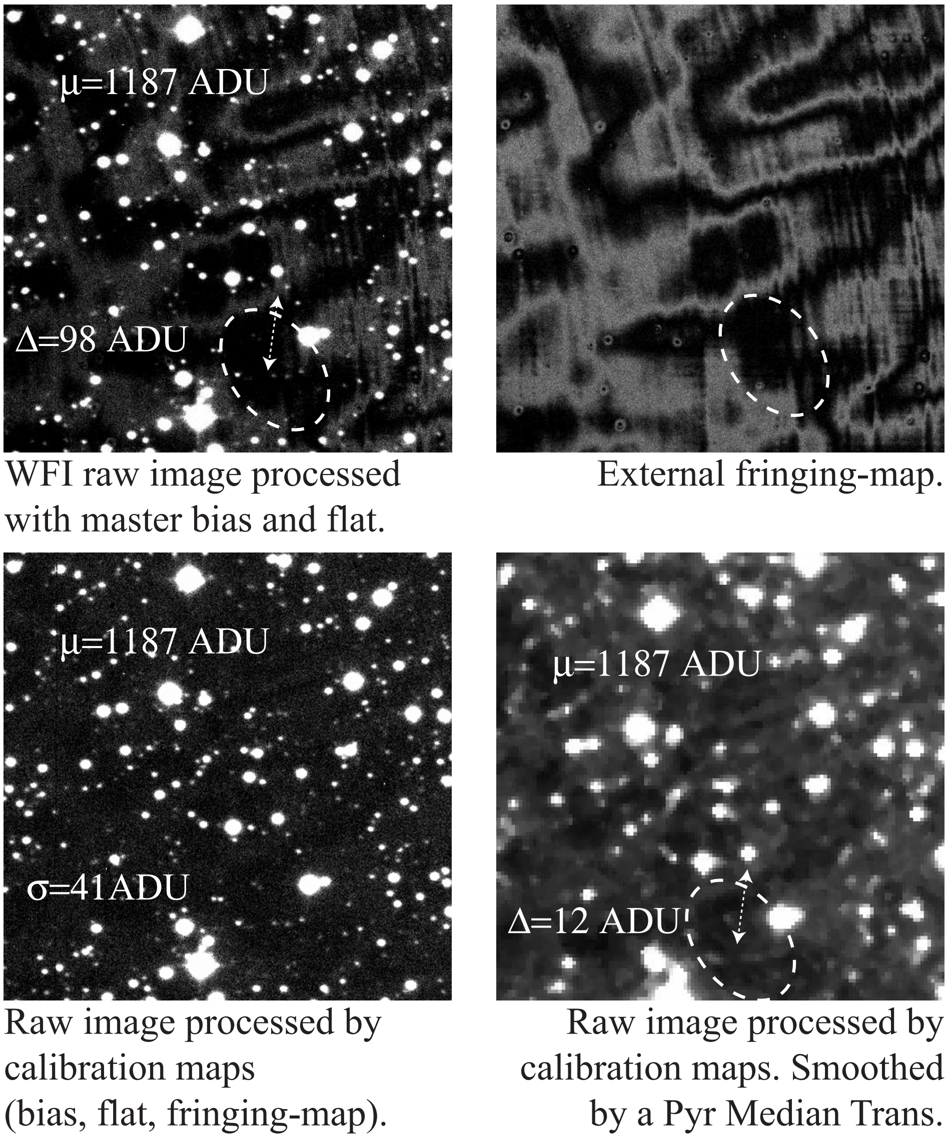

Figure 4.32: Application of a fringing-map on a scientific image observed with the WFI instrument. Top-left: raw image processed with a master bias and flat. Top-right: fringing-map computed from 10 scientific images. Bottom-left: image processed with master bias and flat, and subtracted by the scaled fringing-map. Bottom-right: same image as before processed with a median smoothing of 7 by 7 pixels.

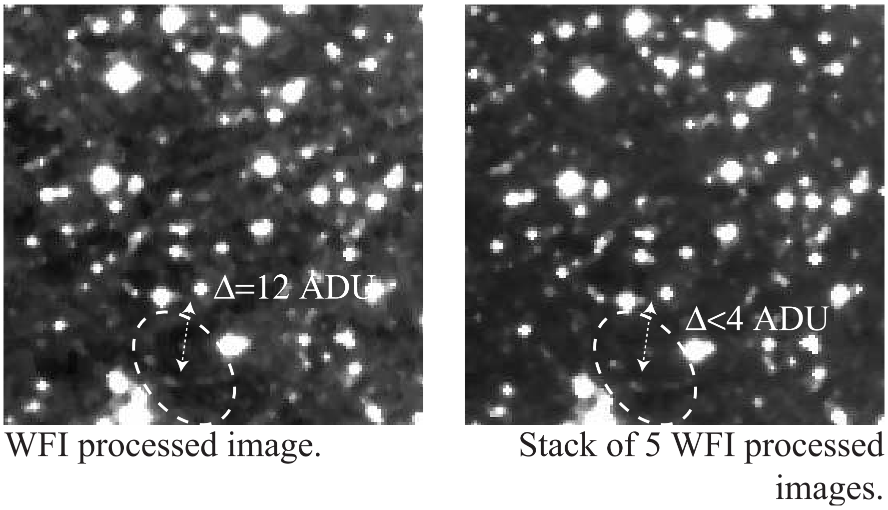

Figure 4.33: Fringe residuals on stacked images.

increases. Fortunately, images are observed with a generous dithering pattern (to fill-in the inter-chip gaps for instance) and the fringe residuals of the stacked image are often negligible. Figure 4.33 illustrates the fringe residuals from: the single image described above (left panel), and the stack of 5 images (right panel). Both images have been smoothed with the pyramidal median transform to decrease the noise. The background shape of the stacked image is much more flat than the single image, and is difficult to measure (amplitude less than 4 ADU). It is worth to emphasizing that the fringe residuals observed on final products are weak, and are characterized by middle range frequencies as the sharpest details have been smoothed by the dithering pattern of observation.

4.7 Astrometric Calibration: the Multi-resolution approach

The astrometric calibration is a critical step used to register an image versus a catalogue of well known objects, or versus another image of the same field. The registration is made by associating the extracted sources of the images to be calibrated with the sources of an astrometric catalogue or sources of another image. From the numerous associations a distortion model is deduced. The most problematic step of the astrometric calibration, is the association part. The quality of the astrometric solution and therefore the expected precision of the photo-center of the extracted sources depends on this step. Several methods exist to associate catalogues of points. Recently the most common one is based on triangulation recognition. This study is based on the wavelet transform. The first implementation of this procedure was applied for remote sensing images of Earth. This method has the advantage to be fast, and solve easily very crowded fields as LMC for instance.

This section presents, the wavelet approach to compute the astrometric solution; A procedure to compute translations between images; the warping strategy using a sub-pixel kernel.

4.7.1 The wavelet approach

In the pipeline, astrometric solutions are computed either in a relative or an absolute way. For instance, relative astrometry is done for the stacking of an RB using one of the images as reference, while an absolute astrometric calibration requires an astrometric reference catalogue and a re-mapping grid. In both cases the solution is found using the concept of multi-resolution, by comparing low-resolution images obtained from a wavelet decomposition. In the case of a reference catalogue this is done by first creating a mock image to map the objects listed in the catalogue onto a reference image according to the chosen grid convention. This method is referred to as pixel-based image registration (Djandji et al., 1993).

It is important to emphasize that this method is very efficient and fast to unambiguously associate sources from different images even in case of very dense stellar fields, but is not able to associate sources observed on two images with a different pixel size and rotation. By contrast the other casual procedure named *triangulation*, is able to compute unknown rotation, scale and translation from two catalogues. As described later, this procedure relies on the pre-knowledge of the large translation between images, which is computed using cross-correlation technique.

The calculation of the geometrical distortion between the two images requires: 1) the identification of a set of well defined astronomical objects (*control points*, hereafter CP) in both images; 2) the definition of a functional form for the deformation model which maps a point (x, y) in the input image to a point (X, Y) on the reference image; 3) the creation of the distorted or corrected image, which requires the adoption of an interpolation or warping method. The third point is an independent algorithm. This section focuses on the two first points, while the third is given is section 4.7.3.

The distortion model adopted by the pipeline is a pair of bivariate polynomials given by:

$$\begin{cases} X_i & = \sum_{p=0}^{N} \sum_{q=0}^{N-p} a_{pq}\, x_i^p y_j^q = \quad P\,(x_i, y_i) \\ Y_i & = \sum_{p=0}^{N} \sum_{q=0}^{N-p} b_{pq}\, x_i^p y_i^q = \quad Q\,(x_i, y_i) \end{cases} \tag{4.7}$$

Where (X_{i}, Y_i) are the coordinates of the i^{th} CP in the reference image and (x_i, y_i) the corresponding CP from the input image. N is the degree of the polynomial. Usually, the degree of the polynomial is one or two for instruments with a small field-of-view and up to four otherwise. Then follows the computation of the unknown parameters ($\frac{(N+1)(N+2)}{2}$ for each polynomial) using the least mean square estimator (LMSE).

The most difficult step of the process is to associate the CPs from the input image with the CPs from the reference image. CPs are randomly spread and can be very dense. The association cannot be done using any *window search* because multiple associations will occur and will bias the distortion estimation. The idea of the wavelet transform, is to work with different resolutions and therefore give a constraint for the minimum distance between CPs. Figure 4.34 illustrates the procedure using the wavelet transform:

Let I_r be the reference image and I_i be the input image. On each image the wavelet transform with the so called *algorithm ‡ trous* (Mallat, 1989) is performed up to the scale L producing two wavelet images W_{il} and W_{rl} with: $l \in (1, L)$ from the two images I_i and I_r. L being the initial dyadic step, it corresponds to the large details of the images. A detection procedure on W_{iL} is achieved and only the local maxima with amplitude greater than three times the sigma of the noise are kept. These local maxima play the role of CPs. They correspond to significant image patterns, and have to be found in the corresponding wavelet plan of the reference image W_{rL}. The association is done with a window search. The search radius is set to 2^{L-1} pixels, and corresponds to the half of the maximum wavelength (Shannon constraint) appearing at the scale L. This radius assures no multiple associations. At this scale identical CPs can be matched with confidence, and therefore the relationship between the coordinates of the different images can be determined. This provides a rough estimation of the distortion model. Considering now the wavelet images of order $L-1$, a new set of maxima in each wavelet plan is detected. The coordinates of each maximum detected are then transformed into the reference image system using the previous estimation of the distortion model. This follows an iterative process until the last scale corresponds to the wavelet plan of the best resolution (in practice equal to scale 2 corresponding to the seeing size), establishing thus the best geometrical correspondence. A first degree polynomial is used for the scale L, but the degree can be increased for the last scales.

The first window search applied on the catalogues issued from the highest wavelet scale L may be too small if the residual shift between the images is larger than the search radius. In fact the wavelet approach cannot solve large translations, nor rotation or very large distortions. A first approximation should or must be given to feed the first step of the wavelet approach. This pre-knowledge is schematically illustrated with figure 4.34 on the top: "External distortion information". The actual implementation of the pipeline will search for this pre-knowledge in two ways:

1. DISTORTION BETWEEN THE RAW IMAGES TO THE FINAL PROJECTION GRID. If an

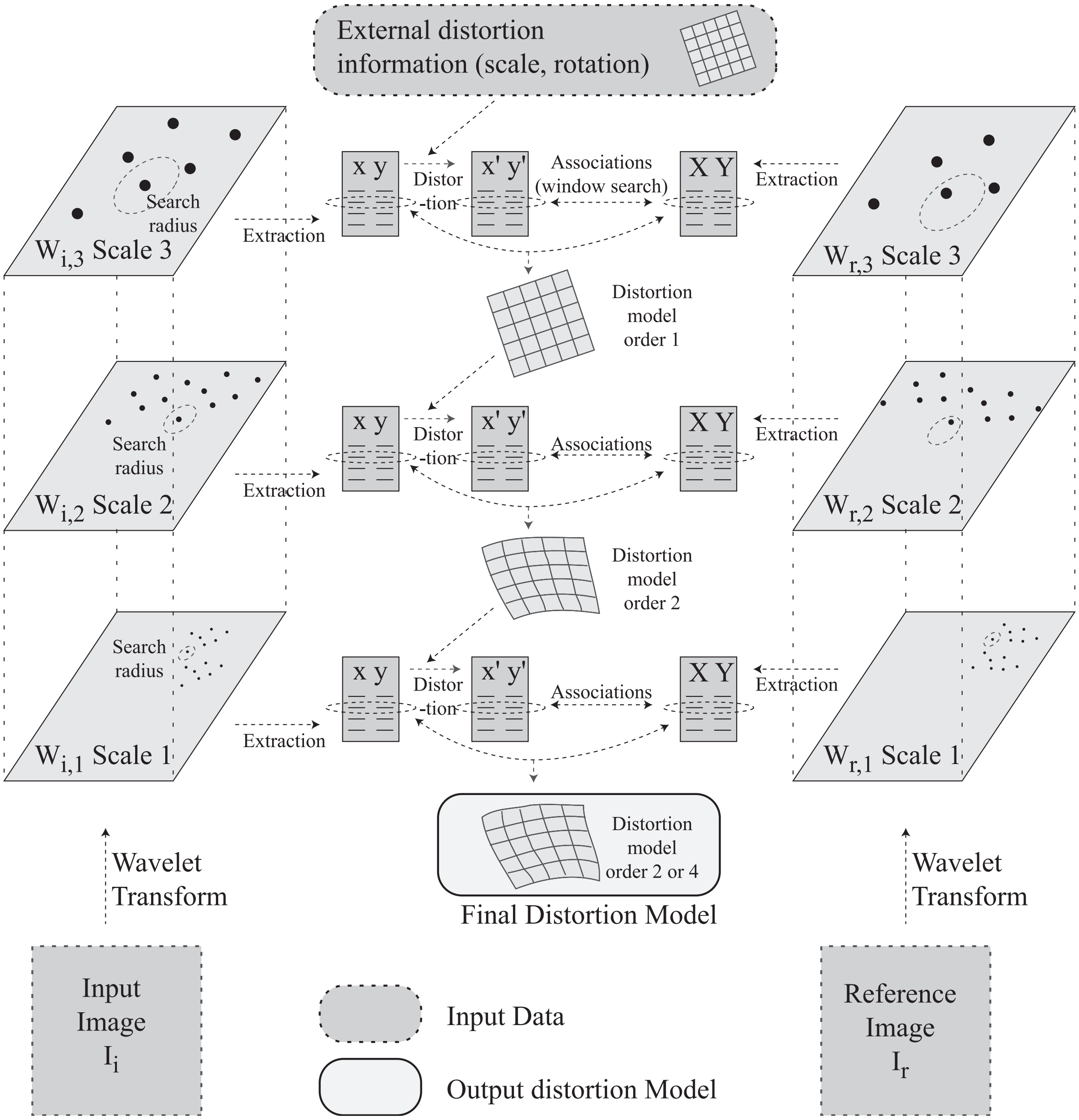

Figure 4.34: Procedure using the bi-orthogonal wavelet transform to compute a distortion model between one image and another used as reference.

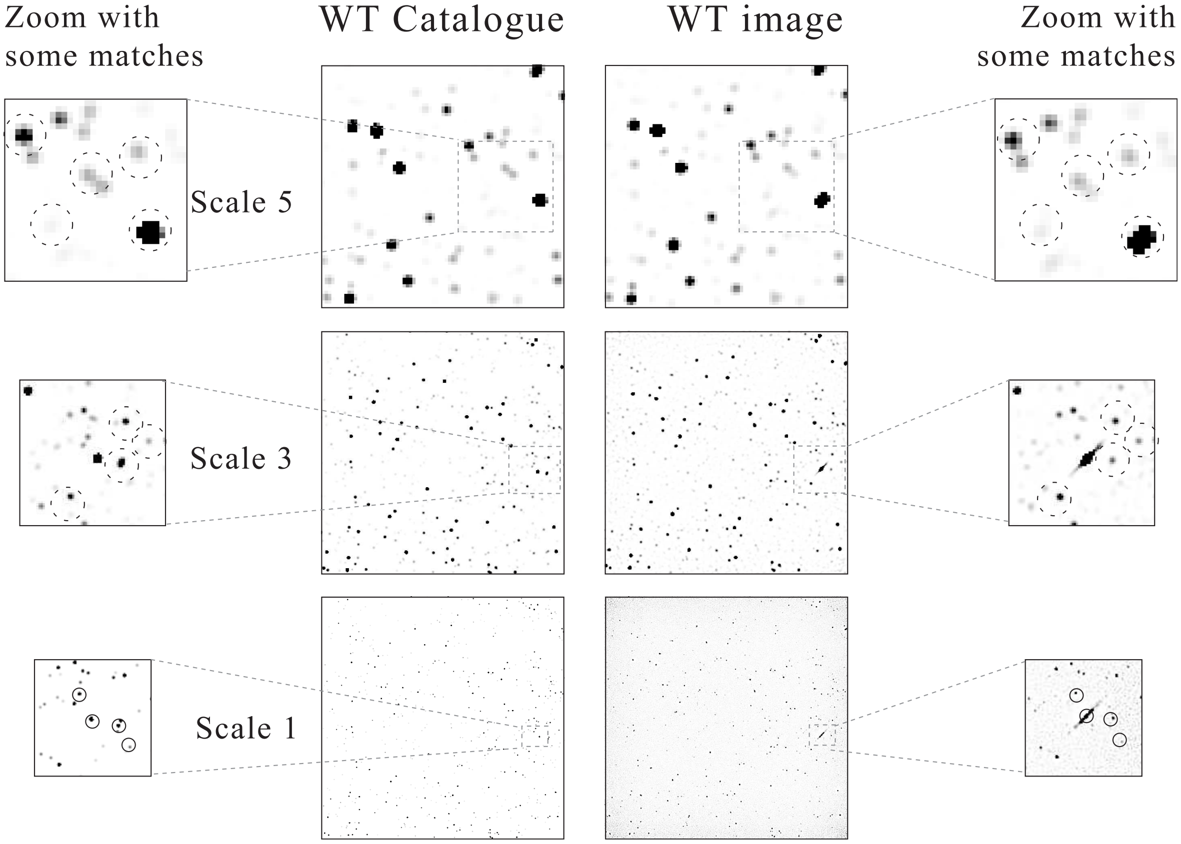

Figure 4.35: Wavelet transform of the reference image (simulated image from a catalog), and the wavelet transform of the input image to be registered. The circles show some associations done with the window search scale by scale. Only a part of the wavelet planes are shown via a zoom from one scale to a lower one, in order to improve the visibility. Scale 5 is the last scale (lowest-resolution) of the wavelet transform. A rough distortion model is deduced from this scale. It is then refined with the other scales up to scale 1. The final distortion model is made with a second or fourth order polynomial depending on the field-of-view.

external grid is specified, the astrometric solution is computed directly from the raw images reference system to the projection grid. The astrometric solution will include a rotation and scale factor if the raw image projection system is rotated/scaled with respect to the reference grid. It will also include a dilatation or a contraction if the pixel size of the reference grid is different from the one of the raw images.
This distortion is solved by projecting 2 orthogonal unitary vectors in pixel space into the sky coordinate system according to the projection grid of the first image, and then project them back to pixel space using the projection grid of the second image. From the 2 vectors expressed in the 2 pixel based systems, one gets a first order distortion between the 2 reference grids. This computation solves rotation and zoom. Note that this computation does not include translations.

2. Shift between the two images to be aligned. A small shift may exist between two images observed with a dithering pattern while computing a relative astrometric

solution. A residual shift may also occur between an image and an astrometric catalogue if the reference pixel of the image is not very accurate.
In both cases, the translation is computed using a cross-correlation technique in Fourier space. This technique is detailed in the coming sub-section (4.7.2).

It is important to emphasize that the raw images must have an accurate description of their pixel-size and orientation or the astrometric calibration may fail when using the wavelet approach. For instance, if an instrument is rotated by several degrees from its expected position and if this rotation is not reported to the header of the raw images, then the wavelet approach may fail if the rotation is large enough such as the window-search is too small to handle all possible associations spread on the full image. In some case this can be solved by increasing L. The present pipeline is not looking for unknown rotation. Such cases occur rarely with the WFI instrument. By comparison, the triangulation procedure has the advantage to be insensitive to rotation and zooming. A complete solution should be to compute a first rough astrometric solution by using a triangulation approach applied to the catalogues of the highest scales (lowest resolution). This upgraded version will be fast as the triangulation is applied on small catalogues (they are issued from low resolution details). The need of a pre-knowledge for the astrometric calibration based on wavelets does not mean it is a bad solution. Inded the computation is very fast and the results are very accurate also for very crowded star fields. For the time being, the pipeline is just checking for the reference pixel of the raw images (large translation error) during the preparation phase (as described in section 3.2 step: Reference pixel check).

4.7.2 Large-amplitude translation: correlation approach

A robust procedure to estimate the translation between two similar images is built for the pipeline. This procedure is used for two different tasks: Firstly, to correct the reference pixel of the raw images (by computing the translation between an extracted catalogue versus an astrometric catalogue see 3.2), and secondly to search for residual translations before computing the astrometric solution of consecutive images observed with a dithering pattern of observation. In both cases the translation is computed using images (either simulated of real).

The procedure is based on the well knows correlation method. The correlation point obtained with two similar images gives the value of the shifts. This algorithm must be adapted for astronomical images where cosmic-rays or very bright stars perturb the correlation point. A procedure is defined to find a rough estimation of the translation between I_r and I_i, by pre-filtering the similar images before searching for the correlation point.

Let $F(x)$ be a one dimensional signal and $F(x-\tau)$ a translated version of it. Using $f(\nu)$, the Fourier transform of $F(x)$, the correlation of two translated signals in direct space is converted in a multiplication with a phase term in the Fourier space:

$$F(x) \circledast F(x-\tau) \;\Leftrightarrow\; f(\nu).f(\nu).e^{2i\pi\tau}$$

The phase term, can be assimilated to the Fourier transform of a translated Dirac function. The right hand side of the equation can be rewritten as:

$$f(\nu).f(\nu).e^{2i\pi\tau} \Leftrightarrow F(x) \circledast F(x) \circledast \zeta_\tau$$

Where ζ_τ is the Dirac function translated by τ. The correlation image is the autocorrelation of $F(x)$ translated by τ. The autocorrelation of $F(x)$ is a centered signal, which can be roughly assimilated to a thin Gaussian-like function located on the axis origin. This Gaussian like function is shifted by τ, the measurement of the photo-center gives a direct measurement of the translation. This demonstration can be propagated to signals of higher dimensions.

The algorithm needs to be automatic and very robust. The astrometric solution using the wavelet approach needs the value of the shift before using the first window search at the last scale. Most of the astrometric solutions fail if this pre-knowledge is not computed properly. This procedure is crucial for the automation, it has been through several versions, and now achieves a stable and generic solution.

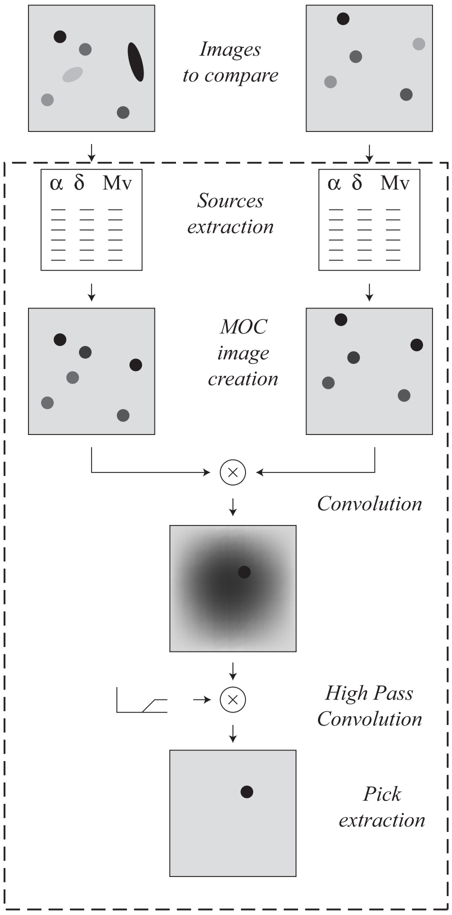

Figure 4.36: Procedure used to compute translation between two similar images.

The Fourier space approach used to compute the translation is very efficient but needs to be adapted in the case of astronomical images. Several sources of parasites can fail the translation estimation. Firstly, the backgrounds of the two images to be compared may be quite similar, and are not shifted as the astronomical objects are. Therefore, in the convolved image two peaks appear, one located at the origin related to the background, and a translated one related to the shift of the objects. The translation may be estimated to zero, if the signal of the background is higher than the total signal of the objects. Also, another source of perturbation are the stars located on the border of one image, and not observed in the other one. If those stars are very bright (several magnitudes brighter than the others) the peak in the convolved image is dissolved.

A special procedure is defined to handle those cases of perturbations (see figure 4.36). First, a quick source extraction is applied on the two images to be compared. It consists of collecting the local maxima several times greater than the noise of the images. The two catalogues of positions and maxima are converted into position and magnitude. This is used to give comparable weights to all objects, and lower weights for bright objects. Then two simulated images are created from the two catalogs, faint Gaussians are plotted with amplitude equal to the magnitude of the objects. The created images are convolved using the Fast Fourier Transform. The convolved image is then filtered with a high-pass filter in order to improve the signal to noise of the peak of correlation. The pixel of the highest value in the filtered image gives the location of the peak of correlation. The translation is the distance between the middle of the image to the location of the peak.

The procedure is accelerated when working on low resolution of the input images. For instance, in the case of the reference pixel recovery, a typical under-sample of the input images of 8 makes this procedure very fast compared to other main procedures (wavelet transform for instance).

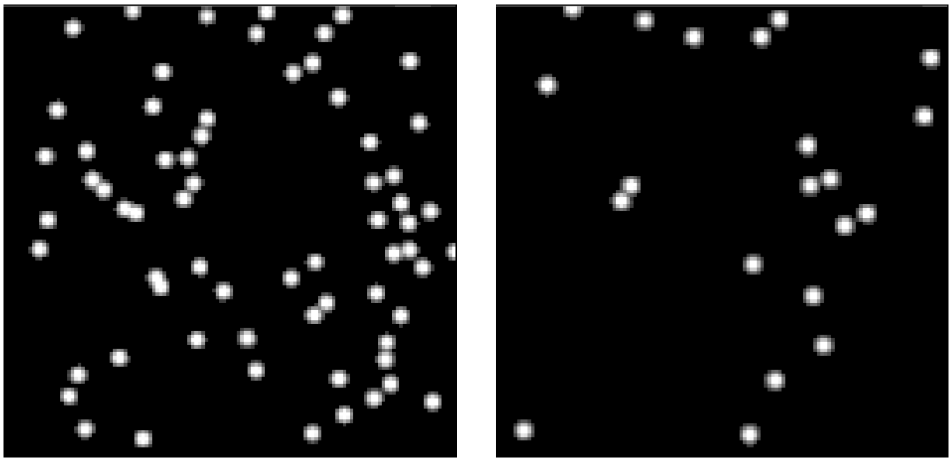

Figure 4.37: Simulated images build from the extracted sources of the two images. The right image is created from extracted sources from the stacked RB. The left image is created from the points of the catalogue used for the absolute astrometric solution. Note that the field-of-view is 5×5 arcmin, and therefore the reference catalogue does not appear very dense on the image.

This procedure is illustrated using a case of a SOFI stacked IR RB just before the absolute astrometric solution. The goal is to find the shift between the stacked image and the simulated image from the catalogue used for the absolute astrometric solution. Figure 4.37 shows the two created images. The field-of-view of the images is 5 arcmin. The two images do not have the same densities of stars (the stacked RB is deeper than the optical catalogue), and have not the same magnitudes (the catalogue comes from optical observations, whereas the stacked RB comes from IR observations). Nevertheless, the correlated image shows a very sharp peak of correlation with a high signal to noise (as illustrated in figure 4.38).

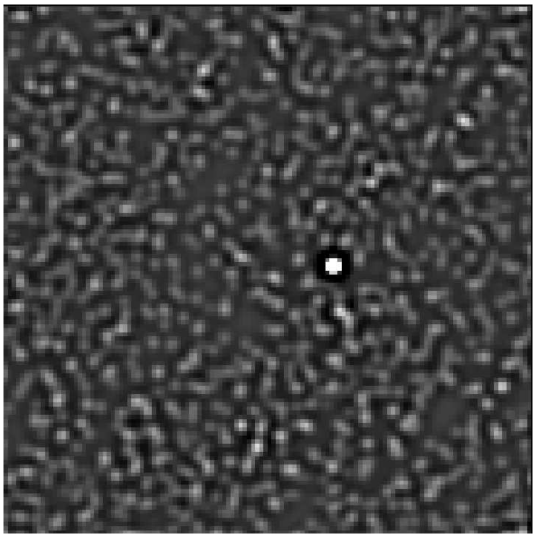

Figure 4.38: Convolution of the two created images (cf Fig: 4.37). The bright peak has a Signal-to-Noise of 145, the second highest peak (top-left of the image) which is a false-positive, has a $S/N \sim 21$. The identification of the correlation point is without ambiguity. The location of it, gives a direct information about the shift of the two images.

4.7.3 Image warping

In order to combine the images of a RB, first they must share the same projection grid. Each one has its own projection convention (translation between themselves for instance) given by the distortion model computed by the astrometric calibration. The model indicates how a coordinate from the raw image is converted into the coordinate of the reference grid. The application of a distortion model to one image is named *warping*. After the images has been warped, they share the same grid and can be easily combined to produce a final reduced image.

To warp an image, the pixels are converted to their new position according to the distortion model. For each input pixel (i, j) is computed the distorted location (k, l), where $k = P(i, j)$ and $l = Q(i, j)$. The coordinates of the distorted pixel (k, l) are generally not integers. As the images are defined in a sampled space, the pixels have integer coordinate. Therefore, the new pixel coordinate is not compatible with the sampling. In other word, it is impossible to warp a sample signal, and only an approximation is feasible. The flux of the pixel will be distributed to the pixels close to the new non-integer (k, l) coordinate. The redistribution of flux depends on an interpolation function and numerous families exist. Nearest-neighbor, bi-linear, and Lanczos interpolations are the most widely used (Bertin, 2002). Currently, only the nearest-neighbor and Lanczos are implemented with the latter providing the best results. The Lanczos function family is defined by: $\prod_d sinc(\pi x_d) \cdot sinc(\frac{\pi}{n} x_d)$ with $-n \leqslant x_d \leqslant n$.

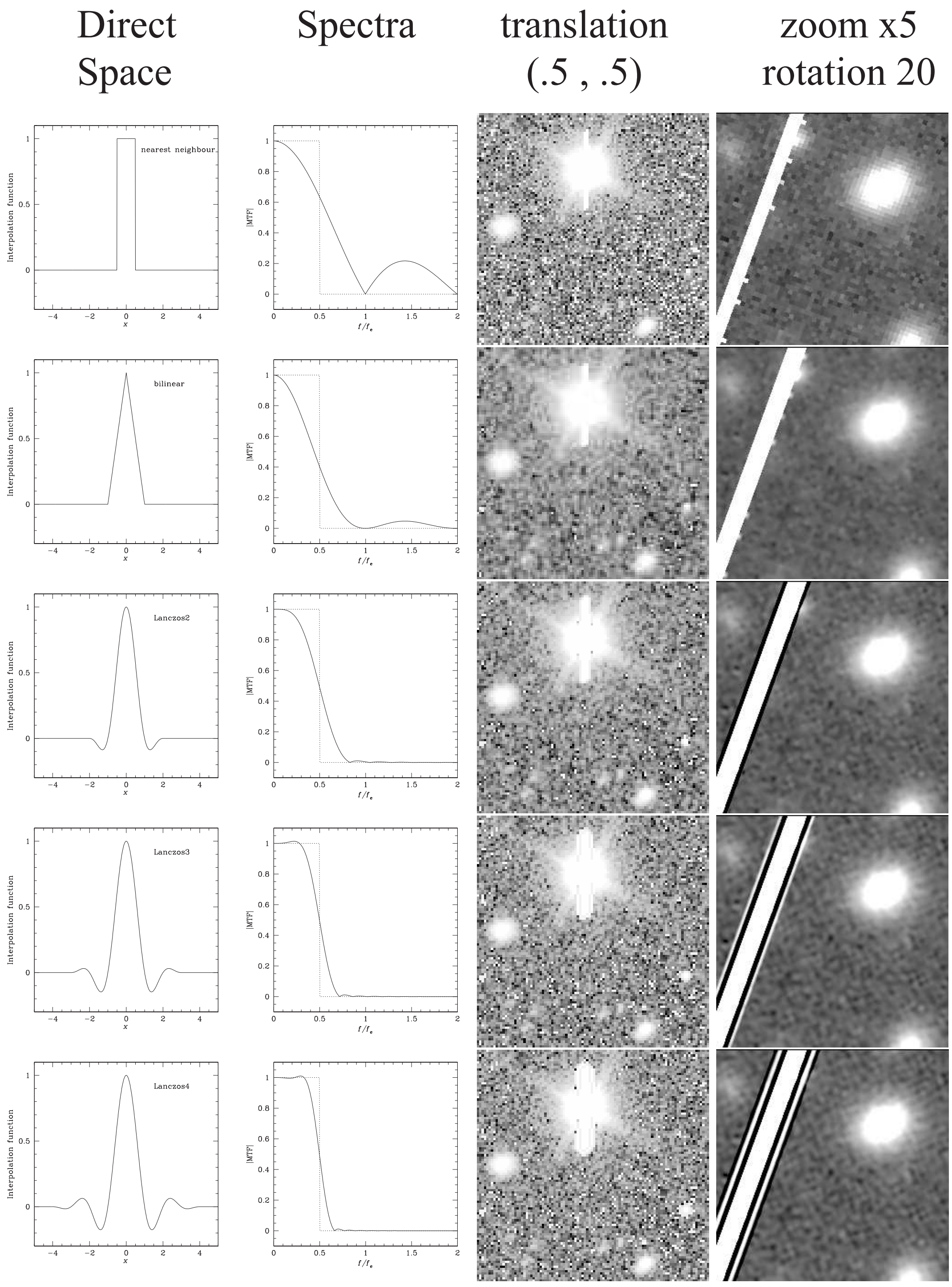

Figure 4.39: Comparison between resampling methods. From top to bottom: nearest-neighbour, bilinear, Lanczos2, Lanczos3, Lanczos4. From left to right: Interpolation function profile, Modulation Transfer Function, result from shifting an image by half a pixel in both direction, and result for a 5× zoom + rotation by 20 degrees.

Where n is the parameter defining the family of functions.

The warped images are different from the raw images because the flux have been re-distributed. Depending of the interpolation family used, the resulting images have distinct properties. Figure 4.39 (issued from the Swarp user manual (Bertin, 2002) page 17) illustrates the properties of the 5 kernel families: the nearest-neighbor, bi-linear, Lanczos order 2, 3 and 4. For each kernel, the first column illustrates the shape if the interpolation function. The second column gives the Fourier transform of the kernel. And the two last column illustrates the warping applied on an image distorted by first: a translation by 0.5 pixel in both directions, and second: a zoom by 5 and a rotation of 20 degrees. One notices the negative ring around the point like cosmic. This cosmic is similar to a Dirac function. The warped version reveal the kernel used for warping.

The warping affects the noise and the PSF of the resulting images. The noise of the raw image is white, its spectrum envelope is constant, or in other words, the noise value of one pixel has no correlation with the neighboring ones. The warping step uses a kernel that cut the high frequencies (second column of figure Figure 4.39), and therefore modifies the noise spectrum. The noise becomes correlated and its amplitude decrease. A first estimation of this effect can be modeled by a so-called *fudge factor* f used to characterize the noise correlation. It is defined by the ratio between σ_w the noise amplitude of the warped image, and σ_r the noise amplitude of the original image. $f = \sigma_w/\sigma_r$. For instance, when one refers to a 3 sigma detection, it corresponds in fact to $3 \cdot f$ sigma measured on the warped image to take the fudge factor in consideration. The warping of an image also impacts on the PSF because of the smoothing. This effect is negligible in the case of well sampled images following the Shannon constraint.

4.7.4 Procedure description

The following procedure description completes the first description of the Reduction Mode (see sub-section 3.3.2 step number 4 and 5). This enumeration details the cosmic rays rejection and the warping procedures (figure 4.40 illustrates schematically the different steps).

1. Simulated image creation - A simulated image is created with the reference grid and the astrometric catalogue.

2. Wavelet Transform - Each image of the RB and the simulated image are converted in Wavelet space. Note that for each raw image, the bad-pixels registered by the weight-map (amplitude equal to zero) are replaced by the mean of the corresponding image to avoid false signals.

3. Astrometric calibration

   (a) *Search for distortion between the raw images and the projection grid of the final product* - This distortion is computed with the matrix elements. This distortion is the pre-knowledge needed by the wavelet approach.

   (b) *Residual translation computation* - The residual translation between the reference image and the other ones is computed with the the special procedure defined in sub-section 4.7.2).

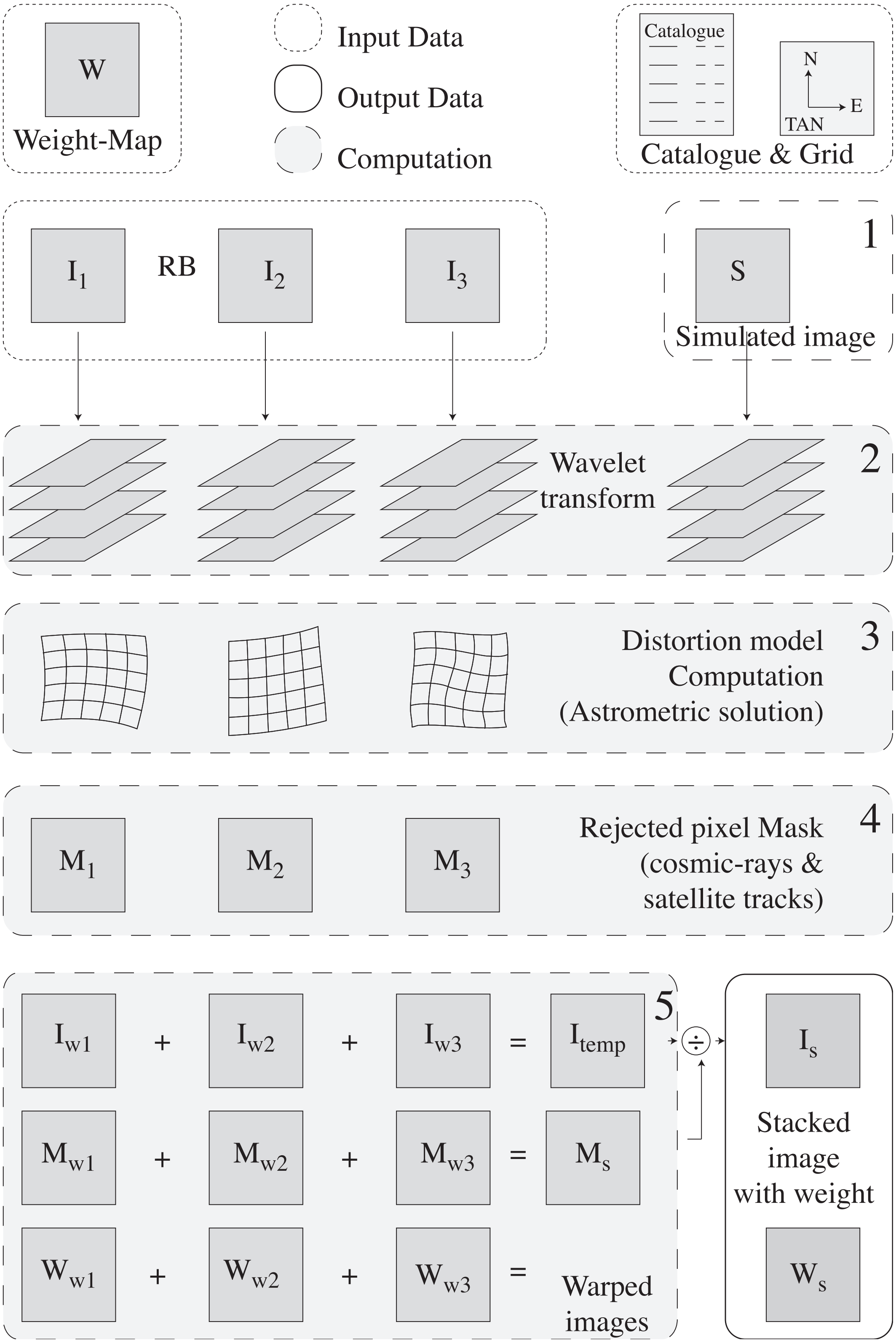

Figure 4.40: Main steps to compute astrometric calibration, warping and stacking of a stacked image from an RB.

(c) *Wavelet approach* - Iterative window search (as illustrated in figure 4.35) from the highest scale to scale of maximum resolution to compute the distortion model. In practice, scale two is the last scale used for iteration as it corresponds to the resolution of the seeing. On scale one, very few sources are significant.

4. BAD PIXEL REJECTION - For each raw image of the RB, a mask is created. It is equal to zero for pixels rejected by the weight-map, and the pixels rejected by one of the two following procedures. The rejected pixels are marked with a "special value", and will not be taken in consideration during the warping phase.

   (a) *Satellite track detections with the Hough transform.* Satellite tracks are detected and masked as described in section 3.3.2. The Hough procedure is executed before the cosmic ray rejection step, as the bright tracks could be removed by the latter, which would make the track detection impossible.

   (b) *Cosmic ray rejection.* The cosmic rays are detected and masked as described in section 3.3.2.

5. IMAGE WARPING AND STACKING

   (a) *Image warping* - For each raw image of the RB, a temporary mask is created. It is made of zero for the rejected pixels recorded on the weight-map (bad-pixels detected from master calibrations), and the ones recorded by the special value on the image: tracks and cosmic rays just being detected. The other pixels of the mask are set to one. On figure 4.40, the i^{th} image is named I_i, the corresponding mask M_i and the weight common for all images is named: W. Each tripled I_i, M_i, and W is warped according to the astrometric calibration of image i. The warped image I_{w1} is added to the I_{temp} temporary image. The warped weight-map W_{wi} multiplied by the exposure time of I_i and is added to the final staked weight-map W_s. The warped mask M_{wi} multiplied by the exposure time of I_i and is added to the final stacked mask M_s.
   The normalization of M_{wi} and W_{wi} done with the exposure time is made to normalize the final stacked image to 1 second, and also to give an optimum ponderation taking into consideration the different noise amplitude of images of different integration time. This strategy assumes that the noise amplitude is constant on different images of same integration time. This assumption is valid because RB contains images observed during a maximum of one hour of stable sky condition.

   (b) *Image merging* - The temporary image I_{temp} are divided by the corresponding exposure time, and must be normalized such as the final stacked image I_s is made of the mean of the contributing images. This is done by dividing I_{temp} by the stacked mask M_s. Note that M_s is first thresholded to 0.5 to prevent the warping kernel diffusion on the border of the valid pixels of I_{temp} which is masked by the thresholded M_s. This actual implementation assumes the followings firstly, the images have the same noise amplitude, and secondly, the astrometric calibrations do not have large variation of stretching. The first assumption is quite good, as the images of an RB has been observed within the same hour. Also, if the noise amplitude varies, a special option is made to reject raw images with too high noise compared to the other ones of the RB (see section 3.3.2). The second assumption is true and the maximum stretching variation is less than 0.2 percent with the WFI images. The normalization with M_s provides a fast and iterative computation using a minimum of memory. M_s, W_s and I_{temp} are created iteratively with the warping of the raw images. This strategy may evolve in future if its impact on the photometry is too important. In this case a scale factor will be computed from the input images, and not assumed equal to the exposure time of I_i.

4.8 Satellite track detection: The Hough transform approach

A frequent problem encountered in imaging surveys using wide-field imagers is the presence of a significant number of satellite tracks. This is a non-trivial problem for survey work since these features, if not identified in the original exposures, will appear in the final co-added images. The presence of these tracks are not only unpleasant from the cosmetic point of view but also have a considerable impact on the derived products (catalogues). Once propagated to the final image, none of the available options are adequate. One can either mask the final image, which may continue to affect the source extraction, or go back to the individual exposures, mask the visible tracks, and stack the images again. While this manual process can be done for a few images it is certainly not feasible for large data flows given the high incidence of these features. Therefore, a robust system must be able to identify and remove these unwanted features automatically during the processing phase which precedes the stacking (Vandame, 2001).

Before detecting and masking the observed tracks, one must ensure the nature of them in order to remove only tracks caused by satellites. The observed tracks mostly cross the full field-of-view of the instrument during the integration time. For instance with the WFI instrument, most of the tracks are crossing the full field of view (30 arcmin), whatever is the integration time (1 or 10 minutes). The apparent proper motion of an observed object is at least 30 arcmin per minute of observation. By comparison, the apparent proper motion of the solar system objects do not reach such speed. For instance the Hale-Bopp comet having a very fast proper motion, was moving at best at 0.06 arcmin per minute. Therefore the observed tracks can only be due to satellites. The procedure defined is not sensitive to short tracks (couple of arcmin long) caused by the fastest asteroids for instance. Note that the slower satellites are the geostationary ones, moving at 15 arcmin per minute (as the telescope is following the stars), the other ones are moving relatively to the ground and thus have an larger apparent motions.

This section firstly presents the Hough transform, and a special procedure that makes its computation very fast. Secondly, the statistical and geometric properties of the Hough space are illustrated. Thirdly, the implemented procedure used to detect and mask out the satellite tracks is described. Fourthly, an illustration is given, and finally this section ends with a description of the limitations of the implementation.

4.8.1 The Hough transform and the Bresenham algorithm

The task of detecting a satellite track can be modeled by detecting aligned points within a flux of points distributed randomly within an image. One supposes that images are analyzed with local maxima such as a track appearing with several points aligned. Indeed a track cannot have an equal flux along its trajectory because of the noise and the pixel sampling. Therefore a local maximum extraction provides several aligned points for significant tracks even if a casual threshold provides a unique elongated object for a very bright track. The flux of points distributed randomly is caused by the local maxima extraction of the significant astronomical sources.

Aligned points are commonly detected in the Hough space (Hough, 1962). The method is based on the fact that the Fast Hough Transform (FHT) converts points in the original space (direct

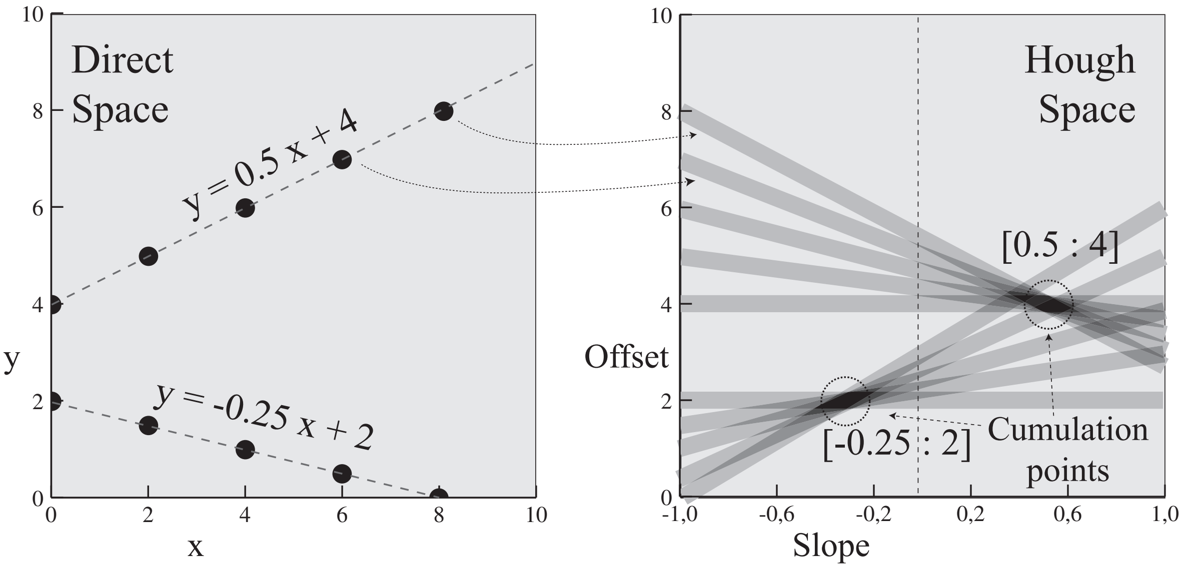

Figure 4.41: Example of the Fast Hough Transform of two sets of aligned points. LEFT: catalogue of aligned points observed in the direct space. RIGHT: Hough transform of the aligned points. Each point of the direct space is converted into a line in Hough space. The Hough space is represented in a schematic view with negative intensity. The figure illustrates the cumulation of lines in Hough space caused by aligned points in the direct space. The two points of maximum amplitude in the Hough space give the coordinates of the 2 sets of aligned points of the direct space.

space) into lines in the Hough space. In this space the intersection of the lines corresponds to the parameters of a straight line in the original space.

The Hough space is a two-dimensional space in which each point $[x, y]$ in the direct space is transformed into a line given by $Y = -x * X + y$. The amplitude in the Hough space is the sum of the number of points contributing at each position in this space. The alignment of N points in real space following the relation $y_i = s * x_i + o$, where $i \in [1, N]$, will imply a peak in the intensity of the amplitude N in Hough space at the point $(X = s, Y = o)$ given by $o = -x_i * s + y_i$. The parameters s and o are respectively the *slope* and the *offset* of the line. This transformation is illustrated in Figure 4.41 where two tracks in real space are shown in the left panel and the Hough transform of all points along these two lines are represented in the Hough space in the right panel. As discussed above the intersection of the point-transformed leads to an intersection in the Hough space yielding a local maximum. The identification of these high-amplitude peaks yields the coefficients a and b that correspond to the slope and the offset of the track in the direct space.

The complexity (time consuming) of the Hough Transform depends on N, the number of points of the input catalogue, and depends also of the complexity to draw lines within a matrix (The Hough is sampled). Drawing a line in a sampled space is impossible because pixels are defined with integer coordinates and some points of a line have discrete coordinates, an approximation is used instead. A fast procedure named the *Bresenham's algorithm* is used to draw lines.

The Bresenham's algorithm draws an approximation of a line, such as the distance between

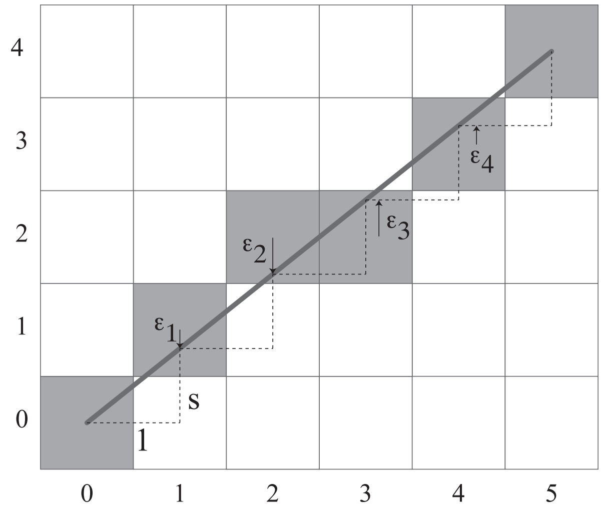

Figure 4.42: Schematic illustration of the Bresenham's algorithm to draw lines within a matrix. Application to a line with a slope of $s = 4/5$. The ε_n are the errors between the continuous version of the line versus the pixel approximation.

the real line, and the pixel selected for the approximation, is always smaller than 0.5 pixels. Lets consider the case of a line with slope $s \in [0, 1]$ starting at location $x = 0, y = 0$. Figure 4.42 illustrates the Bresenham's algorithm for a line with slope equal to $4/5$. The starting point of the line is the pixel $[0, 0]$, the next consecutive pixel used to represent the line is either $[1, 0]$ or $[1, 1]$, the decision depends on the slope of the line. If $s > 0.5$ then the pixel $[1, 1]$ is chosen, else the pixel $[1, 0]$ is chosen. The distance error between the real line, and the selected pixel is equal to $\varepsilon_1 = 1 - s < 0.5$. The next selected pixel is chosen with the same criterion taking into consideration $\varepsilon_1$and s. Iteratively, the line is drawn.

For slope greater than 1, a mirror strategy is used. The algorithm is very fast, and can be optimized to deal with only integers. The efficiency to draw lines makes the Hough Transform a very fast transformation.

4.8.2 Statistical and geometrical properties

The Hough space has 2 dimensions: the first axis represents the slope, the second axis represents the offset. The slope s and offset o of the possible lines included in an image of the direct space are within infinite boundaries. The Hough space is therefore infinite and must be analyzed entirely to detect all the possible cumulation points. To bind the Hough boundaries with finite values, one focuses first on small slopes. Lets consider a catalogue of N points $[x_i, y_i]$ with $x_i \in [0, N_x]$ and $y_i \in [0, N_y]$. The boundaries of the Hough space are defined by the following equation:

$$o \in \begin{cases} \left[0; 2N_x - \left(s\frac{Nx}{Ny} + 1\right) N_x\right] & for \quad s < 0 \\ \left[-s\frac{N_x}{Ny} N_x; N_x\right] & for \quad s > 0 \end{cases} \tag{4.8}$$

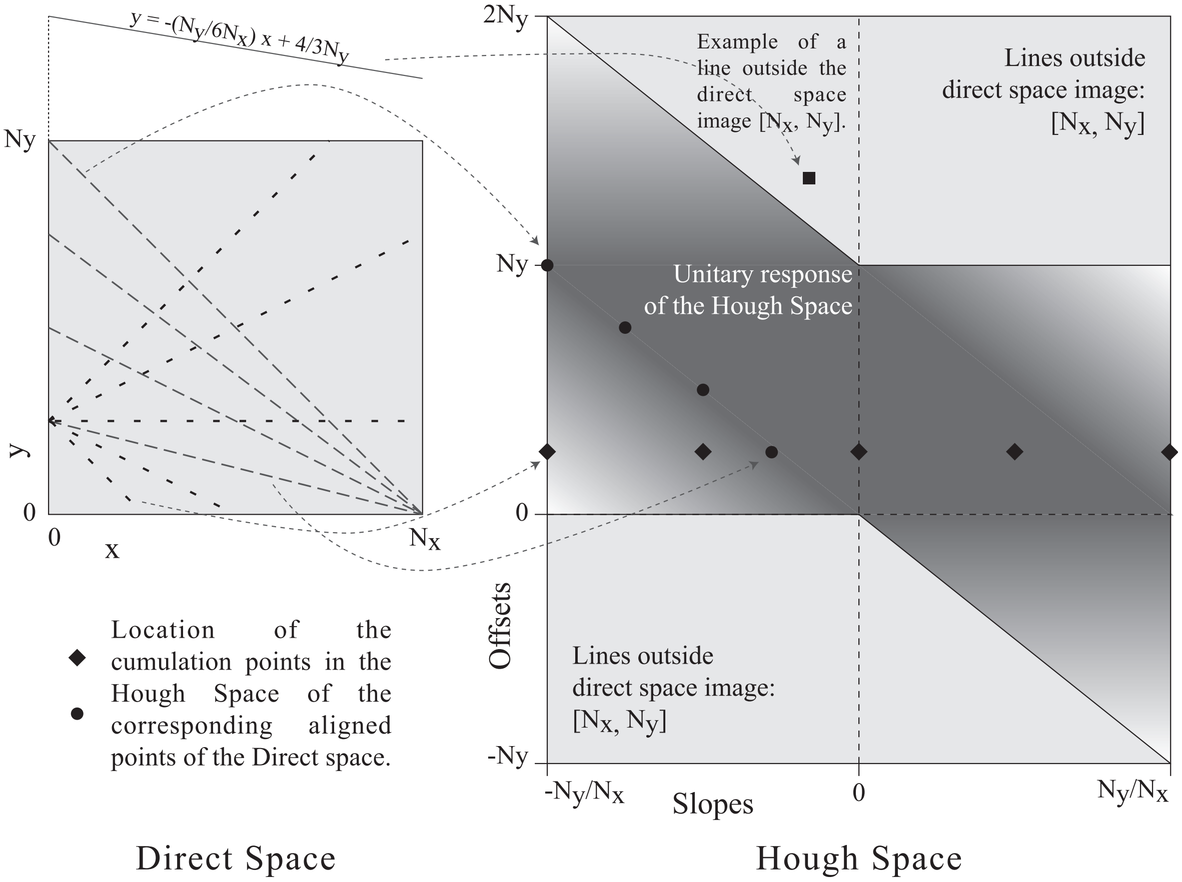

Figure 4.43: Boundaries of the Hough space used to detect lines of small slope $|s| < N_y/N_x$. The Hough space boundaries shape comes from the rectangular boundaries of the direct space where lines are plotted.

The figure 4.43 represents graphically the Hough space boundaries defined in equation 4.8 for slope $s < \left|\frac{N_y}{N_x}\right|$. The intensity represents the unitary answer of the Hough Transform (negative intensity scale). It corresponds to the Hough transform of all catalogued pixels within the image of size $[N_x, N_y]$. The unitary response shows the boundaries of the Hough space.

Only small slopes are considered, in order to detect lines of high slopes: $|s| > N_y/N_x$, the input catalogue is flipped. The converted coordinates are defined by: $x'_i = y_i$ and $y'_i = x_i$. A line flipped is now defined by: $s' = \frac{1}{s}$ and $o' = \frac{o}{s}$. The large slopes are inverted in the flipped catalogue. The detection of condensation points in the Hough space is done with similar boundaries as before in order to detect lines of small slopes of the input flipped catalogue. The detection of aligned points in the Hough space is done in 2 steps, from the catalogue and a flipped version of the catalogue.

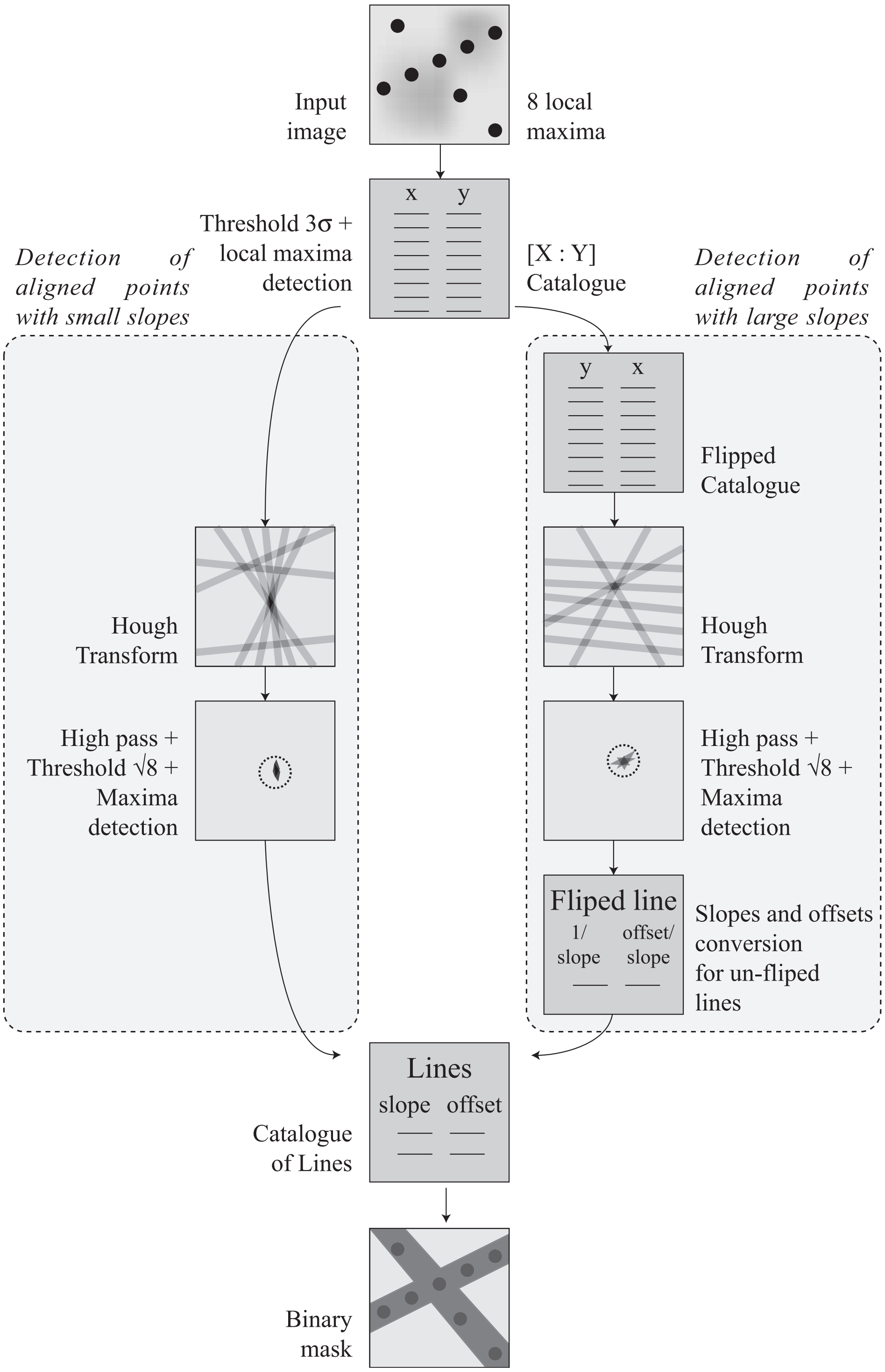

Figure 4.44: Schematic illustration of the procedure defined to detect and mask satellite tracks using the Hough transform. The Hough transform is applied two times: first on the catalogue of local maxima, and then to the flipped version of the catalogue. This second analysis, is made to detect tracks of large slopes.

4.8.3 Procedure description

The aligned points in the direct space, are detected by condensation points in the Hough space. To quantify the detections of the cumulation points, one needs to establish the probability density of random points transformed in the Hough space to establish a proper threshold.

The problem is to define the probability to have p aligned points within N random points. Another problem is also the notion of alignment. In fact the local maxima of a track are never strictly aligned due to noise of the observed positions. The quality of the alignment is perceptible by the sharpness of the cumulation point. Local maxima from satellite track observations are quasi perfectly aligned, and provide sharp cumulation points (quasi punctual). In order to focus on quasi aligned points, the Hough Transform is filtered by a high pass filter to keep only the very high frequencies. The diluted cumulation points are suppressed, and only the sharp ones are highlighted. Another advantage of the high-pass filtering is to remove the constant answer of the Hough space.

Empirically, one defines the probability of aligned point as a function of $\sqrt{N}$. This assumption assumes the random points to be spread within a square image. The threshold to detect the cumulation points are set to $k\sqrt{N}$ with k is a sensitivity factor. In practice faint tracks are detected with $k = 1$ and with no fake detection. One can select $k = 0.5$ with the risk of detecting also the blooming around the very bright stars. The procedure works this way:

1. Catalogue extraction from the input image of size $[N_x, N_y]$.

   (a) To improve the S/N of astronomical sources, the input image is smoothed by the typical value of the seeing (modeled by a Gaussian function of sigma set to 1 pixel),

   (b) The statistic of the image are computed to get the mean background μ and the noise amplitude σ.

   (c) The image is thresholded to a significant level: typically $\mu + 3\sigma$.

   (d) A catalogue of local maxima is extracted. A local maxima is a pixel with a value greater than its 8 neighbors. The catalogue registers the pixel location of the N local maxima.

2. Hough Transform and cumulation points detection for lines of large slopes.

   (a) The catalogue is projected on the Hough space. The boundaries are defined for small slopes $s < \frac{N_y}{N_x}$. The size of the Hough space is chosen with the same size as the input image. Between the true Hough space coordinate and the image representing the Hough space, one defines a scale factor to convert pixel coordinates in Hough space coordinates.

   (b) The Hough Transform is filtered with a high pass filter. Typically a convolution with the mask: $\begin{bmatrix} -1 & -1 & -1 \\ -1 & 9 & -1 \\ -1 & -1 & -1 \end{bmatrix}$. Its effect corresponds roughly to an image subtracted by its smoothed version by a sharp Gaussian.

   (c) The filtered image is thresholded to $k\sqrt{N}$ typically with $k = 1$.

(d) The local maxima are extracted within the thresholded image. Their location are converted in the Hough space, and gives the slope and offset of aligned points. One also gets an indication of the number of aligned points by the value of the cumulation point.

3. Hough Transform and cumulation point detection for lines of large slopes.

   (a) The extracted catalogue is flipped (x are replaced by y values and vice versa).

   (b) The flipped catalogue is analyzed through step 2.

   (c) The observed lines characterized by a slope s' and an offset o' are converted to the original un-flipped catalogue, with $s = \frac{1}{s'}$ and $o = \frac{o'}{s'}$. If s' is equal to 0.0, it corresponds to a vertical line of image coordinates: $x = o'$.

4. Mask creation from the detected lines

The procedure is applied to a portion of a WFI image (see figure 4.47). The input image is 2000x2000 pixels. The local significant maxima are extracted. The catalogue of 1359 extracted sources are showed on figure 4.45. The zoom of the catalogue shows the density of local maxima along the satellite track. Around the bright star, (bottom left) lots of local maxima are detected. The procedure can be improved by smoothing the input image with a Gaussian filter larger than the seeing (see procedure steps 4.8.3), then less points appears, but this means also less point for the satellite track.

Figure 4.46 shows the Hough transform done to detect the track of large slope. The condensation point appear very sharp. The result of the high-pass filter applying on the Hough transform is shown on the right panel of figure 4.46. The cumulation points are detected by a threshold done at 37 corresponding to the square root of the number of extracted sources. The intensity of the detected cumulation point is equal to 142. This number corresponds to the number of local maxima detected along the track.

The cumulation point gives the coordinate of the line. The coordinate of the line are transformed to correspond to the line of the original catalogue, instead of the flipped version. Figure 4.47 shows the original image with a dashed line showing the line issued from the computation. The detected line and the real track correspond very precisely.

The procedure is very robust with a very safe detection (no fake track detection). The speed of the procedure can be increased by under-sampling the input image by a factor of 2. The computation is 4 time faster without decreasing its sensitivity.

4.8.4 Limitations of the Method

The sensitivity of the procedure is limited by the density of astronomical objects. For instance a track observed in a dense stellar field is difficult to detect compared to a similar track observed in a deep field. In practice, the faint tracks are detected and masked efficiently except for quite dense stellar field. To improve the sensitivity of the procedure one can lower the threshold value, lots of tracks will be detected with higher probability for fake detection. Note that blooming of bright stars can be detected as tracks as well. Two constraints can be added to reject the fake detections:

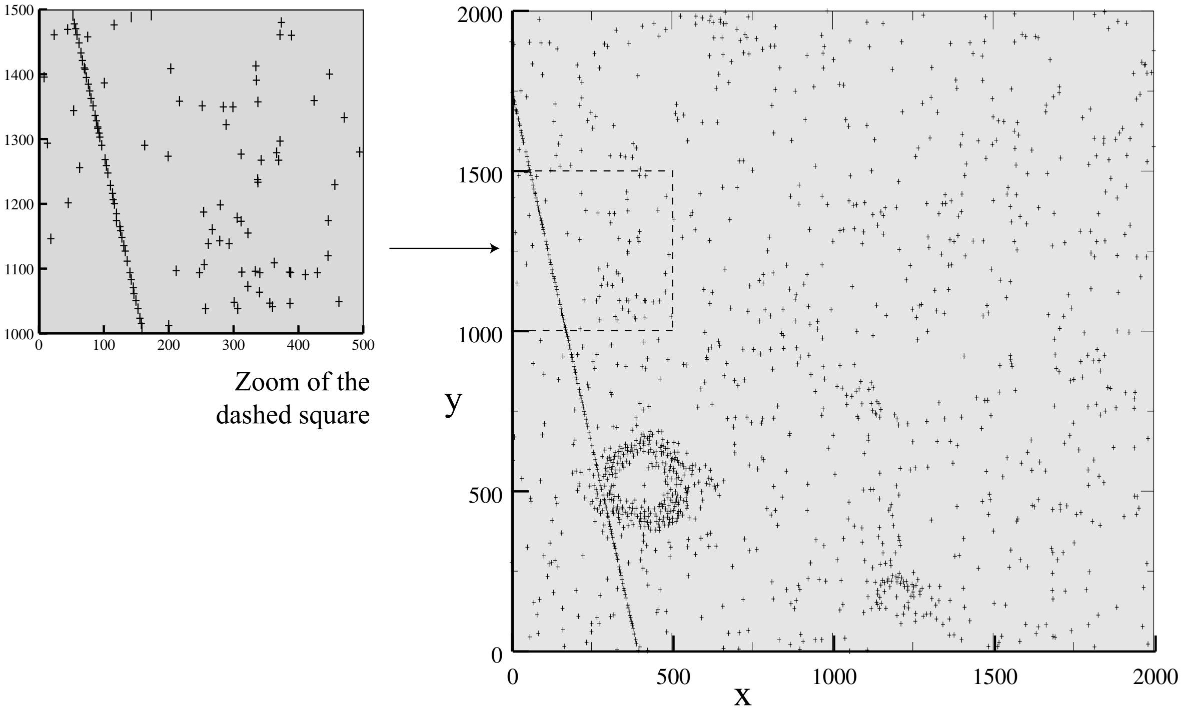

Figure 4.45: Catalogue of extracted significant local maxima. The small left panel shows a zoom of the dashed square visible on the main graph. Note the density of points along the satellite track. The bright star in the main graph (bottom left) provides lots of local maxima.

- The blooming of bright stars can be detected. Fortunately, a typical blooming provides few local maxima, and the actual procedure is quite insensitive to large blooming. Nevertheless, if the threshold is lowered, the risk of detecting blooming star is higher. The idea is then to compare the detected tracks observed from a group of images observed at the same position in the sky. If the blooming is detected in all images, then all corresponding tracks are detected at the same sky position. All multiple similar detections from a group of two or more images can be rejected.

- When a track is detected, one can test locally the presence of the track by executing the procedure on a smaller portion of the image around the expected location of the detection. Several smaller portions are defined and the procedure is iterated for all defined portions. The signal to noise of a track within a portion is higher in the Hough space, because the density of random points decreases with the area of the portion, whereas the density of aligned points from the track decreases with the length of the selected portion. A fake track will not be detected in smaller portions, whereas true tracks will be better detected.

The track detection by portions can be systematized by applying the procedure in each cell of a matrix used to split the original image. This approach is equivalent to a curvelet analysis, where the Radon transform (similar of the Hough transform) is executed on cells of different sizes. The curvelet transform is certainly more sensitive but the great advantage of the Hough

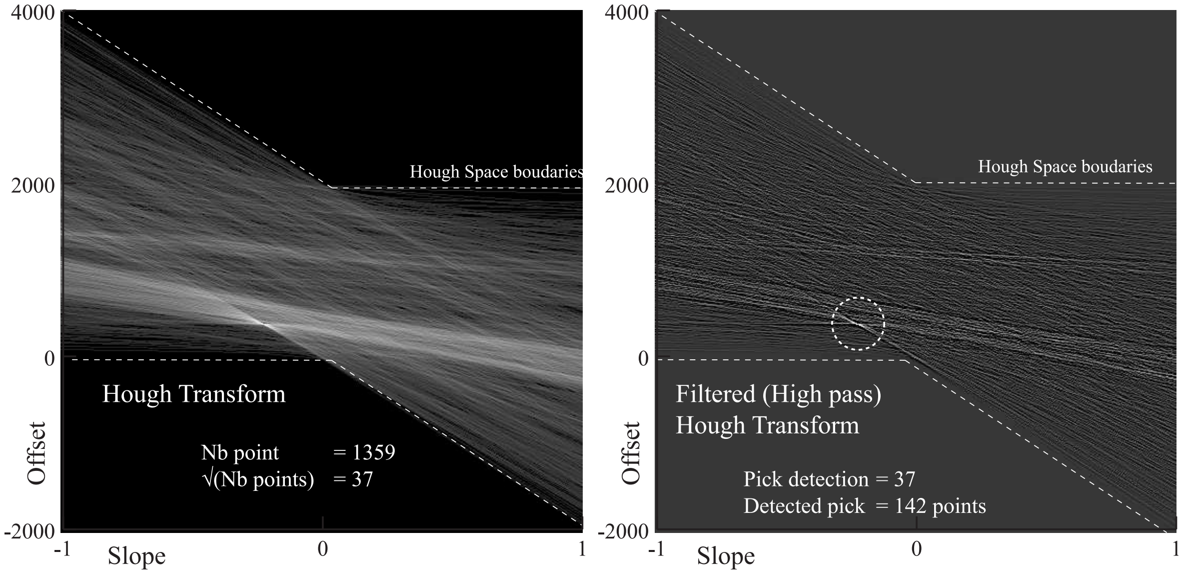

Figure 4.46: Hough Transform of the extracted sources. The transformation is applied on the flipped catalogue (shown at figure 4.45) to detect tracks of large slopes. LEFT: Hough Transform of the flipped catalogue. RIGHT: High pass filter applied on the Hough transform in order to remove the constant response of the Hough space. The cumulation point is surrounded by the dashed circle. Note also the Hough space boundaries represented by dashed lines.

transform is to focus only on aligned structures with very fast computation.

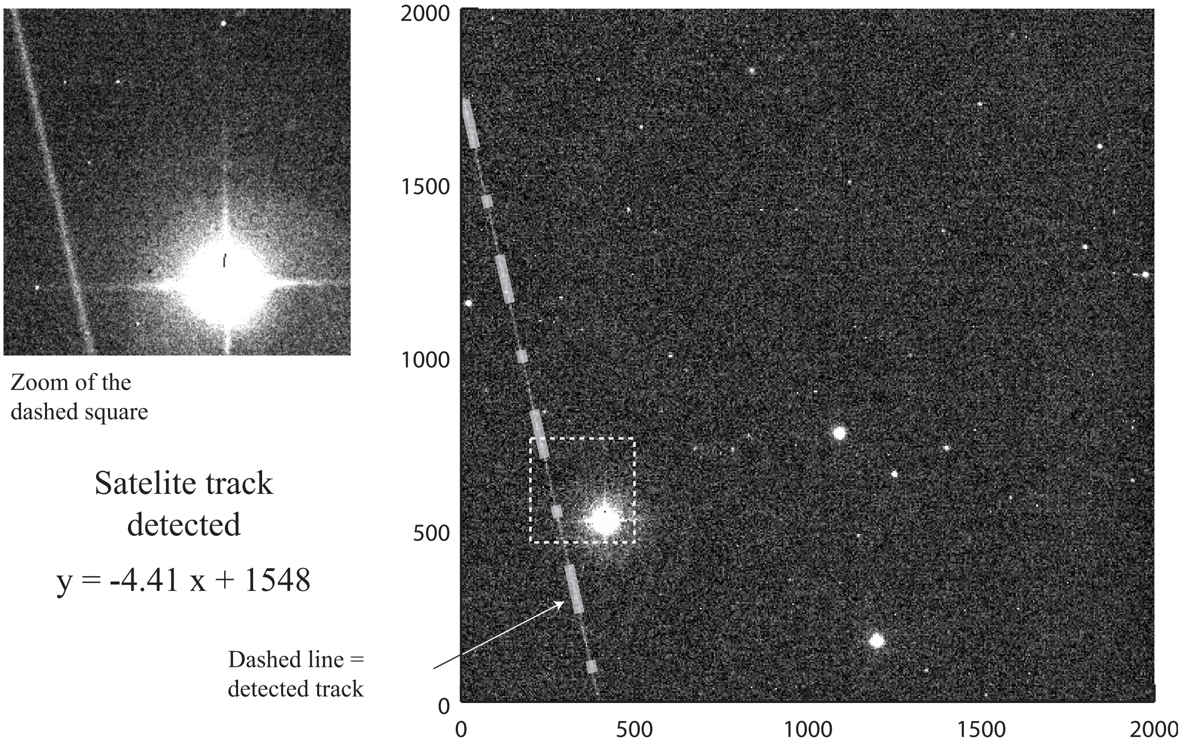

Figure 4.47: Detected track compared to the image. The right panel shows a zoom version of the dashed square. The detected track is represented by the semi transparent dashed line. The detected line is exactly on top of the real observation.

Chapter 5

Applications

This chapter describes the reduction of large surveys handled by the EIS team, and reduced by the EIS/MVM pipeline. The surveys consist in a variety of targets observed since 1997 which includes infrared data from SOFI, ISAAC, and the WFI imager. In the process over 2400 SOFI, 7200 ISAAC and 2400 WFI images covering the entire wavelength range have been processed, examined and used to optimize the algorithms implemented. While a first version of the pipeline was used as early as 2000, considerable improvements have been made over the past 4 years.

This chapter presents the reductions carried in a stand-alone mode, and then feed to the EIS survey system in order to photometrically calibrate the images, and to release the reduced products. The results for the following surveys are presented: EIS-DEEP, and DPS-IR as examples of SOFI reductions; GOODS data to illustrate the results obtained with ISAAC; Pre-FLAMES, DPS optical and XMM to illustrate the results obtained for WFI images under a variety of conditions and employing different techniques.

Each survey strategy presents a new challenge and requires a proper investigation. It is also worth mentioning that during the phase of investigation extensive use has been made of the ESO Science Archive searching for additional test data, as will be briefly presented below.

5.1 Multi-color survey of the Chandra Deep Field South

The first survey reduced by the new pipeline, and released in February 2001, was the Deep Public Survey of the Chandra Deep Field South (CDFS). This deep multi-band survey, was observed using two instruments: first, the WFI for the optical part with the broad-band filters U, B, V, R and I, and second, the SOFI for the IR part with the broad-band filters J and Ks. The field-of-view defined is 30×30 acrmin for the optical part achieved by one pointing of the WFI instrument, and 20×20 acrmin for the IR part made by a 4×4 SOFI pointings.

The challenges of this survey were multiple: First, the administration of numerous observations spread in more than two years from 1999 to 2001; Second, the astrometric calibration of the U-band images which have a poor S/N; third, the estimation of the fringes of the I-band images, and the IR observations.

Together with the February 2001 release of the IR final products, a paper has been submitted, this article is presented in appendix A. Unfortunately, several weeks latter, a bias in the photometry of faint sources extracted from the reduced images has been reported. Despite of all the efforts to develop an unbias sky estimator (as explained in section 4.5), the data were reduced as if the pixel-based background estimation was computed with in one step leading to a photometric bias. After a debugging phase, an administration error was found: the option responsible for the creation of the mask for the unbias sky estimator, was not initialized by the value indicated in configuration files. Consequently, the masks were created with only very bright sources, and the faint sources were not masked. It is worth emphasizing that for this survey, the pipeline was not finished, and the administration was made by temporary Perl scripts used to encapsulate the online modules written in C++. The error was in one Perl script where an option was misspelled. Of course, this error was naturally corrected in the next development phase because of the homogeneous C++ integration (has explained in section 2.3). This bad experience was a strong argument for an homogeneous implementation in C++, to avoid errors in the encapsulation of the algorithms with a script language.

Those IR observations are now being re-reduced with the last version of the image pipeline. The final products will be released at the end of 2004. Also, this new release includes the CDFS and also 2 other deep regions.

The optical final product of the CDFS was released in March 2001 together with a paper (Arnouts et al., 2001). This article is presented in appendix B.

5.2 GOODS: the Great Observatories Origins Deep Survey

In the tradition of the Hubble Deep Fields (HDF-N and HDF-S), the Great Observatories Origins Deep Survey (GOODS) is designed to push the performance of major modern observational facilities to their sensitivity limits. GOODS unites the deepest observations from ground- and space-based facilities at many wavelengths, and was selected in late 2000 as one of six Legacy programs for the Space Infrared Telescope Facility (SPITZER: the fourth of NASA's Great Observatories after Hubble, Chandra and Compton). The Legacy program is meant to maximize the scientific utility of SPITZER by yielding an early and long-lasting scientific heritage, and to produce data that will enter the public domain immediately. Under the leader ship of Mark Dickinson at STScI, the program will map two fields with SPITZER, one Northern one Southern, exceeding a total of 300 square arcmin. GOODS will produce the deepest observations with the SPITZER IRAC instrument at 3.6-8 microns and at 24 microns with the MIPS instrument.

The essential purpose of GOODS is to provide the most sensitive census of the distant Universe, making it possible to follow the mass assembly history of galaxies and the nature and distribution of their energetic output (from both stars and black holes) over a broad span of cosmic history. With SPITZER in the mid-infrared, the rest-frame near-IR light from evolved stars (which trace the baryonic mass) can be followed to high red-shifts. The combination of mid-infrared and hard X-ray observations allows the use of their intrinsically isotropic radiation in these bands to find and identify essentially all of both the type 1 (un obscured) and type 2 AGN which fall in the GOODS files.

The two fields selected are already the most intensively studied areas of the deep extragalactic sky: HDF-N (around 12.6 hr RA and 62 deg Dec) and the southern Chandra Deep Field (CDF-S: around 3.5 hr RA and -28 deg Dec). Both areas have already been imaged with the Chandra X-ray satellite with an exposure time of one million seconds (the deepest X-raw observations ever). CDF-S has been extensively observed by ESO telescopes: fairly deep optical and near-infrared imaging (SUSI2, SOFI, WFI) has been secured as part of the EIS project and further observations are planned, while several VLT program targeting this field have been executed (FORS deep imaging and ISAAC deep imaging).

ESO is providing a lot of ground-based images from optic to IR wavelength. Table 5.1 gives the telescope and instrument used to observe the CDF-S field.

The ISAAC field-of-view of 2.5×2.5 acrmin, is much smaller than the ongoing observation of the GOODS field scaled on the SPITZER used as reference. To cover the SPITZER observations, a mosaic of 32 ISAAC tiles have observed, they cover an area of 20×20 arcmin. Figure 5.1 shows the layout of the ISSAC mosaic and also the mosaic of other instruments contributing to the GOODS survey.

The observations have been carried out by 4 different observation programs spread from year 2000 to 2003. The 3 first proposals are private observations done with the J and K filter at the center of the CDF-S field (field $F10$, $F11$, $F15$ and, $F16$). The first proposal is centered on $F10$, then the second proposal completes observations with the pointing $F11$. The third proposal enlarges the first ones with the new pointings $F15$ and $F16$. Nevertheless, the large proposal 168.A-0485 contains most of the observations, and the complete observations made with the filter H.

Instrument	Filter	Integration time	FOV total	$5\sigma MV_{ab}$
WFI@2.2	U	24h	30' × 30'	26
"	B	10h	"	26.4
"	V	8h	"	25.4
"	R	12h	"	25.5
"	I	16h	"	24.7
SOFI@NTT	J	20h	20' × 20'	23.4
"	Ks	20h	"	22.6
FORS1@VLT	R	15h	15' × 15'	27.9
"	I	15h	"	26
ISAAC@VLT	J	100h	15' × 15'	25.4
"	H	80h	"	24.8
"	Ks	150h	"	24.4

Table 5.1: ESO observations of the CDF-S. Per instrument and Filter the main characteristic of the observation is given. The field of view (FOV) gives the size of the merged observations. An estimation of the limiting magnitude in AB scale is given for a 5σdetection. The integration time give the total time planned per filter.

The observations are spread over 4 periods from October 1999 to March 2003. The images are taken in service-mode, and therefore they have been observed, in a "random" sequence of nights.

5.2.1 Reduction strategy

Master calibrations computation

The IR detector should be calibrated with a bias, a dark and a flat. In IR the bias is not a stable constant, but a signal which depends on the mean value of the image. Therefore, the bias is a function of the observations (as details in section 3.3.1). The bias level is more important for flat observations because the mean flux is high. Figure 5.2 details the different sources of electrons within a pixel.

For a proper calibration, one should remove the unstable IR bias before dividing an image by a flat. At the NTT telescope, where the SOFI detector is installed, a special procedure is executed to compute the bias level of the flat-dome observations.

As the bias is a function of the illumination it must be computed while the detector point to the sky. The proposed solution is to mask a small part of the detector where the bias can be computed (as illustrated in figure 5.3). The mask must be small enough to be negligible in comparison with the illuminated area, and must be large enough (50 pixels for instance) to have a significant statistic of the bias. Note that the bias is computed on images subtracted with a corresponding master dark calibration.

This strategy allows to compute master flat calibrations which provide scientific images of better quality. Unfortunately, this special procedure is not used with the ISAAC instrument.

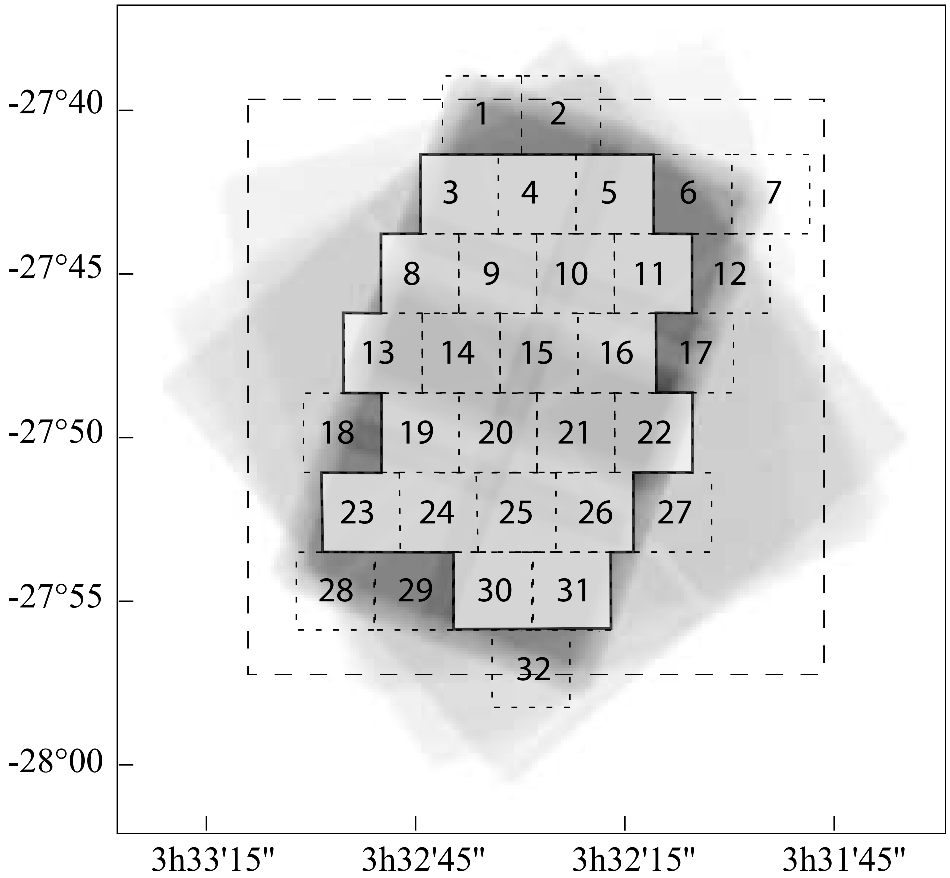

Figure 5.1: Layout of the ISAAC GOODS observations. The Field of view is fully contained in half a degree size corresponding to the coverage of the WFI instrument (solid line rectangle). The SOFI/GOODS observations are indicated in dashed line. 32 different pointing are defined for the ISAAC/GOODS observations. Only the centered one (surrounded by a large solid line have been observed and released. The background image of this chart, indicates the exposure map of the SPITZER field (mapped by the ISAAC/GOODS pointing), and the exposure map of the Chandra observations of the GOODS field.

The ISAAC/GOODS observations have been reduced with the classical flat-sky. The bias is therefore not estimated, and one expects the ZP to have larger noise amplitude.

The master calibrations (flat and dark) are observed from time to time at the beginning or end of the observation night. The electronic of the near IR detector is quite stable, therefore to produced a master flat, the raw sky flats can be merged within a large time scale. A study made by the NTT team dealing with the SOFI IR instrument, shows a 2% stability with a master flat calibration used during a year (NTT Team, 1997). For the ISAAC, there were enough flat observations, and they were grouped within 14 nights. A statistical test to get the mean background value is performed on each image of each group to remove raw flat observations with too low or too high counts (respectively 7000 and 26000 ADU). The darks are observed every night and are grouped by exposure time every 4 days. The time grouping constraint defined for flat and dark observations ensures that the scientific images

Proposal	#Pt	Filter	#img/OB	#OB	T/img	#img/pt	T/pt	#img	tot T
168.A-0485	28	J	30	5	120s	150	5h	4200	140h
	32	H	30	5	120s	150	5h	4800	160h
	28	K	40	6	90s	240	6h	6720	168h
68.A-0544	2	J	20	4	180s	80	4h	160	8h
	2	K	25	10	100s	250	7h	500	14h
66.A-0572	1	J	20	4	180s	40	4h	80	4h
	1	K	15	10	100s	250	7h	150	7h
64.O-0643	1	J	20	4	180s	40	4h	80	4h
	1	K	25	10	100s	250	7h	15	7h

Table 5.2: Observation history of the ISAAC/GOODS field as a function of the 4 proposals. The first one lists is the Large Program that contains most of the observations. The 3 other proposal are private observations made public for the GOODS project.

are processed with master calibrations obtained less than 7 nights for the flat, and 2 nights for the dark.

Grouping of scientific images

One RB contains typically 1 or 2 hours of continuous observations of the same pointing with the same filter. The RB are computed to be as identical as possible to the OBs. The observed OBs are sometimes uncompleted, due to bad weather, or the beginning of the twilight. The RBs are created with the rules described in section 3.3.2. The maximum integration time of a RB is set to 1h40', and the minimum number of images is set to 10.

Figure 5.4 shows the typical number of images per created RB. In practice 75% of the RBs have the same number of images than the constructed OBs. Four categories of RBs can be distinguished:

- RBs equal to OBs: The main peaks of the histogram correspond to the prepared OBs: 40 images in Ks 30 images in J and H for the last larger proposal, 25 images in Ks 16 images in J for the 3 first proposals (cf. table 5.2).
- Very small RBs: where the number of images per RB is less than 15. In most cases, the observations were stopped because of very bad weather conditions (mainly clouds). Those RBs are discarded because they are difficult to reduce (the two-pass background estimation may produce a large number holes on the reduced images as highlighted in section 4.5), and the images are observed with poor sky transparency.
- Partially completed RBs: These RBs are close to completion (36 images instead of 40 for instance). The observations are not completed because of the beginning of the twilight, or the weather conditions changing suddenly.
- Larger RBs: These RBs contain more images than the created OBs. They correspond to larger observations to complete partially observed OBs of previous nights.

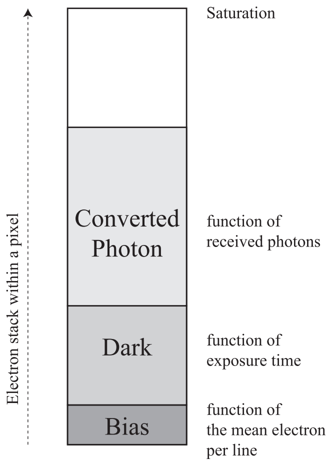

Figure 5.2: Stacked electrons within a pixel of an IR detector. The bias level is a function of the mean number of electrons cumulated per line of the detector. The dark is function of the exposure time. Finally, the received photons are function the observed sky and astronomical objects.

The tow main criteria used to create the RBs prove to be efficient to create optimum RBs following the OB strategy when possible. Note, that the computations has no prior knowledge of the defined OBs. Only the sky position, filter, and exposure-time are used. The airmass and seeing criteria are used in later stages.

Filtering of bad quality images within an RB

Within RBs some images must be rejected depending of their image quality relative to the others. In the pipeline the noise amplitude is the criteria used to reject bad images before the stacking (as described for the module (4) of the RM in section 3.3.2).

The noise amplitude of the images is evaluated after the modules (1) instrumental effect removal is achieved, and just after the fringe pattern estimation one-pass is executed. At this level of reduction, the images need to be stacked to estimate a mask for the second pass of the fringe pattern estimation. Before computing the relative astrometry and stacking the cube of observations, the noise amplitude is computed with a standard sigma clipping applied on each image of the RB. The noise amplitude, at this step of processing, depends on the internal noise of the image and the noise of the residual fringes. Indeed the fringe pattern is estimated per sub-block of the RB (typically every 15 images) and the fringe pattern used for a certain image is a weighted combination of the fringe pattern estimated for the previous and next sub-block. For instance, in a case of a cube of 60 images where the fringe patterns $F_{[15k,15(k+1)]}$ are estimated every 15 images, the fringe pattern used for image number 25 will be equal to $\frac{(5*F_{[0,15]}+10*F_{[15,30]})}{15}$). The residual of fringes is sometimes greater for image indexes close to: $15k$ (using the previous settings). Some images will be rejected if their noise amplitude is too high in comparison to the other ones.

In practice this criteria is useful when the sky is unstable and the fringe pattern is evolving in amplitude, and the estimation of the pixel-based background can be bad. Therefore some

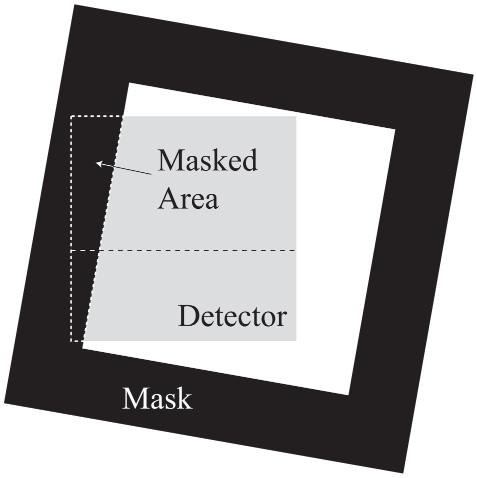

Figure 5.3: Rotated mask used to mask the beginning of each line of the detector (dashed horizontal line for instance). The rest is illuminated normally. The bias, which depends on the flux received per line, is computed on the masked area where the value of the pixels are equal to the bias.

images of the RB have lots of fringe residuals. They are detected by their high amplitude of the noise. Figure 5.5 illustrates the noise amplitude of each image of an RB observed in H passband. The evolution of the noise amplitude of the processed images is a sign of a variation of the sky quality (the transparency is not constant: the night is not photometric). The noise amplitude of the background subtracted images is quite stable around 24 ADU. The noise criteria selection is set to the median of the noise amplitude plus 5 times the median of the absolute variation around the median. With this criteria, the last 5 images are rejected because their noise amplitude is greater than 30 ADU (24+1.2*5).

astrometric references

The absolute astrometric solution is computed after stacking the RB. A relative astrometric solution is computed for each image and then, they are warped and stacked to produce a stacked RB. The absolute astrometric solution is applied on the resulting image. The ISAAC field-of-view (2.5×2.5 arcmin) is small, therefore, the astrometric solution must be computed using a dense catalogue to have a significant associations between the catalogued and extracted sources. The common astrometric catalogues (USNO or GSC2.2) are too sparse, especially for high galactic latitudes and cannot be used, only couple of stars are observed per field-of-view. Also note that in this field, few stars are visible and the astrometric reference catalogue must include galaxies. A dense astrometrically calibrated catalogue is needed. The catalogue used was extracted from WFI reduced images of the same field. The GOODS surveys is achieved by numerous instruments, the WFI is the larger one used (30×30 arcmin). To get an astrometric catalogue, a collection of 10 WFI images observed in R passband have been processed and astrometrically calibrated using the USNO catalogue. The reduced image has been extracted with the Sextractor software, and the sources brighter than 24.2 are used as references for the astrometric calibration of the ISAAC/GOODS stacked RBs. This very dense catalogue

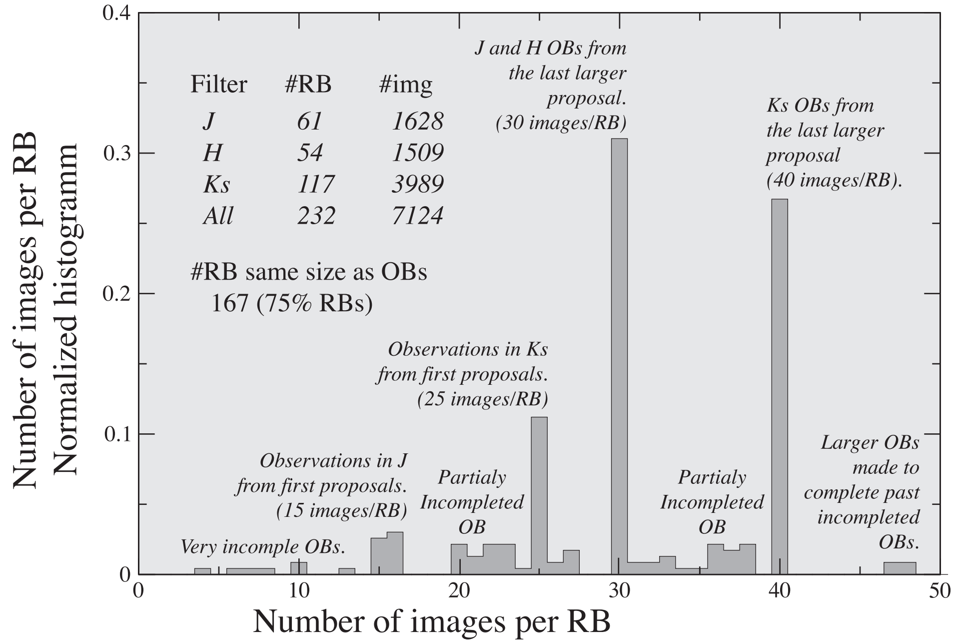

Figure 5.4: ISAAC/GOODS: number of images per created RB from the full set of observations.

contains 25560 sources including 4000 stars (see (Arnouts et al., 2001) for more details).

The astrometric calibrations of the reduced ISAAC RBs is made with at least 40 associations per field-of-vew. The distortion model applies on the ISAAC reduced RB is a first order polynomial function. This model is enough as the ISAAC field-of-view is very small, and the higher orders are assumed negligible. Note that an ultimate astrometric solution, could be a combination of a first order computed from the data, and higher orders computed from dedicated observations (as for instance dithering observations of a globular clusters). The astrometric accuracy of the final J and Ks mosaic containing all the fields, has been compared to reduced images of the recent ACS camera mounted on the Hubble Space Telescope (HST). The comparison shows a RMS smaller than 0.1 arcsec, and with no trend throughout the full mosaic. Note that images of the ACS camera are very well calibrated as they come from a space telescope. This test proves that a catalogue extracted from optical detectors can be used with confidence to astrometrically calibrate IR images, and, the optical and IR centroids are the same.

The images are warped according to an unique defined projection. such as all the stacked RBs share the same astrometric reference grid. The reduced images are then easy to combine. The selected projection is characterized by:

- Position. The center of the projection is set in the middle of the observations (53.1 deg, -28.1deg).
- Pixel size and orientation. The images are warped at the same sample as the original ones (0.15 arcsec per pixel) and the orientation is chosen to have North Up and East Right on the warped images

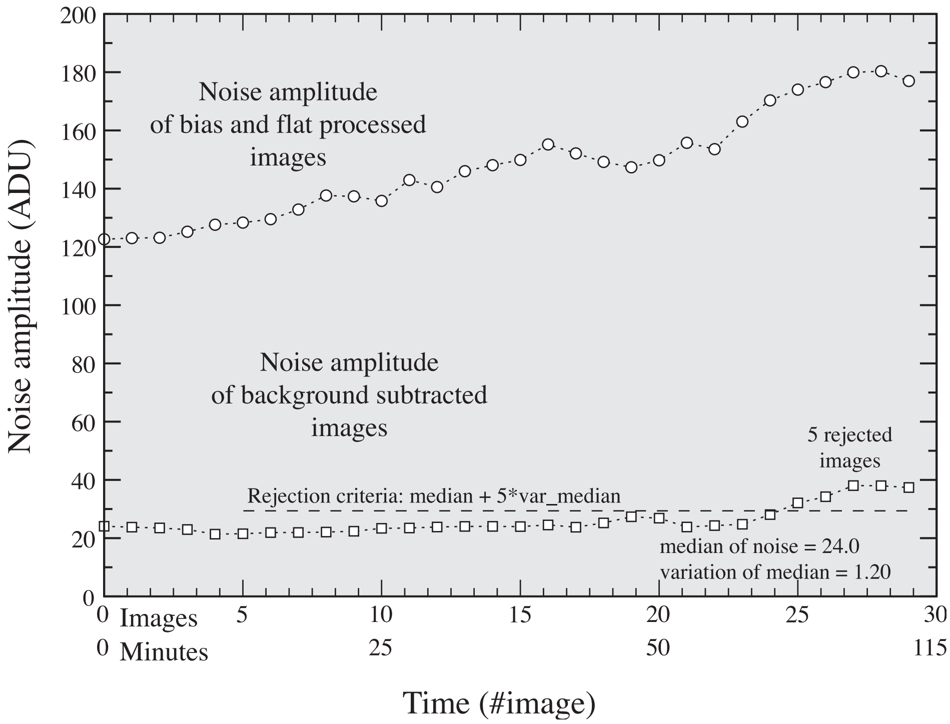

Figure 5.5: Noise amplitude criteria selection to reject images.

- Projection mode. The Tangential mode is chosen because the total field of view is small and compact.

Final product creation

The RBs are reduced exclusively with the *deep* RM defined for the ISAAC instrument (as detailed in table 3.8). With this RM, the pixel-based background is estimated within each RB. An human inspection of the reduced RBs has been done in order to reject images that show important remaining fringes or complex background shapes. 10% of the reduced RBs have been rejected, especially for filter H, and Ks.

For each reduced RB, the absolute ZP is computed using the extracted catalogues of the reduced images versus the catalogues extracted from the SOFI/CDFS survey that has been photometrically calibrated. The photometric calibration of the ISAAC/GOODS takes advantage of the calibration achieved with the SOFI/CDFS survey reduced two years before as described in section 5.1.

The reduced RBs are then grouped into SBs. The SBs are typically made of 6 reduced RBs for the Ks filter, and 5 reduced RBs for the filter H and J. The SBs are stacked taking in consideration the absolute ZP of the reduced RBs. The final products are built with an absolute ZP of 26.0 mag (in the Vega system). Only the filter J and Ks have been photometrically calibrated because no H observations have been made with the SOFI/CCDFS survey. The stacks are multiplied by their corresponding fluxscale, and have been released in May 2004.

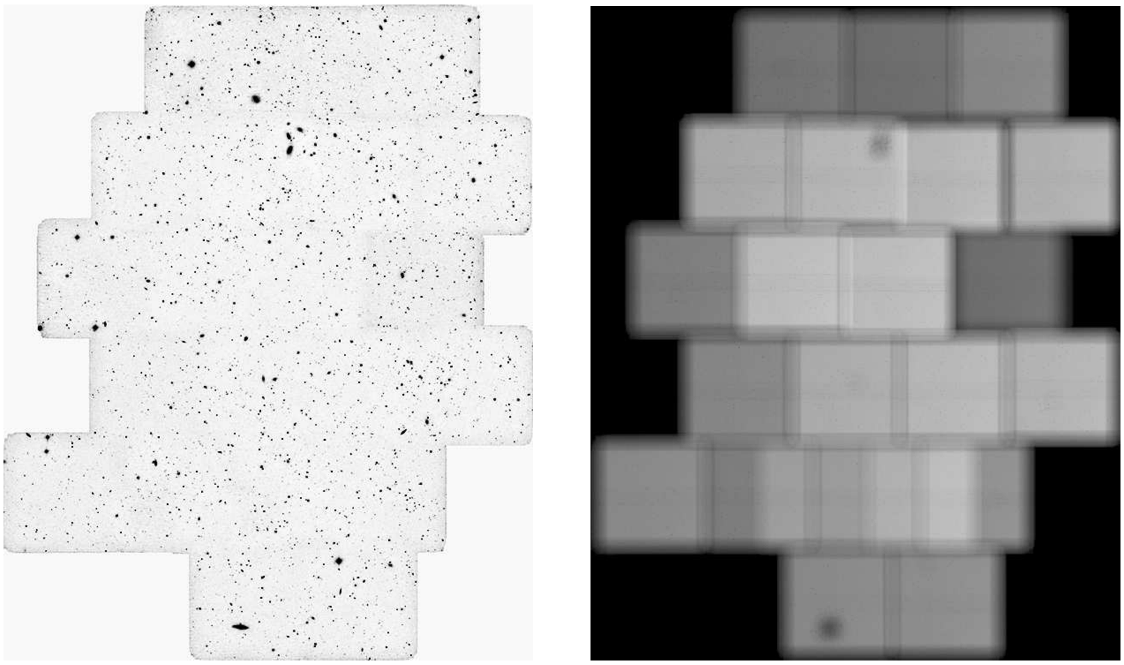

Figure 5.6: Left panel: Final mosaic of the ISAAC/GOODS field for filter Ks (negative intensity scale). Right panel: Corresponding weight map. The weight-map give an indication of a relative exposure time, and is used to define a proper threshold of constant signal to noise on the final mosaic. The two holes (top and bottom) visible on the weight-map are the signature of the two step fringing estimation when astronomical objects are as large as the dithering pattern of observation. One notices at the same location on the image the extended galaxies making the sky estimation problematic.

Also appended to the release are the mosaics made by merging of all reduced SBs sharing the same filter. The J and Ks final mosaics are large images combining more than 240 hours of observations in total. Figure 5.6 shows the mosaic observed with filter Ks and its corresponding weight-map.

5.2.2 Impact of the cross-talk effect removal on the photometry

The cross-talk effect is affecting the ISAAC observations (see section 3.1 for details about this effect, and section 3.3.2 for the dedicated module (C) implemented to remove it).

To benchmark the impact on the photometry of the cross-talk effect removal, 2 distinct reductions of the same SB are compared. The field $F11$ observed with filter Ks shows strong cross-talk effects due to 3 bright stars. The first reduction was made in 2001 and no cross-talk effect was implemented at this time, the second reduction was made for the Mars 2004 release, with the newly implemented module. Figure 5.7 shows the 2 reduced images of the 2 releases. One can notice the mirror effect of the cross-talk from the upper and lower quadrants. The photometric comparison of the two extracted catalogues is shown in figure 5.8. The dark line is computed by a running median of the points. No trend is observed, and therefore on concludes that the module does not impact on the photometry of reduced images.

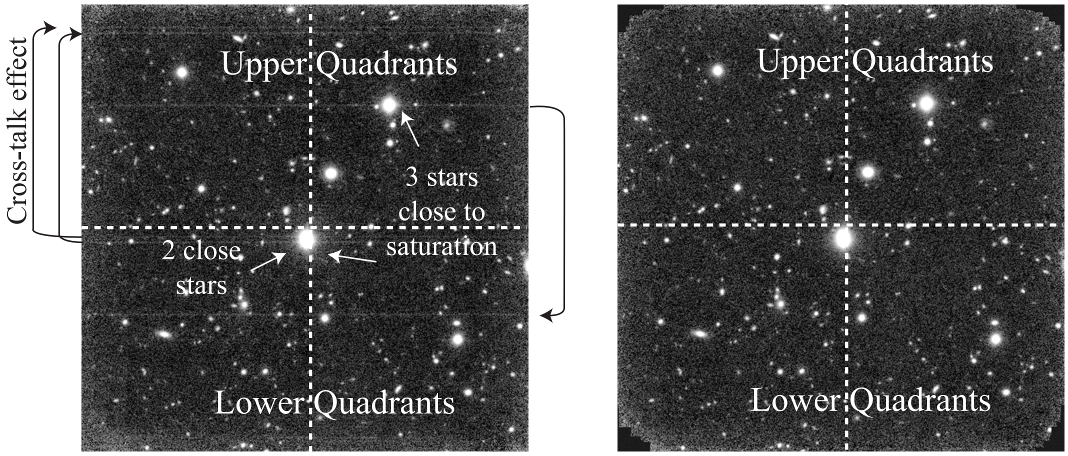

Figure 5.7: Cross-talk effect impact on reduced images versus clean reduced images.

5.2.3 Comparison with other Authors

The two-pass approach is compared with an external reduction handled by the DIMSUM package developed with IRAF. The pointing used is $F11$ the heart of the ISAAC/GOODS field observed observed with the Ks filter. The SB consists in 305 images of 100 seconds each (spread in 10 sub-integrations of 10 seconds). The data are organized into 6 RBs. The final product is computed from a SB containing the 6 reduced RBs. 286 images have been used the other ones have been rejected because of the hight amplitude of their noise.

From the final products to be compared, two catalogues are extracted and the magnitude of the sources is computed with the Sextractor MAG_APER estimator (3 arcsec). Figure 5.9 shows the magnitude differenceof the associated sources of the reduced image versus the reduction made by the DIMSUM package. A running median, characterizing the trend of the points, is also plotted. No bias appears, the two softwares give similar results, they both use a two-pass approach.

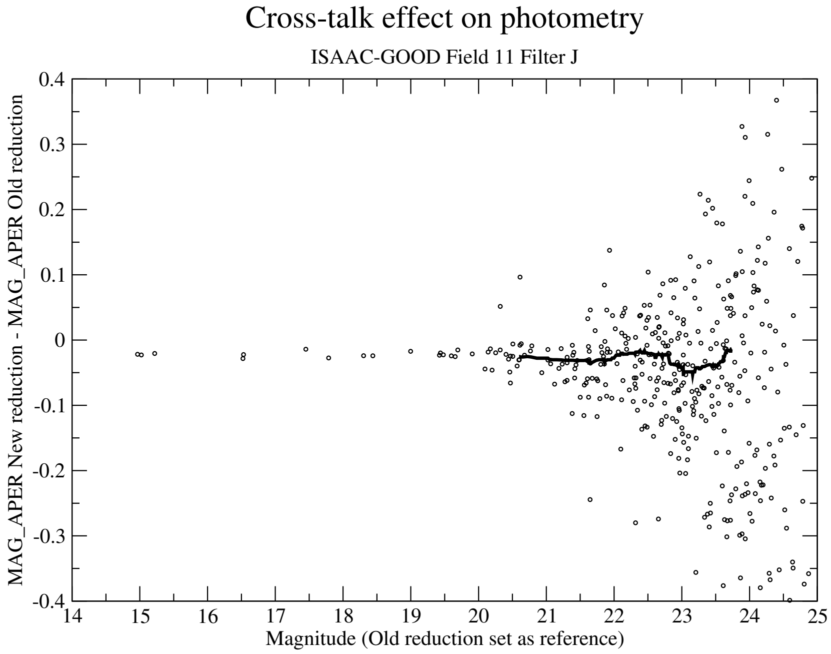

Figure 5.8: Cross talk effect removal impact on the photometry of reduced images. The two images (figure 5.7) are extracted with sextractor. The sources are associated and the aperture magnitude are compared. The comparison shows good agreement from the two distinct reduction. Note that magnitude shift from the comparison is due to the default Zero Point set to the newly reduced images not yet photometry calibrated.

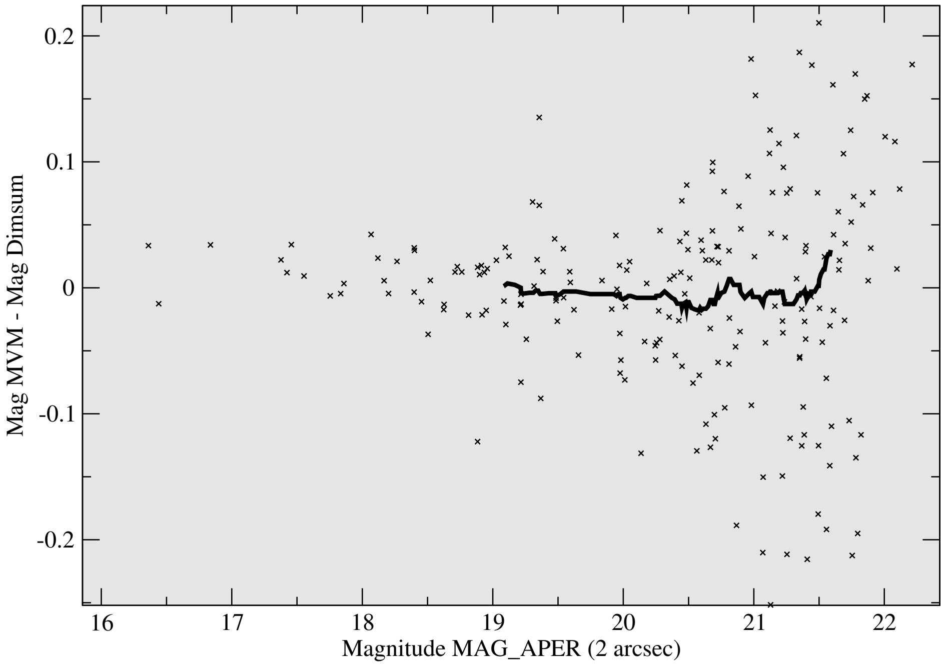

Figure 5.9: Magnitude comparison with reduction made by IRAF/DIMSUM Package. The scatter of the bright objects (brighter than 19) is quite large, this is maybe due to the different strategy to build the mask for the second-pass (DIMSUM does not use enlargement. The mask is just a 3σdetection of the stacked image). Also the aperture measurements may be perturbed because of the complex shape of the weight-map. Nevertheless, the comparison shows a good agreement between the two reductions.

5.3 The Pre-FLAMES survey

The main point of the Pre-FLAMES survey is to provide with a very good astrometric solution, images and catalogues of many galactic objects. They are dedicated for the recent spectrometer FLAMES mounted on one of the VLT telescopes. This new instrument has not imaging capability, and must be feed by very precise positions. The primary goal is to have target up to magnitude 20 with a precision of at least of 0.2 arcsec. Note that this precision is achieved by the UCAC catalogue up to the 17 magnitude. The WFI was used for this survey to benefit from its large field-of-view (half a degree).

This proposed survey is made of numerous galactic pointings to provide lots of targets spread in different area of the sky. The proposed pointings are: 32 Globular Clusters, 34 Open clusters, 18 pointings of the Milky Way close to the bulge, 7 pointings (made of 4 WFI fields each) of local groups of galaxies, 17 pointings in the Sagittarius dwarf galaxy, 34 pointings made in the Large Magellanic Cloud, and, 8 pointings made in the Small Magellanic Cloud. Each pointing is observed in 3 passbands: B, V and I. Each passband is observed with 3 images: one of short integration time set to 30 seconds, and 2 dithered images of 240 seconds each. The first image is name the shallow image and the 2 last are named the deep images. This strategy adopted is made to provide 2 catalogues, one including the bright sources, and a second for the shallower sources.

The challenges for a proper reduction are: Firstly, the astrometric catalogues of the galactic targets suffer from proper motions and lack of resolution (most binary stars are catalogued as one object). The astrometric calibration must be robust to properly reject the moving objects, and fast to deal with the large density of stars; Secondly, from the observations, the sky background cannot be estimated because some astronomical targets are as large as the sky background variations. Therefore the sky background is not estimated and kept in the reduced images; Thirdly, the subtraction of fringes are made difficult because of the extended sources, and the fringing-map must be computed from other observations.

5.3.1 Reduction strategy

Per target, 2 RBs per filter are built. One with the short exposure time, and a second one with the two long exposures. Images of different integration time are not merged because the short exposure is used to observed bright sources which are saturated with the long exposures. Note that some pointings have been added to the Pre-FLAMES survey during the observations, and few targets have been observed with the U and R filter.

The calibration images used are the bias and flat-sky observations. The validity time to build the bias RBs is chosen to 5 nights of observation, and 7 nights for the flat-sky RBs. With those criteria, sufficient valid flats images have been found, avoiding the need to use the flat-dome observations. This point is mandatory when applying the illumination-maps that have been computed from deep science images (external of this survey) reduced with flat-sky master calibrations.

The RBs are reduced with the *stellar* RM. This choice is justified by the nature of the targets made of dense stellar fields, or extended objects. The image reduction is then simple and only the instrumental effect removal, and the absolute astrometric calibration warping and stacking modules are activated.

Most of the targets are observed close to the milky way and are within dense star fields. The astrometric catalogue chosen was the GSC2.2 because it is accurate ($<$0.2 arcsec RMS accuracy) and is computed from recent observations (within 10 years). The USNO catalogue made with older observations was not selected even if its limiting magnitude is larger. One reference grid for the astrometric solution is defined for each independent pointing. Some targets are observed with a matrix of 2×2 or 2×1 WFI field-of-view (most of SMC, LMC and SG observations). For those cases, one reference grid is defined with the projection point set in the middle of the matrix. The projection mode is chosen tangential, because the final image size is small enough (less than 1 degree).

The scientific observations made in the I band suffer from fringes that cannot be estimated from the science RBs because they contain 1 or 2 images only. Instead, external fringing-maps are used to reduce the science RBs. Those are computed with the deep I-band images of the CDFS/WFI survey (see section 5.1) observed in parallel with the Pre-FLAMES targets.

The Pre-FLAMES survey is made of more than one hundred of targets spread in all the South sky hemisphere. It has been observed during 2.5 years from 2000 to Mid 2002. And three releases have been made to cover all the observations and reductions.

The first release was made in June 2001 with 6 pointings only. At the same time of the release, a paper (Momany et al., 2001) given in appendix C was submitted, and is now accepted. This article presents the astrometric results using USNO and GSC2.2 astrometric catalogues, and the main limitations of the pipeline used at that time. The two limitations were first: the warping kernel, used to warp the images, binds to the nearest neighbor, and second: the lack of the procedure used to scale an external fringing-map with the fringes observed on raw images. Therefore no I-band images were released.

A second release made of half of the targets, including the first ones, was made in Mars 2003 (see table 5.4 for a complete list of the reduced targets). For this release, three important improvements, compared to the previous released, were achieved: 1) the procedure used to compute the cross-correlation factor between the external fringing-map and the raw images was implemented (as described in section 4.6); 2) the procedure used to harmonize the relative mean gain of the 8 WFI chips (see section 4.2) was improved and comparisons with the first released images illustrate the impact (see next section 5.3.2). 3) the warping of the images was made with the Lanczos interpolation kernel offering sub-pixel warping and leading to better astrometric accuracy of the reduced images as illustrated in section 5.3.3.

The third and last ongoing release concerns the half remaining pointings. The reduced images are now illumination-corrected for all filters, with the exception of some few R passband observations. The main challenge achieved for this release was the successful computation of illumination-maps deduced from external deep observations as illustrated in section 5.3.4.

A selection of 6 reduced images is presented in figure 5.10. The illustrations are represented in inverted grayscale. They are made by stacking the 3 reduced RBs made of the long exposures. From left to right and top to bottom, the targets are: 1) NGC 2477 an open cluster; 2) Trumpler 14 an open cluster within the Eta Carina nebula. This image illustrates the impossibility to dissociate the sky background from the extended nebula. Note that on all reduced images, some white holes are visible, they correspond to the inter-chip gaps that cannot be masked with only two dithered exposures; 3) selected target within the LMC; 4) is a selected target within the SMC where the stars are incredibly dense. Note that no error

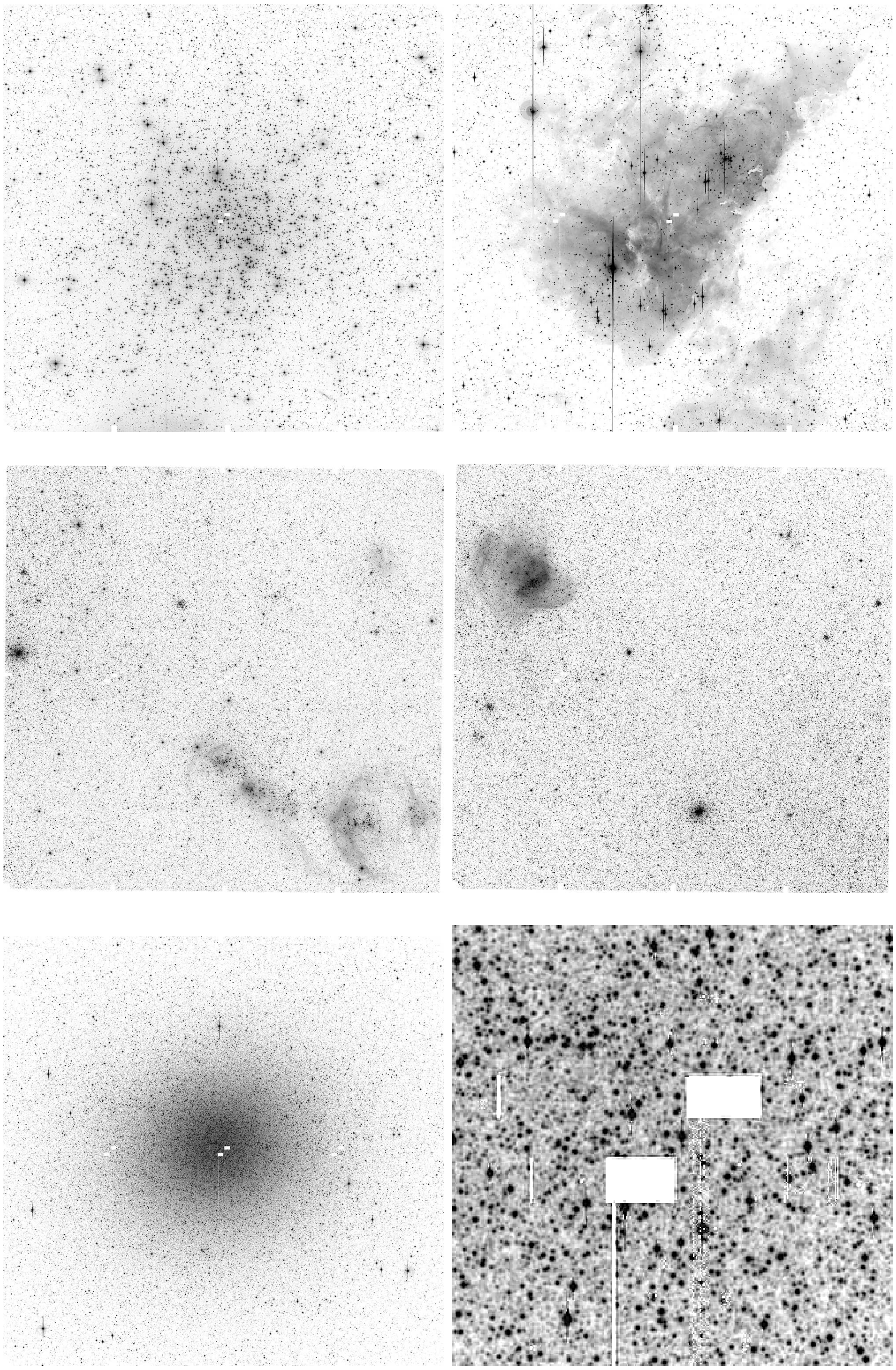

Figure 5.10: Selection of 6 reduced images of the Pre-FLAMES survey. From left to right and top to bottom, open cluster NGC2477, open cluster and nebula Trumpler 14, selected target in the LMC, selected target in the SMC, the largest globular cluster visible NGC5139, central portion of the previous image (on notices remaining gaps not filled-in by the two observations). Note that a negative intensity scale is used.

in astrometric calibration occurs even if only 3% of the 30000 GSC2.2 stars of this field was used to compute the distortion model for each raw image; 5) NGC 5139 the largest globular cluster visible. Note that the center of this globular cluster is set in the middle of the WFI camera and, consequently the heart of the target is spread in the 4 middle chips of WFI. It is worth emphasizing that the GSC2.2 catalogue does not provide sources for the heart of this globular cluster because it is too bright for the photographic plates. Therefore, no catalogue associations are possible in the border of the central chips, and the distortion model is not properly constraint; 6) central portion of the globular cluster described above. No duplication of stars are visible on the heart of the target observed on different dithered chips. The white rectangles and the white columns are pixels where no images contribute, respectively because of the dithering pattern (only 2 images per RB), and the numerous bad-columns not filled-in by the second observation of the RB (inter-chip gaps).

5.3.2 Mean gain harmonization validation

The relative mean gain harmonization procedure has evolved, the recent procedure use the background value of the 4 borders of each chips (see section 4.2 for full details). Before, the relative mean gain was deduced by using the mean background of the entire chips compared together, using a deep image has reference. The smooth sky background is evolving within a chip, and this first procedure was a little biassed.

The 2 versions of the procedure are compared with the open cluster NGC6253 filter V reduced two times for the first and second releases. The procedures are compared by analyzing the background steps from a smooth version of the two reduced images (Figure 5.11). In both case the procedures give acceptable results, the second version of the reduced image shows a maximum steps 3 times smaller than the primary reduction. The local approach to compute the relative mean gain is more robust with a peak-to-peak of 1%, which leads to a mean gain harmonization better than 1%. Note that for two first releases, the illumination correction was not applied.

5.3.3 Astrometric validations with the UCAC catalogue

The main goal of the Pre-FLAMES survey is to provide very accurate astrometric catalogues of numerous galactic pointings for the new spectroscopic instrument. The following tests evaluate the astrometric accuracy of the reduced images. They are organized in two steps. First an internal comparison shows the efficiency of the Lanczos kernel while warping the image. Second series of tests focus on the astrometric solution robustness using two different catalogues taking advantage of the recent astronomical catalogue UCAC-1 (Zacharias et al., 2000), with an accuracy of 0.1 arcsec, versus the older photographic catalogue GSC2.2 (Bucciarelli et al., 2001).

The comparisons are done with the rich open cluster NGC6253 observed 30 seconds with the filter B and V. This field is chosen to have a dense enough catalogue for UCAC-1 which has a limiting magnitude of 17. The two images are reduced separately with the same RM, two times for the two different catalogues GSC2.2 and UCAC-1. Only the instrumental effect removal and the absolute astrometry-stacking modules are activated with this RM. The distortion model is a second order polynomial function and the warping is done with the Lanczos kernel of

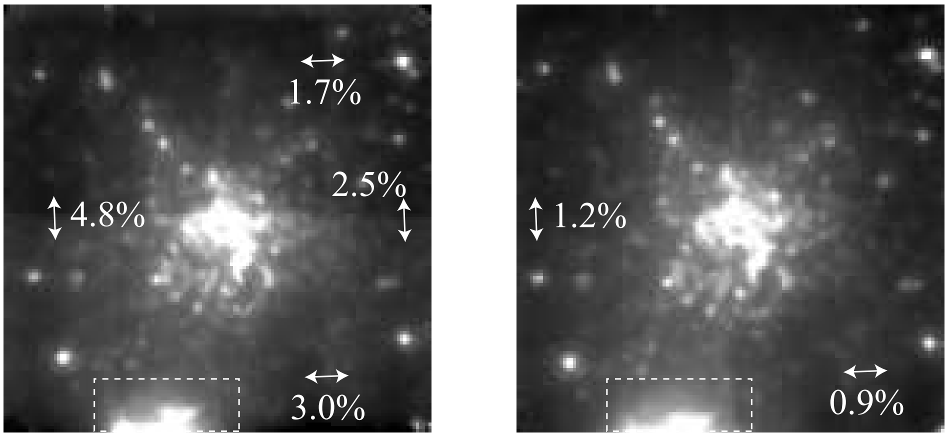

Figure 5.11: Comparison of two similar procedures to compute the relative mean gain between chips. On the left panel is showed a smooth version of a reduced images where the master flats have been harmonized with a rough method using the mean background of all chips. On the right panel is showed a median smoothed version of the same reduced image where the used master flat has been harmonized with a fine method using sky background computed on each border of the chips. Also quoted with the withe arrows are the variation of sky background from neighborhood chips. The dashed square isolate an area of the image where the illumination gradient due to a bright star perturbate the local background measurement.

third order. Three final images referenced: $WFI-V_{Gsc2.2}$, $WFI-V_{Ucac-1}$ and $WFI-B_{Ucac-1}$ assembling the 8 chips of the WFI are build. Three catalogues are extracted with Sextractor.

First test establishes the internal stability of the astrometric procedure: the extracted sources $WFI-V_{Ucac-1}$ and $WFI-B_{Ucac-1}$ are associated and compared (cf. figure 5.12). The RMS of the matched positions is equal to 0.031 arcsec, corresponding to 1/8 the size of a WFI pixel and 1/3 of the UCAC-1 accuracy. In the previous paper (Momany et al., 2001) page 440 (see appendix C) only a nearest neighborhood approach with sub-pixel computation (3×3) was available to warp the images. This technique is less accurate because the precision of the warping is limited to 1/3 of a pixel. Now with the newly implement Lanczos kernel, no sub-pixel warping is needed anymore, because the kernel allows an exact repositioning of a warped pixel.

The following tests benchmark the astrometric calibration when using different reference catalogues. The aim is to show the robustness of the astrometric solution comparing results issued with the classical GSC2.2 astrometric catalogue obtains from Schmidt plates versus the results issued with the last very accurate CCD astrometric catalogue UCAC-1. The latter as an internal accuracy of 0.1 arcsec and observations have been done close in time to the one made with WFI, so proper motions of stars are negligible, whereas, the GSC2.2 is older and with a larger internal RMS.

The two catalogues are matched and compared for objects inside the field of view of the WFI instrument, (cf. Figure 5.13). The RMS of the residuals is large and mainly due to proper motion stars and the internal accuracy of the GSC2.2 catalogue. According to the internal RMS of the UCAC-1 one can established a rough RMS estimation of 0.2 arcsec for GSC2.2.

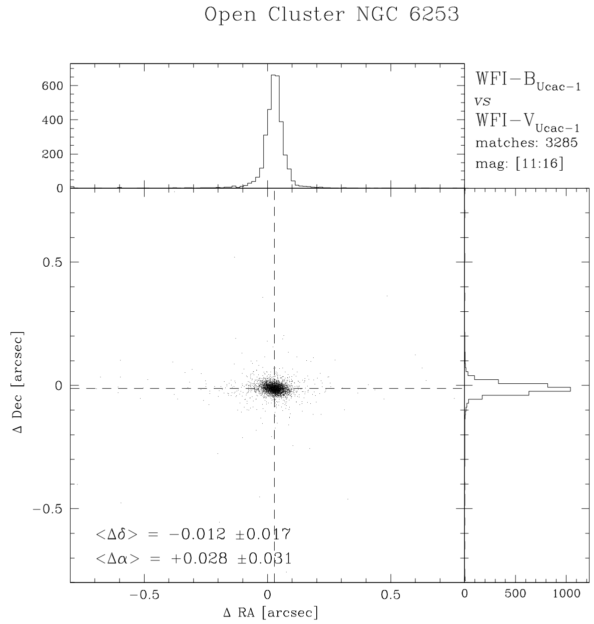

Figure 5.12: The two-dimensional (Ra,Dec) distribution of positional residuals obtained from the comparison of the astrometrically calibrated $WFI - V_{Ucac-1}$ versus $WFI - B_{Ucac-1}$catalogues of the open cluster NGC6253. The vertical and horizontal dashed lines mark the mean residuals in RA and Dec after applying a 3σ clipping to the data. The mean values with the final 1σ RMS are given on the figure. Also shown are the histograms of the residuals as a function of RA (top) and Dec (right). The number of matches and the limiting magnitude is specified on the top-left part of the figure. Also to be noticed, is the elongated shape in RA axes of the matches. It is due to the extraction software used with no PSF model, and therefore provides more uncertainties on the photo-center estimation of the objects in the RA axe because of the tracking of the telescope.

Now the comparisons are done using the reduced V images using the GSC2 catalogue $WFI - V_{Gsc2.2}$ versus: 1) the GSC2 reference catalogue (Figure 5.14), 2) the UCAC-1 reference catalogue (Figure 5.15) and 3) with the reduced V image using the UCAC-1 catalogue (Figure 5.16). The RMS measured versus the GSC2 catalogue is very similar to the RMS of the GSC2 catalogue versus the UCAC-1, as one can expected from the internal accuracy of GSC2.2. But the RMS obtains from the comparison with the UCAC-1 catalogue shows a decrease by a factor of 1.8. Theses measurements prove that the algorithm for the astrometric calibration using the GSC2.2 has rejected the proper motion stars. This is confirmed by the direct comparison of the extracted sources from the two image $WFI - V_{Gsc2.2}$ and $WFI - V_{Ucac-1}$ (Figure 5.16), where the RMS of the residual is 0.07 arcsec (1/3.5 the WFI pixel size) which is also the internal accuracy of the UCAC-1 catalogue. The shape of this residual shows some correlations due to the divergences of the astrometric calibrations at the borders of the chips. Indeed a theses locations, the astrometric solution has less constraints than in the middle of a chip, therefore the astrometric calibration diverges more in the chip borders using GSC2.2

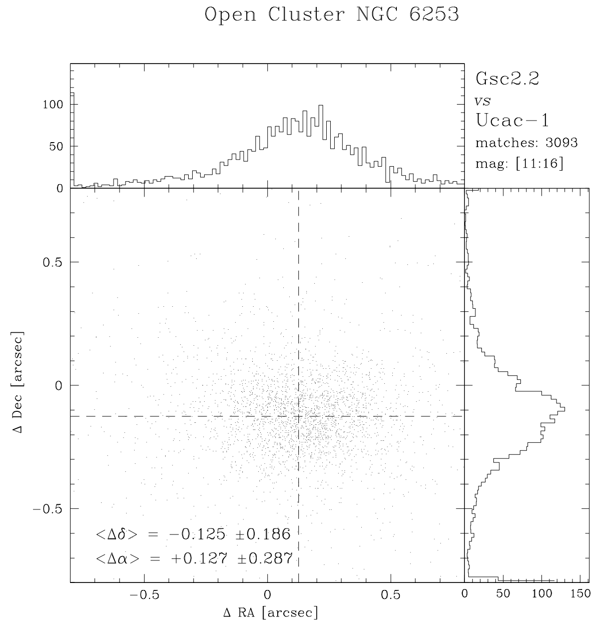

Figure 5.13: Comparison of the two independent astrometric catalogue GSC2.2 and UCAC-1 for objects inside a box of 40 arcmin around the open cluster NGC 6253. The plot show the two-dimensional (Ra,Dec) distribution of positional residuals from the two catalogues. The figure indications (mean and sigma) follow the same rules as in figure 5.13.

catalogue than the UCAC-1. Theses tests establish the robustness of the algorithm used for the astrometric calibration when using different reference catalogue for the calibration.

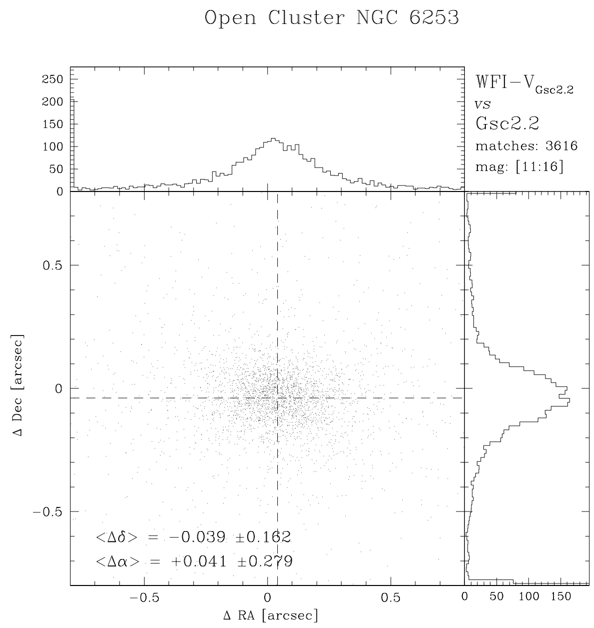

Figure 5.14: Comparison of the astrometric calibration of $WFI{-}V_{gsc2}$ versus: top) the GSC2.2 catalogue, middle) the UCAC-1 catalogue, 3) the astrometric calibration of $WFI - V_{Ucac-1}$.

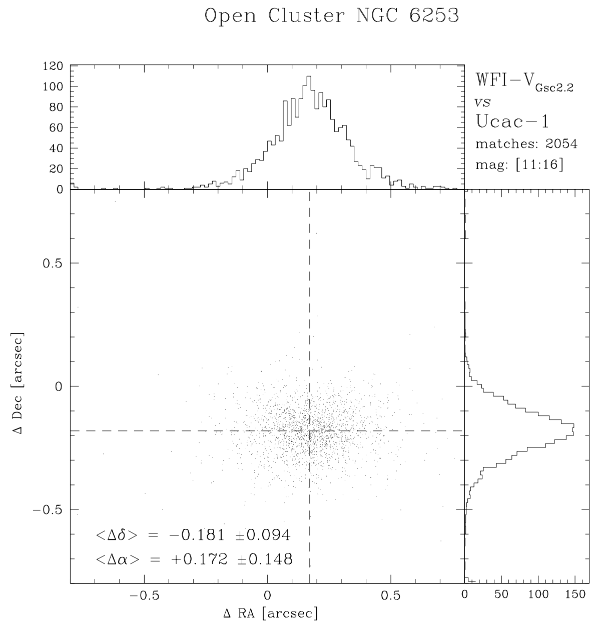

Figure 5.15: Comparison of the astrometric calibration of $WFI{-}V_{gsc2}$ versus: top) the GSC2.2 catalogue, middle) the UCAC-1 catalogue, 3) the astrometric calibration of $WFI - V_{Ucac-1}$.

Pointing	Filter	α	δ	Pointing	Filter	α	δ
NGC3201	B V I	10:17:36	-46:24:39	Carina	B V I	06:42:35	-50:45:00
NGC4590	B V I	12:39:28	-26:44:34	Carina	B V I	06:39:55	-50:45:00
NGC4833	B V	12:59:35	-70:52:28	Carina	B V I	06:39:55	-51:10:59
NGC5139	B V I	13:26:46	-47:28:36	Carina	B V I	06:42:35	-51:10:59
NGC5904	B V	15:18:34	+02:04:58	BAR LMC	B V	05:38:40	-70:04:59
NGC6121	B V I	16:23:35	-26:31:31	BAR LMC	B V	05:33:05	-69:04:59
NGC6171	B V I	16:32:32	-13:03:12	BAR LMC	B V	05:33:05	-69:34:59
NGC6254	B V I	16:57:09	-04:05:57	BAR LMC	B V	05 33 05	-70:04:59
NGC6352	B V	17:25:29	-48:25:22	NGC2257	B V I	06:27:53	-64:19:36
NGC6366	B V I	17:27:44	-05:04:36	NGC2257	B V I	06:32:30	-64:19:36
NGC6362	B V I	17:31:55	-67:02:53	ESO121SC3	B V I	05:59:58	-60:31:00
NGC6540	B V	18:06:08	-27:45:55	ESO121SC3	B V I	06:04:02	-60:31:00
MW Halo	B V I	16:02:31	-10:59:44	NGC2210	B V I	06:14:19	-68:52:18
Blanco1	B V I	00:04:15	-29:56:17	NGC1866	B V I	05:13:39	-65:27:54
Berkeley20	B V I	05:32:58	+00:13:04	NGC1978	B V I	05:28:05	-66:19:59
Melotte66	B V I	07:26:19	-47:44:05	NGC1978	B V I	05:33:15	-66:19:59
NGC2477	B V I	07:52:17	-38:32:48	NGC2004	B V I	05:28:05	-66:49:59
NGC2506	B V I	08:00:11	-10:47:17	NGC2004	B V I	05:33:15	-66:49:59
NGC3293	B V I	10:35:49	-58:13:33	NGC2004	B V I	05:28:05	-67:19:59
Collinder228	B V I	10:43:01	-60:00:45				
Trumpler14	B V I	10:43:56	-59:33:46				
NGC3766	B V I	11:36:08	-61:36:35				
NGC3960	B V I	11:50:53	-55:41:40				
NGC4755	B V I	12:53:36	-60:20:16				
NGC6231	B V I	16:54:00	-41:47:52				
NGC6253	B V I	16:59:04	-52:42:32				
NGC6281	B V I	17:04:48	-37:54:06				
NGC6475	B V I	17:53:56	-34:48:33				
NGC6611	B V I	18:18:50	-13:46:44				
M67	B V I	08:51:22	+11:49:00				
NGC330	B V I	00:56:45	-72:19:00				

Table 5.4: List of the released images of the WFI Pre-FLAMES survey. The pointing are made of: open clusters, globular clusters, large Magellanic cloud, small Magellanic cloud.

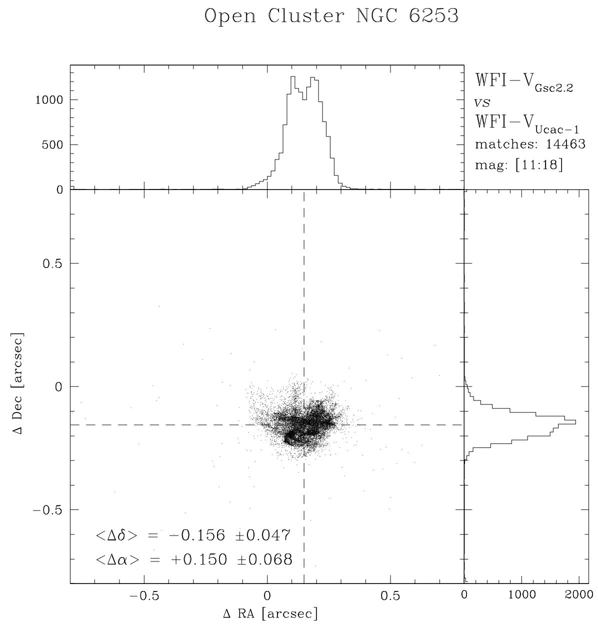

Figure 5.16: Comparison of the astrometric calibration of $WFI{-}V_{gsc2}$ versus: top) the GSC2.2 catalogue, middle) the UCAC-1 catalogue, 3) the astrometric calibration of $WFI - V_{Ucac-1}$.

5.3.4 Illumination correction

Data mining to compute WFI illumination maps

The illumination map were computed with the so-called "relative approach" as described in section 4.3.2 (a map is computed with several consecutive images of the same field observed with a generous dithering pattern of observation). A good candidate is made of typically 5 images of an homogeneous field containing bright stars. In section 4.3.4 numerous illumination-maps were computed using the old EIS survey named *Pilot*. This one mixes galactic and stellar fields (mainly globular clusters). The deep observations were enough full of bright stars for a good estimate of the illumination-maps, and the globular clusters were ideal cases to validate the results. Those observations permit to compute the illumination-map for filter B-842 and V-843, for the year 1999. Thanks to the latter private observations of the same globular clusters, one could derive an illumination-map for filter B-878, I-879 and U-877 for the year 2000 to 2002. One assumes the illumination-maps stable in time from 1999 to the end of 2002 where the internal baffling of the instrument was upgraded. For the 1999-2002 perido, some filters where not calibrated such as: the old I-845, and the R-847.

The Pre-FLAMES observations start in 2000 and are spread in more than two years. The filters used are the two B, the V and the two I. Some latter observations use the R-844 filter. As for the Pilot survey, Pre-FLAMES observations were shared with the Deep Public Survey (DPS). Unfortunately, only one target from the three of the DPS provides good OBs for the computation of illumination-maps. The two other ones are empty fields with too few bright stars. To compute the illumination-maps for the new un-calibrated filters (I-845, and R-847), it was necessary to exploit intensively the WFI archives. Thanks to the ESO policy, all observations older than one year are public domain.

The exploitation is difficult, as good image candidates for illumination-map computation may not match the observations strategy of the numerous private runs. Hundred of science WFI images have been downloaded and reduced especially with filter I-845 and R-847. In practice most of the OBs were not good candidates for one of the following reasons:

1. Inappropriate targets - The targets are inappropriate for illumination-map computation as for instance: 1/ very extended objects (nearby galaxies, nebula), 2/ very crowded sources making the aperture magnitude polluted by faint sources, 3/ targets with couple of very bright stars affecting some chips. Those observations were discarded.

2. OB with too few images - Numerous WFI observations are organized with small OBs containing less than 5 images. Lots of scientific or technical reasons can justify this choice: 1/ to optimize the efficiency of the instrument by doing less observations with longer exposure time, 2/ to make observations with different integration times and then optimize the instrument efficiency by making OBs of couple of images, 3/ some targets do not need to fill-in the inter-chip gaps and few images are sufficient. Those observations were discarded.

3. Inappropriate integration time - Some private runs are made with short exposures (less than 30 seconds). In general, the observed stars have a weak S/N, and their magnitude error are too important for illumination-map computation. Observations

with long exposure time have also been discarded as the probability of sky transparency variation is higher. In practices observations with 1 to 5 minutes where considered.

4. Dithering pattern of observation too small or inappropriate - The next criteria is the minimum size of the dithering pattern of the OBs. A small pattern cannot be used as the magnitude variations are too small to compute an illumination-map. The patterns are either: conventional as suggested in the WFI user manual (5 images with large isotropic offsets), or, defined by the users. With the latter case one distinguishes: 1/ the very small offsets used to keep constant PSF anisotropy of stacked images, 2/ patterns with redundant positions, for instance with 9 observations made at distinct 3 positions (this is equivalent to 3 OBs of 3 images with the same 3 points pattern), 3/ pattern with preferential direction (several points quasi aligned). In general most of the user defined patterns were discarded. Note that a pattern size is difficult to guess from the ESO archive Query Form. they were validated after downloading the data, making the datamining time consuming.

After this crude selection, lots of images are discarded. It is worth emphasizing that half of the OBs are made of less than 5 images, and have their own pattern of observation. About 300 scientific images have been downloaded and reduced. The typical OBs made of 5 images are used to compute illumination-maps with the relative approach. As presented in section 4.3.5, the relative ZP variation between the 5 images, is used as an estimator to qualify the computed illumination-map. It worth emphasize that most of images observed while the moon is bright, are subject to photometric variations and have been discarded. Also, OBs with photometric ZP stable within 1% variations are strongly correlated with weather conditions. Thanks to the archive facility, the seeing monitor and other quantities are easily available. One observed the most stable photometric conditions with dry nights (humidity less than 30 %), and with winds of constant speed (5 to 10 m/s) and direction. A smaller wind (from 0 to 5 m/s) was not very correlated with stable photometric ZP. In general those conditions are associated with a good seeing. The reverse is not true, good seeing occurs with relative ZP variations greater than 1%.

In practice the data-mining was not too productive: the computed illumination-maps were difficult to validate for filter I-845 and R-847 as no adequate globular clusters where observed with the same filter. Finally the I-845 illumination-maps has been computed thanks the deep images of the DPS used to compute the fringing-maps for the Pre-FLAMES target. It consists in 5 images where the ZP variations were very small (0.04%). This new map is validated thanks to special overlapped Pre-FLAMES observations (see following section). The illumination-maps computed for R-847 were discarded as no validations could be done.

Illumination-map validations with Pre-FLAMES overlapped observations

Most of the Globular Clusters part of the Pre-FLAMES survey are not adequate to validate illumination-maps. The ones observed are either too small, or with a large random differential reddening. Fortunately, 4 regions within the Sagittarius Galaxy have been observed. They are made of 4 WFI images taken with generous overlaps as illustrated in figure 5.18. For each of the 4 regions, the middle (8×8 arcmin) is located on a small globular cluster which is therefore observed 4 times. For each of the 4 common areas (30×8, or 8×30 arcmin)

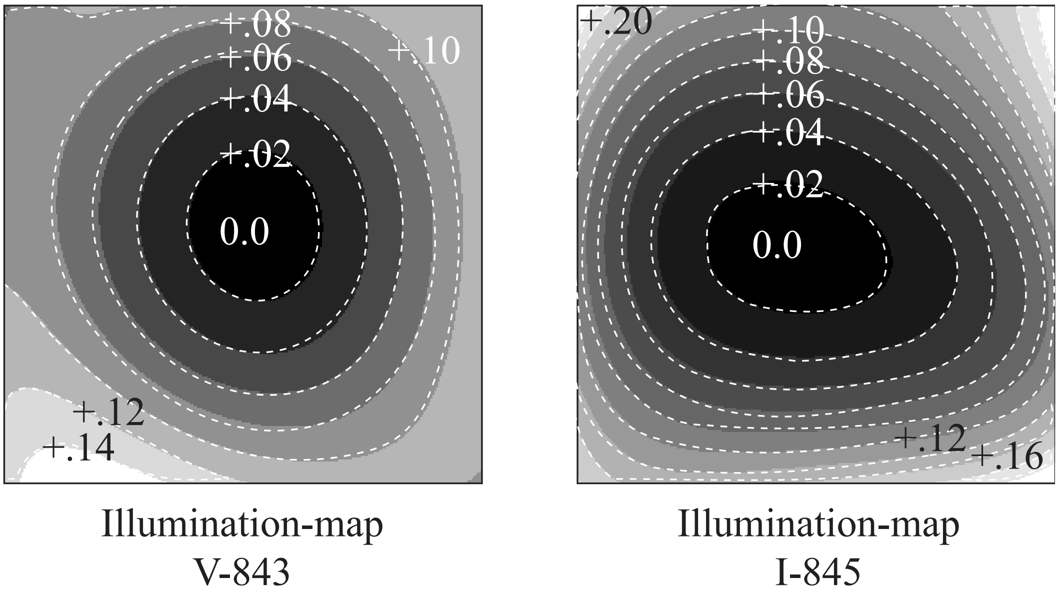

Figure 5.17: Illumination-maps comparison for WFI filter V-843 and I-845. One notices the larger illumination-error of filter I (the maximum error is going up to 0.2 Mag, whereas the maximum is 0.14 for the V filter). Also note the weak upper border of the I illumination-map; All borders are around 0.16 Mag and the upper one is only 0.12 Mag.

observed by 2 distinct images, the illumination-error is evaluated by association of extracted sources from the 2 reduced images. Each source observed 2 times gives a delta ZP function of the sky position (Right ascension and Declination). Note that this test is made on the borders of the WFI instrument where the illumination-errors have large gradients.

The images SG01, SG02, SG03 and SG04 form a region of 52×52 arcmin (as illustrated in figure 5.18). The images are reduced 2 times, first with no correction, and then with an illumination-map. For each image, a catalogue is extracted with DaoPhot that provides accurate photometry. The catalogues are associated for overlaps: 1-2 and 1-3 and the magnitude are compared. Figure 5.19 and 5.21 illustrate the delta ZP with no correction for respectively for overlaps 1-2 and 1-3. Figure 5.20 and 5.22 illustrate the delta ZP when illumination-maps are applied for respectively overlaps 1-2 and 1-3. The target is dense of stars and the tendency of the illumination-error is easily seen on the plots. The denser parts correspond to the central globular cluster observed on all images. From the uncorrected data, one deduces the errors are larger for the I-845 filter than the V-843 (see gradients on figures: 5.19 bottom panels, and5.21 upper panels). The corrected data show much smaller ZP dispersion and proves the efficiency of the illumination-maps. One notices the arc shape of the I-845 corrected data (Figure 5.20 upper panel) that indicates a too weak correction of the illumination-map on the upper part of the instrument. This default seems to be visible in the upper part of the I-845 illumination-map (Figure 5.17 left). Also, one observed a ZP step chip to chip on V-843 corrected data (Figure 5.20 upper panel). This gap is difficult to observed on the reduced image that still have the sky background. Globally the corrections improved the precision of the ZP. The corrected dispersion of illumination-corrected images of 0.02 Mag is at least four times smaller than the original dispersion of the uncorrected data. These tests are carried out

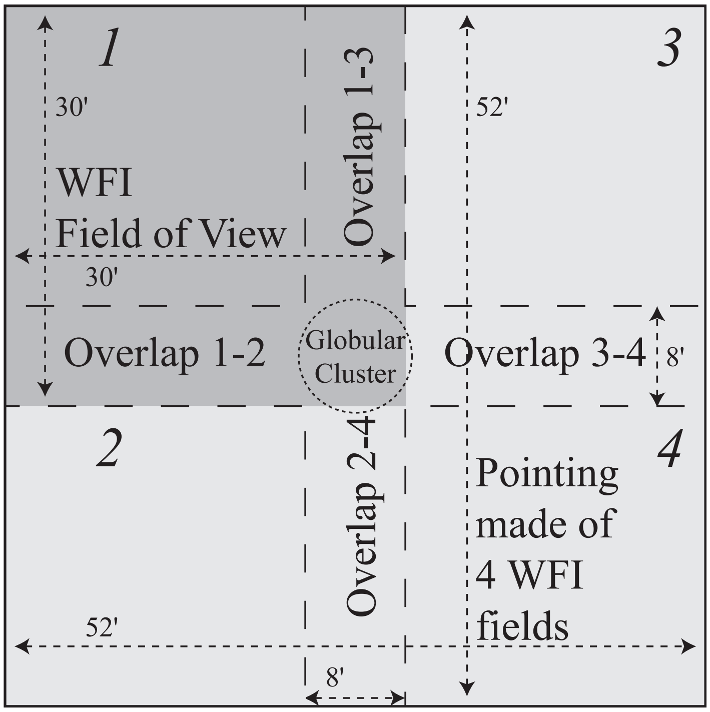

Figure 5.18: Layout of the Sagittarius Galaxy pointing. A region is made of 4 WFI images observed with 8 arcmin overlap. For each of the 5 series of 4 pointing, a medium size globular cluster is set if the middle of the small 8 × 8 arcmin common area of the 4 images. Each observation is labeled from 1 to 4. The overlaps are labeled 1-2, 1-3, 2-4 and 3-4.

on the external part of the WFI instrument. In the center one expects better correction as the illumination-errors are smaller.

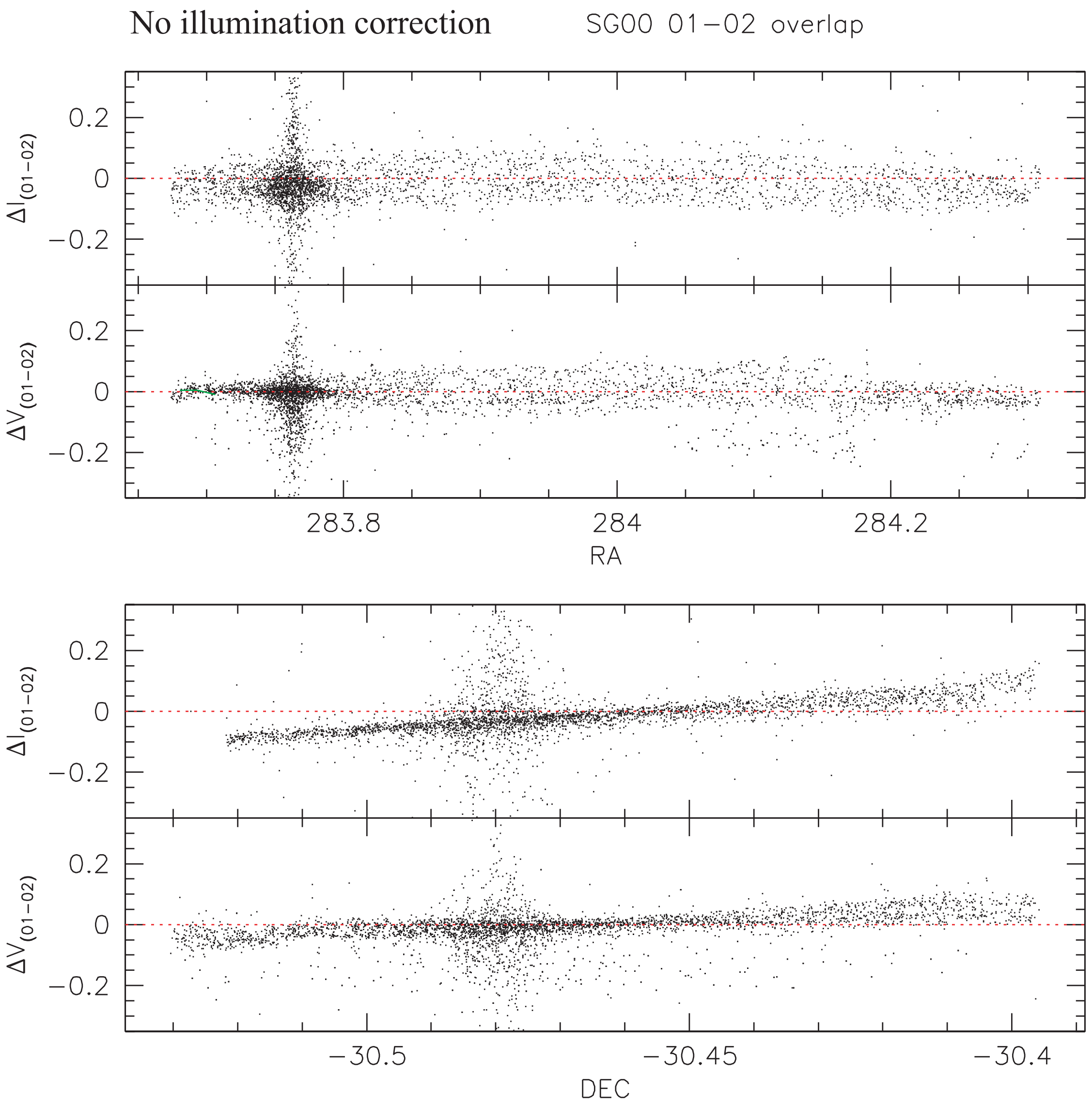

Figure 5.19: Impact of the illumination error on WFI un-calibrated images. Tests made on the left and right border of the instrument.

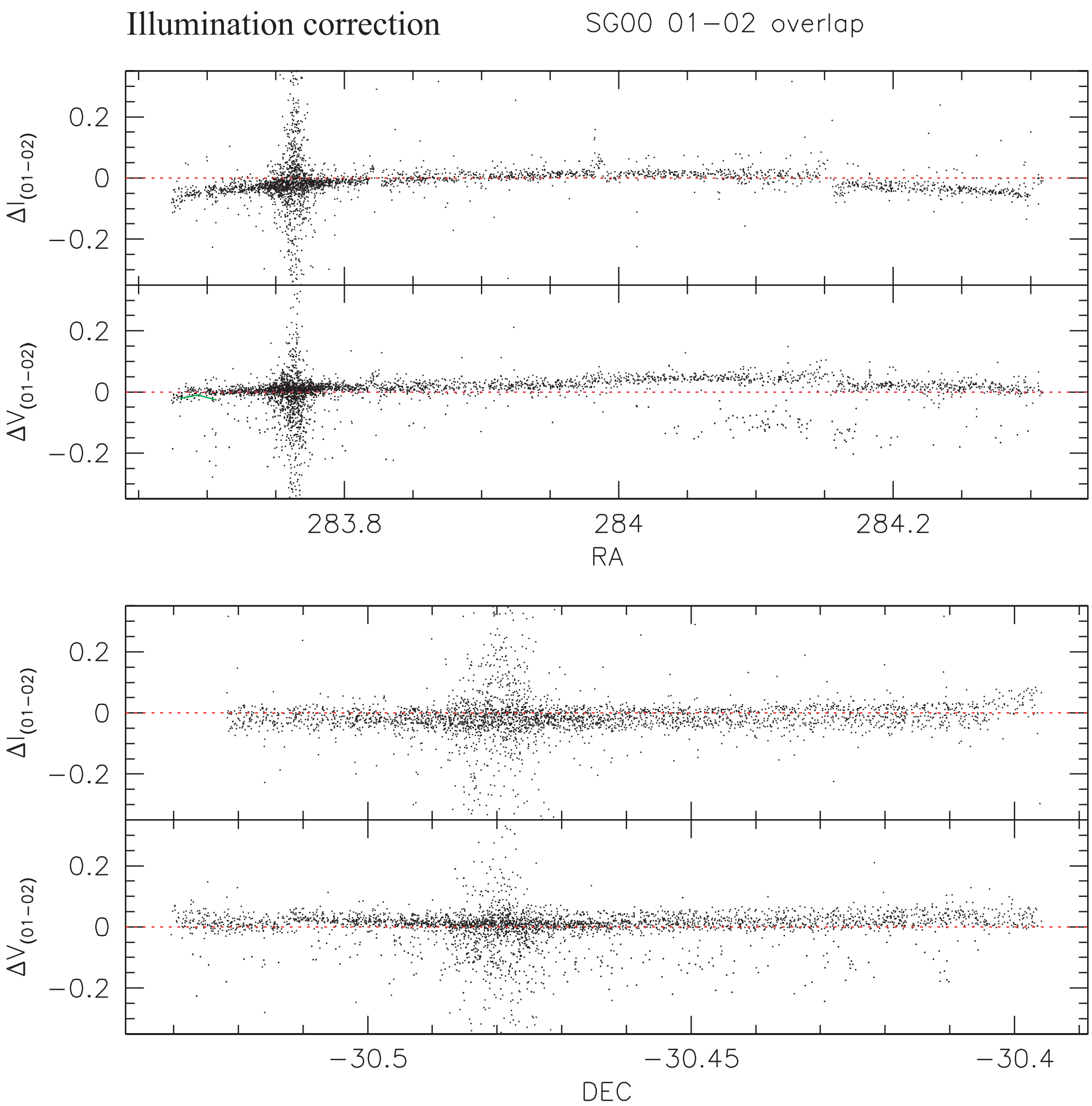

Figure 5.20: Impact of the illumination error on WFI un-calibrated images. Tests made on the left and right border of the instrument.

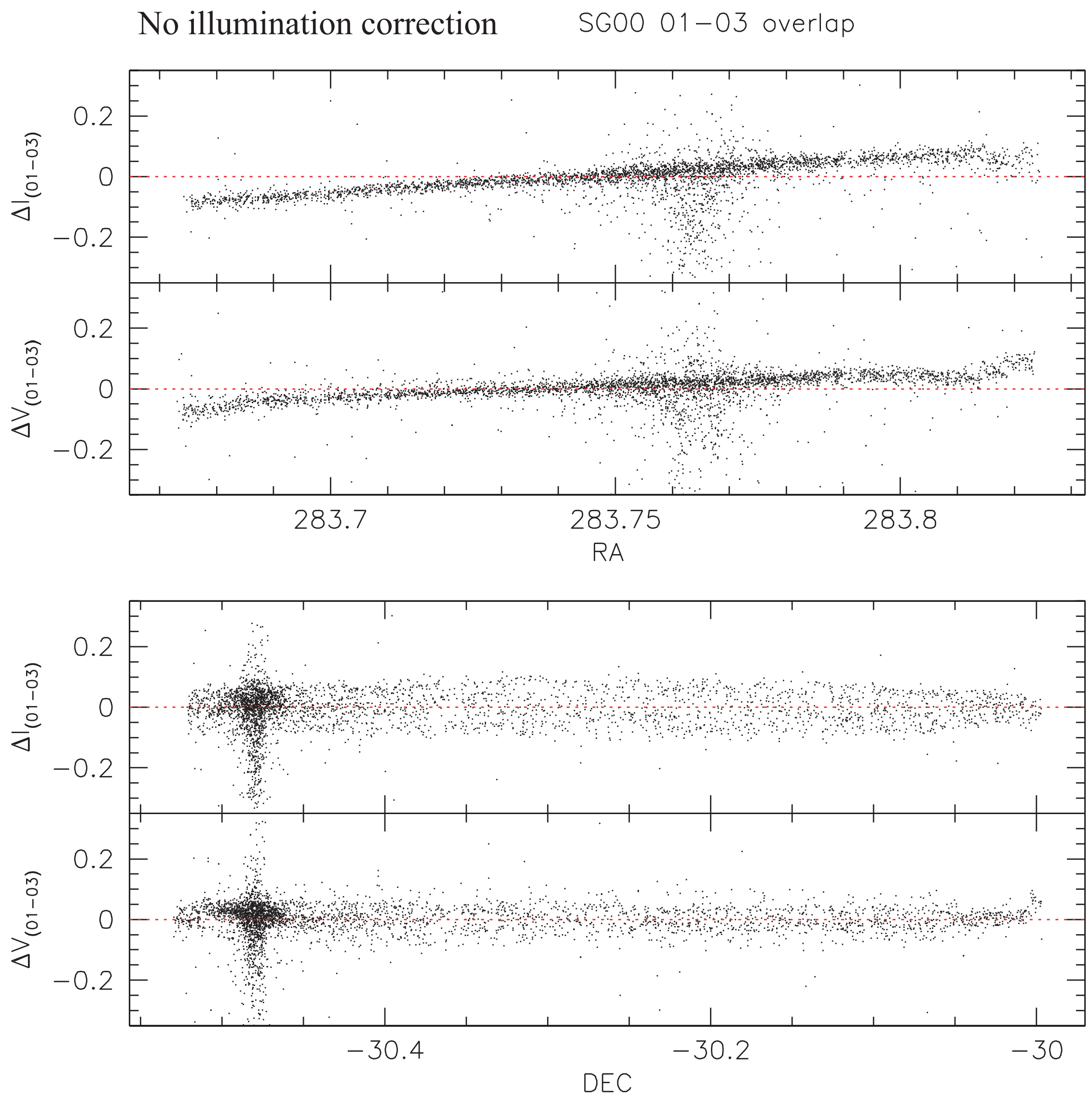

Figure 5.21: Impact of the illumination error on WFI un-calibrated images. Tests made on the left and right border of the instrument.

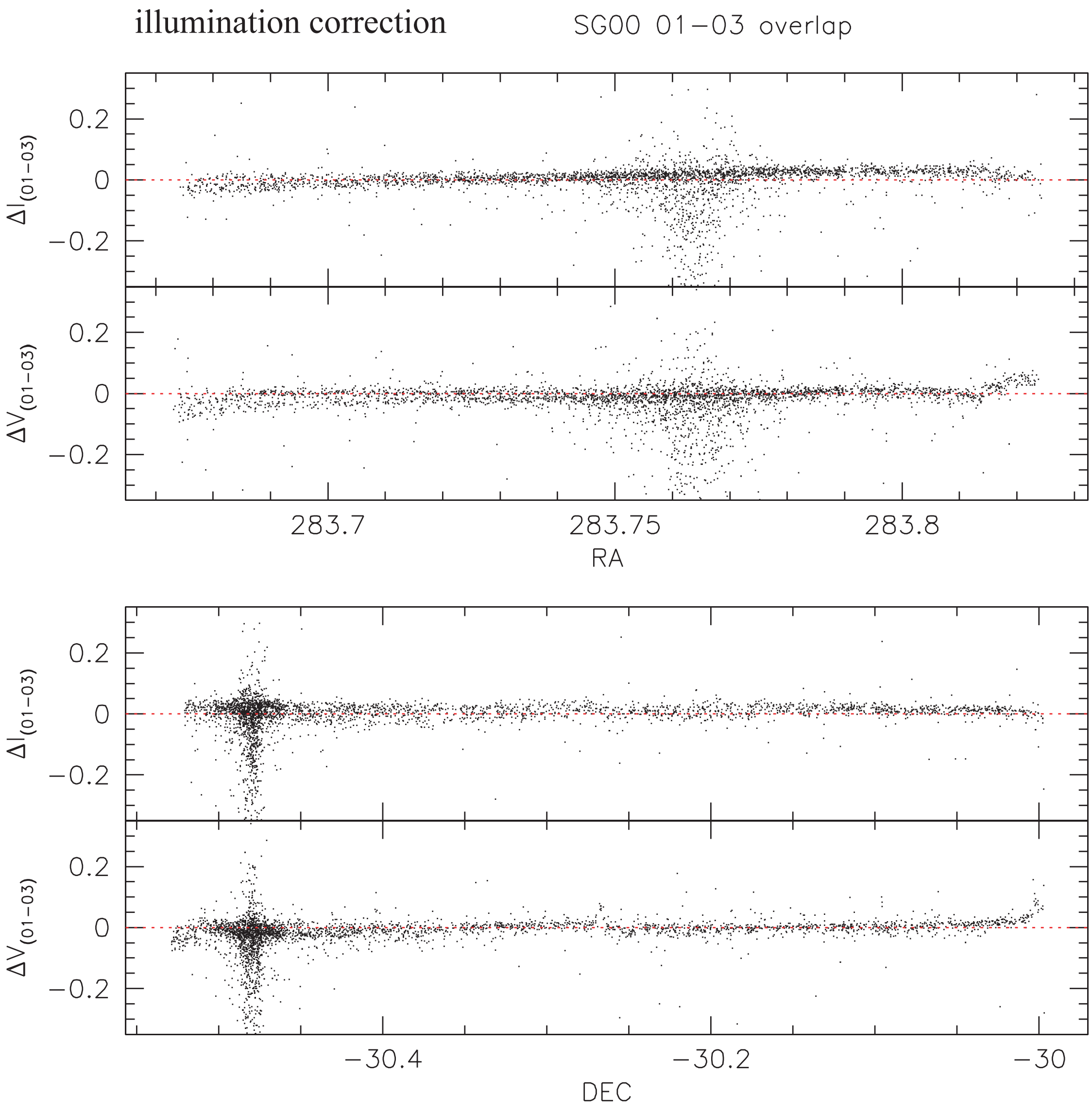

Figure 5.22: Impact of the illumination error on WFI un-calibrated images. Tests made on the left and right border of the instrument.

5.4 The XMM optical follow-up WFI survey

Based on ideas submitted by the ESO community and evaluated by ESO's Survey Working Group (SWG), the XMM survey (administered by the ESO Imaging Survey (EIS) and the Public Survey Group (PSG) teams) consists of follow-up optical observations of the XMM-Newton Serendipitous Sky Survey (XSSS) using the ESO Wide Field Imager (WFI) at the ESO/MPG 2.2m telescope at the La Silla Observatory. This survey seeks to obtain WFI images in B-, V-, R- and I- passbands (for minimum spectral discrimination and photometric red-shift determination) of XMM fields publicly available in the XMM archive. The fields were selected and prioritized by a collaboration of interested parties from the XMM Survey Science Centre (SSC), the Bonn group (led by P. Schneider) and an appointed committee of the SWG. The observations were originally proposed to cover a total area of approximately 10 square degrees (40 fields) to a limiting magnitude of 25 (AB, 5 sigma, 2 arcsec aperture).

Data for the XMM survey are being provided by:

- The ESO Large Program 170.A-0789(A) (Principal Investigator: J. Krautter, as chair of the SWG) which has accumulated data from January 27, 2003 to March 24, 2004 at the time of writing.
- The contributing programs 70.A-0529(A); 71.A-0110(A); 71.A-0110(B) with P. Schneider as the Principal Investigator, which have contributed data from October 14, 2002 to September 29, 2003

The present release consists of data from the above programs accumulated until October 16, 2003, corresponding to a total of roughly 130 and 720 science OBs and exposures, respectively, and 80 hours on-target integration. About 15% of the B-band and 85% of the R-band data are from the contributing programs.

With the present release 83% of the data accumulated as part of the Public Survey over 15 fields (roughly 3.75 square degrees) have been reduced. On the other hand, the observations for the XMM survey correspond, at the time of writing, to less than 35% of the original goal of 40 fields.

5.4.1 Reduction strategy

The images have been observed in service mode, therefore the observations are spread in numerous noncontinuous nights. To calibrate the scientific images, a master bias and a flat per passband must be estimated in a time-scale of 10 days and 5 days respectively for stability reasons. The master flats are harmonized to have the same gain for all the chips. But no illumination correction were applied because the procedure was still underdevelopment for the release.

The scientific images are regrouped into RBs such as they share same filter, sky location and have been observed within one hour. An additional constraint is applied to create the RBs such as the SBs contain at least three reduced RBs. This last constraint is made to removed cosmic rays in a second step, and also comic observed at the border of chips.

Pointing Name	Other name	α	δ
XMM-01	J09525.7-4758	09:25:46.0	-47:58:17
XMM-02	J0720.4-3125	07:20:25.1	-31:25:49
XMM-03	HE1104-1805	11:06:33.0	-18:21:24
XMM-04	MS1054.4-0321	10:56:60.0	-03:37:27
XMM-05	BPM16274	00:50:03.2	-52:08:17
XMM-06	SHARC-2	05:05:20.0	-28:49:05
XMM-07	LBQS 2212-1759	22:15:31.7	-17:44:05
XMM-08	NGC4666	12:45:08.9	-00:27:38
XMM-09	Q1246-057	12:49:13.9	-05:59:19
XMM-10	PB5062	20:05:09.8	-02:55:18
XMM-11	Sgr A	17:45:40.0	-29:00:28
XMM-12	WR 46	12:05:19.0	-62:03:07

Table 5.5: Location of the 12 pointings of the XMM optical follow up.

The RM used for this survey is the *deep* mode. Most of the pointing are extra-galactic pointings, and the sky background can be estimated. The challenging I-band observations were reduced by estimating a fringing-map from the RB themselves. The RBs of I observations contain 10 images following the OB strategy made with a large dithering pattern of observation. For some galactic observations (XMM-02, XMM-11 and XMM-12), the density of stars is too important, and the estimation of the pixel-based background can not be applied within the RB. For those I-band RBs, the RM used is *deep-fr* (as described in table 3.8). With this RM, the background is subtracted by using a fringing-map which were computed from the extra-galactic observations such as the XMM-06 and XMM-04.

The reduced RBs were released in september 2004. The final products computed by stacking the SBs made of the reduced RBs, were not released to the public for this version. In order to check the astrometry and made some visual inspection, the SBs have been stacked without taking into consideration the relative ZP of the reduced RBs. The 12 final product for the filter V are presented in figure 5.23. The pointings XMM-01 to XMM-12 are presented from left to right, and top to bottom. The XMM-01, XMM-02, XMM-10, XMM-11, XMM-12 are dense stellar regions. On the reduced image XMM-08, an over-estimation of the sky background is visible around the top-right bright galaxy. For this field the stellar RM would have been more adequate. Instead, the deep RM was used, because the actual weighted co-addition procedure used to stack the SBs, is only able to stack images with no remaining sky background (In stellar mode, the smooth sky background is kept, and the SB made of several reduced RBs, can not been merged). The default occurs only for this image around the bright galaxy.

5.4.2 WFI electronic benchmark

Bad pixel detection

Taking advantage of the large set of data observed during more than one year, the stability of the hot-pixels is evaluated. Three groups of scientific observations of three distinct pointings are selected for the benchmark. They correspond to three dates distant of five months each.

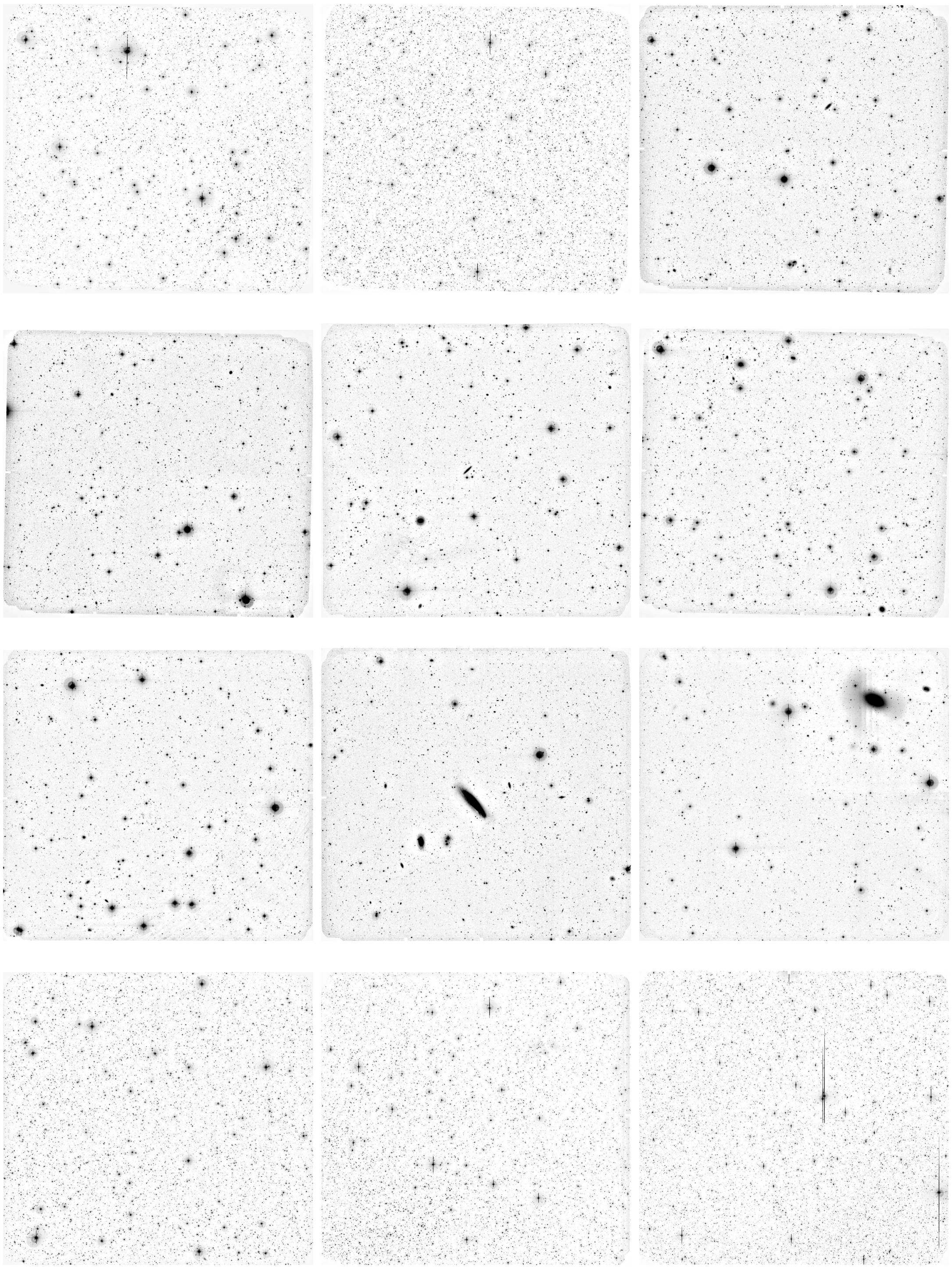

Figure 5.23: The pointings XMM-01 to XMM-12 are presented from left to right, and top to bottom. A negative intensity scale is used.

The bad pixels of chip seven are computed with the procedure described in section 4.1. The three catalogues of detected bad pixels are associated from one date to another (see table 5.6 for results). The minimum correspondence of 72 percent, indicates the good stability in time of the location of bad pixels for a period of 11 months. The figure 5.24 shows the location of the bad pixels detected from the first group of scientific images (observed the 11 of November 2002).

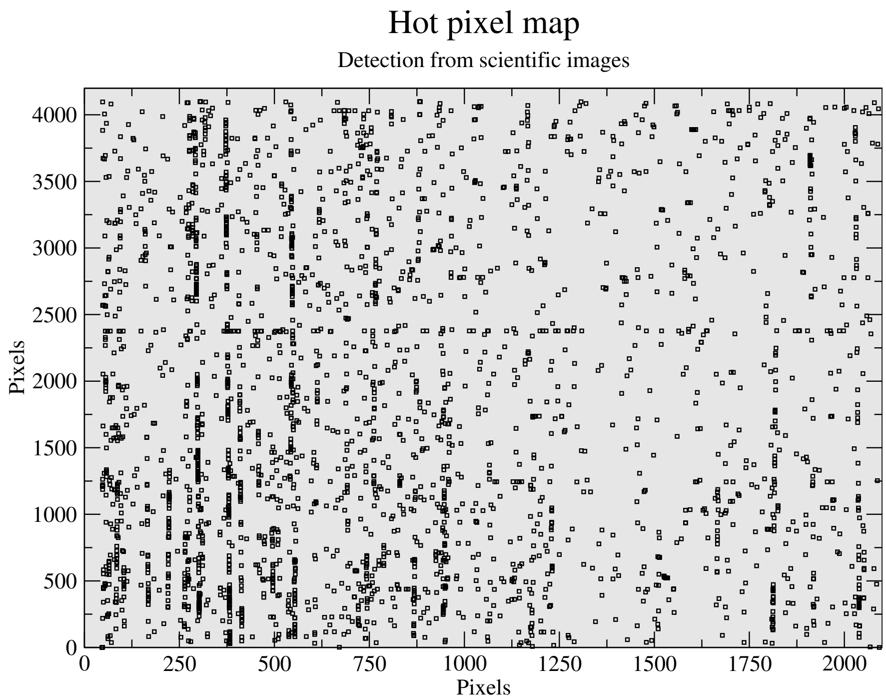

Figure 5.24: Localization of the bad pixels on the WFI imager chip 7 detected by combining five scientific images observed the second of November 2002. Note that this detection gives the bad pixels and also the bad pixels visible only with long exposure time.

The bad pixel detected from the special procedure to recover the lack of Dark observations has an impact on the final products.

Relative gain harmonization statistics

The large quantity of images spread over 1 year of observation is a good wide set of data suitable to evaluate the mean gain variation chip to chip as a function of time and wavelength. The data are spread in 13 groups of continuous nights. This quite large number is due to the service-mode way of observing. The notion of run of observation is made obsolete with the service-mode. From the full set of images, 26 masters flats have been built: 7 for filter B, 6 for filter V, 5 for filter R and 8 for filter I. The master flats have been normalized to have the same mean gain on all chips using a raw flat observations each time to compute the gain step from one chip to another. The chip 6 is used has reference for all filters. The figure 5.25 illustrates for the 4 filters used the mean gain of the 8 chips as a function of time. Note that

	Date 1	Date 2	Date 3
Date of observation (YYYY-MM-DD)	2002-11-02	2003-04-03	2003-09-29
Number of images used	5	5	5
Filter used	R	V	R
Number of bad pixels detected (10σ)	2585	2475	2694
Pixels in common with Date 1		85%	82%
Pixels in common with Date 2			72%

Table 5.6: Time stability of the hot pixels detected from three different groups of scientific images. Each columns of the table gives information

all the observations with filter B, V, R and I have not been done at the same time, and the measurements for a filter may not correspond to the same date for another filter. From the filter B, V and I, the date of observation corresponds quite well, one notices the stability in time of chips 2, 3, 5 and 6 (the chip location within the instrument is illustrated with figure 5.26) are stable within couple of percent, whereas the 4 external chips (chip number 1, 4, 5, 8) show discontinuities after night 210. This observation is conformed to the chip grade quality given by ESO. The external chips (1, 4, 5, and 8) are engineering grade, and the other chips are science grade. The science grade chips have been tested and are electronically stable and with a flat thickness backside anti-reflection coating. In case of the R filter, the mean gain variation from the days 0 to 17 (corresponding to the 15 October 2002 and 1 November 2002) shows variations within 3% for the internal chip. The external chips have greater mean gain variation. From the mean gain variation observations, one can conclude that the external and internal chips work in 2 different modes. The external ones shows instability within 8% of their mean gain, whereas the internal chips mean gain variation are within 2-3%. For proper photometry calibration, each master flat must be normalized to have same mean gain, the computation done with a sky images provides relative mean gain accuracy smaller than 1% RMS (as illustrated in sub-section 5.4.4).

The mean gain harmonization is analyzed to test the wavelength dependencies chip per chip. The 8 CCDs are similar but each one has been coated and polished separately, the Quantum Efficiency (QE) is not exactly the same. The mean gain is a relative indicator to get the color relative term of the detectors. From all the master flats, 4 dates have been retained. The February 2 2003 and the April 9 2003, within 5 days, 4 master flats of the 4 filters are compared. Also, for the June 12 2003 and July 22 2003, within 5 days, 3 master flats from the 3 filters B, V, I could be compared. Figure 5.26 illustrates the relative gain as a function of the mean wavelength of the 4 filters. The chip 6 is the reference for all filters. From the wavelengths comparison, again, one notices the stability of the 4 internal chips.

5.4.3 Statistic on satellite tracks

The EIS/MVM pipeline is using the Hough transform to automatically detect and then mask the satellite tracks. The large amount of scientific images is an opportunity to quantify precisely the probability to detect a satellite on raw images. Table 5.7 gives the statistics from the Hough procedure applied on the 739 scientific images of this survey. The procedure has

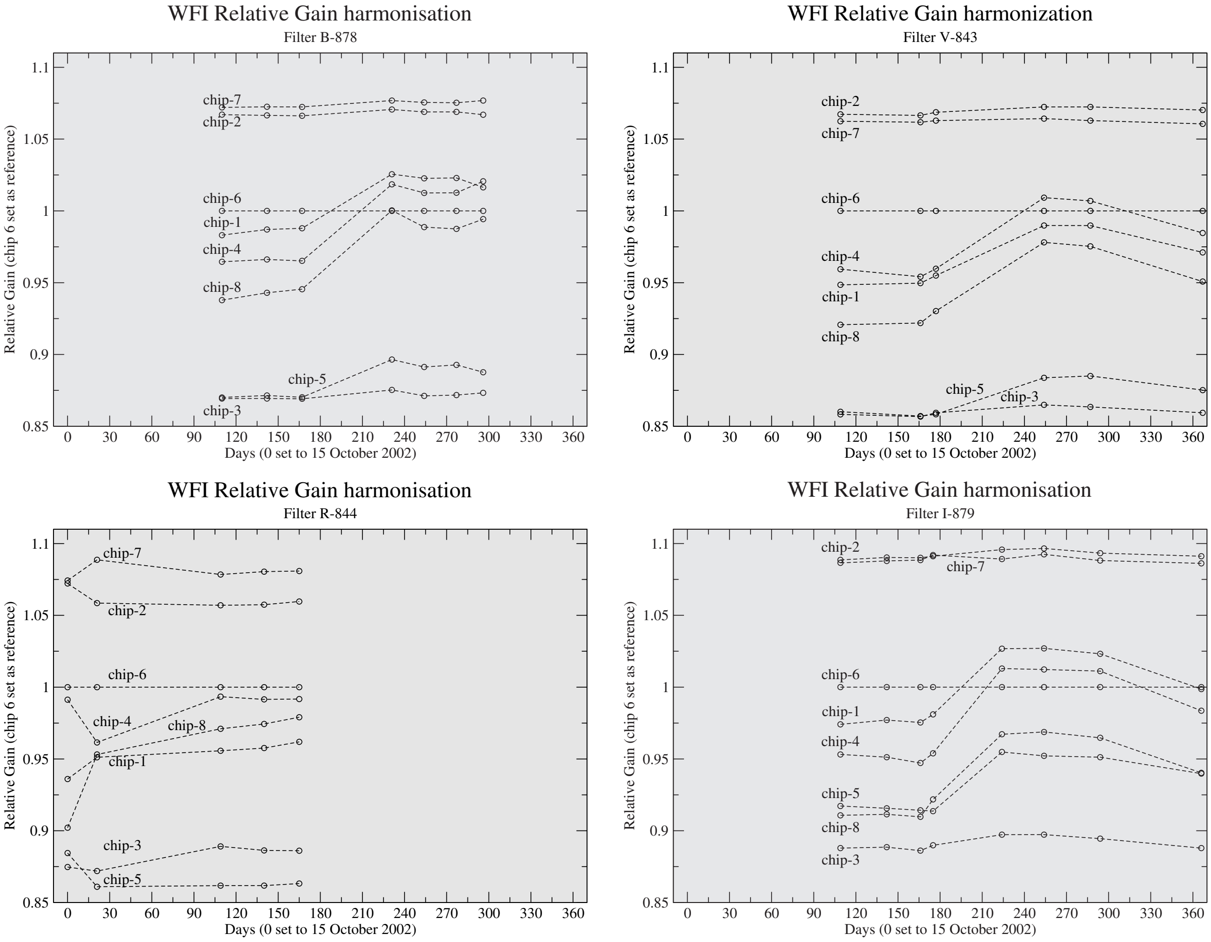

Figure 5.25: Time variation of the relative gain of the 8 CCDs of the WFI imager. The number following the passband name is the ESO identifier for the filter (and has no connection with wavelength).

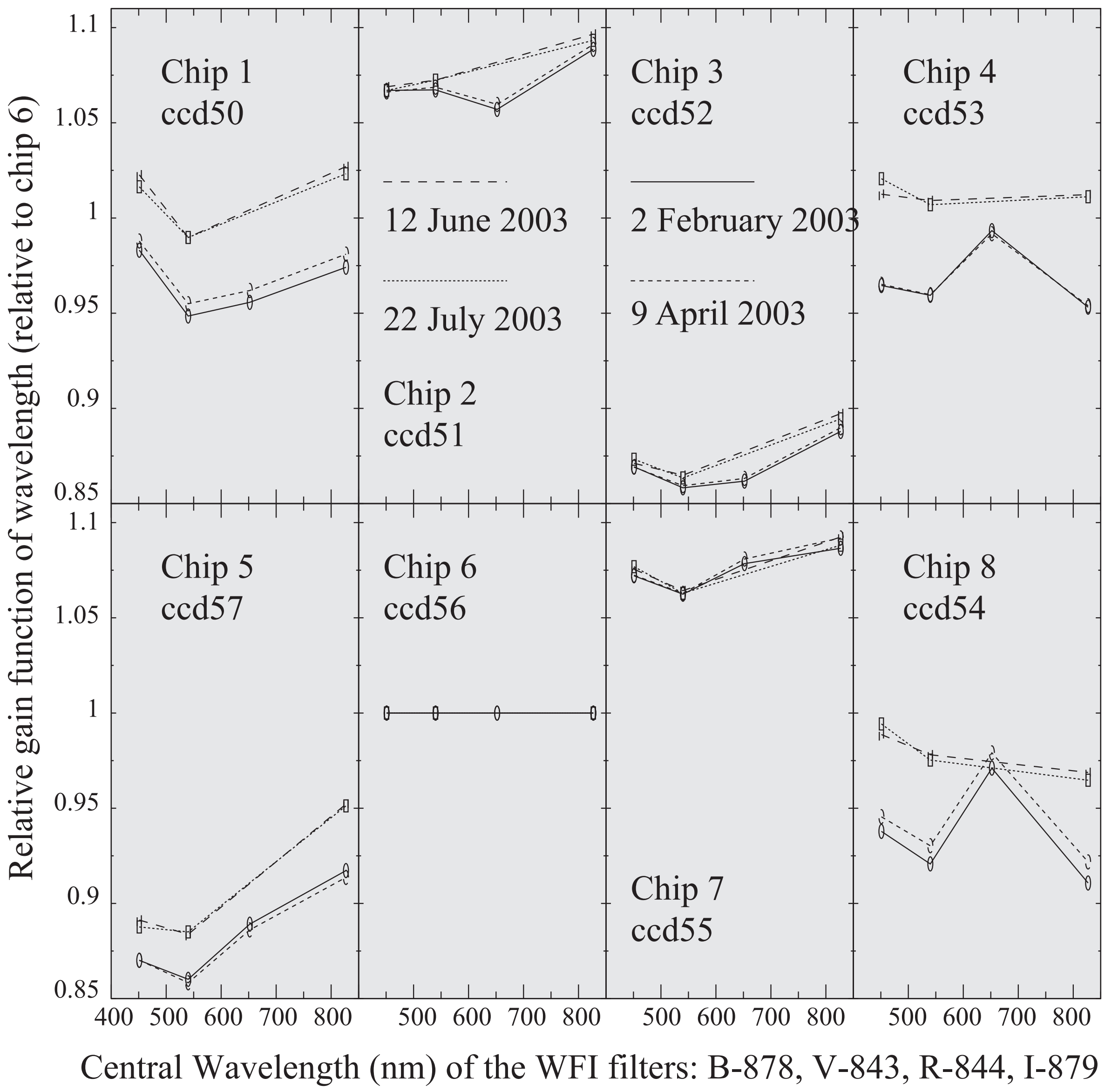

Figure 5.26: Variation of the relative gain of the CCD as a function of the central wavelength of the 4 filters used for the XSSS survey: B-878, V-843, R-844, I-879. The mean gain comparison is done relatively to the chip 6 used as reference.

detected different types of tracks: the ones caused by satellites crossing the field of view, the ones caused by internal light reflections, a track caused by a very long cosmic ray, tracks due to very bright stars, fake detections due to aligned bad pixels, and finally the random fake alarms. Figures 5.29, 5.30 and 5.31 shows the various types of satellite tracks observed, and also some examples of tracks issued by other events.

	Full detector	Chip base
Number of scientific images	739 images	5912 images
Total amount of observation time	84.11h	84.11h
Detected track by the procedure (total)	111	200
satellite track	72	158
Reflexion light	4	7
Very long cosmic ray	1	1
Faint wing of very bright stars	22	22
Bad pixel aligned	10	10
Fake detection	2	2
Missing detection	10	12
Incomplete detection on other chip	9	11
Missing detection (bright satellite)	1	1
Probability to observe a satellite per hour of observation	0.86 sat/hour	1.88 sat/hour
Tracks detected per image because of bright stars	3%	0.37%
Tracks detected per image because of bad pixels	1.3%	0.17%

Table 5.7: Summary of the detected tracks for the XSSS survey. The statistics are given for the full detector (middle column), and also on a chip based (left column).

The Hough procedure has detected successfully a total of 72 satellite tracks observed on 158 chips. Most of the tracks appear as thin as a point like source. Some appear much larger because they are issued from the closest satellites. The sampling of the WFI imager is 3 pixels for 1 meter resolution at the distance of 300 km. Some tracks are 20 pixels large corresponding to a size of 7 meters at the same distance. This resolution explains the large shape of some observed tracks.

Most of the observed satellites cross more than a chip. In some case, tracks have been observed incompletely due to the absence of detection on some chips where the satellite should be visible. The lack of detection has 2 origins. Either the track is very faint and is at the limit of detection, or the satellite is crossing a only short distance within the detector. This later case is not yet optimized by the actual procedure. A detected track on a chip could be extrapolated and propagated on the other chips, this cross-chip information is not yet used. Therefore, in case of short traveled distance on a chip, a satellite may not be detected (Figure 5.31 upper panel, illustrates a case of a bright satellite crossing a small section of the chip 6). The Hough Space unitary normalization (as described in section 4.8) compensates the amplitude of the condensation points whatever is the length of the corresponding traveled distance. The problematic of the normalization is to properly define the noise amplitude depending on the location in the Hough Space. Actually, no normalization has been applied on the Hough transform. In practice, a bright track crossing only one chip has not been detected, and 7 tracks have been partially detected. The Hough Space normalization by the unitary response was not used to prevent degeneracies in the boundaries of the Hough space (as illustrated in figure: 5.27). An improved version of this procedure will defined the proper threshold of the normalized Hough Space as a function of the unitary answer. This new version is not trivial to define because the Hough Space (normalized or not) is not thresholded directly, it is first processed by a high-pass filter. The filtering improves the signal to noise of the faint condensation points, and also it prevents fake detections from the numerous local maxima around brights stars that produce a very smooth condensation points in the Hough Space. Further tests and models will provide an ultimate threshold. Several attempts have been performed to bind the degeneracies due to the normalization, but unfortunately no robust results have been achieved yet even if in many cases the results were promising.

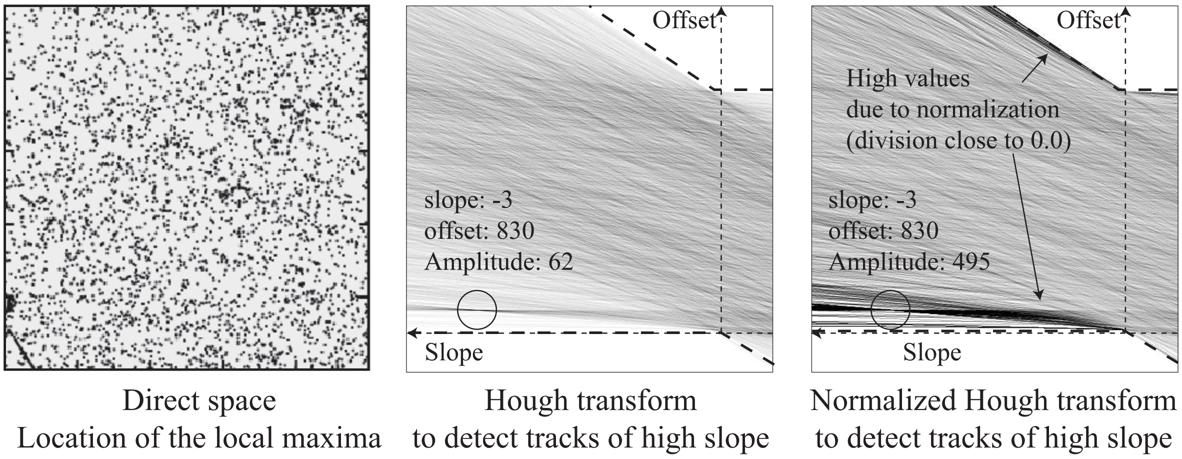

Figure 5.27: The figures illustrate the problematic normalization of the Hough Space to highlight detection of lines in the border of a chip. The left panel shows the local maxima extracted from the chip where the satellite is crossing a small portion. The middle panel show the Hough transform of the local maxima. The right panel is the previous Hough transform normalized by the unitary response (as detailed in section: 4.8). In both version of the Hough Space, the condensation point are visible. In case of the natural transform, the condensation point is not detected after high pass filtering. With the normalized Hough Space, the local maxima amplitude is as if the track was crossing the full chip (495 aligned points, instead of 62 aligned points observed). Unfortunately the normalization provide degeneracies in the boundaries of the Hough Space. One notices the homogeneity of the noise amplitude in the normalized transform in comparison of the natural Hough transform (boundaries excluded).

Due to very bright stars, 22 tracks have been detected on 22 chips. 15 of those detections are caused by 2 bright stars of magnitude 7 and 8. The 7 other cases are caused by 2 other bright stars. Very bright stars produce faint horizontal track crossing a large fraction of a chip. Those tracks are naturally detected, and should be discarded because of a bright stars in the middle of them, actually the procedure has not this facility. Note that these detected tracks are due to very bright stars polluting a large part of the chip by: the saturated pixels, the faint wing of the star, and the smooth large ghost made by secondary reflections. Also the number of detections must be compared to the amount of scientific images processed.

Some aligned bad pixels perturbate the Hough procedure, and 10 fake detections occur. Even if most of the hot pixels have been estimated from the bad pixels procedure (see section 4.1) some are remaining and enlarge the fake detection risk. Half of the detections where due to the same columns of chip 7.

The last types of detected tracks are an exceptional long cosmic ray, and some very elongated reflection lights. Only one chip from the 5912 analyzed shows a very long cosmic ray, visible on half a chip (see Figure 5.30 middle panel). Also visible on 4 images of the same pointing, a large ring of parasite reflection lights. This default was detected by the procedure only because of its quasi linear shape. Those detections are achieved at the limit of the detection which is designed to focus only on points exactly aligned. One can not rely on this approach to isolate the numerous parasites lights.

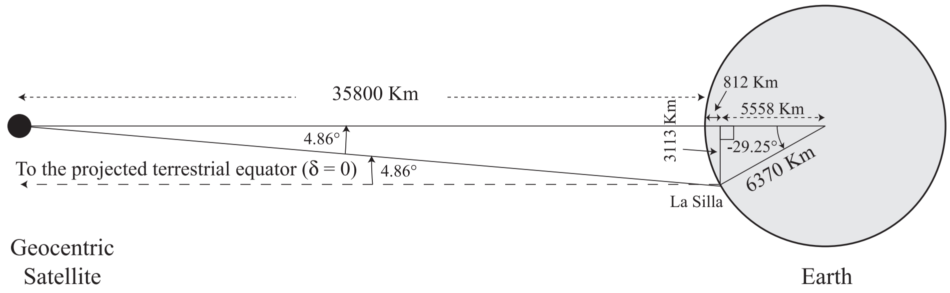

Figure 5.28: Location of the geocentric satellite from the observatory of La Silla.

Another interesting case not mentioned in the statistic is the observation of geocentric satellites. One of the field observed during the XMM survey (actually not a XMM target) is located in the geocentric belt. Due to parallax, from La Silla observatory the geocentric belt appears at latitude not equal to 0.0 (see figure 5.28 for illustration). The probability of observing a satellite at this latitude is 20 tracks per hour observations. The tracks issued from geocentric satellites are mainly horizontal. A case where 5 tracks are visible in 5 minutes of observation is illustrated at figure 5.30 (bottom panel).

5.4.4 Comparison with the Bonn pipeline

The reduced images are compared with the reduced images obtain from the Bonn pipeline. This pipeline is developed by Thomas Erben and Mischa Schirmer. It consists in numerous shell script and C binaries developed on top of existing tools: FLIPS (Cuillandre, 1999) for image manipulation, Eclipse tools (Devillard, 1997) to manipulate headers, LDAC (Deul, 1990) software to compute the astrometric solution, IRAF/drizzle (Fruchter and Hook, 2002) to warp the images, Sextractor (Bertin, 2003) to extract sources from images. This is a generic pipeline able to cope with different type of instruments. This pipeline is not yet publicly available.

In collaboration with Joerg Dietrich, comparisons of reduced images from the Bonn pipeline versus the images produced by the EIS/MVM pipeline have been achieved and are presented in this section. The tests focus on the XMM-03 to XMM-06 pointings.

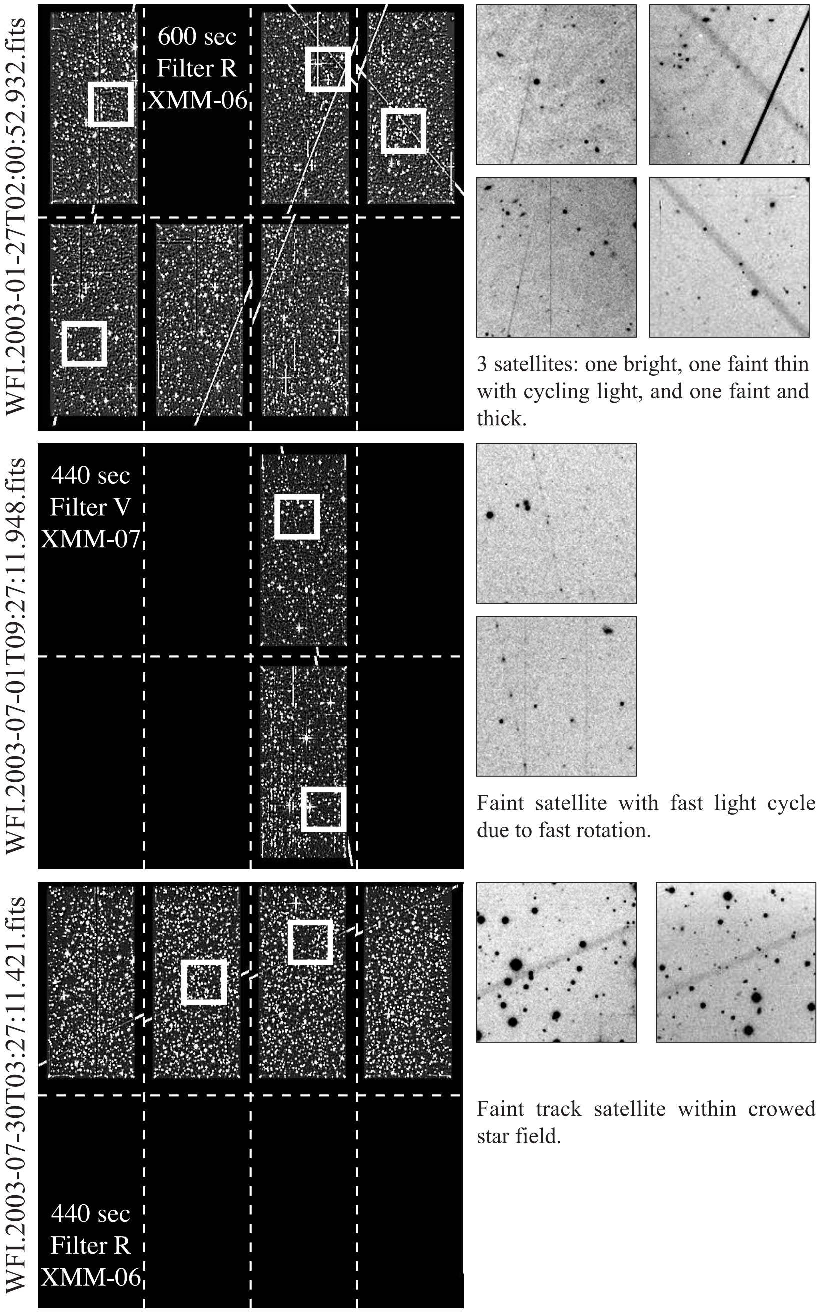

Figure 5.29: Example of detected satellite tracks with the WFI imager. The left images shows the low resolution of WFI observations, where the white dashes indicate the chip boundaries. On the right, some small square images show portions where tracks are visible on the raw observations (negative intensity scale). In the first example three tracks are detected on one observation of ten minutes. One is very bright and as thin as the seeing (chip 6, 3 and 4). Another track is faint, thin as the seeing and with light variations with a slow cycle (chip 5 and 1). The last track is much larger than the size of the seeing (chip 3 and 4). The second example details a faint track with a fast rotation period observed as a point dashed line. The third example illustrates the detection of a track, larger than the seeing within a crowed area.

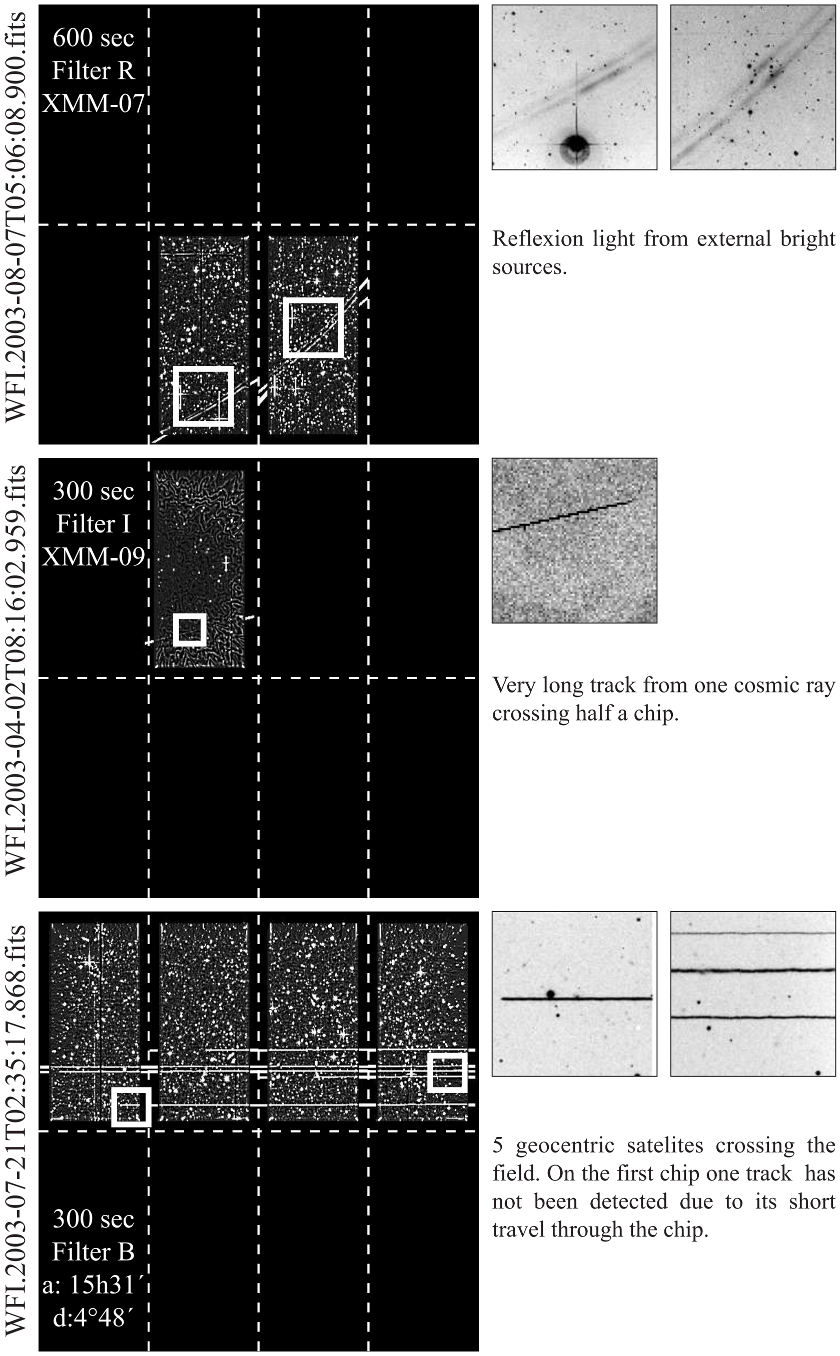

Figure 5.30: Example of detected satellite tracks with the WFI imager. The left images shows the low resolution of WFI observations, where the white dashes indicate the chip boundaries. On the right, some small square images show portions where tracks are visible on the raw observations (negative intensity scale). The first example shows the detection of a reflection light appearing as a large ring spread on chip 6 and 7. The amplitude of the ring is much more smaller on the other chips, they have not been detected by the procedure. The rings was detected only due to its very elongated shape. The second example illustrates a rare event: a cosmic ray crossing half of a chip. The last case illustrates the detection of the tracks where geocentric satellites are visible. Five tracks are visible with chip 4. Note that the short contribution of a track in chip one has not been detected.

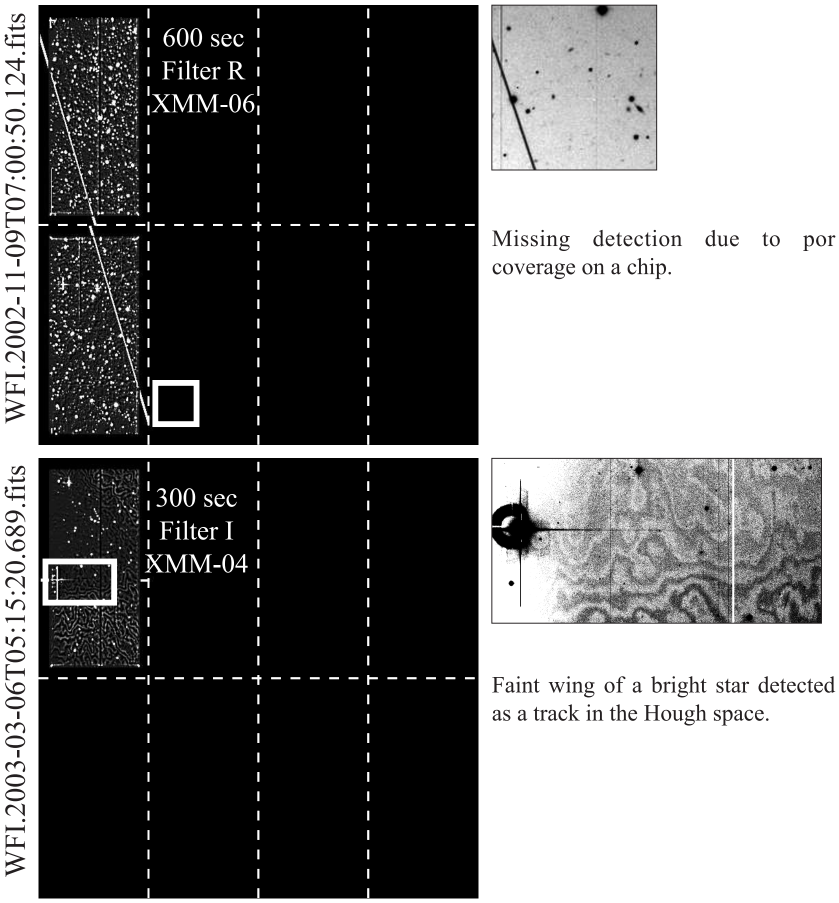

Figure 5.31: Example of detected satellite tracks with the WFI imager. The left images shows the low resolution of WFI observations, where the white dashes indicate the chip boundaries. On the right, some small square images show portions where tracks are visible on the raw observations (negative intensity scale). In the first case, a track has been partially detected from chip 1 and 5, but no track has been detected on chip 6. This is due to the poor coverage of the track long of 450 pixels in the chip 6. The second illustration shows a detected track at the location of a bright star. The cut out show the long and faint wing of the star that cross half of the chip.

Local defaults removal comparison

On the reduced images, no cosmic rays are visible from the two reductions. One may notice some remaining cosmic rays spread close to the borders of the reduced images issued from the EIS/MVM pipeline. At those locations less than three RBs are stacked and the rejection using a minimum of three images cannot been used. The Bonn pipeline uses Sextractor applied on the individual images to recognize cosmic rays from other astronomical sources. The photons issued from the astronomical sources are affected by the atmosphere, and the corresponding sources appear smoothed. By contrast, cosmic rays cross the atmosphere with no interaction, and appear very sharp on the raw images. The extracted sources smaller than the mean seeing are assumed to be cosmic rays. This procedure is robust. If the mean seeing is poorly sampled (pixel scale smaller than two times the mean seeing), stars also appear as sharp points and the dissociation with cosmic rays is made difficult. In summary, this approach gives good results for groundbased instruments, where the sampling is beyond the Shannon constraint. In case of WFI, the pixel scale is 0.24 arcsec, and the seeing is typically 0.8, to 1 arcsec.

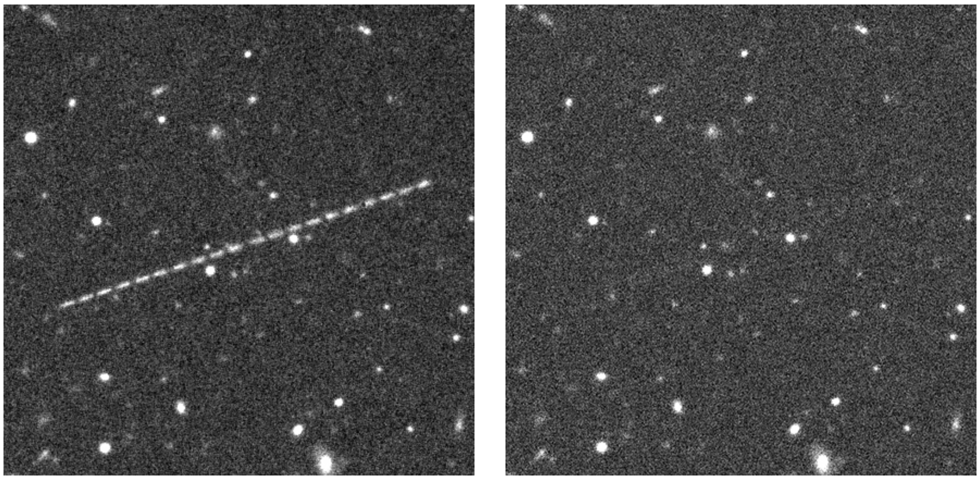

Figure 5.32: Comparison of the Bonn reduced images (left panel) versus the EIS/MVM reduced image (right panel) where a moving asteroid is observed. The asteroid is masked on the left image, one can notice faint wings that as not been removed by the sigma clipping rejection. The reduced image combined 40 raw images observed in two distinct nights. The asteroid appears 20 times.

The two different procedures to remove cosmic rays provide similar results. In case of slow moving objects (far asteroids for instance), the reduced images may be different. A moving asteroid will not be classified as cosmic rays because its shape is comparable to an elongated star larger than the mean seeing. By contrast, the sigma clipping procedure will remove the significant pixels of the asteroid if it moves sufficiently enough from one image to the others within a RB. In summary, the sigma clipping procedure will remove all objects including asteroids with significant signal to noise (set to 2.5 in the case of the EIS/MVM pipeline). The shape analysis approach will not removed moving asteroids. Figure 5.32 shows a cutout of the XMM-04 target observed with the I filter. A total of 40 images observed in two distinct nights are combined. The asteroid appears as 20 marks. Each one as its flux divided by 40 due to the number of combined images. A remaining default appearing on one image has its flux divide by N the number of combined observations, and its signal to noise ratio decreasing by $1/\sqrt{N}$. Concerning the moving or variable objects, both strategies are not suitable. A special study of the images before stacking should be done to observed the moving or variable sources.

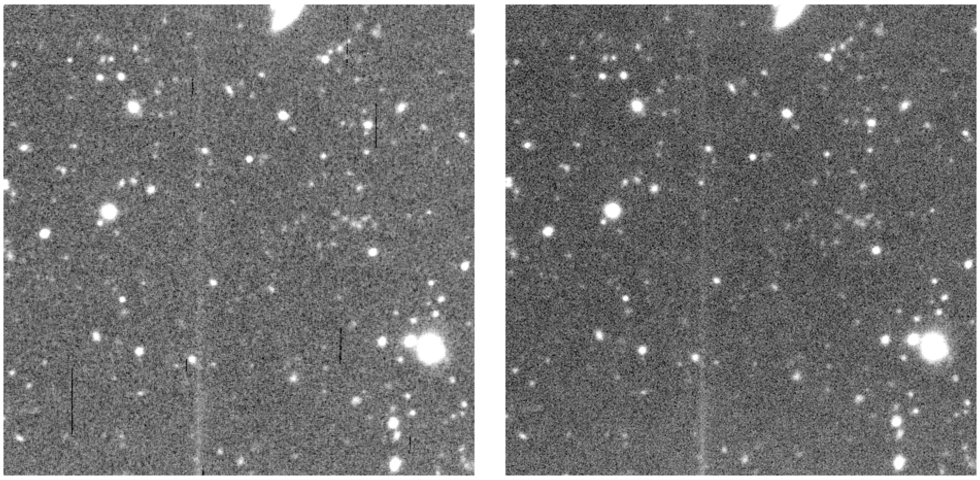

Figure 5.33: Comparison of the Bonn reduced images (left panel) versus the EIS/MVM reduced image (right panel) where a moving asteroid is observed. The asteroid is masked on the left image, one can notice faint wings that as not been removed by the sigma clipping rejection. The reduced image combined 40 raw images observed in two distinct nights. The asteroid appears 20 times.

Another important point of comparison is the remaining bad-pixels and bad-columns. The hot-pixels are detected by the special procedure used to recover the lack of dark observations. In case of the Boon pipeline, no special strategy is adopted when no dark observations are taken. Figure 5.33 illustrates the final product made of 40 images. The cut-out shows a small portion of the chip 7 of the WFI instrument. This one suffers from numerous hot-pixels. The procedure adopted for the EIS/MVM pipeline shows its positive cosmetic impact of the reduced images.

Noise properties of the reduced images

The noise correlation is analyzed by computing the power spectra of the noise of the reduced images observed in the Fourier space. The noise is isolated from the astronomical objects using a wavelet decomposition. The significant objects are masked in the wavelet plan, and an image is rebuild from the non significant coefficients. This strategy gives a good images empty of astronomical objects showing only the noise. The power spectra of the noise is then smoothed with an pyramidal median transform to highlighted the envelope of the power spectra in lower spectra resolution. Figures 5.34 illustrates the noise correlations of a reduced image by the Bonn pipeline (left panel), and the noise correlation of a reduced images by the EIS/MVM pipeline (right panel). One sees clearly the imprint of the kernel used for the warping procedure. For the Bonn pipeline reduced image, the power spectra shows clearly its

Gaussian shape. In case of the EIS/MVM reduced images, the power spectra is characterized by sharp edges as expected for the Lanczos warping.

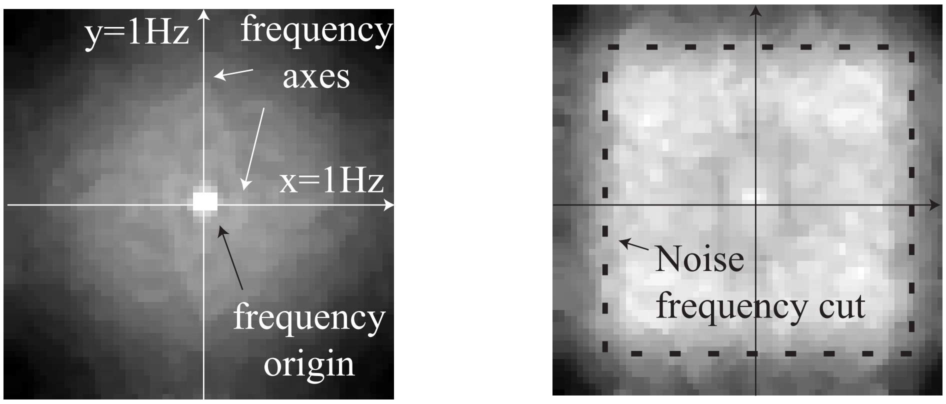

Figure 5.34: Noise correlation property as function of the warping kernel.

Astrometric calibration comparison

The 4 reduced pointing XMM-03 to XMM-06 observed in R passband are used to compare the astrometric residual of the extracted catalogues from the reduced images of the 2 different pipelines versus the GSC2.2 catalogue. Figures 5.35 and 5.36 shows the astrometric residuals for the 4 reduced images. One can notice that the residual given by the EIS/MVM pipeline are always smaller by 30%. This accuracy is due to the astrometric catalogue used. The images processed by the Bonn pipeline have been calibrated with the USNO catalogue. This one is deeper than the GSC2.2 but suffer from large proper motion (the catalogue is older) and larger internal residuals.

From the astrometric comparison with GSV2.2 (see figure 5.35), one notices the large residuals of the XMM-05 reduced image from the Bonn pipeline. In order to explain this large RMS, the astrometric residual of the 2 astrometric catalogues USNO and GSC2.2 are compared, and then the UCAC2 catalogue, used as reference, is used to validate the GSC2.2 catalogue. The residuals (see Figure 5.37) proves that the 2 catalogues USNO and GSC2,2 are not in agreement. The small astrometric residuals from UCAC2 and the GSC2.2 shows the expected internal accuracy of the GSC2.2 catalogue, therefore the USNO catalogue has large residuals at this sky location. The reduced image of XMM-05 from the Bonn pipeline suffers from the imprecise USNO catalogue. This observation should lead us to chose GSC2.2 catalogue for astrometric solution even if this one is one or two magnitude shallower than USNO. Indeed, the deep objects of the USNO catalogue do not provide better statistics because the faint observed stars have larger photo-center uncertainties.

PSF anisotropy analysis

The comparison of the Point Spread Function are done with the Kaiser-Squites-Broadhurst (KSB) algorithm. The PSF anisotropy is evaluated by analyzing the ellipticity of the observed

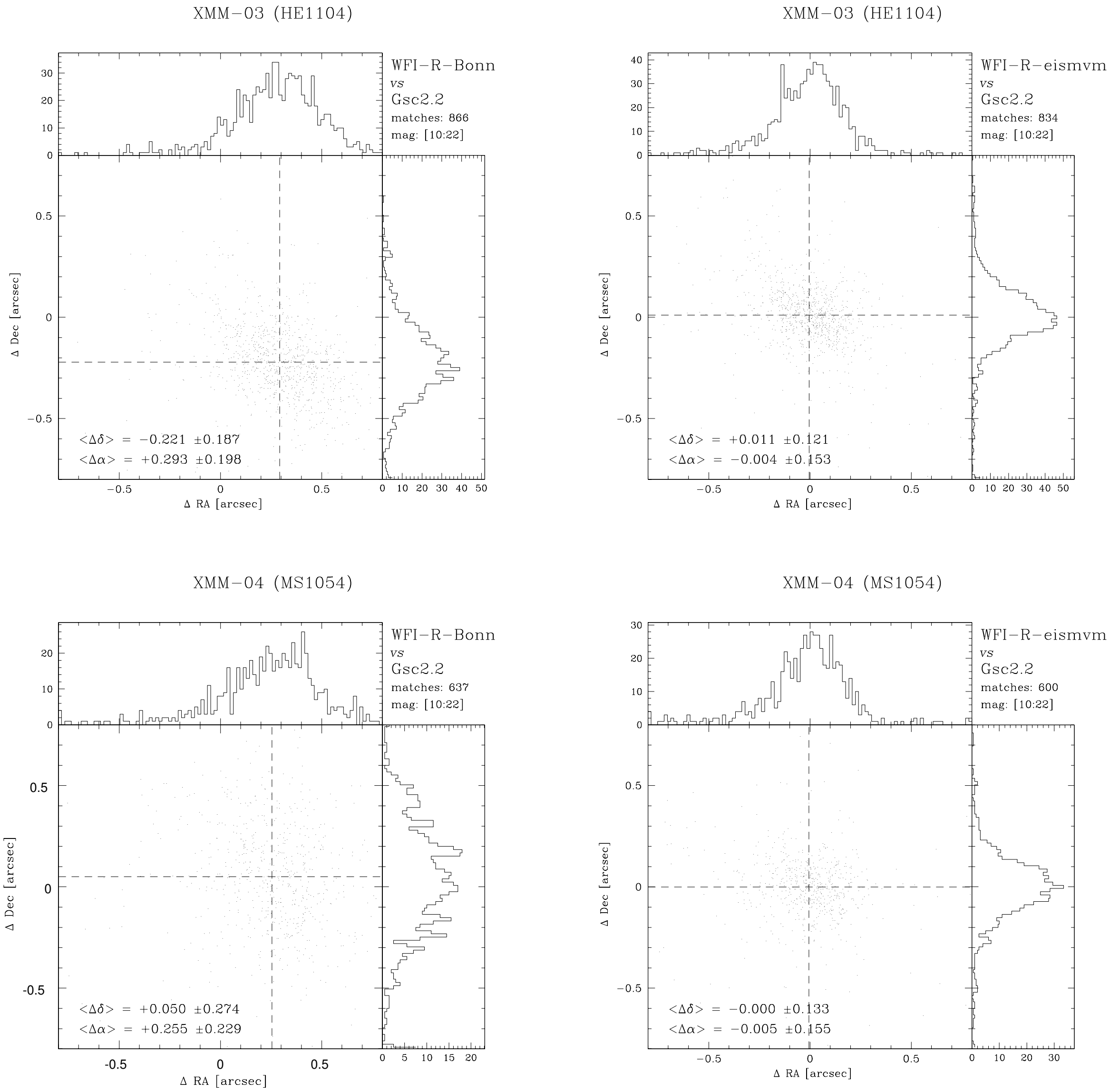

Figure 5.35: Astrometric comparison of the reduced WFI images from the EIS/MVM pipeline and the Bonn pipeline. 4 pointing observed in R passband are compared: XMM-03, XMM-04, XMM-05 and XMM-06. The 8 plots show the astrometric residual of the extracted catalogues from the reduced images associated with the GSC2.2 astrometric catalogue. The right column gives the 4 astrometric residual obtain with the images reduced by the Bonn pipeline, the left column refers to the EIS/MVM reduction.

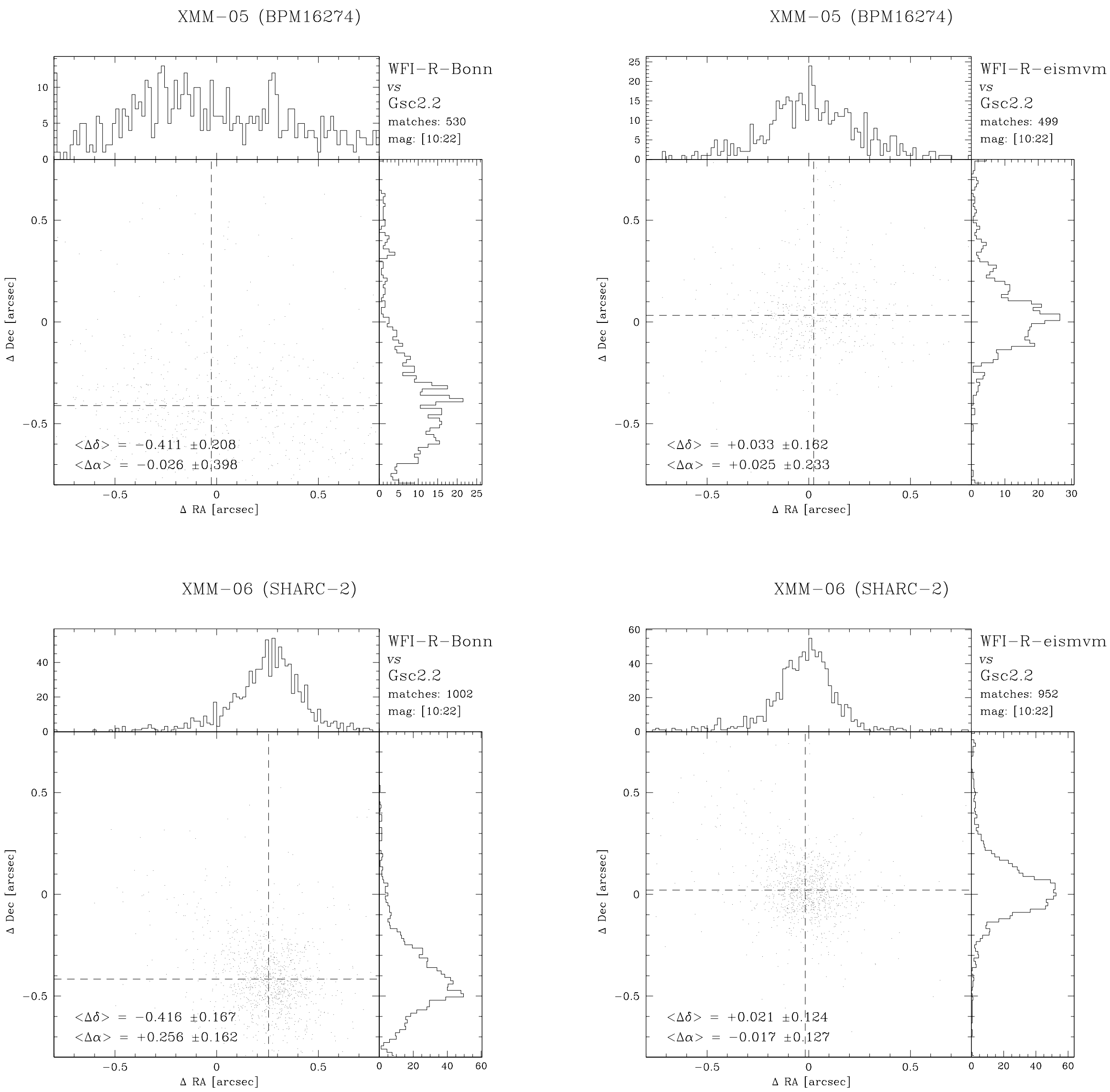

Figure 5.36: Astrometric comparison of the reduced WFI images from the EIS/MVM pipeline and the Bonn pipeline. 4 pointing observed in R passband are compared: XMM-03, XMM-04, XMM-05 and XMM-06. The 8 plots show the astrometric residual of the extracted catalogues from the reduced images associated with the GSC2.2 astrometric catalogue. The right column gives the 4 astrometric residual obtain with the images reduced by the Bonn pipeline, the left column refers to the EIS/MVM reduction.

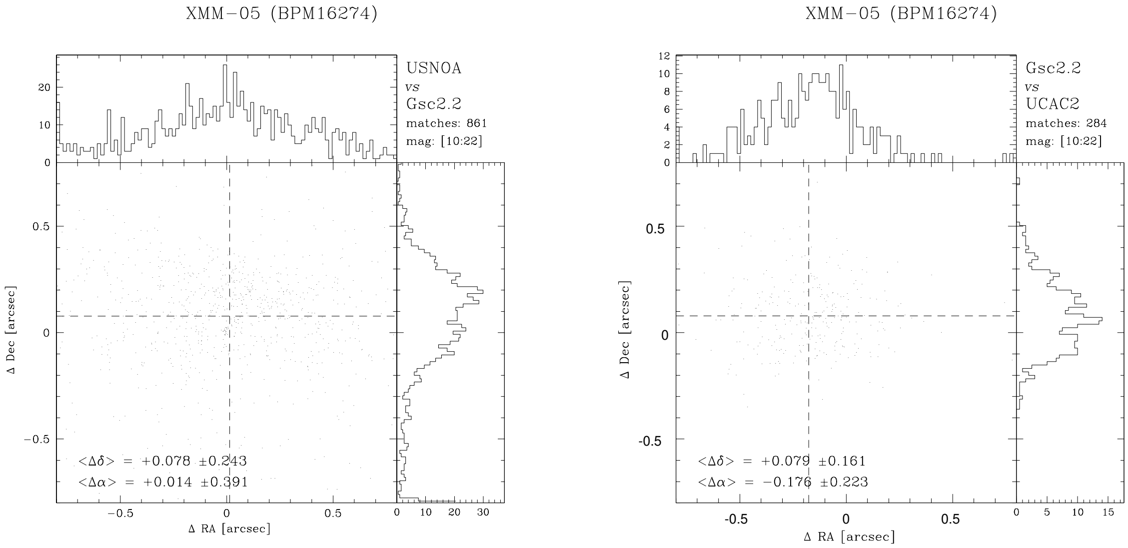

Figure 5.37: Astrometric residual of the USNO catalogue versus the GSC2.2 (right panel), Astrometric residual of the UCAC2 versus GSC2.2. One notices the large asymmetric residuals of the USNO versus GSC2.2 whereas, the GSC2.2 agreed quite wheel with the UCAC2 catalogue.

stars spread on the full reduced field. The reduced images used for the comparison are the stack of 5 images observed in R passband of the XMM.02 target (SHARC-2). The variation of the ellipticity is modeled by a polynomial function. The Figure 5.38 shows the modeled ellipticity of the PSF as a function of the location of the observed stars within the image. Both model are similar. The remaining PSF anisotropy after modeling is 0.6% in both case.

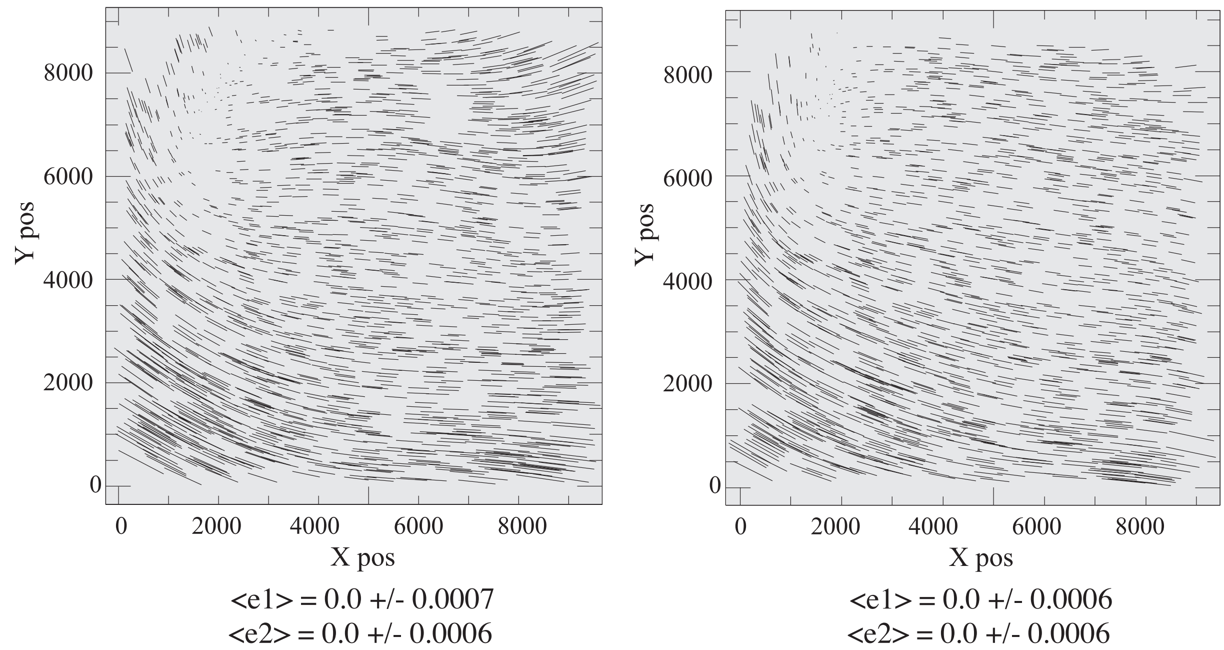

Figure 5.38: PSF anisotropy computed with the KSB algorithm of the WFI reduced images of the XMM-02 by the Bonn pipeline (left panel), and by the EIS/MVM pipeline (right Panel). The 2 plots are similar and give the same ellipticity variation. One can notice on the upper-left corner of both plot the larger ellipticity of the

Photometric comparison

The images reduced by the Bonn pipeline are photometrically calibrated using the standard stars observations. Both pipelines are not removing the illumination effect. The photometry of the reduced images is compared to check the homogeneity of the ZP within the chips. The extracted catalogues of the reduced images are associated and for each association one plots the magnitude difference versus the magnitude of the Bonn reduced images taken as reference. The magnitude are computed using Sextractor. The aperture magnitude with 4 arcsec diameter is chosen. The MAG_AUTO magnitude cannot be used to check the different magnitude because this one is affected by the noise correlation and the objects are estimated brighter with stronger noise correlation. The aperture magnitude is independent of the noise frequency-cut.

Figure 5.39 illustrates the photometric comparison of the four fields observed with the R filter. For the three first cases (XMM-03 to XMM-05), the photometric comparison shows good agreement between the 2 reductions. The comparison are not zero centered because no photometric solution have been computed for the reduced images from the EIS/MVM pipeline, only a default ZP have been applied. For the bright sources (brighter than magnitude 16) the sources issued from the Bonn pipeline reduction appears shallower (up to 1 magnitude shallower for objects of magnitude 13). Those bright sources are observed in the non-linear part of the detector (from 40000 ADU to 64536 ADU the saturation level). Pixels of high value (greater than 40000 ADU) have been masked (set to 0) during the pre-reduction of the images by the Bonn pipeline. The final weight map show holes equal to zero, and therefore sextractor is not integrating the pixel value to the integrated flux of the objects. The flux of the bright sources are therefore underestimated, and appear shallower.

The last field XMM-06 compared in Figure 5.39 (bottom, left), shows different modes of agreement of the photometric comparison. The multiplication of lines are due to badly corrected relative mean gain chip-to-chip. In order to validate the relative mean gain harmonization of the EIS/MVM reduced images, one of the four RBs stacked is reduced by keeping its background (using the stellar RM). The reduced images is then transformed with the pyramidal transform up to scale 7 (see illustration Figure 5.40). This very smoothed images does not show any step from one chip to another. The largest step is 1% from the 2 bottom-right chips. This image proves that the mean gains of the chips have been properly harmonized. Note that for all the 4 photometric comparisons, one can see for middle bright associated sources a dispersion of 0.04 magnitude that can be due to residual of gain harmonization. The photometric dispersion of the XMM-06 pointing caused by the Bonn pipeline has been fixed and the tool is now more robust.

Photometric comparison of I passband images

The I filter of the WFI imager provides lots of fringes on the raw images. 2 different ways can be used to estimated and remove the fringes. The Bonn pipeline strategy use a fringing-map computed by merging all the raw images observed with the I filter during couple of nights. The computed fringing-map is then scaled to each raw images to clean them. The EIS/MVM pipeline was tuned to estimated the fringes from the Reduction Blocks (RBs) themselves. Each time, 10 WFI I images have been observed consecutively. Per RB a fringing-map is computed with a two-pass approach exactly like for IR date cube.

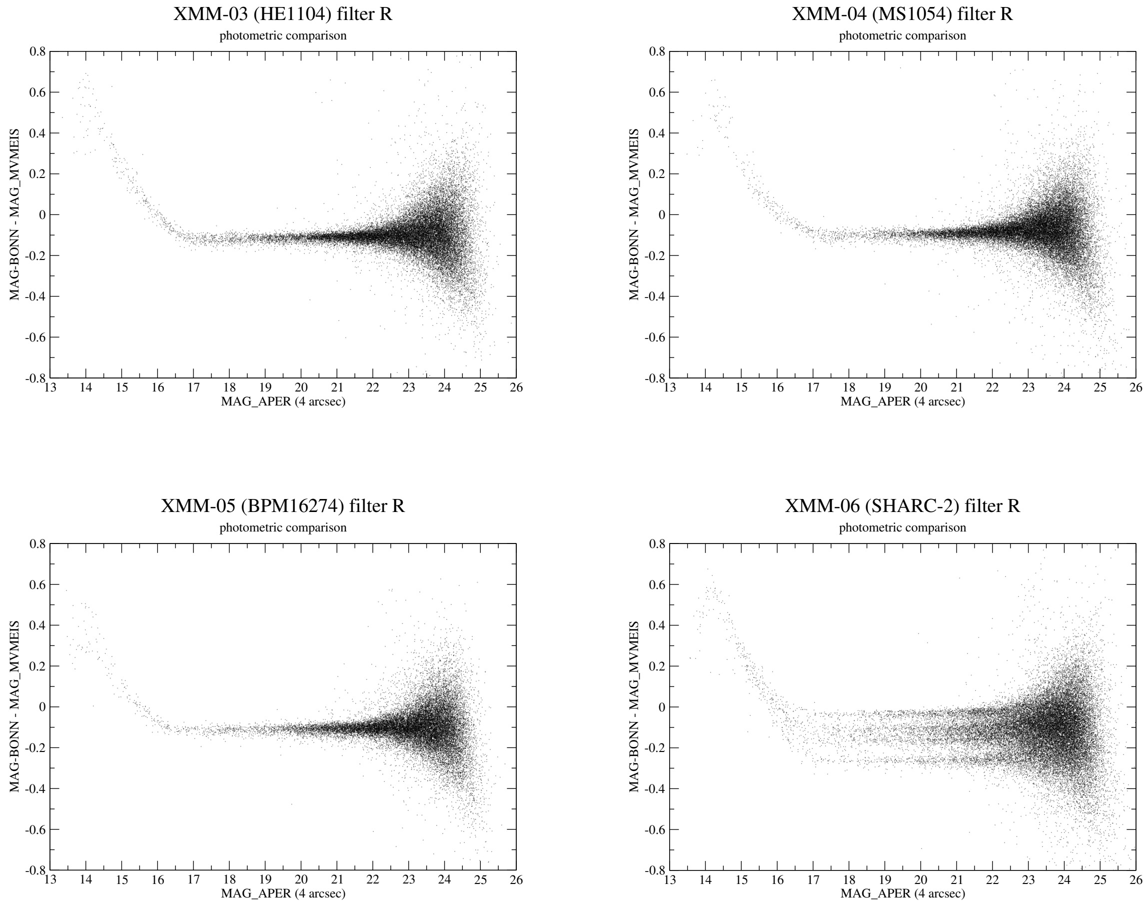

Figure 5.39: Photometric comparison of the reduced WFI images from the Boon and EIS/MVM pipeline of the XMM-03 to XMM-06 R filter pointing. The photometry is computed with an aperture magnitude of 4 arcsec diameter. The comparisons do not show chip to chip ZP variation except for the XMM-06 pointing.

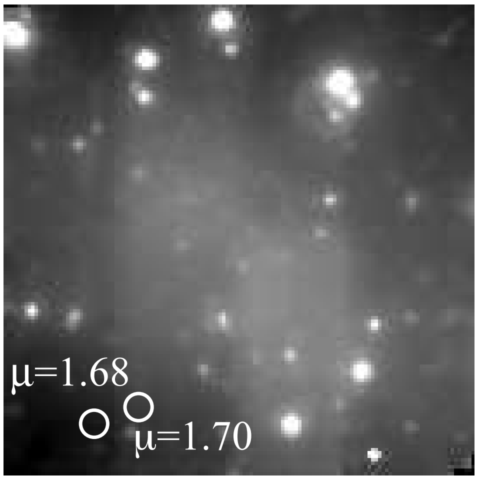

Figure 5.40: Reduced image of a RB containing 5 images observed in R passband. The background has not been removed to check the gain variation chip to chip. The image shown is a smooth version of the reduced one with a pyramidal median of 7 scales. This smoothed version with no noise highlight the steps between chips. The maximum step is given by the background amplitude from the 2 right-bottom chips. The mean background value for the 2 circles is written on the image. The maximum amplitude variation is 1%.

For each pipeline, the XMM-04 reduced image observed with filter I is used to benchmark the photometry. The reduced images do not show image quality differences, no fringe residuals are visible by eye even on smoothed images. The two extracted catalogues are associated and then compared, figure 5.41 shows the magnitude differences. The continuous gray line gives the running median of the points. No special trend is observed from the photometric comparison. The two procedures offers same results and quality. Note that the EIS/MVM pipeline can be operated in both mode: fringing-map estimation from a technical RB, or within a science RB.

Comparison summary

The table 5.8 gives the summary the comparison from the 2 pipeline strategies.

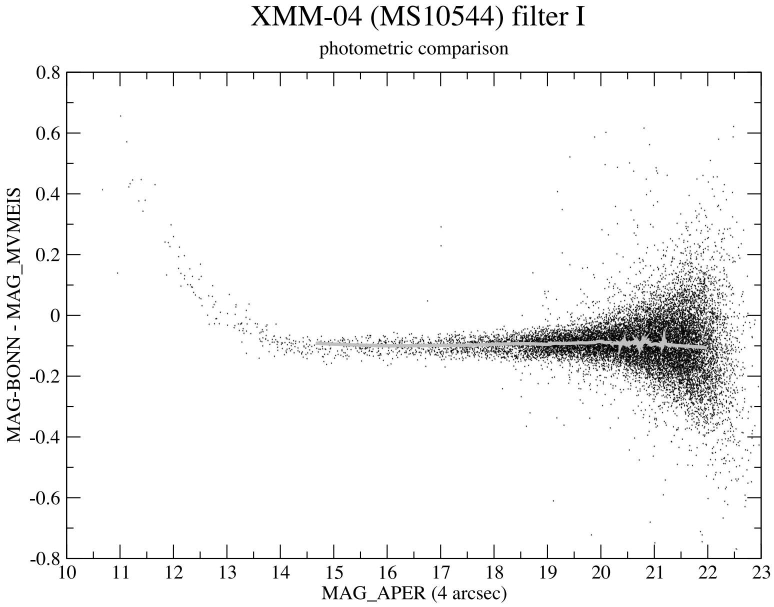

Figure 5.41: Photmetric comparison of the I reduced images from the Bonn pipeline versus the EIS/MVM pipeline. The constant magnitude shift is due to the un-calibrated images reduced by the EIS/MVM pipeline. The bright objects (brighter than magnitude 15) looks shallower than the EIS/MVM reduced images. This effect is due to the masking of saturated pixels from the Bonn pipeline (this phenomena is also highlighted at Figure 5.39). The quite large magnitude distribution from the middle bright associated objects (0.07 magnitude) is maybe due to residuals of mean gain computation or by residual fringes (that are not visible by eye). The fain end of the magnitude comparison to not show significant trend.

Designation	Bonn pipeline	Eismvm pipeline
Fringe pattern estimation	Background map built from all observations.	Background map build from the RB themselves.
Astrometric catalogue	USNO	GSC2.2
Astrometric solution	No faillure	No faillure
Warping kernel	Gaussian Kernel (drizzle)	Lanczos kernel
Cosmic rejection	From extraction analysis	From sigma clipping rejection (3 or more images), during stacking and mosaicking
Satellite tracks removal	Manual masking	Automatic masking with the Hough Transform
Relative photometry (chip to chip)	From objects observed with 2 different chips from dithered observations.	From sky background value of the background sky of scientific images.
Absolute photometry	Yes	No. Standard are reduced but no photometric solution is computed.
Implementation	Fusion of low levels tools (Sextractor, Drizzle, IRAF, FLIPS, Eclipse tools, LDAC) organized in 40 UNIX shell scripts, 100 individual C programs.	Integration with an unique source code: 1 binary and 1 configuration file.
Reduction rate	5 WFI images per hours with Beowulf 8 CPUS Athlon 2800+ machine.	20 WFI images per hour with 2 CPUS Athlon 2000+.

Table 5.8: Comparison summary of the Bonn pipeline versus the EIS/MVM pipeline for the XSSS WFI imager observations.

Survey name	Camera	V	Band	#fields	Volume	#raw	Int	Release date
CDFS	WFI	1	U.B.V.R.I	1	5.5 Gb	400	60h	07 03 2001
CDFS	SOFI	1	J.Ks	16	0.4 Gb	2400	40h	09 05 2001
XSSS	WFI	1	B.V.R.I	12	77 Gb	740	85h	30 08 2004
GOODS	ISSAC	1	J.H.Ks	8	0.2 Gb	2300	80h	09 04 2002
"	"	2	J.Ks	24	0.9Gb	7200	250h	19 04 2004
FLAMES	WFI	1	B.V	6	6.2Gb	36	20min	06 07 2001
"	"	2	B.V.I	53	151Gb	480	23h	24 03 2003
"	"	3	B.V.I	87	261Gb	780	39h	end 2004
Total	ISAAC			24	0.9 Gb	7200	31 n	
Total	SOFI			16	0.4 Gb	2400	5 n	
Total	WFI			153	0.5 Tb	2400	26 n	

Table 5.9: Summary of the realised achieved with the pipeline.

5.5 Application summary

Table 5.9 summarizes the surveys that have been reduced during the Ph.D by myself. In column (1) is given the name of the survey, the instrument used is specified in column (2). Some surveys have been released several time, column (3) gives the number of the release. The filters used are given in column (4). The number of sky region connected or discontented is given in column (5). The volume of the raw science images that have been reduced is given in column (5), the unit is GigaByte (Gb), or TeraByte (Tb). The number of science processed raw images is in column (6). The total integration time of all the science frame reduced is given in column (7), the unit adopted is hour (h), or minute (min), or night (n). And finally the date of the release is given in column (9). The three last lines of the table indicates per instrument (WFI, SOFI, and ISAAC) the cumulated statistics of columns (5) to (8). The total integration time given is in unit of night. It is computed assuming that during a night, 8 hours are dedicated to science observations. Note, that all those numbers do not include the reduction of calibration frames and photometric standard fields, even if both have been reduced. It is important to emphasize that the numbers quoted in the table do not include the reduction carried by other members of the EIS team. All the mentioned surveys were reduced by myself, and were an experimentation field for exhaustive tests made to validate the reduced images. In practice, the mentioned surveys have been reduced couple of times up to 6 times in order to improve the low level options of the RMs. The development of the software was dictated by the experiences achieved on the various releases.

It is worth comparing the total integration time of the reduced images with the total integration time of the science images archived at ESO since the first light of the instruments. If one assumes that 75% of the nights are used for science observations, taking in consideration the bad-weather and the technical nights around the full moon, then one gets 274 nights per year of operation. In case of ISAAC, the instrument is used since 2000, and 1370 nights have been observed up to the end of 2004. The total integration time of ISAAC reduced images corresponds to 2.3% of the total integration time of the science images archived at ESO. In case of WFI one gets a value of 1.6% compared to the archived images that are cumulated since the beginning of 1999. Note that if one includes the last EIS release of the WFI/DPS survey, the ration is increasing up to 3.6%. The two ratios indicate that a significant fraction of the ESO archived images have been successfully reduced and released to the community. Also, the ratios prove the ability of the pipeline to cope with very large set of data with a volume comparable to a full archive system.

With the released surveys, most of the observational type of targets have been reduced successfully. In optical domain, pointings from very deep fields such as the CDFS, to the most crowded fields such as globular clusters or LMC have been handled. In case of optical domain, only deep surveys have been reduced. The strategy using external fringing-map for the IR observations of extended sources has not been tested.

Also, the exhaustive tests presented in this chapter illustrate the following points: First, the signal processing developed for astronomical images benefits from algorithms developed for other fields of application such as the Hough transform and the bi-orthogonal wavelet transform; Second, the development of the pipeline with an integrated implementation gives lots of facilities offering high speed processing; Third, the XML format used for the configuration files and the reduction logs proves to be optimum and offers a total and flexible control for all parameters; Fourth, the exhaustive tests and released surveys were mandatory to make the procedures converging to robust results.

Chapter 6

Conclusion

Since December 2003, the pipeline has been made publicly available. It consists of the complete source codes (100 000 lines) that is compatible with most of computers (Linux, Alpha, Sun, Irix). A documentation of 100 pages is given to operate the pipeline in both simple or expect modes. The following institutes have used successfully the pipeline: Marseilles observatory, Trieste observatory, ESO (non EIS), Nice observatory, Leiden university, Louvain university. This short list is not exhaustive, and concern only people in contact with the EIS team. The diffusion of the software is made thanks to collaborators of the team. Currently people are using the pipeline for small set of data (couple of nights only), and mainly for WFI images. Note the promising experience of the Louvain University using the pipeline for a future single-chip detector mounted on a telescope based on the Canary island. Currently, the EIS/MVM pipeline has been downloaded by 70 persons around the world.

One objective of the pipeline was to handle variety of current and ongoing instruments. For the time being, the pipeline has been extensively used for the WFI, SOFI and ISAAC instruments. Also other ESO imagers have been handled such as FORS1, FORS2 and VIMOS (see instrument layout figure 3.1). The future large ESO instruments are VST and VISTA:

- VST - The first one will be operational mid 2005. This one square degree instrument is made of 32 CCDs ($2k \times 4k$ pixels each). The data volume is estimated to 48 to 152 Gbyte of data per night (4 times the WFI rate), or in other words 0.35 to 2.12 MegaPixel per second. This acquisition rate is comparable to the one obtains by the pipeline when reducing WFI images: 0.38 MegaPixel per second (one machine AMD Athlon, 2 CPUS, 1.7 MHz). It is worth emphasizing that with the current configuration (software and computer), the VST images could be reduced as fast as they are observed.

- VISTA - The future VISTA instrument is a large IR mosaic made of 16 CCDs (2k pixels each) mounted on a 4 meters telescope. The data volume is estimated to roughly 400 GByte per night. The data rate is estimated from 2 to 12 MegaPixel per second. This rate is higher than the VST one even if both instrument have the same number of pixels. The exposure times are much shorter for IR detectors (from 10 seconds to 1 minute), thus imposing a higher rate. With the current settings, the reduction rate of ISAAC/SOFI images is 0.3 MegaPixel per second. In order to reduce VISTA images at the same rate as the acquisition, the reduction must be speed up by 7 to 40.

This speed improvement needed for VISTA images is accessible by faster machines with several CPUs. It is important to say that fast machines are not characterized only by the CPU speed. Indeed, a large set of WFI images has been reduced with exactly the same time by 2 similar computers except for the CPU speed: 1.7 MHz and 2.7 MHz (one could expect an improvement of 60%). In fact, when dealing with large data, the main limitation is the time to access the data located in RAM of the computer. To simplify the computer architecture, the internal CPUs clock is typically several GHz, and the RAM is accessed by a clock of typically 128 MHz (more recently 512 MHz to 1GHz). A small and fast memory named *cache* plays the role of buffer between the CPUs and the RAM. The RAM access is artificially speeds up for data smaller than the cache size. Unfortunately, caches are typically 4 or 8 Mbyte, which is too small to handle large images (32 MByte in float format for a CCD of $2k \times 4k$ pixels). In practice, the CPUs are "waiting" for the data located into the RAM. Note that the pipeline is optimizing the hard-disk access as most of the procedures are exclusively executed in memory, and only 15% of the total reduction time is dedicated to input/output operations. Therefore the reduction rate would be drastically improved using recent computer with fast RAM access. Using existing machines with 4 times the RAM access and 4 CPUs, one gets an improvement of 8 in comparison to the current EIS survey machines, thus reaching a reduction rate of 2.4 MegaPixel per second.

The current pipeline implements a generic instrument made of one or several chips arranged into a matrix. Also the current framework imposes the chips to have the same orientation and pixel scale. With this definition, the instrument with more complex geometry are not supported. For instance the LBT telescope is mounted with an instrument of 4 rectangular CCDs: 3 verticals and one horizontal on the top. This layout is not yet compatible even if the images could be reduced partially. It is worth emphasizing that only the keyword filtering of the preparation part, and the mean gain harmonization of the reduction part, cannot been executed.

A test has been made on the CFHT 12k camera. This one is made of 2 by 6 CCDs of $2k \times 4k$ pixels each. The chips are arranged into a matrix, but unfortunately the upper and lower CCDs are not coded in the same way. The lower ones are rotated by 180 degrees from the upper one. This layout is not compatible with the current pipeline, and the two mentioned steps were not activated. Nevertheless, a group of 5 images has been reduced successfully, as illustrated in figure 6.1. One notices the steps between some chips, as the mean gain has not been harmonized. Also some bad-columns are visible (top-right). The raw images are already processed by a master bias and flat, and the master flats are not available therefore the bad pixels could not been detected with the current procedures. The images have been reduced in "stellar" mode: the sky background has not been estimated and is still present on the reduced image. Note that the raw images have been handled fully automatically after the instrument has been described into the configuration file.

The next administration improvement will be dedicated to support detectors with complex chip geometry, and for detector with the ability to rotate from one exposure to the next (as for instance the spectro-imagers FORS1 and FORS2).

The astrometric calibration implemented by the pipeline is carried out on a chip based. In other word, an instrument made of N chips is considered by the astrometric calibration procedure as N independent instruments. This strategy does not take in consideration that chips are connected and one should use this knowledge. If one assumes that the N chips have

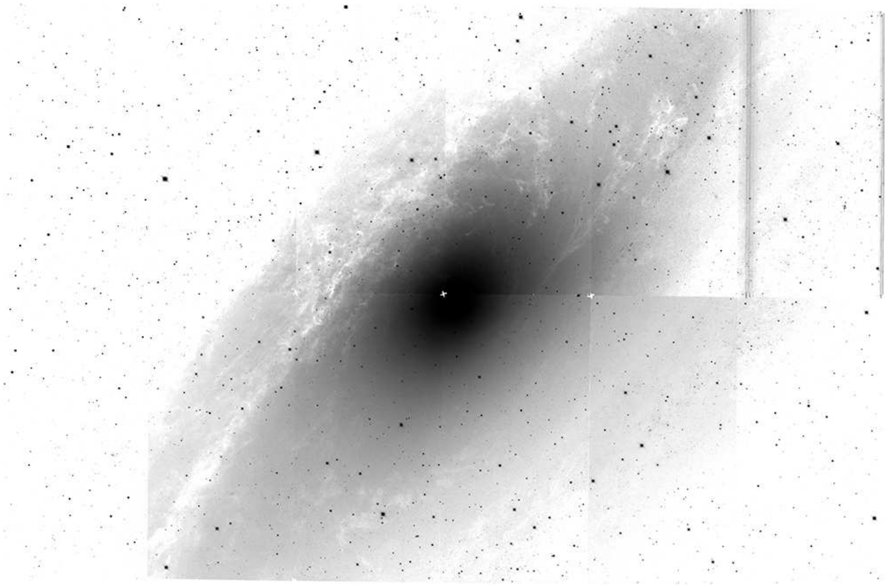

Figure 6.1: Reduced image of M31 observed with the 12k camera mounted at the CFHT telescope. The Reduction bloc is made of 5 images observed with the V filter. The total exposure time is 150 seconds.

always the same location between themselves, then $N-1$ first order relations (6 free parameters each) are sufficient to describe their geometrical relations. A typical absolute astrometric solution of order p is characterise by $(p+1)(p+2)$ free parameters. With the current implementation. An astrometric solution is made of $N(p+1)(p+2)$ free parameters. If one considers the geometrical relations between chips, an optimized astrometric solution is made of $(p+1)(p+2)+6(N-1)$. The number of parameters is asymptotically divided by N with the second approach when the number of chips is increasing. In fact in this case, the global astrometric solution depends mainly on the order of the astrometric distortion, and few on the number of chips. One expect more robust astrometric solution at the borders of chips, and also a global better adjustment with a global strategy.

Several algorithms presented in chapter 4 have some limitation, and needs better pre-filtering to achieve better results. The following list gives the mean direction of the improvements:

- Satellite detection with Hough Transform - Two main improvements are
  - True thresholding of the Hough Space - The current threshold made in the Hough space does not give a good weight to potential tracks observed at the border of the chips (see limitation 5.27). The natural Hough normalization (presented in section 4.43) gives degeneracies in the border of the Hough Space. A post-filtering should be defined to removed fake candidates.
  - Sub-image detection - The Hough detection is applied on a chip based. The detection of track is optimal for the one crossing the full chips. A sub-window analysis should offer better signal to noise for the rare track crossing only a portion of the chip.

  - Blooming and satellite dissociation - The blooming of the bright stars is crossing a full CCD. This alignment is detected as a track with the Hough procedure. A post filtering should defines if a detected track is caused by a bright star. Then these tracks would be discarded.

- Illumination correction - The main limitation to compute a valid illumination-map with the “differential approach” (see section 4.3.2) is the short time variation of photometric ZP. In practices, only observations with special atmospheric conditions could be used for a successful computation. More systematic tests could quantify the illumination-error implies by the sky when the transparency varies.

- External fringing-map - A fringing-map is scaled to a scientific image using an cross-correlation coefficient. A more complex procedure could compute cross-correlation coefficient by sub-portion of the image. This might improve the fringes subtraction for large extended sources where fringe amplitudes are larger.

- Sky background estimation multi-chip - The sky background is estimated per chip. In general the sky background is a very smooth signal that could be estimated over the full detector. For multi-chip instruments, the estimation could be carried out after assembling all reduced chips to one final image. This technique shall provide more robust results in comparison to a single chip estimation.

The present works was motivated by the need of automatic reduction of images observed from various instruments. This goal has been achieved thanks to robust procedures and an integrated strategy. The automation has been pushed up to a level where very few manual interactions are still needed, such as: downloading of the images, description of the final products (projection grid, pixel scale), check of invalid data. An improved version of the pipeline shall tend to automatize the few remaining manual steps. Reaching this level, the entrance point of the pipeline could be just a collection of raw images from different instruments. Connected to an archive system, the pipeline could process by itself images automatically selected from the archive, and then it could deliver optimum final products in a multi-instruments context. This paradigm is accessible by improving the preparation steps and adding the following items:

- Image selection from the archive - Just by knowing a target name or a location in the sky, a procedure can select all corresponding science images with their corresponding calibration frames, this whatever is the instrument requested. This procedure imitates the data retrieval that was done by hand for most of the reduced surveys presented in chapter 5.

- Raw image analysis from downloaded data - The scientific images have not the same quality because of the varying atmospheric conditions. Some should be discarded. A procedure based on sky background value, PSF properties could select robustly the images to be discarded.

- Final product definition in multi-instrument context - Currently, the final products are defined (projection grid) for on instrument at a time. The final products could be defined in a multi-instruments context in order to harmonize the reduced final products. For instance, the GOODS project is dealing with a large variety of telescopes and a typical grid has been defined, such as all reduced images share the same reference, or a scaled version of it by an integer factor. A proposition to split the sky in different pointings in a multi-resolution context has been proposed (O'Mullane et al., 2001; Górski et al., 2002), an application of the HEALPIX sky splitting is presented in (Górski and et al., 1999).

- Absolute photometric calibration - The pipeline does not compute any ZP, even if the reduced images have an homogeneous gain (multi-CCD detectors), and a flat ZP. This step is currently done by external procedures implemented in the EIS systems. This is a missing link from the reduced images to the final products. The pipeline will be more complete by integrating a photometric calibration.

These future developments are mainly motivated to handle the archive systems. In other word, this work is a first step toward an image pipeline developed in an Virtual Observatory context.

Appendix A

Deep Public Survey: Infrared Data for the Chandra Deep Field South

Astronomy & Astrophysics manuscript no.
(will be inserted by hand later)

ESO Imaging Survey

Deep Public Survey: Infrared Data for the Chandra Deep Field South*.

B. Vandame[1], L.F. Olsen[2], H.E. Jørgensen[2], M.A.T. Groenewegen[1], M. Schirmer[1,3], S. Arnouts[1], C. Benoist[4,1], L. da Costa[1], R. P. Mignani[1], C. Rité[1,5], R. Slijkhuis[1], E. Hatziminaoglou[1], R. Hook[1], R. Madejsky[1], and A. Wicenec[1]

[1] European Southern Observatory, Karl-Schwarzschild-Str. 2, D–85748 Garching b. München, Germany
[2] Astronomical Observatory, Juliane Maries Vej 30, DK-2100 Copenhagen, Denmark
[3] Max-Planck Institut für Astrophysik, Karl-Schwarzschild-Str. 1, D-85748 Garching b. München, Germany
[4] Observatoire de la Côte d'Azur, BP 229, 06304 NICE cedex 4, France
[5] Observatório Nacional, Rua Gen. José Cristino 77, Rio de Janerio, R.J., Brasil

Received ; accepted

Abstract. This paper presents new J and K_s near-infrared data obtained from observations of the Chandra Deep Field South (CDF-S) conducted at the ESO 3.5m New Technology Telescope (NTT). These data were taken as part of the ongoing Deep Public Survey (DPS) being carried out by the ESO Imaging Survey (EIS) program, extending the EIS-DEEP survey. Combined these surveys now provide a contiguous coverage over an area of 400 square arcmin in the near-infrared, nearly matching that covered by the deep X-ray observations of Chandra, four times the area of the original EIS-DEEP survey. The paper briefly describes the observations and the new techniques being employed for pipeline processing jittered infrared observations, which include unbiased de-fringing and sky-background subtraction, pixel-based astrometry and stacking and pixel registration based on a multi-resolution decomposition of the images. The astrometric solution is based on a pre-release of the GSC-II catalog and has an accuracy of $\lesssim$0.15 arcsec. The final images for 12 pointings presented here reach median 5σ limiting magnitudes of $J_{AB} \sim 23.4$ and $K_{AB} \sim 22.6$ as measured within an aperture 2×FWHM. The frame to frame variation of the photometric zero-point is estimated to be $\lesssim$0.09 mag. The data are publicly available in the form of fully calibrated J and K_s pixel maps and source lists extracted for each pointing. These data can be requested through the URL "http://www.eso.org/eis".

Key words. catalogs – surveys– stars: general - galaxies: general

1. Introduction

Deep multi-wavelength observations of selected regions of the sky from space and ground-based facilities, combined with spectrographic observations from large-aperture telescopes, offer the most promising means to probe the distant universe and study in a comprehensive way the evolution of galaxies and large-scale structures over a broad interval of look-back time. Preliminary steps towards this goal are already underway with the completion of deep X-ray observations of the Chandra Deep Field South (CDF-S; $\alpha = 03^h32^m28^s$ and $\delta = -27°48'30''$; Giacconi *et al.* 2000). These observations will eventually be complemented by observations with HST, XMM and SIRTF as well as VLT.

Foreseeing the need for ground-based multi-color data the Working Group for public surveys at ESO recommended the ESO Imaging Survey (EIS, Renzini & da Costa, 1997) project to undertake deep, optical/infrared observations of the HDF-S and CDF-S regions. Original observations of these fields were conducted in 1998 (da Costa *et al.* 1998; Rengelink *et al.* 1998, to be superseded by da Costa *et al.* 2001; Benoist *et al.* 2001a) and fully calibrated images, source catalogs and high-redshift galaxy candidates were immediately made public prior to the Science Verification of the first unit of the VLT. However, these observations covered only a small fraction of the field of view of Chandra, requiring the original coverage of EIS to be enlarged. Full coverage of the CDF-S $\lesssim$350 square arcmin field and flanking regions in optical and infrared is one of the primary goals of the Deep Public Survey (DPS) now being conducted by EIS. DPS consists of two parts: first, a deep, optical multi-passband ($UBVRI$) survey reaching limiting magnitudes $m_{AB} \sim 26$ mag covering three distinct strips (DEEP1, DEEP2 and DEEP3). These stripes consist of four adjacent pointings (denoted by a-d in decreasing order of right ascension) of the wide-field imager (WFI), mounted on the ESO/MPG 2.2m telescope at La Silla, yielding an area of one square degree each; second, the contiguous coverage in the infrared passbands JK_s of two distinct regions (DEEP-2c and DEEP-3a) 450 square arcmin each. The infrared part of DPS is a joint effort between

Send offprint requests to: bvandame@eso.org

* Based on observations collected at the European Southern Observatory, La Silla, Chile within program ESO 164.O-O561.

the EIS team and an external group of scientist from ESO member states. Further details about DPS can be found at the URL "http://www.eso.org/eis". The primary goal of the survey is to produce a data set from which statistical samples of galaxies can be drawn to study the large scale structures at high redshift. These data should also be valuable for many other areas of investigation, in particular for cross-identification with X-ray sources detected from the deep X-ray exposure of Chandra.

The purpose of the present paper is to describe and present the data from the new infrared observations of the CDF-S region. The data reported here complement those obtained by the original EIS-DEEP survey (Rengelink *et al.* 1998), which are being re-analyzed and will be presented in a separate paper (Benoist *et al.* 2001a). Section 2 reviews the overall observing strategy and describes the observations. Section 3 discusses the techniques employed in the data reduction and the photometric and astrometric calibration of the images. Section 4 presents the photometric parameters of the sources detected on each image corresponding to different pointings and passband. Due to time constraints other products such as image mosaics, catalogs extracted from them, optical/infrared color catalogs, statistical samples and lists containing other targets of potential interest will be presented elsewhere. Even though the goal of the present paper is not to interpret the data, Section 5 presents the results of comparisons between the present observations and those of other authors. This is done for the sole purpose of assessing the quality of the astrometry and photometry of the present data set. Finally, a brief summary is presented in Section 6.

2. Observations

Infrared observations in the near-infrared passbands J and K_s were obtained using the SOFI camera (Moorwood, Cuby & Lidman 1998) mounted on the New Technology Telescope (NTT) at La Silla. SOFI is equipped with a Rockwell 1024^2 detector that, when used together with its large field objective, provides images with a pixel scale of 0.29 arcsec, and a field of view of about 4.9×4.9 square arcmin. The infrared pointings were chosen to produce a contiguous coverage of a 4×4 mosaic when combined with those of EIS-DEEP. They were also required to produce sufficient overlap between adjacent pointings to enable the construction of an image mosaic, avoiding severe decrease in the effective exposure time due to the jitter pattern used and enabling a common photometric zero-point to be determined. The inner 2×2 subset correspond to the EIS-DEEP pointings reported by Benoist *et al.* (2001a). The remaining 12 pointings are those observed as part of the present survey which are listed in Table 1. The table gives: in column (1) the identification of each tile in the mosaic represented by the indices (i, j), where i decreases with declination and j decreases with right ascension; and in columns (2) and (3) the J2000 coordinates of the pointing. A schematic view of the coverage is illustrated in Figure 1 which shows the relative positions of the region with $UBVRI$ coverage, the EIS-DEEP infrared data and the newly accumulated data. In the convention described above the pointings with (2,2) (2,3), (3,2) and (3,3), correspond to those obtained by the EIS-DEEP program.

Table 1. Central position of the 12 SOFI fields observed as part of the DPS infrared survey of CDF-S (DEEP2c).

(i, j)	α (J2000)	δ (J2000)
(1,1)	$03^h32^m57^s$	$-27°41'45''$
(1,2)	$03^h32^m37^s$	$-27°41'45''$
(1,3)	$03^h32^m17^s$	$-27°41'45''$
(1,4)	$03^h31^m57^s$	$-27°41'45''$
(2,1)	$03^h32^m57^s$	$-27°46'10''$
(2,4)	$03^h31^m57^s$	$-27°46'10''$
(3,1)	$03^h32^m57^s$	$-27°50'35''$
(3,4)	$03^h31^m57^s$	$-27°50'35''$
(4,1)	$03^h32^m57^s$	$-27°55'00''$
(4,2)	$03^h32^m37^s$	$-27°55'00''$
(4,3)	$03^h32^m17^s$	$-27°55'00''$
(4,4)	$03^h31^m57^s$	$-27°55'00''$

The original goal of the observations was to reach 5σ magnitudes of J_{AB}=23.5 and K_{AB}=23.1 requiring a total integration time of 1800 sec and 7000 sec in J and K_s, respectively, as estimated from the SOFI exposure time calculator. Following a Working Group (WG) recommendation, the total integration time of 8400 sec was later split into 3600 sec in J and 4800 sec in K_s to reach $(J - K_s) \sim 2$ (Vega system) at the limiting magnitude of the survey. The J exposures were taken as a sequence of 60 one-minute exposures, while the K_s observations were split into two sequences of 40 one-minute exposures. However, during the reductions images with very high noise level and/or unexplained gradients in the background were detected and rejected from further processing. Therefore, in some cases the effective exposure time may vary with respect to those originally planned (see Section 5). In other cases, additional exposures were obtained for a pointing. These additional exposures typically originate from aborted exposure sequences, which were later re-observed in their entirety.

A total of 16 nights were allocated to the infrared part of DPS split into three runs: one in period 64 and two in period 66. The observations was carried out for both the DEEP2c and the DEEP3a regions, and a summary of the observations carried out in the DEEP2c region is given in Table 2, which lists: in column (1) the date of the observations; in column (2) the pointing as defined above; in column (3) the filters used; and in columns (4) and (5) the range and average seeing during the night as measured by the seeing monitor at La Silla. The observations were conducted under fairly good weather and seeing ($\lesssim$1.1 arcsec) conditions, nearly all in photometric nights, except for occasional light cirrus. Unfortunately, the last run was cancelled due to technical problems with the NTT. At the time of writing the J pointing (4,4) had been observed in service mode and will be made available as soon as possible.

The infrared observations were jittered relative to the centers given above in order to estimate the sky level from the data themselves. The procedure consists of a series of short exposures with small position offsets from the target position. The jitter strategy has been implemented as a standard observing template (AutoJitter) for the SOFI instrument. Each exposure consisted of the average of six ten-second sub-exposures. Using

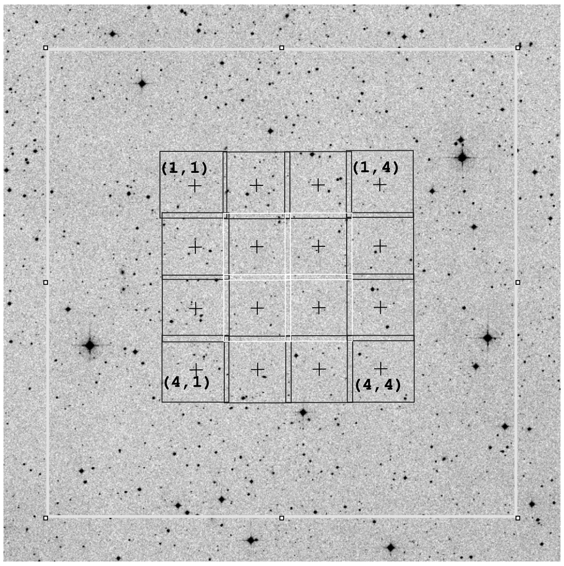

Fig. 1. Relative positions of the area with *UBVRI* coverage (outer square) and the infrared data from EIS-DEEP (inner bright square) and the current survey. It can be seen that the infrared data forms a contiguous mosaic covering a significant fraction of the optical survey area. It also nearly coincides with the area covered by the deep observations of Chandra.

this template, offsets are generated randomly within a square box of a specified size, chosen originally to be 40 arcsec, approximately 10% of the SOFI detector field of view. This value was later increased to 70 arcsec for the November 2000 run to improve the background estimate. These offsets are constrained so that all distances between pointings, in a series of 15 consecutive pointings, are larger than 9 arcsec.

3. Data Reduction

3.1. Image Processing

The infrared images were reduced using a new routine designed for the EIS pipeline for automated reduction of optical/infrared images (Vandame *et al.* 2001). The routine produces fully reduced images and weight-maps carrying out bias subtraction, flatfielding, de-fringing and subtraction of the background, first-order pixel-based image stacking (allowing for translation, rotation and stretching of the image) and astrometric calibration. De-fringing, sky-subtraction and elimination of image artifacts are done adopting a two-pass procedure: first, a preliminary image is obtained by stacking a set of sky-subtracted frames, with the background estimated using a running median; second, objects are identified in this stacked image and masks are created; finally, the de-fringing/sky-subtraction step is repeated with the object masks mapped to the jittered position of each individual image. Deviant values are sigma-clipped and masked pixels are neglected. More details about the package will be presented when it is made publicly available (Vandame *et al.* 2001).

The primary reason for developing an entire new code was to improve on the photometric accuracy of faint objects which had been achieved in the earlier processing of the EIS-DEEP data. Further analysis of these data carried out by the EIS team and by other users (Cimatti 1999; see also the eclipse home page[1] and Devillard 1999 for more information) revealed a trend to underestimate the flux of objects, in some cases of $\sim$0.2 mag at faint magnitudes. Another important advantage of the new software package is that it produces weight-maps which are critical for the construction of image mosaics.

The effect of the two-step procedure is illustrated in Figure 2 which shows the sky-subtracted image obtained after the two-pass sky-estimation (left panel) and the residual after subtracting the first-pass image from the two-pass one (right panel). It can clearly be seen that a single pass leads to the loss of a significant fraction of flux leading to biases in the estimated magnitudes of up to $\lesssim$0.3 mag. This effect is caused by the biased sky-estimation in the outer regions of the objects where the faint light level contribution cannot be distinguished from the sky-background in the individual images. This effect is clearly visible in the lower right corner where the background around the bright galaxy is too high in the first pass estimate. Furthermore regions with a high density of individual faint sources, none of which can be detected prior to the final stacking, would contribute to the background in the single pass approach.

1 http://www.eso.org/projects/aot/eclipse/

Table 2. Log of the observations for the infrared data for DEEP2c.

Date	Pointing (i,j)	Filter	Seeing range (arcsec)	Mean seeing (arcsec)
31-01-2000	(1,3)	K_s	–	–
01-02-2000	(1,3)	K_s	–	–
	(1,2)	K_s	0.66 – 1.07	0.90
03-02-2000	(1,3)	J	0.79 – 1.35	0.97
	(1,2)	K_s	0.60 – 0.92	0.76
04-02-2000	(1,2)	J	0.68 – 1.37	0.91
	(4,3)	K_s	0.69 – 1.17	0.87
05-02-2000	(4,3)	J	0.44 – 0.83	0.60
06-02-2000	(4,3)	K_s	0.43 – 0.63	0.52
19-11-2000	(4,2)	K_s	0.70 – 1.00	0.83
	(4,2)	J	0.68 – 1.17	0.85
	(1,1)	J	0.70 – 2.26	1.14
	(1,1)	K_s	0.56 – 2.07	0.95
20-11-2000	(1,1)	K_s	0.54 – 0.96	0.75
	(2,1)	K_s	0.54 – 1.01	0.77
	(2,1)	J	0.61 – 1.04	0.79
	(3,1)	J	0.63 – 1.17	0.81
	(3,1)	K_s	0.69 – 1.71	1.10
21-11-2000	(4,1)	K_s	0.56 – 1.11	0.82
	(1,4)	K_s	0.64 – 1.33	0.87
	(4,1)	J	0.60 – 1.98	1.16
	(1,4)	J	0.54 – 1.58	0.80
	(2,4)	K_s	0.72 – 1.52	1.01
22-11-2000	(2,4)	K_s	0.50 – 1.19	0.79
	(2,4)	J	0.60 – 2.40	1.14
	(3,4)	K_s	0.57 – 1.26	1.00
	(3,4)	J	0.62 – 1.49	0.94
	(4,4)	K_s	0.53 – 0.86	0.68

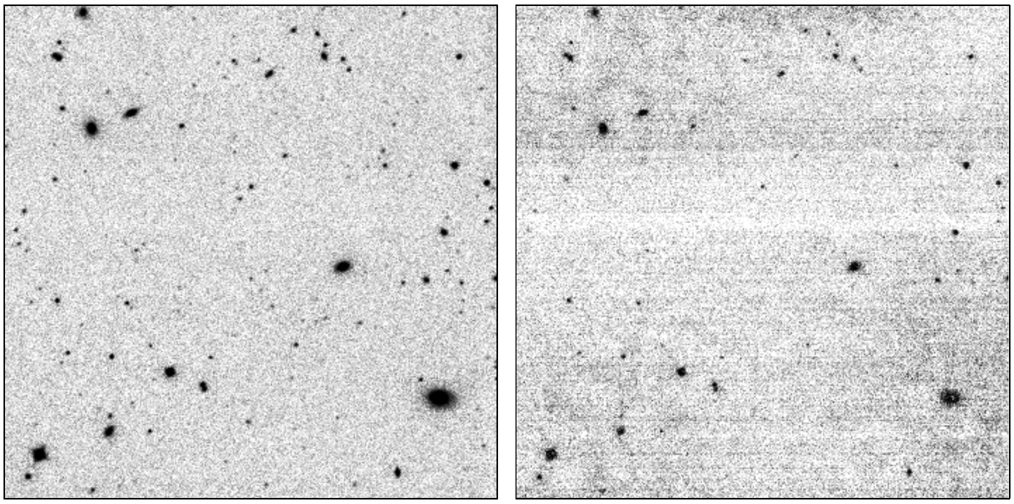

Fig. 2. Effect of the two-pass approach for the sky-estimation. The left panel shows the final sky-subtracted image (note the inverted fluxscale) after the second pass. The right panel shows the residuals after subtracting the first pass image from the second pass one. The large amounts of residual flux at the object positions indicate the necessity for the second pass background estimation.

3.2. Astrometric Calibration

The astrometric calibration of the infrared frames was performed using as the reference catalog objects extracted from optical images obtained over the same region (Arnouts *et al.* 2001) using the method developed by Djamdji *et al.* (1993). The method is based on a multi-resolution decomposition of images using wavelet transforms (MVM) developed over the years by Bijaoui and collaborators and extensively applied in remote sensing. An implementation of these algorithms to stack images, referred to as MVM-astrometry, has been done for EIS. This package has proven to be efficient and robust for pipeline reductions. The estimated internal accuracy of this technique is about half a pixel (∼0.15 arcsec). The optical images were calibrated relative to objects drawn from the pre-release version of the *Guide Star Catalog-II* (GSC-II). The GSC-II (McLean *et al.* 2001) is based on multi-passbands all-sky photographic plate surveys including the Palomar Observatory Sky Survey (POSS-I-II), the SERC and the ESO Red Survey. The astrometric calibration of GSC-II has been obtained relative to Hipparcos (Perryman *et al.* 1997) and Tycho catalogs (Høg *et al.* 1997) and the *ACT* (Urban, Corbin & Wycoff 1998).

This two-step approach to astrometrically calibrate the infrared images has been taken for two main reasons. First, by using the deep astrometrically calibrated optical images as the reference the number of objects typically available within a SOFI field ($\gtrsim$150) is a factor of four larger than the typical number of GSC-II reference stars (∼ 40). Therefore, this procedure provides a better constraint for a second-order polynomial fit. Second, this approach ensures a robust relative astrometry between the optical and infrared images, overcoming the problems identified in the earlier release of the CDF-S data. As pointed out by Benoist *et al.* (2001b) small relative shifts between the position of objects extracted from the optical and infrared images significantly affected the color catalog for that data set. The new procedure being adopted here should prevent similar problems from occuring in the future.

3.3. Photometric Calibration

The photometric calibration for each night is based on observations of standard stars taken from Persson *et al.* (1998). Typically two to seven stars were observed over a range of airmasses. For all nights independent photometric solutions were obtained with errors of $\lesssim$ 0.03 mag in both passbands and negligible color terms. Examining deviant measurements showed that some of the selected standard stars (at least 3 cases) may be variable. A more careful analysis of these cases will be presented elsewhere.

Using the individually calibrated images, the consistency between their respective zero-points was examined considering the magnitude differences of pairs of objects located in regions of overlap. An average magnitude difference was then computed for each set of overlapping frames yielding a mean value of ∼ 0.03 mag and a scatter of $\lesssim$0.09 mag for both bands. A more detailed discussion of this point will be presented in a forthcoming paper when the complete data set has been analyzed and a final mosaic is created.

3.4. Image Products

The images being released are fully astrometrically (COE projection) and photometrically calibrated (normalized to 1 sec exposure time). The provided FITS files include both the pixel and weight maps as FITS extensions. The astrometric information is stored in the world coordinate system (WCS) keywords in the FITS headers. Similarly the photometric calibration is provided by the zero-point and its error available in the header keywords ZP and ZP_ERR. The zero-point includes the normalized zero-point of the photometric solution and the atmospheric extinction correction. In the header one can also find a product identification number (P_ID) which should always be used as reference. The headers also provide information on the number of stacked frames and the on-source total integration time. Additionally the seeing obtained by measuring the FWHM of bright stars in the final stacked images is stored in the header keyword SEE_IMA.

An example of a final image and corresponding weight map is shown in figure 3 for one pointing in K_s. Note that the size of the image ($\sim 5.8 \times 5.8$ square arcmin) is much larger than that obtained using the earlier version of the EIS pipeline which clipped the image to the best sampled region. Comparing the image and the weight map one sees how the noise increases at the edges as the effective exposure time decreases. However, proper use of the weight maps facilitates and greatly increases the efficiency of building up infrared mosaics.

It is worth mentioning that, a satellite track visible at the north-eastern corner in one of the J-band images (pointing $(2,4)$) led to the masking of a large region which caused the rejection of a large fraction of the frame from the final stack. Proper use of the Hough transform, as currently done for the optical images, will be used to correct this effect in future data products.

4. Source Lists

Source extraction was performed using the SExtractor software (Bertin & Arnouts 1996; ver. 2.2.1). Detection was carried out separately using the co-added image of each passband and field. The main parameters in the detection are the smoothing kernel, taken to be a Gaussian with a FWHM equal to 0.8 of that of the PSF measured on the frame; the SExtractor detection threshold, taken to be 0.8; and the minimum number of pixels above the detection threshold, taken to be 7 pixels for SOFI images. As an illustration, the tabulation of the first 40 entries in one of the J-band source catalogs is presented in Table 3. All magnitudes are given in the AB system, using $J_{AB} = J + 0.90$ and $K_{AB} = K_s + 1.84$. The table lists:

Column (1): the EIS identification name

Columns (2) and (3): right ascension and declination (J2000.0);

Columns (4)-(9): total, isophotal and aperture (3 arcsec diameter) magnitudes and respective errors. The first two magnitudes correspond to the `mag_auto` and `mag_iso` mag-

Table 3. CDF-S J-band source list (all magnitudes are given in the AB system).

#	α	δ	m_{tot}	ϵ	m_{iso}	ϵ	m_{aper}	ϵ	S/N	A	r_h	b/a	PA	$class$	$Flag$	$EISflag$
EISJ033244.08-274048.6	03:32:44.08	-27:40:48.6	21.71	0.22	22.17	0.14	22.06	0.21	6.92	1.68	2.27	0.88	-10.45	0.90	24	1
EISJ033244.18-273942.3	03:32:44.18	-27:39:42.3	17.45	0.01	17.46	0.01	18.84	0.01	121.95	38.44	5.22	0.72	19.20	0.03	26	1
EISJ033244.20-273856.5	03:32:44.20	-27:38:56.5	22.04	0.23	22.49	0.22	22.23	0.53	4.49	0.50	0.66	0.82	46.70	0.92	16	1
EISJ033244.24-274111.0	03:32:44.24	-27:41:11.0	20.55	0.06	20.58	0.04	20.71	0.05	24.81	4.37	1.79	0.89	-3.05	0.98	16	1
EISJ033244.31-273953.9	03:32:44.31	-27:39:53.9	22.44	0.19	22.70	0.15	22.48	0.26	6.54	1.26	1.63	0.79	60.43	0.86	0	1
EISJ033244.33-273937.6	03:32:44.33	-27:39:37.6	20.23	0.05	20.29	0.04	20.54	0.04	25.06	5.55	2.15	0.87	43.58	0.97	19	1
EISJ033244.35-274036.4	03:32:44.35	-27:40:36.4	21.35	0.11	21.60	0.09	21.78	0.09	11.36	3.45	2.55	0.74	52.88	0.40	0	1
EISJ033244.42-274130.0	03:32:44.42	-27:41:30.0	22.14	0.26	23.24	0.19	22.85	0.26	5.33	0.93	3.27	0.74	38.08	0.67	0	1
EISJ033244.42-274422.4	03:32:44.42	-27:44:22.4	21.05	0.23	22.53	0.20	22.36	0.22	5.11	1.26	5.03	0.41	-25.72	0.93	0	1
EISJ033244.45-274108.4	03:32:44.45	-27:41:08.4	19.77	0.04	19.86	0.03	20.34	0.03	36.63	9.42	2.91	0.82	48.70	0.03	0	1
EISJ033244.48-274116.5	03:32:44.48	-27:41:16.5	22.20	0.17	22.37	0.12	22.45	0.19	8.23	1.93	2.14	0.62	-74.09	0.76	0	1
EISJ033244.52-274121.1	03:32:44.52	-27:41:21.1	22.10	0.16	22.30	0.12	22.26	0.17	8.38	2.19	2.14	0.88	32.19	0.92	0	1
EISJ033244.54-274221.6	03:32:44.54	-27:42:21.6	22.84	0.21	23.25	0.19	22.88	0.36	5.33	0.93	1.49	0.86	44.43	0.72	0	1
EISJ033244.56-273951.1	03:32:44.56	-27:39:51.1	22.45	0.19	22.76	0.16	22.51	0.25	6.30	1.35	1.69	0.82	-88.35	0.89	0	1
EISJ033244.63-273949.0	03:32:44.63	-27:39:49.0	21.53	0.17	22.08	0.10	22.11	0.13	9.67	2.44	2.90	0.78	-58.30	0.59	0	1
EISJ033244.65-274227.0	03:32:44.65	-27:42:27.0	22.88	0.20	23.24	0.16	22.92	0.32	6.12	0.84	1.40	0.70	0.67	0.56	0	1
EISJ033244.66-274202.7	03:32:44.66	-27:42:02.7	20.61	0.05	20.67	0.04	20.87	0.04	25.13	5.05	2.23	0.91	24.74	0.74	0	1
EISJ033244.67-274352.2	03:32:44.67	-27:43:52.2	21.95	0.19	22.64	0.15	22.52	0.18	6.76	1.60	2.55	0.74	30.18	0.90	0	1
EISJ033244.81-274406.7	03:32:44.81	-27:44:06.7	17.74	0.01	17.77	0.01	18.55	0.01	103.09	31.54	3.57	0.99	43.12	0.03	0	1
EISJ033244.94-274053.7	03:32:44.94	-27:40:53.7	22.85	0.32	23.58	0.22	22.92	0.30	4.47	0.76	1.83	0.85	18.15	0.61	0	1
EISJ033244.97-273915.8	03:32:44.97	-27:39:15.8	21.85	0.28	22.58	0.18	22.39	0.22	5.58	1.18	2.43	0.58	-72.83	0.91	0	1
EISJ033244.98-274309.5	03:32:44.98	-27:43:09.5	22.65	0.20	22.70	0.15	22.72	0.24	6.63	1.18	1.87	0.83	89.02	0.67	0	0
EISJ033245.04-274122.7	03:32:45.04	-27:41:22.7	22.04	0.14	22.10	0.10	22.08	0.15	10.46	1.93	1.70	0.88	-18.79	0.96	0	0
EISJ033245.06-274110.0	03:32:45.06	-27:41:10.0	19.89	0.05	20.01	0.03	20.86	0.03	29.85	11.69	4.18	0.58	-26.76	0.05	2	0
EISJ033245.06-274331.9	03:32:45.06	-27:43:31.9	18.35	0.01	18.35	0.01	19.20	0.01	94.34	30.36	3.75	0.92	54.48	0.03	0	0
EISJ033245.09-273913.7	03:32:45.09	-27:39:13.7	21.32	0.16	21.52	0.10	21.70	0.14	9.56	2.86	2.56	0.67	-60.67	0.70	0	0
EISJ033245.12-274256.1	03:32:45.12	-27:42:56.1	22.29	0.26	23.36	0.21	22.87	0.21	4.71	1.01	2.97	0.71	-68.73	0.53	0	0
EISJ033245.18-274147.5	03:32:45.18	-27:41:47.5	22.40	0.26	22.73	0.13	22.59	0.26	7.69	1.43	1.82	0.79	-46.23	0.92	0	0
EISJ033245.22-274058.0	03:32:45.22	-27:40:58.0	21.67	0.16	21.96	0.09	22.06	0.12	11.49	2.69	2.27	0.77	-1.86	0.57	0	0
EISJ033245.27-274052.1	03:32:45.27	-27:40:52.1	21.51	0.16	22.19	0.11	22.39	0.13	8.92	2.61	3.72	0.85	-59.45	0.02	1	0
EISJ033245.36-274249.8	03:32:45.36	-27:42:49.8	22.10	0.20	22.47	0.12	22.59	0.15	8.24	2.19	2.52	0.60	-25.28	0.39	0	0
EISJ033245.41-274225.6	03:32:45.41	-27:42:25.6	22.36	0.19	22.57	0.12	22.49	0.18	8.30	2.02	2.05	0.88	0.28	0.90	0	0
EISJ033245.41-274133.3	03:32:45.41	-27:41:33.3	21.17	0.08	21.32	0.06	21.55	0.07	16.78	4.21	2.41	0.84	20.64	0.63	0	0
EISJ033245.42-273923.2	03:32:45.42	-27:39:23.2	21.82	0.16	22.25	0.14	22.15	0.16	7.11	2.19	2.61	0.79	23.87	0.84	0	0
EISJ033245.43-274057.1	03:32:45.43	-27:40:57.1	20.94	0.10	21.32	0.06	21.63	0.07	16.31	4.37	3.25	0.87	56.58	0.44	3	0
EISJ033245.48-273915.5	03:32:45.48	-27:39:15.5	20.82	0.12	20.89	0.07	21.19	0.08	14.18	4.29	2.50	0.84	-81.82	0.78	2	0
EISJ033245.53-273913.7	03:32:45.53	-27:39:13.7	22.01	0.20	22.48	0.18	22.36	0.21	5.53	1.51	2.17	0.91	22.42	0.88	3	0
EISJ033245.53-274053.6	03:32:45.53	-27:40:53.6	19.68	0.04	19.82	0.03	20.58	0.02	39.22	13.88	3.91	0.83	28.41	0.03	3	0
EISJ033245.58-274114.4	03:32:45.58	-27:41:14.4	21.32	0.12	21.75	0.08	22.12	0.10	12.11	3.87	3.53	0.54	41.68	0.30	0	0
EISJ033245.58-274245.8	03:32:45.58	-27:42:45.8	22.42	0.16	22.50	0.11	22.51	0.19	9.26	1.93	1.71	0.89	-57.59	0.95	0	0

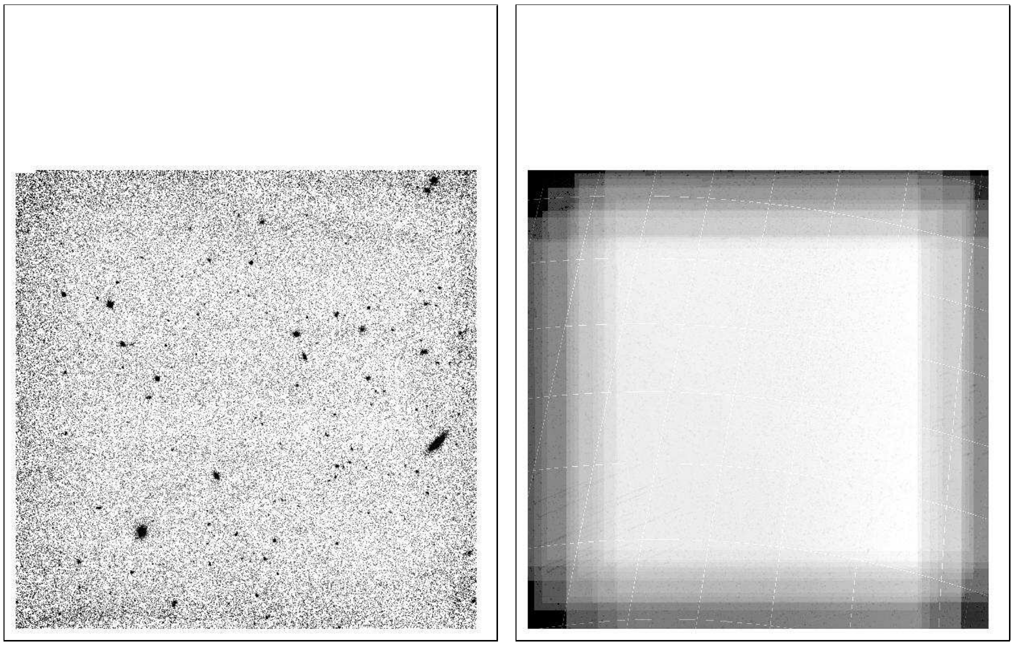

Fig. 3. An example of the final coadded image (left panel) and the corresponding weight map (right panel). The lines seen in the weight map are caused by the astrometric remapping of the frames.

nitudes measured by SExtractor. The magnitudes have been corrected for Galactic extinction taken from Schlegel *et al.* (1998). The errors are those estimated by SExtractor and include only the shot-noise of the measured source and background counts. Only objects detected with signal to noise $S/N \geq 3$ (based on the isophotal magnitude errors) are included.

Column (10): an estimate of the S/N of the detection, by the inverse of the errors estimated for the isophotal magnitude;

Columns (11): the isophotal area A of the object in square arcsec;

Column (12): the half-light radius r_h in arcsec;

Column (13) and (14): minor to major-axis ratio and the position angle;

Column (15): the stellarity index computed by SExtractor;

Column (16): SExtractor flags (see Bertin 1998)

Column (17): EIS flags; these flags are used to identify objects in regions with very low weight or close to bright objects. Objects detected in regions with weight $\geq 40\%$ of the maximum weight (proportional to the total integration time) and not affected by bright stars have EIS flag=0. Objects with weight $< 40\%$, located at the edges of the frame, have EIS flag=1. Finally EIS flag=2 indicates that the object is located in a region masked out due to the presence of a bright object.

Similar tables for each pointing and passband are available upon request in ASCII format. Catalogs for the mosaic and optical/infrared color catalogs will be distributed as soon as they become available. Note that besides distributing catalogs in tabular form as done here, catalogs in FITS formats will become part of the distribution of final products. These catalogs will include considerable more information such as the parameters defining the trimmed and masked regions used to determine the EIS flags. The final catalogs will be described by Arnouts *et al.* (2001).

5. Discussion

The characteristics of the data obtained by the present infrared survey are summarized in Table 4 which lists: in column (1) the identification of the pointing; in column (2) the filter; in column (3) the effective exposure time for each final image; in column (4) the seeing of the final co-added image; in column (5) the number of detected objects with $S/N \geq 3$ as described above; in columns (6) and (7) the 5σ and 3σ limiting AB magnitude measured within an aperture $2\times$FWHM. At the 5σ limiting magnitudes the fraction of spurious objects is estimated to be $\sim 5\%$ and $\sim 11\%$ in J and K, respectively, rapidly rising to over 50% at the 3σ limit. The fraction of spurious objects was estimated by creating catalogs from the survey images multiplied by -1. The mock images were then used as input to the catalog production and from the comparison between the catalogs of the mock and real objects the fraction of false-positives was estimated.

Table 4. Data summary.

Pointing	filter	Eff.Exp.Time (sec)	Seeing (arsec)	N_{obj}	$5\sigma m_{lim}$ (mag)	$3\sigma m_{lim}$ (mag)
(1,1)	J	3600	0.99	662	23.39	23.94
	K_s	4800	0.84	530	22.43	22.98
(1,2)	J	3600	0.77	736	23.48	24.03
	K_s	4800	0.76	795	22.54	23.09
(1,3)	J	3600	0.84	549	23.23	23.78
	K_s	4680	0.69	722	22.82	23.37
(1,4)	J	3600	0.77	871	23.59	24.14
	K_s	4500	0.77	663	22.64	23.19
(2,1)	J	3600	0.83	699	23.47	24.02
	K_s	4740	0.68	654	22.60	23.15
(2,4)	J	3600	0.82	534	23.02	23.57
	K_s	4800	0.81	566	22.43	22.98
(3,1)	J	3600	0.69	896	23.85	24.40
	K_s	4800	0.84	442	22.40	22.95
(3,4)	J	3600	0.87	697	23.47	24.02
	K_s	4800	0.77	602	22.62	23.17
(4,1)	J	3600	1.03	627	23.14	23.69
	K_s	4800	0.68	602	22.63	23.18
(4,2)	J	3720	0.86	588	23.38	23.93
	K_s	4920	0.85	415	22.37	22.92
(4,3)	J	3600	0.66	810	23.42	23.97
	K_s	7200	0.77	633	23.02	23.57
(4,4)	K_s	4800	0.67	710	22.71	23.26

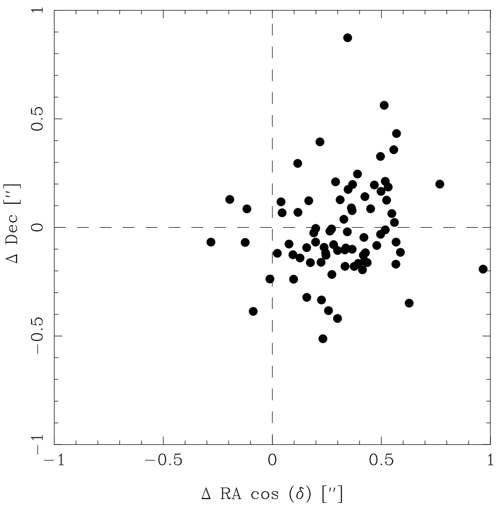

Fig. 4. Comparison between the location of objects in common with the 2MASS survey, offsets are computed as $EIS - 2MASS$.

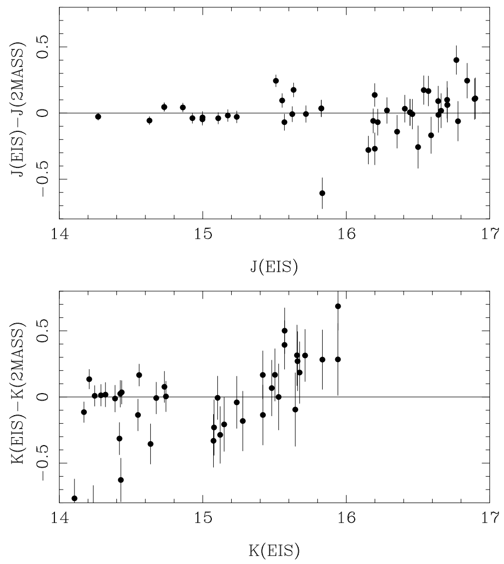

Fig. 5. Comparison between the measured J (upper panel) and K_s (lower panel) magnitudes of objects in common with the 2MASS survey.

In order to externally verify the results obtained here the source list presented above was cross-correlated with that available from the 2MASS survey (Cutri *et al.* 2000) using a search radius of 1 arcsec. A total of 80 objects were found in common and their relative positions and magnitudes (for objects considered "good" in both catalogs) were computed and are shown in Figures 4 and 5. Apart from an offset of about 0.33 arcsec in right ascension one finds good agreement between the astrometric calibrations yielding a scatter of $\lesssim 0.23$ arcsec. Assuming similar errors for both data sets one finds an astrometric accuracy of ~ 0.16 arcsec consistent with the estimated internal accuracy of the technique adopted in the present work. The asymmetry of the distribution reflects a small systematic increase of the right ascension residuals noted near the eastern edge of the region. This effect is likely due to the large offset of the CDF-S position relative to the center of the original plate used for GSC-II object extraction. This problem is being addressed for the final release of the catalog. Considering objects brighter than $J = 16.0$ and $K_s = 15.0$ (Vega system), roughly corresponding to the 2MASS limiting magnitudes, the measured magnitudes of the two data sets are in good agreement, except for three outliers, showing a mean offset of 0.016 mag in J and -0.031 mag in K_s. The scatter is found to be 0.077 mag and 0.14 mag, respectively, consistent with the estimated uncertainty of the overall zero-point (Section 3).

Finally, Figure 6 shows the comparison of galaxy counts as a function of the total magnitude with those obtained for other data sets. The derived slopes of the counts are 0.33 ± 0.02 in J and 0.35 ± 0.02 in K, in good agreement with those obtained by Saracco *et al.* (1999) as well as other studies. The galaxy counts shown in the figure is the mean counts obtained averaging all the individual catalogs and the error bar is the scatter. The individual catalogs were obtained drawing objects with stellarity index less than 0.95 or fainter than 20.5 mag and only including objects with $S/N > 3$. Bad objects were discarded based on the SExtractor and EIS flags.

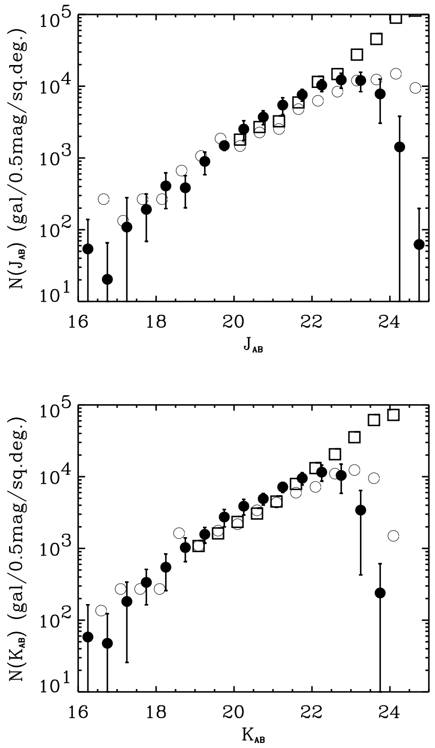

Fig. 6. Comparison of galaxy number counts between: the present work (full circles); da Costa *et al.* (1998) obtained from EIS-DEEP (open circles) and those of Saracco *et al.* (1999, squares).

6. Summary

This paper presents the first results of the infrared data accumulated by the ongoing Deep Public Survey being conducted by the EIS program. The paper describes the observations and the first set of products being publicly released including fully calibrated pixel maps and source lists covering the CDF-S region. Given the current interest in this area of the sky it was decided to release the data in the simple format presented. Other derived products will be described in forthcoming papers of this series. Hopefully, the source lists presented here will be of immediate value for cross-identification with X-ray sources.

Acknowledgements. The Guide Star Catalogue-II is produced by the Space Telescope Science Institute in collaboration with the Osservatorio Astronomico di Torino. Space Telescope Science Institute is operated by the Association of Universities for Research in Astronomy, for the National Aeronautics and Space Administration under contract NAS5-26555. Additional support is provided by the Association of Universities for Research in Astronomy, the Italian Council for Research in Astronomy, European Southern Observatory, Space telescope European Coordinating Facility, the International GEMINI project and the European Space Agency Astrophysics Division. The UK Schmidt Telescope was operated by the Royal Observatory Edimburgh, with funding from the UK Science and Engineering Research Council (later the UK Particle Physics and Astronomy Research Council), until 1988 June, and thereafter by the Anglo-Australian Observatory

This publication makes use of data products from the Two Micron All Sky Survey, which is a joint project of the University of Massachusetts and the Infrared Processing and Analysis Center/California Institute of Technology, funded by the National Aeronautics and Space Administration and the National Science Foundation.

We thank all of those directly or indirectly involved in the EIS effort. Our special thanks to M. Scodeggio for his continuing assistance in a variety of issues, A. Bijaoui for allowing us to use tools developed by him and collaborators over the years and past EIS team members for building the foundations of this program. We would also like to thank A. Renzini and the members of the Working Group for Public Surveys.

References

Arnouts, S. *et al.* , 2001, In preparation
Benoist, C. *et al.* , 2001a, In preparation
Benoist, C. *et al.* , 2001b, In preparation
Bertin, E. & Arnouts, S.; 1996, A&AS, 117, 393
Bertin, E., 1998, SExtractor, User's guide, v2.0
Cimatti, A, 1999, Private communication
Cutri, R.M.; Skrutskie, M.F.; Van Dyk, S.; *et al.* , 2000, Explanatory Supplement to the 2MASS Second Incremental Data Release
da Costa, L. *et al.* , 2001, In preparation
da Costa, L. *et al.* , 1998, astro-ph/9812105, submitted to A&A

Devillard, N., 1997, The Messenger, 87, 19
Devillard, N, 1999, ADASS, 98, 333
Djamdji, J.P.; Bijaoui, A. & Manière, R.; 1993, Photogrammetric Engineering and Remote Sensing, 59, 645
Giaconni, R; Rosati, P.; Tozzi, P.; *et al.* , 2000, astro-ph/0007240, submitted to ApJ
Høg, E.; Bässgen, G.; Bastian, U.; *et al.* , 1997, A&A, 323, L57
McLean, B.; Greene, G.; Lattanzi, M.; *et al.* , 2001, in Mining the Sky, Proc. of ESO Workshop, Springer-Verlag, In press
Moorwood, A.; Cuby, J.G.; & Lidman, C.; 1998, The Messenger, 91,9
Perryman, M. A. C.; Lindegren, L.; Kovalevsky, J.; *et al.* , 1997, A&A, 323, L49
Rengelink, R. *et al.* , 1998, astro-ph/9812190, submitted to A&A
Renzini, A. & da Costa, A., 1997, The Messenger, 87, 23
Saracco,P.; D'Odorico, S.; Moorwood, A.; *et al.* , 1999, A&A, 349, 751
Schlegel, D.; Finkbeiner, D. & Davis,M.; 1998, ApJ, 500,525
Urban, S. E.; Corbin, T. E. & Wycoff, G. L., 1998 AJ 115, 2161
Vandame, B. *et al.* , 2001b, In preparation

Appendix B

Deep Public Survey: Multi-color optical data for the Chandra Deep Field South

A&A 379, 740–754 (2001)
DOI: 10.1051/0004-6361:20011341

Astronomy & Astrophysics

ESO imaging survey

Deep public survey: Multi-color optical data for the Chandra Deep Field South*

S. Arnouts[1], B. Vandame[1], C. Benoist[2], M. A. T. Groenewegen[1], L. da Costa[1], M. Schirmer[3], R. P. Mignani[1], R. Slijkhuis[1], E. Hatziminaoglou[1], R. Hook[1], R. Madejsky[1,4], C. Rité[5], and A. Wicenec[1]

[1] European Southern Observatory, Karl-Schwarzschild-Str. 2, 85748 Garching b. München, Germany
[2] Observatoire de la Côte d'Azur, BP 229, 06304 Nice Cedex 4, France
[3] Max-Planck-Institut für Astrophysik, Karl-Schwarzschild-Str. 1, 85748 Garching b. München, Germany
[4] Universidade Estadual de Feira de Santana, Campus Universitário, Feira de Santana, BA, Brazil
[5] Observatório Nacional, Rua Gen. José Cristino 77, Rio de Janerio, Brasil

Received 5 March 2001 / Accepted 17 September 2001

Abstract. This paper presents multi-passband optical data obtained from observations of the Chandra Deep Field South (CDF-S), located at $\alpha \sim 3^{\rm h}32^{\rm m}$, $\delta \sim -27°48'$. The observations were conducted at the ESO/MPG 2.2 m telescope at La Silla using the 8k × 8k Wide-Field Imager (WFI). This data set, taken over a period of one year, represents the first field to be completed by the ongoing Deep Public Survey (DPS) being carried out as a part of the ESO Imaging Survey (EIS) project. This paper describes the optical observations, the techniques employed for un-supervised pipeline processing and the general characteristics of the final data set. Image processing has been performed using multi-resolution image decomposition techniques adapted to the EIS pipeline. The automatic processing steps include standard de-bias and flat-field, automatic removal of satellite tracks, de-fringing/sky-subtraction, image stacking/mosaicking and astrometry. Stacking of dithered images is carried out using pixel-based astrometry which enables the efficient removal of cosmic rays and image defects, yielding remarkably clean final images. The final astrometric calibration is based on a pre-release of the GSC-II catalog and has an estimated intrinsic accuracy of $\lesssim$0.10 arcsec, with all passbands sharing the same solution. The paper includes data taken in six different filters ($U'UBVRI$). The data cover an area of about 0.25 square degrees reaching 5σ limiting magnitudes of $U'_{AB} = 26.0$, $U_{AB} = 25.7$, $B_{AB} = 26.4$, $V_{AB} = 25.4$, $R_{AB} = 25.5$ and $I_{AB} = 24.7$ mag, as measured within a $2 \times FWHM$ aperture. The optical data covers an area of ∼0.1 square degrees for which moderately deep observations in two near-infrared bands are also available, reaching 5σ limiting magnitudes of $J_{AB} \sim 23.4$ and $K_{AB} \sim 22.6$. The current optical/infrared data also fully encompass the region of the deep X-ray observations recently completed by the Chandra telescope. The optical data presented here, as well as the infrared data released earlier, are publicly available world-wide in the form of fully calibrated pixel and associated weight maps and source lists extracted in each passband. These data can be requested through the URL "`http://www.eso.org/eis`".

Key words. catalogs – surveys – stars: general – galaxies: general

1. Introduction

The successful application of photometric techniques to identify high-redshift galaxies ($z \gtrsim 3$), combined with large-aperture telescopes with multi-object spectrographs, have provided the means to study large-scale structures at high-redshifts and to directly probe their evolution over a broad range of redshifts. Currently, the challenge is to construct well-defined statistical galaxy samples at faint magnitudes and use photometric redshift techniques to pre-select candidates for large spectroscopic surveys probing the high-redshift Universe. To achieve this goal, deep optical/infrared multi-passband surveys covering areas of the order of a few degrees are required.

Interest in this type of dataset is widespread in Europe given the imminent commissioning of the multi-object spectrograph VIMOS, part of the new generation of VLT instruments. Foreseeing this need, the Working

Send offprint requests to: S. Arnouts,
e-mail: `sarnouts@eso.org`

* Based on observations collected at the European Southern Observatory, La Silla, Chile within program ESO 164.O-O561.

Group (WG) for public surveys at ESO recommended in early 1999 the undertaking of a deep, multi-passband, optical survey covering three separate regions of sky one square degree each, with some areas also covered in the infrared. These regions, referred to as Deep-1, 2 and 3, are located over a wide range of right ascension and each corresponds to four adjacent pointings (a–d) of the Wide-Field Imager (WFI) mounted on the 2.2 m MPG/ESO telescope at La Silla. The main goal of the survey is to produce suitable statistical samples to study large-scale structures in the redshift domains $z \lesssim 1$ and $z \gtrsim 3$. Details of the position of the selected regions can be found at the URL "`http://www.eso.org/science/eis/`". One of the selected regions includes the Chandra Deep Field South (CDF-S; Giacconi et al. 2001) chosen because of its low column-density of hydrogen and absence of bright stars, characteristics that make it well-suited for deep X-ray observations with the Chandra (AXAF) telescope. These observations have recently been completed for a total integration time of one million seconds producing the deepest high-resolution X-ray image ever taken (Rosati et al. 2001).

In this paper, the *UBVRI* optical observations with the WFI of one of the selected fields (Deep-2c), covering the CDF-S, are presented. These data are used to make a first assessment of the procedures and overall performance of the optical part of the Deep Public Survey (DPS). The optical data presented here complement those in the near-infrared covering an area of ~0.11 square degrees (Vandame et al. 2001) encompassing the region covered by the Chandra observations. The new data reported here extend earlier optical/infrared observations of this field carried out by EIS at the NTT in 1998, covering a considerably smaller region. These older data are currently being re-analyzed to produce, together with the new data, a homogeneous dataset (Benoist et al. 2001a) which will supersede the earlier 1998 release (Rengelink et al. 1998). Section 2 reviews the overall observing strategy and describes the observations. Section 3 discusses the techniques employed in the data reduction and the photometric and astrometric calibration of the images. While other derived products are expected to be made available in the near future, only photometric parameters of the sources detected in each of the available passbands are presented for the moment in Sect. 4. Even though the goal of the present paper is not to interpret the data being released, Sect. 5 presents the results of comparisons between the present observations and those of other authors. This is done for the sole purpose of assessing the quality of the astrometry and photometry of the present data set and its adequacy to meet the main goals of the survey. Finally, a brief summary is presented in Sect. 6.

2. Observations

The optical observations of the CDF-S region ($\alpha \sim 3^{\rm h}32^{\rm m}$, $\delta \sim -27^{\rm o}48'$) were carried out using the WFI camera at the Cassegrain focus of the MPG/ES0 2.2 m telescope at the La Silla observatory. WFI is a focal reducer-type mosaic camera with 4×2 CCD chips. Each chip is composed of a 2048×4098 pixel array and covers a field of view of 8.12×16.25 arcmin with a projected pixel size of 0.238 arcsec. The 8 CCDs are physically separated by gaps of width 23.8 and 14.3 arcsec along the right ascension and declination directions, respectively. The full field of view of the camera is thus 34×33 arcmin, with a filling factor of 95.9%. Details on the WFI layout can be found, for instance, at the URL "`http://www.eso.org/science/eis/eis_proj/public/wfi_chip.html`" as well as at other locations on the ESO web pages.

Observations of the CDF-S have been performed using the WFI filters summarized in Table 1. The U-band observations were originally conducted using the available narrow filter which was recently (October 2000) replaced by a broader filter to increase the efficiency of the survey. The transmission curves of these filters are plotted in Fig. 1 together with their final throughputs taking into account the optics and the CCD quantum efficiency. It is worth mentioning that very little was known about the performance of the instrument at the time the survey was conceived, especially at the blue and red ends of the wavelength range considered.

Table 1. Filters used in the observations of the CDF-S.

Filter	ESO id	$\lambda_{\rm eff}$ (Å)	*FWHM* (Å)
U	U/38	3710	325
U'	U350/60	3538	560
B	B/99	4556	905
V	V/89	5342	900
R	Rc/162	6402	1595
I	Ic/lwp	8535	1387

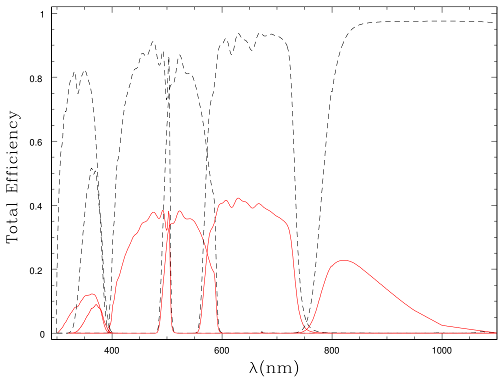

Fig. 1. Transmission curves of the filters (dashed line) and the total throughput of the system (solid line).

The observations in each passband were split into observation blocks (OBs) consisting of a sequence of five exposures with the integration time for each individual exposure ranging from 5 to 15 min depending on the passband. Table 2 summarizes the planned observational strategy, listing: in Col. 1 the passband; in Col. 2 the integration time of each individual exposure; in Col. 3 the number of exposures per OB; in Col. 4 the integration time per OB; in Col. 5 the number of OBs; and in Col. 6 the planned total integration time per band. According to the planned strategy, a total of 210 WFI frames were required to complete a single pointing. In order to minimize the imprint of the inter-chip gaps the choice of pointings were done in the following way. First, the nominal position of each OB (in a given passband) was drawn from a pre-defined list of distinct positions, as given in Table 3. For instance, in the case of U-band which requires 13 OBs, the dithering pattern used is illustrated in Fig. 2. Next, each exposure in the OB sequence was dithered relative to the OB reference position using the offsets in right ascension ($\Delta\alpha\cos\delta$) and in declination ($\Delta\delta$) as listed in Table 4 and illustrated in the inset of Fig. 2. This dithering is essential for de-fringing as well as for efficiently removing cosmic rays and other CCD blemishes.

Table 2. Planned Observing Strategy for the CDF-S observations.

Filter	$T_{\rm tot}$ (s)	$N_{\rm OB}$	$T_{\rm exp}$ (s)
U	60 000	13	900
B	12 000	8	300
V	9000	6	300
R	9000	6	300
I	27 000	9	600

The optical observations span six observing runs over a period of one year (ESO observing periods 64 and 66), distributed over a total of 12 nights. The log of the observations is summarized in Table 5. The table lists: in Col. 1 the date of the observations; in Col. 2 the passband; in Col. 3 the integration time; and in Cols. 4 and 5 the range and average seeing during the night as measured by the seeing monitor. Not listed are the B-band observations taken during the commissioning phase of the WFI, in January 1999, and the U-band data of the COMBO survey (Wolf et al. 2001). Both data sets have been re-processed, for the sake of homogeneity, and used to produce the final combined images. Table 6 summarizes the data available for the CDF-S used in this paper. The table lists: in Col. 1 the band; in Col. 2 the total integration time; in Col. 3 the total number of frames; and in Col. 4 the average seeing of the final co-added images.

To assess the effectiveness of the adopted dithering pattern, Fig. 3 illustrates the exposure time map associated with the final R-band image which is an example of one of the passbands with the shortest exposure and is

Table 3. Nominal coordinates of OBs (see text for definition).

ID	α(J2000)	δ(J2000)
01	03:32:28	−27:48:47
02	03:32:34	−27:48:17
03	03:32:36	−27:49:02
04	03:32:32	−27:49:32
05	03:32:23	−27:49:17
06	03:32:21	−27:48:31
07	03:32:25	−27:48:02
08	03:32:30	−27:47:47
09	03:32:27	−27:49:47
10	03:32:19	−27:50:02
11	03:32:38	−27:47:32
12	03:32:40	−27:50:17
13	03:32:17	−27:47:17

Table 4. Relative offsets of each exposure in a OB.

Dith. #	$\Delta\alpha\cos\delta('')$	$\Delta\delta('')$
1	0	0
2	−70	+21
3	−35	−42
4	+35	+42
5	+70	−21

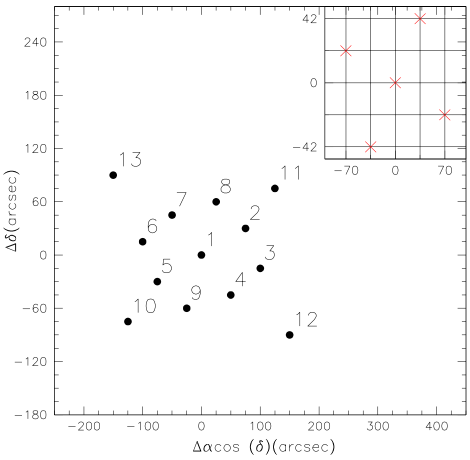

Fig. 2. Schematic view of the dithering pattern used in the observations. Large filled circles mark the coordinates of each OB relative to the nominal center of the field (OB #1 in Table 3). *Inset*: the crosses mark the offset, in arcsec, of each single exposure within an OB, with respect to its center.

Table 5. Log of observations.

Date	Filter	T (s)	seeing range (arcsec)	mean seeing (arcsec)
Nov. 04 1999	U	11 700	0.62–0.97	0.77
	I	8400	0.77–1.71	1.04
Nov. 05 1999	U	13 500	0.74–0.94	0.82
Nov. 06 1999	U	14 400	0.48–0.83	0.64
Nov. 07 1999	I	17 700	0.76–1.26	0.97
Nov. 08 1999	V	13 500	1.40–1.81	1.61
	I	6000	1.20–2.08	1.64
Dec. 03 1999	V	6000	0.46–0.98	0.66
Dec. 04 1999	V	3000	0.48–0.72	0.58
	R	9000	0.47–0.79	0.58
	I	1800	0.67–0.77	0.71
Oct. 26 2000	U'	13 000	0.57–1.04	0.78
Oct. 27 2000	U'	11 700	0.52–1.01	0.70
Nov. 27 2000	U'	9000	0.50–0.76	0.59
Nov. 28 2000	U'	9000	0.67–1.06	0.87
Nov. 29 2000	U'	4500	0.66–1.88	0.76

Table 6. Summary of the CDF-S observations.

Filter	$T_{\rm eff}$ (s)	$N_{\rm f}$	Seeing (arcsec)
U	47 600	55	0.98
U'	43 600	49	1.06
B[a]	24 500	30	1.02
V	9250	33	0.97
R	9250	33	0.86
I	26 900	46	0.93

[a] Commissioning data

thus the least homogeneous (see Sect. 5). In this particular case, the flux ratio of the best sampled region to that at the center of the image is a factor ∼2. This is due in part to the clipping (∼200 pixels) of the CCD frames not taken into account in the original design of the dithering pattern. In the weight-map the effects of at least three satellite tracks can be seen. It is important to point out that some of the survey data have been obtained using dithering patterns different from the one shown in Fig. 3 (e.g., the B-images taken during the commissioning of WFI). In fact, during the course of the survey the pattern has been changed at least once to improve the uniformity of the final image.

The present optical survey complements both recent infrared observations reported by Vandame et al. (2001) as well as optical/infrared observations conducted as part of the EIS-DEEP survey first released in 1998 (Rengelink et al. 1998) and currently under revision (Benoist et al. 2001a). The coverage of this field by these different sets of data is shown schematically in Fig. 4.

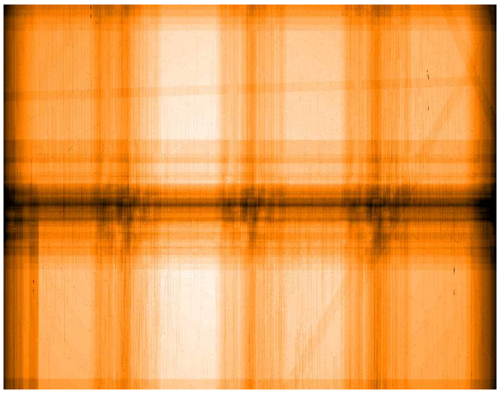

Fig. 3. Weight map corresponding to the final co-added R-band image. The bright regions correspond to locations in the image which have higher sensitivity. While the effect of the inter-chip gaps are minimized, their imprint can still be seen and correspond to the darkest regions of the map (see text for more details). Also note the slightly lower sensitivity in regions where satellite tracks have been detected in individual frames and removed. At least two of them are clearly seen on the upper part and on the right side of the weight map, respectively.

3. Data reduction

3.1. Pipeline processing

The WFI images were processed using the refurbished EIS pipeline (e.g., da Costa et al. 1999; da Costa 2001) which includes new operational modules to enable unsupervised pipeline reduction of WFI images as well as new software routines for carrying out the basic steps of image processing and calibration. Given the scope of the surveys being carried out by EIS, special attention has been given to the development of a survey software system to ensure the adequate and timely processing of large amounts of data for long periods of time in a uniform way. For instance, the complete DPS survey will consist of some 2800 WFI science frames representing over 1 Terabyte of data, to which should be added a comparable amount of data from the so-called Pre-Flames survey not discussed here (Momany et al. 2001). While a detailed account of the extent of these changes is beyond the scope of the present paper, some of the main features are briefly summarized below.

One of the main changes has been the complete removal of different IRAF packages (e.g., xccdred, drizzle) used earlier to process images from CCD mosaics and in the co-addition phase. Instead, WFI images are now split into individual chips at the very beginning of the process. The main advantages of adopting this procedure are that

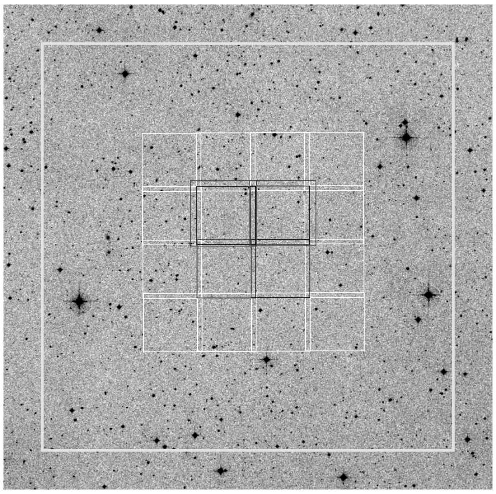

Fig. 4. Schematic view of the coverage of the CDF-S by the EIS program using different instruments. The outer white box delineates the coverage of the present optical survey (WFI). The 2×2 black mosaic and the two overlapping gray boxes delineate the area covered by the infrared (SOFI) and optical (SUSI2) observations, respectively, carried out by EIS-DEEP survey at the NTT. Finally, the 4 × 4 white mosaic represents the complete infrared coverage, including the Deep Public Survey data presented by Vandame et al. (2001). The background image is taken from the DSS.

the pipeline uses a common library of routines, single and multi-chip images are treated in the same way and that the EIS pipeline is more easily adaptable to use PC-based Linux clusters for parallel-processing images, which will eventually lead to a higher throughput.

A major effort has also been made to address specific problems encountered with the data files coming from WFI. These have constantly evolved, which makes them difficult to handle from the point of view of a pipeline. One of the main challenges has been the lack of information in the FITS header regarding the reference pixel. This prevented the unsupervised reduction of the WFI data due to frequent failures in the astrometric calibration from run to run. As the EIS observations with WFI span a long period of time (over two years), during which several upgrades of the data acquisition were made, it was necessary to develop robust procedures to cope with these various changes automatically.

Using tools available from the multi-resolution visual model package (MVM) developed by Bijaoui and collaborators, a special routine was developed to find a first-order astrometric solution for an image, searching a large (∼6×) area surrounding the nominal position of the pointing. The method uses one of the science frames in the run and takes the available information in the image header regarding the pointing only as a first guess. This image is quickly reduced and decomposed using a wavelet transform. The lowest resolution component is then used to cross-correlate features against a low-resolution mock image representing the reference catalog over a much larger area than the original image. The low-resolution science image is then moved around in a spiral pattern starting from its nominal position as given in the image header. At each step a cross-correlation function between the features in the real and mock images is computed and the process resumed. At the end of the search, the position with the largest amplitude of the cross-correlation is used to define a first approximation for the location of the reference pixel for that run. This procedure is aimed at correcting only for large shifts. A more refined astrometric calibration is performed at a later stage.

Another important generic routine was developed to recognize different types of exposures (calibration frames such as dome, sky flats and bias, photometric standard stars or science frames), reject bad frames and associate frames into pseudo-OBs to be reduced according to predefined prescriptions depending on their nature and passband. The association is based on the frame type and on the spatial separation and time interval between consecutive frames. Next, the removal of instrumental signatures such as bias subtraction, flat-fielding and de-fringing are carried out using identical procedures as those applied for infrared images as presented by Vandame et al. (2001). Some of the main features of the software worth mentioning are that the stacking of images is carried out in pixel space (see below), thereby allowing the optimal rejection of cosmic rays and bad pixels using sigma–clipping. Satellite tracks, quite frequent in wide-field images, are efficiently masked on the individual exposures using the Hough transform (Vandame 2001), thereby minimizing their impact on the final stacked image. The number of satellite tracks removed in a single passband ranges from 9 (e.g., R-band images) to 75 (U-band images) depending on the exposure time. In principle, other linear features such as diffraction spikes may also be treated in the same way. The net result of these new developments has been the production of remarkably clean final images, significantly superior to those of earlier releases. These results lead to the production of considerably more reliable source detections since the successful masking of features at the level of individual exposures dramatically minimizes the number of false detections in the final image. Finally, using the sky-flats, a first evaluation of the relative gains of the different chips is conducted for each passband, which it is later applied to the science frames. These relative gains vary from passband to passband and are, in some cases, especially in the UV, as large as 10%.

The stacking of the images is done in two distinct steps. First, the five images belonging to the same OB are warped to the first image of the OB, which is used as reference for the pixel based relative astrometry. All the images in the OB are then averaged. The second step involves warping all the co-added images corresponding to each OB to an absolute astrometric reference catalog (see next section). The resulting images are then co-added taking into account their respective weight-maps, noise and flux scales. For this particular data set the warping of the images has been performed using the *nearest-neighbor* approach. The advantage of this warping is that the noise of the final image is uncorrelated. However, the astrometric solution is less precise due to discreteness effects. A new version of the warping has been developed allowing for a suite of kernel functions.

In contrast to other instruments (e.g., FORS), the fringing observed in I-band with WFI has a peak-to-peak amplitude of ∼10% relative to the background and varies on scales of hours. The de-fringing is performed in exactly the same way as for the infrared images, except that the number of frames in an OB is considerably smaller, making a good estimate harder. Currently, the residual contribution after de-fringing is comparable to the image noise. However, as in the case of the infrared, it would be preferable to decrease the integration time of each exposure and increase the number of dithered images. Based on the current findings, future I-band observations will be done using a different observing strategy.

The implementations described above make the EIS pipeline a tool capable of handling data from different telescope/instrument setups with different implementations of the FITS header. Finally, it is worth pointing out that using the available software several new developments are planned for the future. These include seeing deconvolution, morphological classification and difference image photometry for variability studies.

3.2. Astrometric calibration

The astrometric calibration of the images was performed using as the reference catalog a pre-release version of the *Guide Star Catalog-II* (GSC-II). The GSC-II (McLean et al. 2001) is based on multi-passbands all-sky photographic plate surveys including the Palomar Observatory Sky Survey (POSS-I-II), the SERC and the ESO Red Survey. The astrometric calibration of GSC-II has been obtained relative to Hipparcos (Perryman et al. 1997) and Tycho catalogs (Høg et al. 1997) and the *ACT* (Urban et al. 1998). The astrometric calibration was done using the method developed by Djamdji et al. (1993) based on a multi-resolution decomposition of images using wavelet transforms (MVM). An implementation of these algorithms to stack images, referred to as MVM-astrometry, has been done for EIS as is described above. This package has proven to be efficient and robust for pipeline reductions.

3.3. Photometric calibration

Magnitudes were calibrated to the Johnson-Cousins system using Landolt standards taken from Landolt (1992). While standard stars were observed on every night, to optimize the observing time most observations were used to monitor the zero-point of the night and to compute color terms. For the final calibration, three nights in October 2000, all photometric, were used to obtain measurements of standards over a broad range of airmasses. During these nights, a set of dithered images in each passband was taken overlapping two adjacent pointings (Deep2-b and Deep-2c). These were then used to set the absolute flux scale for all passbands, except the I-band due to problems with de-fringing. For this case, the night of Nov. 4 1999 was used to determine the I-band calibration.

Photometric solutions were obtained using the new EIS photometric pipeline which is fully integrated to the associated database. The tool provides a convenient environment to obtain, verify and store the results of the fits. In the interactive mode it is possible to fit the data after rejecting individual measurements, stars and chips. Alternatively, one can also easily obtain independent solutions for each chip. Unfortunately, the number of standards for the fields considered does not allow independent solutions for each of the eight chips. Therefore, the present calibration had to rely on solutions including all the available chips.

Magnitudes for Landolt stars were obtained using an aperture 6 arcsec in diameter, which proved to be adequate by monitoring the growth curve of all the measured stars. The accuracy of the zero-points are estimated to be in the range ±0.03 mag to ±0.08 mag, with the U-bands having the largest uncertainties. At face value, these results indicate that the gain correction applied to the different chips based on the flatfield exposures is adequate for most passbands with the possible exception of the U-band. A final determination of the relative gains will require a more careful monitoring of the amplitude of these corrections and chip-based solutions. A set of secondary stars for all the Landolt fields considered would also be extremely useful to always allow a chip-based calibration. Efforts in this direction are already underway by several groups.

The computed extinction coefficients compare well with those estimated from the mean extinction curve of the Chilean sites. Finally, the following color terms, relative to the Johnson-Cousins (JC) system, have been empirically determined:

$$
\begin{aligned}
(U_{\rm JC} - U'_{\rm EIS}) &= 0.04 \times (U-B)_{\rm JC},\\
(U_{\rm JC} - U_{\rm EIS}) &= 0.03 \times (U-B)_{\rm JC},\\
(B_{\rm JC} - B_{\rm EIS}) &= 0.14 \times (U-B)_{\rm JC},\\
(B_{\rm JC} - B_{\rm EIS}) &= 0.24 \times (B-V)_{\rm JC},\\
(V_{\rm JC} - V_{\rm EIS}) &= -0.11 \times (B-V)_{\rm JC},\\
(V_{\rm JC} - V_{\rm EIS}) &= -0.21 \times (V-R)_{\rm JC},\\
(R_{\rm JC} - R_{\rm EIS}) &= -0.04 \times (V-R)_{\rm JC},\\
(R_{\rm JC} - R_{\rm EIS}) &= -0.04 \times (R-I)_{\rm JC},\\
(I_{\rm JC} - I_{\rm EIS}) &= 0.25 \times (R-I)_{\rm JC}.
\end{aligned}
$$

These equations can be inverted to a more useful form, expressing the color terms as a function of the observed colors yielding:

$$
\begin{aligned}
(U_{\rm JC} - U'_{\rm EIS}) &= 0.04 \times (U' - B)_{\rm EIS},\\
(U_{\rm JC} - U_{\rm EIS}) &= 0.03 \times (U - B)_{\rm EIS},\\
(B_{\rm JC} - B_{\rm EIS}) &= 0.36 \times (B - V)_{\rm EIS},\\
(V_{\rm JC} - V_{\rm EIS}) &= -0.08 \times (B - V)_{\rm EIS},\\
(R_{\rm JC} - R_{\rm EIS}) &= -0.05 \times (V - R)_{\rm EIS},\\
(I_{\rm JC} - I_{\rm EIS}) &= 0.35 \times (R - I)_{\rm EIS}.
\end{aligned}
$$

These values have a typical error of ± 0.03 and are in good agreement with those computed using the response function of the filters considered, except for U' for which the difference in the color term can be $\sim$0.2 mag. This is because the UV-response of the system is at the time of writing still poorly determined.

The magnitudes were also corrected for galactic absorption, using $E(B-V) = 0.0089$ as derived from Schlegel et al. (1998), yielding $A_U = 0.05$ mag, $A_B = 0.04$ mag, $A_V = 0.03$ mag, $A_R = 0.02$ mag and $A_I = 0.02$ mag. All magnitudes have been converted to the AB system, unless otherwise specified, using the following relations: $U'_{AB} = U' + 1.04$; $U_{AB} = U + 0.80$; $B_{AB} = B - 0.11$; $V_{AB} = V$; $R_{AB} = R + 0.19$; and $I_{AB} = I + 0.50$.

3.4. Image products

The images being released are fully astrometrically (conical equal-area projection; COE) and photometrically calibrated (normalized to 1 s exposure time). The FITS files being provided include both the pixel and weight maps as FITS extensions. A stand-alone software tool to convert the COE images to best-fit TAN projection by modifying the image headers is available through the EIS web pages. The astrometric information is stored in the world coordinate system (WCS) keywords in the FITS headers. Similarly, the photometric calibration is provided by the zero-point and its error available in the header keywords ZP and ZP_ERR. The zero-point includes the normalized zero-point of the photometric solution and the atmospheric extinction correction. In the header one can also find a product identification number (P_ID) which should always be used as reference. The headers also provide information on the number of stacked frames and the on-source total integration time. Additionally, the seeing obtained by measuring the *FWHM* of bright stars in the final stacked images is stored in the header keyword SEE_IMA.

High-resolution images in the different passbands can be found at the URL "`http://www.eso.org/science/eis/`". The image quality of the final images can be assessed by investigating the nature and the amplitude of the PSF distortions. These are measured by using the two components of the so-called polarization vector. These components are derived from the major- (A) and minor-axis (B) and

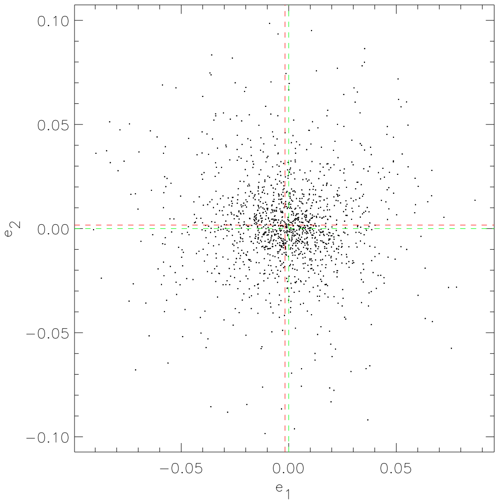

Fig. 5. Amplitude of the PSF distortion over the entire final R-band image. One line is centered on (0, 0), the other on the actual barycenter of the datapoints on (-0.002, 0.002).

the position angle (θ) as measured by SExtractor for point-like sources using the following expressions:

$$
\begin{aligned}
e_1 &= \frac{A-B}{A+B}\cos(2\theta)\\
e_2 &= \frac{A-B}{A+B}\sin(2\theta).
\end{aligned}
$$

The quantities e_1 and e_2 give the amplitude of the distortion. As an illustration, Figs. 5 and 6 show the results obtained from the final R-band image, which consists 30 co-added WFI exposures. Figure 5 shows the distribution of the amplitude of the components, e_1 and e_2, for the individual point sources observed over the entire field and in Fig. 6 the polarization vector field smoothed over a scale of 7 arcmin. The scale of the amplitude of the vectors is set by the length of the small thick line shown on the upper left corner of the figure, which corresponds to an amplitude of 0.0015 (0.15%). These results attest to the excellent quality of the images produced by WFI, leading to a uniform and small PSF distortion throughout the frame with an rms amplitude $\lesssim$2%. Similar results are obtained for the other passbands.

4. Source lists

Source extraction was performed using the latest version of SExtractor software (Bertin & Arnouts 1996; ver. 2.2.1). This version resolves a subtle problem, first identified in the prompt release of the Pilot Survey, which caused the creation of regions devoid of sources when applying SExtractor to WFI frames with weights (Bertin 2001). Detection was carried out separately using the co-added

Table 7. First 40 entries of the CDF-S R-band source list (all magnitudes are given in the AB system).

#	α	δ	$m_{\rm tot}$	ϵ	$m_{\rm iso}$	ϵ	$m_{\rm aper}$	ϵ	S/N	A	$r_{\rm h}$	b/a	PA	class	Flag	EIS flag
EISJ033059.53-275901.2	03:30:59.53	-27:59:01.2	23.99	0.32	24.87	0.29	23.96	0.37	3.41	0.40	2.28	0.71	-12.27	0.78	24	2
EISJ033059.54-275849.0	03:30:59.54	-27:58:49.0	24.27	0.35	24.73	0.26	23.69	0.30	3.87	0.51	1.62	0.62	-52.69	0.69	24	2
EISJ033059.56-275842.9	03:30:59.56	-27:58:42.9	22.29	0.10	22.49	0.08	22.35	0.09	12.59	2.83	2.50	0.66	-6.50	0.85	24	2
EISJ033059.58-275555.1	03:30:59.58	-27:55:55.1	17.66	0.00	17.63	0.00	17.70	0.00	333.33	17.39	2.01	0.67	5.63	0.98	26	2
EISJ033059.62-275314.7	03:30:59.62	-27:53:14.7	22.44	0.09	22.57	0.08	22.39	0.09	13.28	1.76	1.91	0.74	-1.47	0.98	24	2
EISJ033059.65-275044.8	03:30:59.65	-27:50:44.8	22.96	0.18	23.36	0.13	23.00	0.16	7.63	1.53	2.35	0.54	-4.31	0.97	24	2
EISJ033059.66-275250.3	03:30:59.66	-27:52:50.3	22.40	0.18	23.33	0.15	22.86	0.16	6.58	1.87	4.50	0.54	9.65	0.93	16	2
EISJ033059.69-274812.7	03:30:59.69	-27:48:12.7	23.16	0.24	23.77	0.18	23.48	0.26	5.56	1.25	2.61	0.64	-18.88	0.96	24	2
EISJ033059.72-274830.3	03:30:59.72	-27:48:30.3	23.65	0.34	24.29	0.22	23.88	0.41	4.46	0.85	2.63	0.44	-34.08	0.95	16	2
EISJ033059.72-275620.2	03:30:59.72	-27:56:20.2	22.07	0.06	22.08	0.04	22.08	0.08	22.37	1.08	0.63	0.96	-7.29	1.00	16	2
EISJ033059.73-274928.3	03:30:59.73	-27:49:28.3	23.45	0.21	23.67	0.16	23.32	0.26	6.27	1.25	2.01	0.81	55.28	0.96	16	2
EISJ033059.74-275443.7	03:30:59.74	-27:54:43.7	23.27	0.31	23.99	0.20	23.41	0.28	5.07	1.02	2.95	0.63	-22.99	0.95	16	2
EISJ033059.77-274046.7	03:30:59.77	-27:40:46.7	23.62	0.28	24.68	0.27	23.90	0.34	3.72	0.62	3.15	0.32	-3.07	0.87	24	2
EISJ033059.78-274230.4	03:30:59.78	-27:42:30.4	24.15	0.37	25.01	0.31	23.80	0.35	3.22	0.45	1.84	0.79	45.09	0.78	16	2
EISJ033059.78-275538.8	03:30:59.78	-27:55:38.8	21.67	0.06	21.73	0.05	21.70	0.06	20.88	3.74	2.14	0.80	-63.37	0.98	16	2
EISJ033059.79-275147.7	03:30:59.79	-27:51:47.7	23.76	0.35	24.82	0.27	23.65	0.35	3.77	0.40	2.76	0.81	0.56	0.80	16	2
EISJ033059.80-274545.0	03:30:59.80	-27:45:45.0	23.00	0.25	24.02	0.21	23.15	0.22	4.85	0.85	3.54	0.64	-42.96	0.95	16	2
EISJ033059.81-274007.1	03:30:59.81	-27:40:07.1	22.99	0.15	23.15	0.12	22.96	0.16	8.10	1.98	2.24	0.85	-20.05	0.96	24	1
EISJ033059.82-275841.9	03:30:59.82	-27:58:41.9	23.70	0.32	24.18	0.21	23.56	0.32	4.79	0.85	1.98	0.73	-44.84	0.95	0	1
EISJ033059.83-273819.2	03:30:59.83	-27:38:19.2	20.50	0.03	21.14	0.03	21.38	0.03	31.55	5.32	7.04	0.24	3.98	0.12	19	1
EISJ033059.84-273644.5	03:30:59.84	-27:36:44.5	24.29	0.32	24.60	0.23	24.33	0.53	4.33	0.51	1.56	0.61	-36.14	0.88	24	1
EISJ033059.86-273500.1	03:30:59.86	-27:35:00.1	23.35	0.22	24.50	0.24	23.60	0.27	4.12	0.62	4.22	0.56	-3.94	0.94	24	1
EISJ033059.86-273816.7	03:30:59.86	-27:38:16.7	19.54	0.02	19.91	0.02	20.86	0.03	49.50	21.52	10.53	0.39	-21.38	0.03	19	1
EISJ033059.86-273912.9	03:30:59.86	-27:39:12.9	21.98	0.11	22.35	0.08	22.27	0.09	12.11	3.74	3.52	0.80	-59.73	0.27	19	1
EISJ033059.86-274540.4	03:30:59.86	-27:45:40.4	22.57	0.19	23.92	0.20	23.90	0.44	5.09	1.30	11.40	0.15	-0.45	0.99	17	1
EISJ033059.87-275530.7	03:30:59.87	-27:55:30.7	22.00	0.09	22.15	0.07	22.06	0.08	14.97	3.51	2.60	0.78	-51.62	0.76	0	1
EISJ033059.89-273831.6	03:30:59.89	-27:38:31.6	23.47	0.33	24.67	0.29	23.35	0.26	3.45	0.57	2.65	0.41	54.80	0.83	16	1
EISJ033059.89-273957.4	03:30:59.89	-27:39:57.4	23.67	0.26	24.65	0.27	23.50	0.30	3.67	0.62	2.56	0.36	82.30	0.87	16	1
EISJ033059.90-273314.3	03:30:59.90	-27:33:14.3	22.22	0.08	22.27	0.06	22.20	0.08	15.97	2.32	1.94	0.78	-2.79	0.98	24	1
EISJ033059.91-273809.8	03:30:59.91	-27:38:09.8	21.96	0.16	22.41	0.10	22.74	0.15	10.50	4.19	6.41	0.30	-24.84	0.17	19	1
EISJ033059.94-273706.4	03:30:59.94	-27:37:06.4	24.31	0.28	24.64	0.24	24.32	0.65	4.22	0.40	1.17	0.74	-22.64	0.86	16	1
EISJ033059.94-273443.2	03:30:59.94	-27:34:43.2	20.05	0.02	20.06	0.02	20.22	0.02	57.14	10.99	3.70	0.78	35.52	0.13	24	1
EISJ033059.94-274639.7	03:30:59.94	-27:46:39.7	21.83	0.13	22.37	0.08	22.25	0.10	12.09	3.68	4.34	0.72	-7.10	0.34	16	1
EISJ033059.94-275426.9	03:30:59.94	-27:54:26.9	23.92	0.27	24.66	0.27	23.83	0.41	3.66	0.62	2.47	0.26	35.24	0.87	0	1
EISJ033059.95-274650.0	03:30:59.95	-27:46:50.0	23.44	0.25	23.54	0.13	23.22	0.24	7.59	0.79	0.54	0.97	-34.86	0.67	0	1
EISJ033059.97-273531.2	03:30:59.97	-27:35:31.2	22.67	0.23	23.58	0.15	23.14	0.22	6.61	1.30	3.55	0.76	-3.84	0.97	16	1
EISJ033059.97-273818.5	03:30:59.97	-27:38:18.5	19.85	0.02	20.27	0.02	20.77	0.03	41.15	15.41	7.06	0.78	-43.06	0.03	19	1
EISJ033059.98-272943.1	03:30:59.98	-27:29:43.1	23.58	0.23	24.27	0.22	24.04	0.49	4.50	0.79	2.49	0.27	-84.78	1.00	24	1
EISJ033059.99-275040.3	03:30:59.99	-27:50:40.3	23.73	0.30	24.11	0.19	24.02	0.48	5.25	0.79	2.10	0.57	-72.21	0.95	0	1
EISJ033059.99-275906.7	03:30:59.99	-27:59:06.7	23.00	0.24	23.69	0.18	22.99	0.19	5.45	1.30	3.29	0.61	-60.89	0.97	0	1

image of each passband and field. The main parameters in the detection are the smoothing kernel, taken to be a Gaussian with a $FWHM$ equal to 0.8 of that of the PSF measured on the frame; the minimum number of connected pixels above the detection threshold, depending on the seeing taken to be between 8 and 12 pixels, and the SExtractor detection threshold, taken to be between 0.55 (for U) and 0.7 (R and I) depending on the seeing. As an illustration, the tabulation of the first 40 entries in the R-band source catalog is presented in Table 7. All magnitudes are given in the AB system. The table lists:

Column 1: the EIS identification name;

Columns 2 and 3: right ascension and declination (J2000.0);

Columns 4–9: total, isophotal and aperture (3 arcsec diameter) magnitudes and respective errors. The first two magnitudes correspond to the `mag_auto` and `mag_iso` magnitudes measured by SExtractor. The magnitudes have been corrected for Galactic extinction taken from Schlegel et al. (1998). The errors are those estimated by SExtractor and include only the shot-noise of the measured source and background counts. Only objects detected with signal to noise $S/N \geq 3$ (based on the isophotal magnitude errors) are included.

Column 10: an estimate of the S/N of the detection, from the inverse of the errors estimated for the isophotal magnitude;

Columns 11: the isophotal area A of the object in square arcsec;

Column 12: the half-light radius $r_{\rm h}$ in arcsec;

Columns 13 and 14: minor to major-axis ratio and the position angle;

Column 15: the stellarity index computed by SExtractor;

Column 16: SExtractor flags (see Bertin 1998);

Column 17: EIS flags; these flags are used to identify objects in regions with very low weight or close to bright objects. Objects detected in regions with weight ≥30% of the maximum weight (proportional to the total integration time) and not affected by bright stars have EIS flag = 0. Objects with weight <30%, located at the edges of the frame, have EIS flag = 1. Finally, EIS flag = 2 indicates that the object is located in a region masked out due to the presence of a bright object.

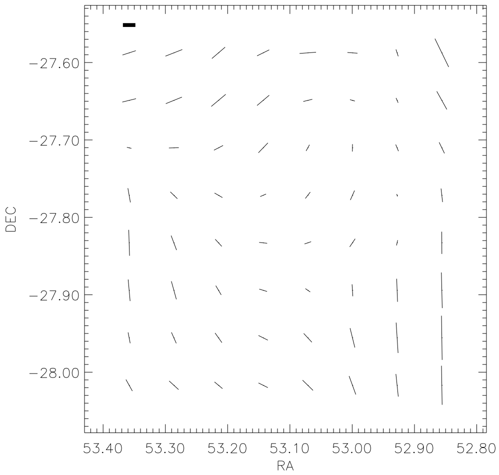

Fig. 6. Vector representation of the PSF distortions for the final R-band image smoothed over a scale of 7 arcmin. RA and DEC are in degrees. The amplitude of the vectors are scaled relative to the thick line segment shown on the upper left corner, which corresponds to an amplitude of 0.0015.

Similar tables for the other passbands are available upon request in ASCII format. Catalogs for the infrared mosaic and optical/infrared color catalogs will be distributed as soon as they become available. Note that besides distributing catalogs in tabular form as done here, catalogs in FITS formats will become part of the distribution of final products. From the inspection of the R-band weight map (see Fig. 3) one sees that, in contrast to catalogs extracted from single chip detectors, describing source catalogs drawn from multi-passband dithered observations of CCD mosaics requires significantly more information than can reasonably be provided in a single ASCII catalog. While the latter is adequate if the derived objects list is to be used for optical cross-identification, it is clearly not sufficient if one is interested in drawing statistical samples with well-defined limiting magnitudes and color coverage. To cope with these deficiencies, future releases will be made using FITS tables which will include: a FITS header with all the relevant information about the observations (pointing, filter, instrument), a FIELDS table which will include: the SExtractor parameters; the magnitude and stellarity index chosen for the star/galaxy classification; magnitude corrections (e.g., AB, extinction) appropriate for the filters used; a variety of limiting magnitudes (point source, turnover, completeness, spurious objects) including the brightest limiting magnitude to extract a homogeneous magnitude-limited sample; the effective area corresponding to this sample taking into account the area removed at the outer edges of the image based on the weight-map and the masks around bright objects, both now being produced automatically by the pipeline according to user-specified parameters. At the same time, no objects will be removed but will carry both their SExtractor and EIS flags, with the vertices of the corresponding masks also being included in the FITS catalogs in a specific fields table. This will also apply to color catalogs which, in addition to information similar to single passband catalogs, must also include others such as the definition of color context to clearly indicate the area of intersection of images in different passbands. In summary, the goal is to produce standard catalogs from which more complex analysis can be carried out with or without the images and associated weight maps.

The output of the new standardized procedures for single passband catalog production is shown in Fig. 7 for the catalog extracted from the final R-band image. The figure shows the outer bounding box defined based on the percentage of the peak exposure time one wants to consider and the masks around saturated or bright objects. Both the magnitude of the objects to be masked and the size of masks can be set by the user. In this example, one sees that not all possibly spurious sources can be eliminated automatically. In particular, in the lower right side of the figure (RA = 53.35, Dec = −27.9 degrees) one sees the effect of a ghost image of a bright star which produces a ring-shaped excess of objects. While attempts are currently being made to identify ghosts and automatically eliminate these regions, it is clear from the diversity of features that in practice, further by-hand clipping of the image is required depending on the specific application of the catalog. Tools for doing so are also implemented in the pipeline with the results being stored in the FITS catalog.

Each catalog produced by the pipeline goes through an automatic verification process which carries out several tests to check the reliability of the products by comparing them with other empirical data and model predictions. The results of some of these tests are described in the next section.

5. Discussion

5.1. Astrometry and photometry

In order to externally verify the accuracy of the astrometric calibration the source lists extracted from the different passbands were compared with that available from the 2MASS survey (Cutri et al. 2000). The number of objects found in common ranges from 286 to 415 depending on the passband considered. Using "good" objects, considering the various flags, in both catalogs the relative positions of coincident pairs were computed and the distribution of the differences in the case of the R-band is shown in Fig. 8. One finds an offset of about 0.12 arcsec in right ascension, a negligible shift in declination and an rms in the differences of $\lesssim$0.23 arcsec, independent of the passband considered. This shows that the astrometric solutions for the different passbands are essentially identical and an overall accuracy of $\sim$0.16 arcsec, probably limited to the internal

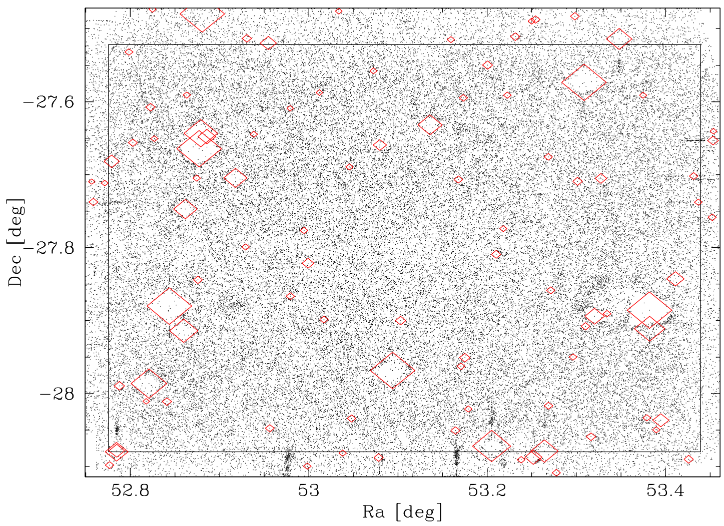

Fig. 7. Projected distribution of galaxies extracted from the R-band image. The figure shows the adopted frame and the masks automatically produced by the pipeline around bright objects which are used to set the EIS flags. It is important to emphasize that these parameters can be re-defined.

accuracy of the reference catalog, is achieved. Note that the shift of the optical data relative to 2MASS is smaller than that obtained with the infrared data. This, however, does not imply any inconsistency in the relative astrometry of the infrared and optical EIS data but rather it reflects the problem described in Vandame et al. (2001) with the astrometry of the pre-release of GSC-II. This problem will be fixed with the official release of the GSC-II.

An independent check of the astrometry can also be carried out by comparing the present astrometry with that determined by Wolf et al. (2001; COMBO survey) who recently obtained deep exposures of the same field in different passbands using the same instrument. In particular, their R-band data reaches $R = 26.0$ (Vega) at 5σ for a total integration time of 23 700 s. Within the overlapping area of both surveys, there are: ∼36 800 objects in common; ∼17 500 detected only by COMBO; ∼4400 only by EIS; and ∼4200 have multiple associations, which are not considered below. Figure 9 shows the result of the comparison of the positions for about 8500 objects in common. These objects include only objects with stellarity index >0.9 in the COMBO R-band source list and satisfying $R_{\rm EIS} < 25$ mag and $S/N(\rm EIS) > 4$. From this comparison, one finds a relative offset of 0.15 arcsec in right ascension and −0.24 arcsec in declination, but more importantly a remarkably small rms of 0.12 arcsec in both directions, possibly suggesting an accuracy of $\lesssim$0.10 arcsec for each individual catalog. This is well within the requirements for slit/fiber positioning, a top requirement for the public survey. These results are insensitive to the exact way the sample is chosen.

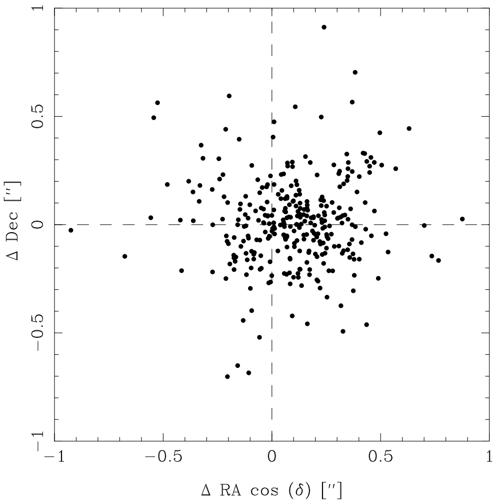

Fig. 8. Comparison in the R-band between the coordinates of objects in common with the 2MASS survey, offsets are computed as $EIS - 2MASS$.

The COMBO data also enables a comparison of the photometric calibration. Figure 10 shows the results of this comparison in the Vega system from which one finds a zero-point offset of ∼−0.01 with an rms of about 0.01 mag for $16 \lesssim R_{\rm EIS} \lesssim 20$ mag, while for objects brighter than

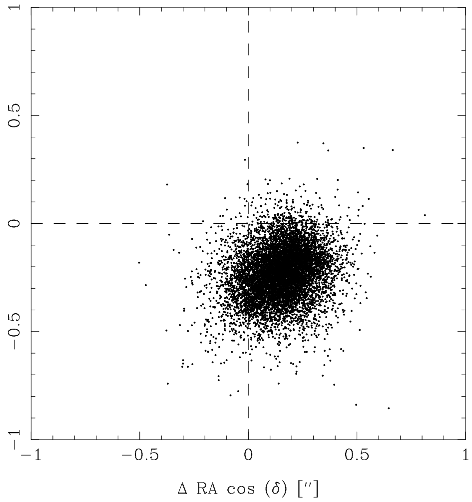

Fig. 9. Comparison between the location of objects in common with the COMBO survey, offsets are computed as EIS-COMBO.

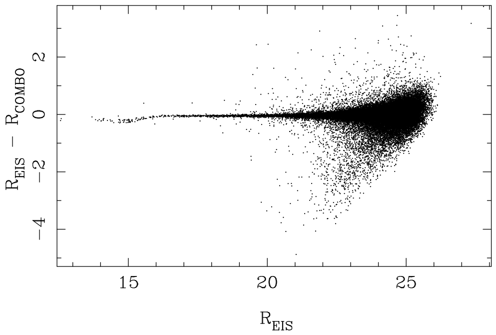

Fig. 10. Comparison between the measured R magnitudes of objects in common with the COMBO survey as a function of the $R_{\rm EIS}$ magnitude (Vega system).

$R \sim 16$ mag saturation sets in. For magnitudes fainter than $R \sim 20$ the scatter increases and beyond $R \sim 22$ one sees the Malmquist bias effect.

5.2. Number counts

A simple statistic that can be used to verify the overall characteristics of the derived catalogs and the parameters chosen for the star/galaxy classification is to compare the number counts of stars and galaxies with model predictions and other empirical data.

Figure 11 shows a comparison of the stellar counts as a function of the total magnitude (Vega system) with those obtained using the Galactic model described by Mendez & van Altena (1996), using the standard parameters described in their Table 1. Considering that no attempt has been made to choose model parameters to fit the observed counts, the agreement between observations and the model predictions is very good. In the B-band, where the present survey is deeper, there seems to be an excess of stellar objects. This is possibly due to QSOs, which are estimated to have a surface density of 120 objects per square degree per 0.5 mag interval at $B = 24$ (Hatziminaoglou et al. 2001). This effect is not expected in V and I because the surface density of QSOs at the magnitude where the stellar counts drop is expected to be small, of order 30–40 per square degree per 0.5 mag interval. Currently, the comparison of the star counts is only possible for the three passbands considered. However, this problem is being addressed and soon a more generic galactic model will be available in the EIS pipeline to compare the predicted counts in all passbands using the transmission curves for the filters being used in a given survey setup (Girardi 2001).

Similarly, Fig. 12 shows the comparison of galaxy counts as a function of the total magnitude, for each of the available passbands, with those obtained for other data sets. In this case, galaxies were defined as objects with a stellarity index less than 0.95 (0.90 in the I-band) or fainter than the classification limit of each passband. The sample includes only objects with $S/N > 3$ and with the appropriate SExtractor and EIS flags and the normalization of the counts takes into account the effective area of each catalog. The U-band counts of Guhathakurta et al. (1990) and I-band counts of Postman et al. (1998) have been corrected assuming an AB correction of 0.8 and 0.45, respectively. As can be seen the observed counts are in good agreement with previously published results indicating that the catalogs being distributed are statistically consistent.

5.3. Survey performance

The characteristics of the data obtained by the present survey are summarized in Table 8 which lists: in Col. 1 the filter; in Col. 2 the seeing of the final co-added image; in Cols. 3 and 4 the 5σ and 3σ limiting AB magnitude measured within an aperture $2 \times FWHM$; and in Col. 5 the number of objects with $S/N \geq 3$, i.e. the number of entries in the catalogs being distributed. At the 5σ limiting magnitudes the fraction of spurious objects with $S/N \geq 5$ is estimated to be $\lesssim 2\%$ for all bands. The fraction of spurious objects was estimated by creating catalogs from the survey images multiplied by -1. The mock images were then used as input to the catalog production and from the comparison between the catalogs of the mock and real objects the fraction of false-positive detections was estimated.

The fact that the COMBO data reaches fainter magnitudes can also be used to obtain a first estimate of the completeness limit of the CDF-S data in the R-band. Figure 13

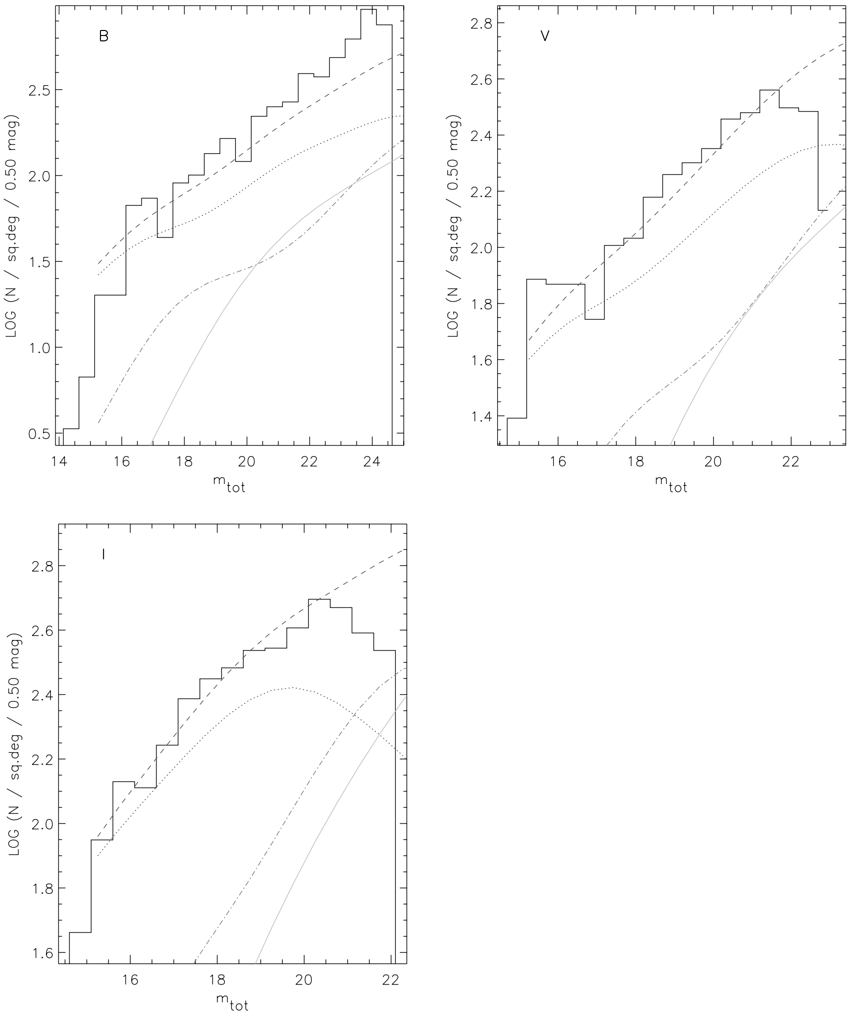

Fig. 11. Comparison of stellar number counts in B (top panel), V (middle panel) and I (lower panel) passbands obtained from the present work (histogram) and those based on the Galactic model of Mendez & van Altena (1996; long-dashed line). In this plot, the magnitudes are in the Vega system. The model includes an old disk population (short dashed line), a thick-disk component (dot-dashed line) and a halo component (dot-dot-dashed line).

shows the ratio as a function of the $R_{\rm COMBO}$ of objects in both catalogs. From this plot, one finds that the R-band catalog is complete to $R_{AB} \sim 24.7$ and 50% complete at $R_{AB} \sim 25.7$. This estimate is probably conservative. A first indication is that there are a large number of objects detected only in the data presented here, most of them at the faint end $R \gtrsim 25.2$. Second, the number of spurious detections at $R \sim 26$ is still relatively small ($\lesssim$30%). Clearly, a determination of the completeness of the catalog from the CDF-S data themselves is highly desirable and will be implemented in the near future.

The limiting magnitudes reached by the present observations are, in general, brighter than those originally proposed ($U_{AB} = 26.8; B_{AB} = 26.0; V_{AB} = 26.0; R_{AB} = 26.3; I_{AB} = 26.0$). For BVR, an increase of the integration time by a factor of two is required to reach the originally stated 5σ limits, representing a 50% increase in the total integration time requested per pointing. Certainly more

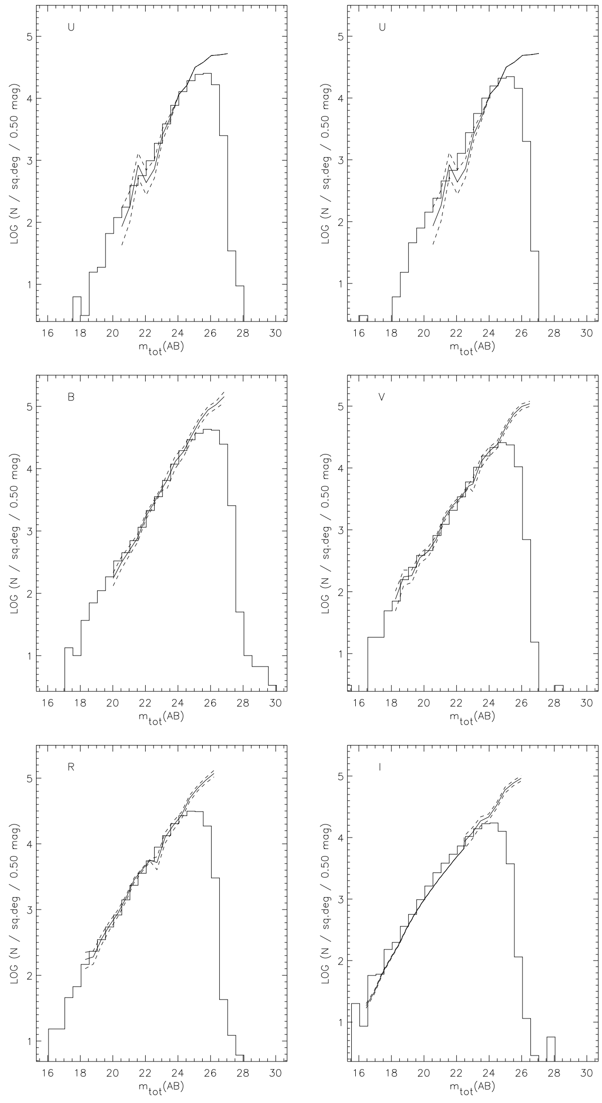

Fig. 12. Comparison of galaxy number counts from the present work (histograms) with those from the following authors: U-band: Guhathakurta et al. (1990); BVR-bands: Arnouts et al. (1997) and Arnouts et al. (1999); I-band: Postman et al. (1998) and Arnouts et al. (1999). The top left panel refers to U', while the top right panel to U. Solid lines represent the mean number counts and the dashed lines the associated errors.

serious is the requirements in U and I, even if more efficient filters are used. From the present data, one finds that the new U' filter has an efficiency at least 5% larger than the original U. A similar increase in efficiency in I is possible using a filter similar to the one available for EMMI for the EIS-WIDE survey. However, even with the new filters the time required to reach the desire magnitudes in U and I involve a large increase (a factor $\gtrsim$4) in their already long integration times. Such an increase would make the desired area coverage unattainable. On the other hand, the limiting magnitudes obtained by the present survey compare favorably with those reached by EIS-DEEP from

Table 8. Properties of the extracted CDF-S catalogs (*AB* system).

Filter	Seeing (arcsec)	$m_{\rm lim}(5\sigma)$ (mag)	$m_{\rm lim}(3\sigma)$ (mag)	$N_{\rm obj}$
U	0.98	25.7	26.3	37094
U'	1.06	26.0	26.6	42087
B	1.02	26.4	27.0	74827
V	0.97	25.4	26.0	45912
R	0.86	25.5	26.1	65148
I	0.93	24.7	25.3	43253

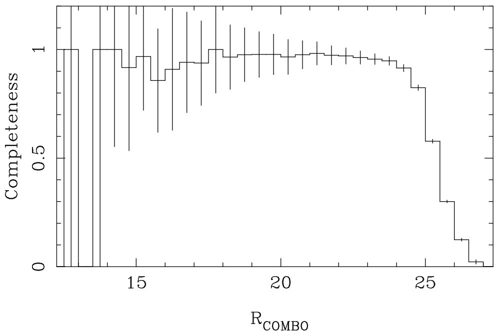

Fig. 13. Estimated completeness, and associated Poisson error, of the CDF-S *R*-band catalog as a function of the $R_{\rm COMBO}$ magnitude in the Vega system.

which Lyman-break galaxy candidates drawn from those samples (da Costa et al. 1998; Rengelink et al. 1998) have been successfully confirmed spectroscopically at $z \gtrsim 2.8$ (Cristiani et al. 2000), strongly suggesting that the primary goal of the present survey is indeed possible. A more detailed discussion of this point will be presented elsewhere when attempts to combine the data obtained using the two different U filters will be made (Arnouts et al. 2001; Benoist et al. 2001b).

Finally, as mentioned in Sect. 2, the CDF-S has already been observed both in optical and infrared passbands as part of the EIS-DEEP survey using the NTT (Rengelink et al. 1998). These old observations are being re-analyzed, using the new methods of the pipeline and compared with the present observations elsewhere (Benoist et al. 2001a). The infrared data from this survey is particularly important as it complements the infrared CDF-S survey recently completed (Vandame et al. 2001).

6. Summary

This paper presents the first optical results of the ongoing multicolor Deep Public Survey being conducted by the EIS program. The observations and the data for the first pointing completed as part of this program which corresponds to the Chandra CDF-S field are described. The set of products being publicly released includes fully calibrated pixel maps and source lists covering the CDF-S region. Given the current interest in this area of the sky both the optical data presented here, covering ∼0.25 square degrees, and the infrared survey recently released, covering an area of ∼0.11 square degrees, are being made available world-wide. Hopefully, this will, together with the Chandra X-ray data, contribute to making this region of the sky a natural target for multi-wavelength observations in the southern hemisphere and an ideal area for cosmological studies. Other derived products from the EIS program will be described in forthcoming papers in this series.

Acknowledgements. We thank all of those directly or indirectly involved in the EIS effort. Our special thanks to K. Meisenheimer and C. Wolf for making their *U*-band images and *R*-band catalogs available to EIS, E. Bertin for his quick response to our request for help, A. Bijaoui for allowing us to use tools developed by him and collaborators over the years and past EIS team members for building the foundations of this program. We would also like to thank A. Renzini and past and present members of the Working Group for Public Surveys. The Guide Star Catalogue-II is produced by the Space Telescope Science Institute in collaboration with the Osservatorio Astronomico di Torino. Space Telescope Science Institute is operated by the Association of Universities for Research in Astronomy, for the National Aeronautics and Space Administration under contract NAS5-26555. Additional support is provided by the Association of Universities for Research in Astronomy, the Italian Council for Research in Astronomy, European Southern Observatory, Space Telescope European Coordinating Facility, the International GEMINI project and the European Space Agency Astrophysics Division. This publication makes use of data products from the Two Micron All Sky Survey, which is a joint project of the University of Massachusetts and the Infrared Processing and Analysis Center/California Institute of Technology, funded by the National Aeronautics and Space Administration and the National Science Foundation. This research has made use of the SIMBAD database, operated at CDS, Strasbourg, France.

References

Arnouts, S., de Lapparent, V., Mathez, G., et al. 1997, A&AS, 124, 163
Arnouts, S., d'Odorico, S., Cristiani, S., et al. 1999, A&A, 341, 641
Arnouts, S., et al. 2001, in preparation
Benoist, C., et al. 2001a, in preparation
Benoist, C., et al. 2001b, in preparation
Bertin, E., & Arnouts, S. 1996, A&AS, 117, 393
Bertin, E. 1998, SExtractor, User's guide, v2.0
Bertin, E. 2001, private communication
Cristiani, S., Appenzeller, I., Arnouts, S., et al. 2000, A&A, 359, 489
Cutri, R. M., Skrutskie, M. F., Van Dyk, S., et al. 2000, Explanatory Supplement to the 2MASS Second Incremental Data Release
da Costa, L., et al. 1998, A&A, submitted `[astro-ph/9812105]`

da Costa, L. N., et al. 1999, The Messenger, 98, 36
da Costa, L. N. 2001, in Mining the Sky, Proc. of ESO Workshop (Springer-Verlag), 521
Djamdji, J. P., Bijaoui, A., & Manière, R. 1993, Photogrammetric Engineering and Remote Sensing, 59, 645
Giacconi, R, Rosati, P., Tozzi, P., et al. 2001, ApJ, 551, 624
Girardi, L. 2001, private communication
Guhathakurta, P., Tyson, J. A., & Majewski, S. R. 1990, in Evolution of the universe of galaxies, Astronomical Society of the Pacific, 304
Hatziminaoglou, E., et al. 2001, A&A, submitted
Høg E., Bässgen, G., Bastian, U., et al. 1997, A&A, 323, L57
Landolt, A. U. 1992, AJ, 104, 340
McLean, B., Greene, G., Lattanzi, M., & Pirenne B. 2001, Astronomical Data Analysis Software and Systems IX, ed. N. Manset, C. Veillet, & D. Crabtree, ASP Conf. Proc., 216, 145
Mendez, R. A., & van Altena, W. F. 1996, MNRAS, 279, 1357
Momany, Y., Vandame, B., Zaggia, S., et al. 2001, A&A, 379, 436
Perryman, M. A. C., Lindegren, L., Kovalevsky, J., et al. 1997, A&A, 323, L49
Postman, M., Lauer, T. R., Szapudi, I., & Oegerle, W. 1998, ApJ, 506, 33
Rengelink, R., et al. 1998, A&A, submitted [astro-ph/9812190]
Rosati, P. 2001, in preparation
Schlegel, D., Finkbeiner, D., & Davis, M. 1998, ApJ, 500,525
Urban, S. E., Corbin, T. E., & Wycoff, G. L. 1998, AJ, 115, 2161
Vandame, B., Olsen, L. F., Jørgensen, H. E., et al. 2001, A&A, submitted [astro-ph/0102300]
Vandame, B. 2001, in Mining the Sky, Proc. of ESO Workshop (Springer-Verlag), 595
Wolf, C., Meisenheimer, K., Dye, S., et al. 2001, A&A, 377, 422

Appendix C

Pre-FLAMES Survey: Observations of selected stellar fields

A&A 379, 436–452 (2001)
DOI: 10.1051/0004-6361:20011325

Astronomy & Astrophysics

ESO imaging survey

Pre-FLAMES survey: Observations of selected stellar fields*

Y. Momany[1,2], B. Vandame[1], S. Zaggia[1,3], R. P. Mignani[1], L. da Costa[1], S. Arnouts[1], M. A. T. Groenewegen[1], E. Hatziminaoglou[1], R. Madejsky[1,5], C. Rité[1,6], M. Schirmer[4], and R. Slijkhuis[1]

[1] European Southern Observatory, Karl-Schwarzschild-Str. 2, 85748 Garching b. München, Germany
[2] Dipartimento di Astronomia, Universitá di Padova, Vicolo dell'Osservatorio 5, 35122 Padova, Italy
[3] Osservatorio Astronomico di Trieste, Via G. B. Tiepolo 11, 34131 Trieste, Italy
[4] Max-Planck Institut für Astrophysik, Karl-Schwarzschild-Str. 1, 85748 Garching b. München, Germany
[5] Universidade Estadual de Feira de Santana, Campus Universitário, Feira de Santana, BA, Brazil
[6] Observatório Nacional, Rua Gen. José Cristino 77, Rio de Janerio, R.J., Brasil

Received 30 July 2001 / Accepted 18 September 2001

Abstract. This paper presents the first set of fully calibrated images and associated stellar catalogs of the Pre-FLAMES survey being carried out by the ESO Imaging Survey (EIS) project. The primary goal of this survey is to provide the ESO community with data sets from which suitable target lists can be extracted for follow-up observations with the new VLT facility FLAMES (Fiber Large Array Multi Element Spectrograph). For this purpose, 160 stellar fields have been selected for observations in B, V and I using the $8\mathrm{k} \times 8\mathrm{k}$ Wide Field Imager (WFI) at the MPG/ESO 2.2 m telescope at La Silla. Out of those, over 100 fields have already been observed. The list of selected fields includes open clusters, globular clusters, regions in the Galaxy bulge, dwarf spheroidal galaxies in the vicinity of the Milky Way, contiguous regions of SMC and LMC and few nearby clusters of galaxies. The present paper discusses the results obtained for a small subset of these data, which include four open clusters (M 67, NGC 2477, NGC 2506 and Berkeley 20) and two regions of the SMC. These data have been used to assess the observing strategy adopted, a combination of short- and long-exposures, and to define suitable reduction techniques and procedures for the preparation of input catalogs for FLAMES. In order to minimize light losses due to misplacements of FLAMES fibers, the astrometric calibration of crowded stellar fields is a critical issue. The impact of different swarping techniques and different reference catalogs on the astrometric calibration of the images is evaluated and compared to those of other authors. From this comparison, one finds that both USNO 2.0 and the recently released GSC 2.2 yield comparable results with the positional differences having a rms of about 0.15 arcsec, well within the requirements (0.2 arcsec) specified by the FLAMES science team. The internal accuracy of the astrometry is estimated to be $\lesssim$0.1 arcsec, primarily limited by the reference catalog used. The major difference between these catalogs is the systematic variation of the positional residuals as a function of the apparent magnitude of the objects, with the GSC 2.2 yielding by far the best results. The astrometric calibration of the images presented here is based on the USNO 2.0 catalog because not all fields considered are covered by the current release of the GSC 2.2. Future EIS calibrations will be done using the GSC 2.2 catalog. The extraction and photometric measurements of stellar sources are carried out using a PSF fitting technique. Comparison with results available in the literature shows that the photometric measurements are in good agreement, apart from possible zero-point offsets, with the magnitude differences having a scatter of $\sim$0.06 mag at $V = 20$ mag. This demonstrates that the data allow for the selection of robust targets down to the expected spectroscopic limit of FLAMES. The combination of catalogs extracted from the short and long-exposures allows one to produce color-magnitude diagrams (CMD) spanning $\sim$13 mag in V and reaching a limiting magnitude of $V \sim 22{-}23$. These data have also been combined with data from the Two Micron All Sky Survey (2MASS) survey allowing for a better color-based object classification and target selection. The Pre-Flames (PF) survey data meet the requirements of FLAMES, and provide a good starting point for detailed studies of the examined systems. The images and catalogs presented here are publicly available and can be requested from the URL address "`http://www.eso.org/eis`".

Key words. techniques: image processing – astronomical data bases: miscellaneous

1. Introduction

The ESO Imaging Survey (EIS) project was conceived with the purpose of producing data sets matching the

Send offprint requests to: Y. Momany,
e-mail: `ymomany@eso.org`

* Based on observations collected at the European Southern Observatory, La Silla, Chile within program ESO 164.O-O561.

foreseen scientific goals and requirements of different VLT instruments (e.g.Renzini & da Costa 1997). With this in mind, EIS has been carrying out for the past two years the Deep Public Survey (DPS), an optical/ infrared deep survey of high-galactic latitude fields, and the so-called Pre-FLAMES (PF) survey. The latter survey consists of selected stellar fields well matched to VIMOS and FLAMES (Fibre Large Array Multi Element Spectrograph, Pasquini et al. 2000) capabilities, respectively.

FLAMES, which will be installed on the A Nasmyth platform of the VLT Kueyen telescope, consists of a fiber positioner, a dedicated fiber-fed spectrograph (GIRAFFE) and a fiber link to the UVES spectrograph located on the B Nasmyth platform. The fiber positioner covers a corrected field of view of $\simeq$25 arcmin in diameter. GIRAFFE will be fed by fibers in one of the following ways: (a) 130 fibers, 1.2 arcsec in diameter, in the MEDUSA configuration; (b) 15 deployable integral field units (IFUs, 2×3 square arcsec with 20 fibers each); (c) one central large unit (ARGUS, 11.5×7.3 square arcsec with 308 fibers). GIRAFFE will have two gratings with a resolving power of $R = 5000$–9000 and $R = 15\,000$–$25\,000$, depending on the fiber mode used. The corresponding spectral coverage will be $\sim$50–120 nm and $\sim$20–50 nm, respectively. The performance of the instrument can be illustrated by the following example: an exposure of one-hour with GIRAFFE in the MEDUSA mode of a $V = 20$ mag point source at $R = 15\,000$ is expected to yield a spectrum with a signal-to-noise ratio of 15 per resolution element. UVES will be fed by 8 fibers and will only use the red arm with a resolving power of $R \sim 45\,000$ and a spectral coverage of 200 nm. An important feature of the FLAMES setup is that it will allow for simultaneous observations with GIRAFFE and UVES.

The relatively small diameter of the fibers and the lack of an imaging mode require the preparation of target lists with accurate astrometry. The positional errors have to be small ($\lesssim$0.2 arcsec) in order to minimize the off-center losses. It is estimated that misplacing a fiber by $\sim$0.5 arcsec, during observations under seeing conditions typical of Paranal ($\sim$0.7 arcsec), would decrease the collected flux by $\simeq$50%. In addition, to take full advantage of GIRAFFE, multi-color source catalogs with reliable photometry (e.g.$\sim$0.03 mag at $V = 20$) over the large field-of-view of FLAMES are required for an adequate preselection of spectroscopic targets and their subsequent analysis.

Foreseeing the need to build suitable data sets for FLAMES, ESO's Working Group for public surveys recommended the EIS project to carry out an imaging survey of selected dense stellar fields, the so-called Pre-FLAMES (PF) Survey. The survey is being conducted with the Wide-Field Imager (WFI) at the MPG/ESO 2.2 m telescope, with a field of view (34×33 arcmin) comparable to that of FLAMES ($\simeq$25 arcmin in diameter). As in the case of other public surveys carried out by EIS, the ultimate goal has been not only to gather imaging data, but develop and test procedures to produce science grade products in the form of fully calibrated images and multicolor stellar catalogs, from which samples for observations with FLAMES can be extracted. The survey was designed to observe a suitable number of fields required for commissioning and first year of operation of FLAMES. The fields should have surface densities >1000 objects per square degree at the magnitude limit of FLAMES. Such fields will provide enough targets for the 130 fibers available in the MEDUSA mode. Considering that in a typical night the MEDUSA mode can produce around 1000 stellar spectra in five to ten different fields (Pasquini et al. 2000), this implies that approximately 500 stellar fields per year can be observed with FLAMES. To this end, a total of 160 fields were selected for observations from suggestions of users as compiled by the FLAMES team. Test runs were conducted during the first semester of 1999, as part of the EIS Pilot Survey. These earlier data helped to define the observing strategy of the PF survey which started in October 1999.

This paper presents the first set of data produced, which is used to assess the procedures being adopted in carrying out the observations and data reduction, to evaluate the results and to illustrate the scientific potential of the data once combined with the spectroscopic observations using FLAMES. This paper is organized as follows: Sect. 2 describes the observations conducted in the period November 27−29, 2000, one of 10 PF runs conducted so far. Section 3 describes the data reduction steps, while Sect. 4 presents a detailed discussion of the astrometric calibration, including the results of tests conducted using different swarping techniques and reference catalogs. In this paper, only the B and V images are presented, leaving to a subsequent paper the description of the reduction of the I band, which requires special treatment because of the strong and variable effects of fringing. The methods used in the preparation of the final photometric catalog, which includes source extraction in crowded fields, magnitude measurements based on PSF fitting, merging of catalogs extracted from short- and long-exposures and from different passbands, are discussed in Sect. 5. Section 6 describes the science products being released, which can be requested from the URL "`http://www.eso.org/eis`". A preliminary evaluation of the data is presented in Sect. 7 which presents and discusses the color-magnitude diagrams for the different stellar systems. Finally, in Sect. 8 the main results of the present paper are summarized and the future implementations are outlined.

2. Observations

The observations for the PF Survey are carried out using the WFI camera at the Cassegrain focus of the MPG/ES0 2.2 m telescope at the La Silla observatory. WFI is a focal reducer-type mosaic camera with 4×2 CCD chips of 2048×4098 pixels. Each chip covers a field of view of 8.12×16.25 arcmin with a projected pixel size of 0.238 arcsec. The 8 CCDs are physically separated by gaps of width 23.8 and 14.3 arcsec along the right

Table 1. Log of the November 27–29, 2000 observing run.

Target EIS name	RA (h m s)	Dec (d m s)	Night	Filter	Exp. Time (sec)	seeing (arcsec)
OC3	05 32 57.9	+00 13 04	27 Nov.	B	$2 \times 240 + 1 \times 30$	1.09−0.99
(Berkeley 20)				V	$2 \times 240 + 1 \times 30$	1.02–1.14
SMC 5	00 56 45.0	−72 19 00	28 Nov.	B	$2 \times 240 + 1 \times 30$	1.36–1.29
(SMC)				V	$2 \times 240 + 1 \times 30$	1.33–1.17
OC14	08 00 10.7	−10 47 17	28 Nov.	B	$2 \times 240 + 1 \times 30$	0.90–0.79
(NGC 2506)				V	$2 \times 240 + 1 \times 30$	0.95–1.02
SMC 6	01 03 35.0	−72 19 00	29 Nov.	B	$2 \times 240 + 1 \times 30$	1.29–1.22
(SMC)				V	$1 \times 240 + 1 \times 30$	1.29–1.33
OC12	07 52 16.7	−38 32 48	29 Nov.	B	$2 \times 240 + 1 \times 30$	1.23–1.09
(NGC 2477)				V	$2 \times 240 + 1 \times 30$	1.09–1.07
OC99	08 51 22.0	+11 49 00	29 Nov.	B	$2 \times 240 + 1 \times 30$	1.36–1.21
(M 67)				V	$2 \times 240 + 1 \times 30$	1.02–0.98

ascension and declination directions, respectively. The full field of view of the camera is thus 34×33 arcmin, with a filling factor of 95.9%. More details about the instrument can be found on the La Silla web page (`http://www.ls.eso.org/lasilla`).

The adopted observing strategy for the PF survey was a compromise between number of required passbands, number of fields, exposure-time, filling factor, and observing overheads. The observations of PF fields were conducted in B, V and I to provide color information for the selection of objects. The integration time was split into a short-exposure of 30 s (SHALLOW), to avoid saturating bright objects, and two deeper exposures of four minutes each (DEEP). These were dithered by 30 arcsec both in right ascension and declination. The long exposures were sufficiently deep to reach the required signal-to-noise at the spectroscopic limit of FLAMES, while the short exposures allows one to recover saturated bright stars in the long exposures exposures (a gain of $\sim$4 mag). Bright stars are also necessary as guide stars for each FLAMES field, which should be in the same astrometric system as that of the target list.

Table 1 shows the log of the observations conducted in the period November 27–29, 2000. The table gives: in Col. (1) the EIS target identification and the name of the primary object being observed; in Cols. (2) and (3) the J2000 right ascension and declination; in Col. (4) the date of observation; in Col. (5) the filters used; in Col. (6) the exposure time and number of exposures for the SHALLOW and DEEP exposures; and in Col. (7) the seeing during the SHALLOW and DEEP exposures, respectively. As mentioned above, the I band images are not presented in this paper.

3. Data reduction

The WFI images were processed using the EIS pipeline, described in more detail by Arnouts et al. (2001) and Vandame et al. (2001). The basic reductions steps performed by the pipeline include the removal of the instrument signature (trimming, de-biasing and flat-field correction), pixel registration, removal of cosmic rays and other image artifacts, image swarping to a fixed astrometric grid and stacking of the swarped images. However, the pipeline was originally designed to deal with high-galactic latitude fields and for a completely different observing strategy than the one adopted for the present survey. In particular, the fact that the number of dithered images is small and the fields are crowded required some changes in the reduction strategy. As discussed below, the results also showed the need for additional modifications of the software, which are currently under way. One of the issues not addressed in the present paper is the procedure required for de-fringing the I-band images for which the solution adopted for the Deep Survey is not applicable to the present observations. It is important to emphasize that the I-filter in use is very red compared to the standard Cousins, with a broad spectral coverage to the red. Tests have also shown the fringing pattern to be variable during the course of one night. Methods for dealing with the fringing and the impact of its removal will be discussed in a subsequent paper.

4. Astrometry

As mentioned above, a key issue of concern regarding the PF survey is the astrometric calibration of the images and of the target lists which will be used for FLAMES observations. In this section, the algorithm used in the calibration of the images and an evaluation of the available reference catalogs are discussed.

The astrometric calibration performed by the EIS pipeline makes extensive use of the method developed by Djamdji et al. (1993) based on the multi-resolution decomposition of images using wavelet transforms. As described in Arnouts et al. (2001), this package is used both to obtain a crude first estimate of a suitable reference pixel for

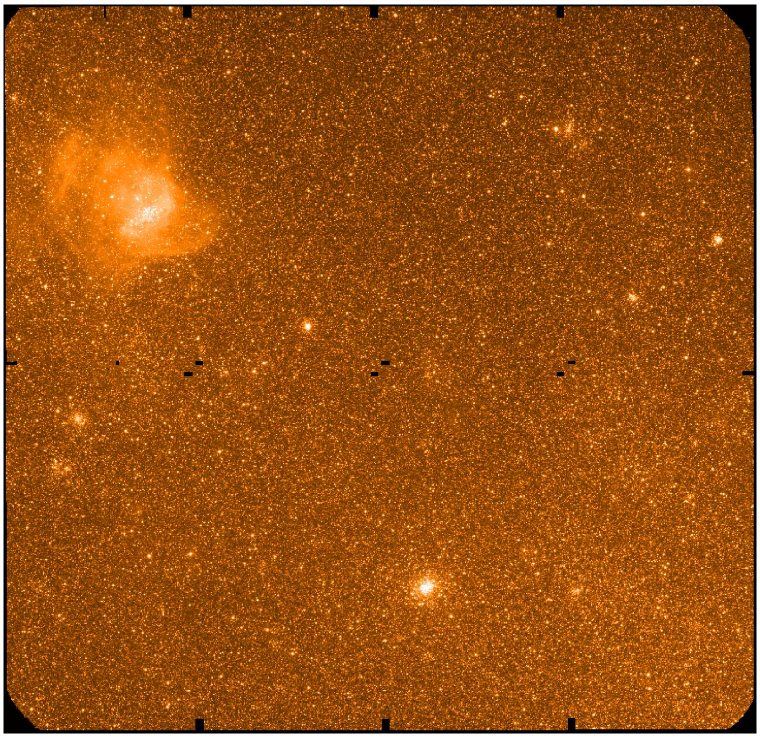

Fig. 1. The V band of the SMC 5 field covering a field of view of 34×33 arcmin. This image is the combination of the two DEEP dithered images. The small black areas seen along the central part of the image and at the edges are the residuals of the inter-chip gaps. In this field the following clusters are present: NGC 346 (the brightest HII region in the SMC), NGC 330, IC 1611, NGC 306, NGC 299, OGLE 109, OGLE 119, OGLE 99.

the WFI images for the run, and an accurate determination of the astrometric solution for each image. Once an adequate reference pixel is available for the run, the science images are decomposed into images of different resolutions. The same is done for a mock image created from the positions of stars taken from the reference catalog being used. The lowest resolution images obtained are then correlated and a first approximation of the astrometric solution, in this case a translation, is determined. This solution is then used to correct the positions of the source catalog extracted from the next higher resolution science image. The source catalog is extracted using a simple algorithm which identified local maxima. This procedure is then repeated for each subsequent resolution, while the search radius used to identify matching objects decreased. At the highest resolution a polynomial of second-order is used and the search radius is half a pixel, which in the case of WFI corresponds to $\sim$0.14 arcsec.

Once an astrometric solution is found for each CCD of the mosaic, the image is then corrected for distortions by swarping it using a *nearest neighbor* criterion to relocate the flux. While this proved to be adequate for the DPS survey, the results of tests discussed below show that this strategy has to be modified for the PF survey due to the small number of images per pointing. In this case, it is necessary to re-sample the images by factors of two and three to obtain the best results. This re-sampling strategy has been adopted as a temporary solution. A more general swarping technique is currently being implemented into the pipeline which will allow for a suite of kernels to be chosen. This technique and their impact on the astrometric calibration will be discussed in a subsequent paper of this series.

After the registration of the individual images, a final combined image can be produced by simply adding the two images using the weight image to eliminate cosmic rays and bad pixels. As an illustration, Fig. 1 shows the final V-band image of the SMC 5 field covering $34\times$ 33 arcmin. The observing strategy adopted leads to a filling factor of 99.91%, albeit with regions less sensitive than others. Note, however, that the imprints of the gaps are not completely removed and can still be seen aligned along the central part of the image and at the edges. It is interesting to note the large number of stellar systems that can be seen in this field, among them: NGC 346, NGC 330, IC 1611, NGC 306, NGC 299, OGLE 109, OGLE 119, OGLE 99.

Considering the importance of an accurate astrometric solution in the preparation of target lists for any fiber system, such as FLAMES, several tests were performed in order to evaluate and fine-tune the "swarp" algorithm and to chose the best reference catalog. These tests were conducted using the data for the nearby open cluster M 67 (EIS target OC99), for which results of several previous work are available in the literature. For instance, the work of Girard et al. (1989) provides a source catalog with positions having a typical internal relative error of $\simeq$0.021 arcsec for a sample of 663 stars, with errors of $\simeq$0.010 arcsec for the stars with $V < 14$. Their estimated external (absolute) error is 0.16 arcsec. The catalog also gives proper motions measurements for each star for a mean reference epoch of 1950.8.

4.1. Fine-tuning the pipeline

A first set of tests were carried out to establish the best re-sampling strategy to be used in the astrometric calibration of the images. First, the SHALLOW and DEEP images of OC 99 were astrometrically calibrated using the nearest neighbor algorithm without image re-sampling, the default mode of the pipeline. Second, the photometric pipeline (see Sect. 5) was run to extract point-like objects and construct catalogs for both the SHALLOW and the combined DEEP images. The reader is reminded that the SHALLOW and DEEP images were astrometrically calibrated separately and thus have independent solutions. The upper panel of Fig. 2 (panel A) shows a comparison between the derived SHALLOW and DEEP catalogs. From the figure, one can clearly see the undesirable effect of the nearest neighbor approach. In this case, the distribution of the positional residuals in RA and Dec are highly non-Gaussian, with the residuals in RA being described by a bi-modal distribution with the peaks separated by $\sim$0.24 arcsec, corresponding to one WFI pixel. This systematic effect is an artifact introduced by the nearest neighbor approach without image re-sampling. This effect becomes obvious when one is dealing with a small number of images, as in the present case. Better results are obtained when the image is re-sampled and each original pixel is split into 2×2 pixels. This case is shown in the middle panel of Fig. 2 (panel B), where the peaks of the bimodal distribution are much closer together and the distribution of the residuals resembles more closely that of a Gaussian. Even better results are obtained using a higher resolution re-sampling with each pixel being split into 3×3 pixels. This is shown in the lower panel of the same figure (panel C). The latter sampling leads to a Gaussian distribution with an rms of $\simeq$0.05 arcsec in both coordinates. For all three cases the variation of the RA and Dec

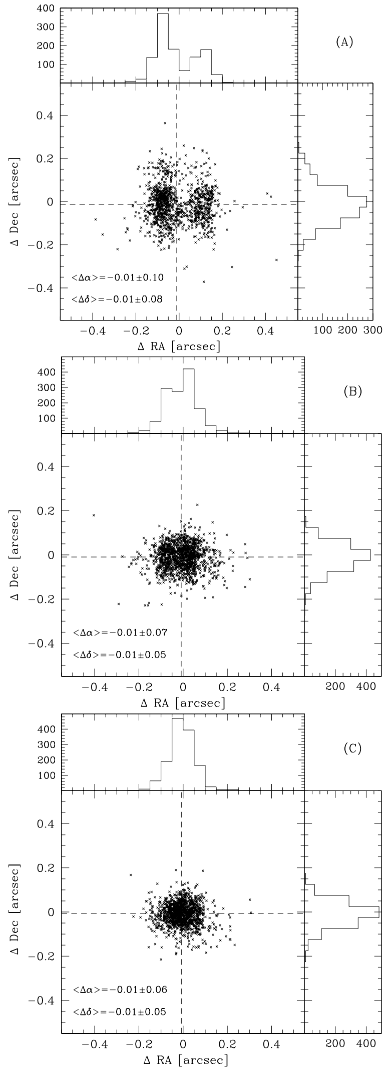

Fig. 2. Comparison of the two independent astrometric calibration of the SHALLOW and DEEP exposures adopting the USNO catalogue for the field of M 67 (OC99). **A)** Nearest neighbor algorithm with sub-sampling of 1×1. **B)** Same as above but with pixel sub-sampling of 2×2. **C)** Same as above but with pixel sub-sampling of 3×3. The vertical and horizontal dashed lines mark the mean residuals in RA and Dec after applying a 3σ clipping to the data. The mean values with the final $1 \times \sigma$ rms are given on the figure. Also shown are the histograms of the residuals as a function of RA (top) and Dec (right).

residuals as a function of magnitude were inspected and were found to be negligible. Note that while the mean offset of the residuals do not change, the rms is significantly smaller in the right ascension direction between the first and last cases.

The results of these tests show that in order to avoid systematic errors between bright and faint sources a re-sampling of the image is required if the nearest neighbor strategy is adopted. In this paper, all images have been re-sampled by splitting the original pixels in 3× 3 sub-pixels. However, since re-sampling the image is costly in processing time, a more general swarping algorithm has been developed to avoid the discreteness effects of the nearest neighbor approach. This algorithm is currently being implemented into the EIS pipeline. It will be used for all subsequent reductions of the PF survey data.

4.2. Choice of the reference catalog

Another important issue to consider is the impact of the reference catalog used. In order to evaluate the available catalogs, the amplitude of the residuals, their dependence on position and on apparent magnitude, and their comparison with an independent astrometric catalog are investigated in this section. It is important to point out that during the analysis of the data presented in this paper only two reference catalogs were available – the USNO 2.0 and the GSC 2.1, a pre-release version of the Guide Star Catalog version 2, used as the reference catalog in the most recent EIS reductions (e.g. Vandame et al. 2001; Arnouts et al. 2001). However, right before the release of these data, the GSC 2.2 version (McLean et al. 2001) became available. While it was not possible to re-analyze all of the data in time for the scheduled release, the GSC 2.2 was used in the tests presented here to assess the differences, if any, relative to the pre-release version. This is important because at the time of writing a number of fields observed as part of the PF were not yet covered by the GSC 2.2. This raised the issue of whether the GSC 2.1 or the USNO 2.0 should be used for the first PF release.

In the present analysis, the SHALLOW images of M 67 were calibrated using the three reference catalogs described above. Next, the positional differences between the calibrated source list and the reference catalog were computed. The RA and Dec residuals are shown in Fig. 3 for each reference used. For consistency, only objects brighter than $m = 18.5$ are plotted, this lower limit corresponding to the magnitude cutoff of the GSC 2.2 catalog. From the figure, one can immediately see the superiority of the GSC 2.2 relative to the other catalogs considered. The distribution of the residuals using the GSC 2.2 catalog is highly concentrated and Gaussian in both directions. This is in marked contrast to the other two which have a much wider spread in the ΔRA–ΔDec plane, and either very skewed (USNO 2.0) or bi-modal (GSC 2.1) distributions. The mean offsets and the rms of the distributions, given on each panel, show that while the systematics of

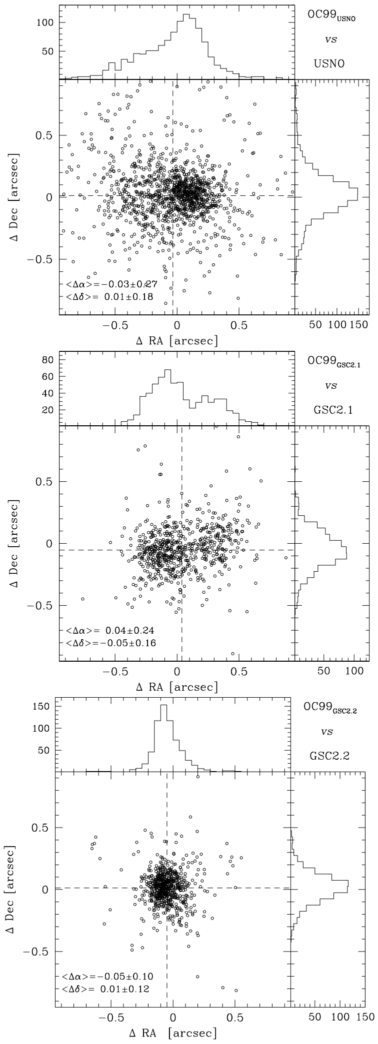

Fig. 3. The two-dimensional (RA, Dec) distribution of positional residuals obtained from the comparison of the astrometrically calibrated SHALLOW catalogs of M 67, using different reference catalogs, and the reference catalog used: USNO 2.0 (upper panel); GSC 2.1 (middle panel); and GSC 2.2 (lower panel). The vertical and horizontal dashed lines mark the mean residuals in RA and Dec after applying a 3σ clipping to the data. The mean values with the final $1 \times \sigma$ rms are given in the figure. Also shown are the histograms of the residuals as a function of RA (top) and Dec (right).

the USNO 2.0 and GSC 2.1 may be different, which could be partly due to the different epoch of the photographic

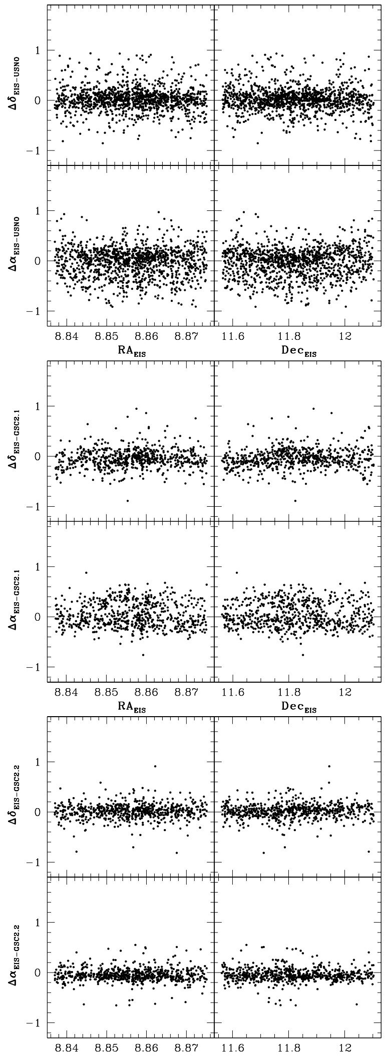

Fig. 4. The positional residuals in RA and Dec computed as in Fig. 3, are shown as a function of RA and Dec of the EIS catalog positions for the USNO 2.0 (upper panel); GSC 2.1 (middle panel); and GSC 2.2 (lower panel).

plates, both have comparable accuracy (∼0.25 arcsec), as measured by the rms of the distribution. On the other hand, GSC 2.2 represents a real improvement with the rms of the residuals being $\lesssim$0.12 arcsec.

To understand the nature of the observed spread of the residuals, the Δ RA and Δ Dec residuals are plotted as a function of RA and Dec taken from the calibrated EIS catalogs. This is shown in Fig. 4 and for each of the considered catalogs. In general, besides the large scatter, no noticeable systematics are seen. Note, however, the two bands of data points seen in the GSC 2.1 residuals, the reason for which is discussed below. It is worth pointing out that while no correlation between the residuals and position were found, other than that previously mentioned, for the particular field considered here, GSC 2.1 did show a systematic variation of the residuals as a function of both RA and Dec in the case of the Chandra Deep Field south located at the edge of the plate (Arnouts et al. 2001). It remains to be seen if this effect has been corrected for in the GSC 2.2.

Table 2. Linear fit parameters for the positional residuals as a function magnitude.

Catalog	Residual	`slope`	`zero-point`	`rms`
USNO	Δ RA	−0.046	0.684	0.262
USNO	Δ Dec	0.011	−0.149	0.232
GSC 2.1	Δ RA	−0.009	0.388	0.180
GSC 2.1	Δ Dec	−0.019	0.248	0.205
GSC 2.2	Δ RA	0.014	−0.268	0.128
GSC 2.2	Δ Dec	−0.024	0.381	0.139

* Only objects brighter than 14.8.

Complementing the above plots, Fig. 5 shows the variation of the right ascension and declination residuals as a function of magnitude for the USNO 2.0 (top panel), GSC 2.1 (middle panel) and GSC 2.2 (bottom panel). Also shown is the linear fit to the residuals as function of magnitude. The fit parameters are given in Table 2. From the figures and the table, one finds a relative strong dependence of the residuals on the magnitude for the USNO 2.0 and a striking discontinuity at $m \sim 15$ in the GSC 2.1. Only GSC 2.2 shows no systematic behavior with magnitude. From the liner fit of the USNO residuals one finds an offset in the RA residuals of ∼0.30 arcsec between bright and faint stars ($12 < V < 18.5$). The effect in Dec computed over the same magnitude interval is negligible. This systematic error is large compared to the required accuracy of the relative positions. This offset is significantly smaller in the case of GSC 2.2, being $\lesssim$0.10, in both directions. The systematic variation of the residuals with the magnitude explains the amorphous distribution seen in Fig. 3. This magnitude dependence has no bearing on the astrometric calibration of the pipeline. Note that this means that one should not use the coordinates of a reference star as listed in the reference catalog. Instead, stars used for pre-setting the telescope must share the same astrometric system as the objects being observed.

As an external check of the different astrometric solutions obtained for M 67, these were compared with the astrometric catalog of Girard et al. (1989). In this

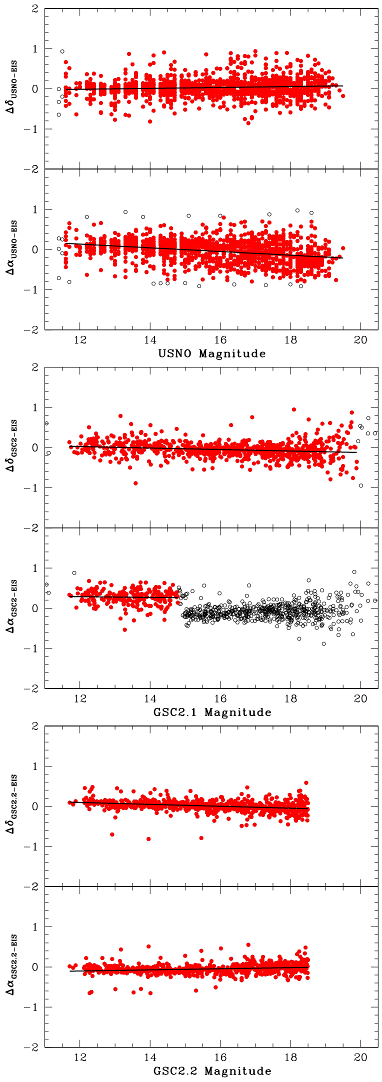

Fig. 5. The positional residuals in RA and Dec computed as in Fig. 3, shown as a function of the magnitude listed in the respective reference catalogs used for the USNO 2.0 (upper panel); GSC 2.1 (middle panel); and GSC 2.2 (lower panel). Points represented by filled circles were used in the linear fit to the data. The fit parameters are listed in Table 6.

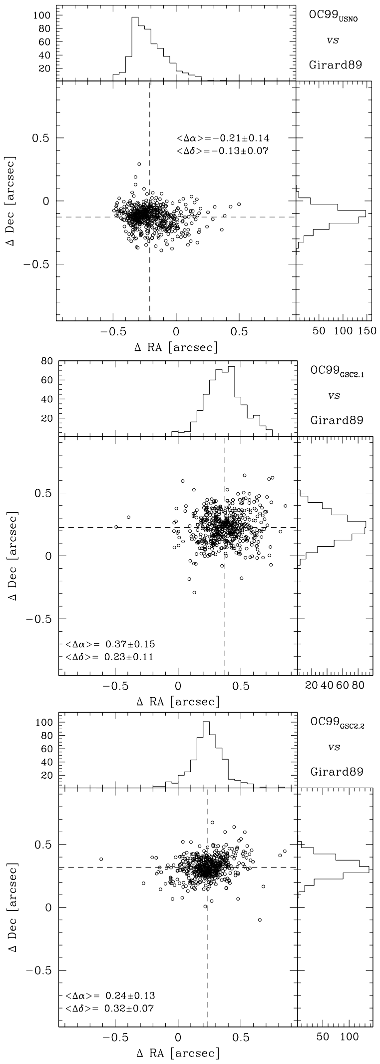

Fig. 6. The two-dimensional (RA, Dec) distribution of positional residuals obtained from the comparison of the astrometrically calibrated catalogs of M 67, using different reference catalogs, with the astrometric catalog of Girard et al. (1989). The EIS catalogs were calibrated astrometrically adopting: USNO 2.0 (upper panel); GSC 2.1 (middle panel); and GSC 2.2 (lower panel). The vertical and horizontal dashed lines mark the mean residuals in RA and Dec after applying a 3σ clipping to the data. The mean values with the final $1\times\sigma$ rms are given in the figure. Also shown are the histograms of the residuals as a function of RA (top) and Dec (right).

comparison, the position of the stars in the Girard et al. catalog were corrected for proper motion to the PF epoch of observation. The distribution of the positional residuals in the RA–Dec plane are shown in Fig. 6 for the EIS catalog produced for M 67 field using USNO 2.0 (top panel), GSC 2.1 (middle panel) and GSC 2.2 (bottom panel). Also shown in the figure are the distributions of the residuals in the RA and Dec directions. In each panel the mean offset and rms, computed after applying a 3σ clipping to the data, are also shown. While the rms values obtained are comparable ($\lesssim$0.15 arcsec), only for GSC 2.2 are the residuals well represented by a Gaussian distribution. Note that the mean offsets are not relevant for the preparation of target lists for FLAMES since its fiber positioner is allowed to move within a 2 arcsec window (Pasquini, private communication).

In conclusion, an analysis of the three reference catalogs currently available for the astrometric calibration of the WFI images shows that the recently released GSC 2.2 catalog yields the best results overall, with less systematics than the USNO 2.0 current in use by EIS. The analysis also reveals some unexpected features of the GSC 2.1 used in the calibration of the Chandra Deep Field south (EIS DEEP 2c field; Arnouts et al. 2001), pointing out the need for a re-evaluation of the astrometric calibration of those images. Nevertheless, it is important to emphasize that in all cases the rms of the residuals are below the 0.2 arcsec upper-limit required for the optimal performance of FLAMES. Since at the time of writing the GSC 2.2 catalog did not cover the SMC fields presented in this paper, the USNO 2.0 was used as the reference catalog. However, the results presented in this section clearly suggest that the GSC 2.2 reference catalog shows no significant systematic errors and is currently the best available. Future EIS calibrations will be done using this catalog, as soon as all the fields of interest are available. The results also demonstrate that the algorithm being employed in the astrometric calibration of the WFI frames in the EIS pipeline is robust, yielding results within the requirements of FLAMES. One also finds that the accuracy of the astrometric solution is limited by the intrinsic errors of the reference catalog used.

5. Photometry

5.1. Source extraction

Source extraction and stellar photometry (PSF fitting technique) were performed using the DAOPHOT/ ALLSTAR package (Stetson 1987). Minor changes to these programs had to be made to enable them to read fits images directly and to handle 8k×8k images, which basically required increasing the memory buffer, the size of the buffer used for determining the sky level and the number of stars used to model the PSF function for a frame. In addition, a number of procedures were implemented to automatize the whole procedure and make it more adaptable to the pipeline framework.

The first step is to create a model PSF for each image. The building of the PSF for each frame was done iteratively using a set of isolated and unsaturated stars. A preliminary list typically containing 500 stars is extracted and a first rough PSF is generated. Objects with poor fits are discarded from the list and a new PSF is created. This process is repeated until the fitting solution is acceptable for all objects. Typically, the process converges after a few iterations with the final PSF determined by at least 300 stars per image. The final model for the PSF is generated with a "Penny" function which has a quadratic radial dependence on the stellar coordinates. The resulting PSF is then used by the ALLSTAR routine to measure the magnitudes of all point sources detected by the FIND command of DAOPHOT. The final star-subtracted image is then visually inspected to check the result.

The above procedure was used to produce stellar catalogs for the SHALLOW and DEEP images of all selected fields in B and V. The catalogs extracted from the combined DEEP images are very sensitive to the detection threshold used. In all cases, the detection threshold was set to 3σ above the background counts, the best compromise between completeness and the number of spurious detections. Lower thresholds cause a large increase in the number of spurious objects. This is especially true for the DEEP images which have a lower signal-to-noise at the edges and over regions sampled by a single image due to the inter-chip gaps. This means that some faint objects within these regions might be missed. Information regarding the location of these regions can be found in the corresponding weight-maps (see Sect. 6).

Since the DAOPHOT/ALLSTAR package only works in pixel coordinates, the astrometric calibration available in the header of the image being processed is used to transform the resulting catalog to the world-coordinate system (*wcs*). This is in contrast to the procedure adopted by the EIS pipeline, which normally uses SExtractor which supports the *wcs* convention. Once catalogs from the SHALLOW and DEEP images are available those in the same passband are matched and the magnitude of objects in the SHALLOW catalogs are scaled to those in the DEEP catalogs. In the process the error weighted mean of the magnitude differences is computed for the stars in common, which never exceed 0.03 mag. It is important to point out that the SHALLOW and DEEP images overlap over an interval of 6 mag. The SHALLOW and DEEP catalogs are then merged and only objects satisfying the conditions $CHI < 1.2$ and $-1.2 < SHARP < 1.2$ are kept in the final combined catalog. The parameters CHI and $SHARP$ are a measure of the quality of the PSF fitting and the sharpness of the light profile of the object, respectively. Their exact definition can be found in the documentation of the DAOPHOT/ALLSTAR package. Finally, a BV color catalog is produced by associating the entries of the combined single passband catalogs described above, using a matching radius of 0.8 arcsec. The color catalogs also include objects detected in only one passband to avoid discarding intrinsically "blue" or "red" stars. The instrumental PSF magnitudes are then aperture-corrected and calibrated as described in the next section.

Table 3. Total number of sources in the released BV catalogs.

Name	EIS name	Number
Berkeley 20	OC03	7190
NGC 2477	OC12	38800
NGC 2506	OC14	18900
Messier 67	OC99	4290
SMC	SMC 5	280000
SMC	SMC 6	246000

5.2. Photometric calibration

The images were calibrated to the Johnson-Cousins system using observations of Landolt (1992) standard stars. Photometric solutions were determined using mean extinction coefficients and empirically determined color terms given by the equations:

$$B_{\rm JC} = B_{\rm EIS-842} + 0.29 \times (B - V)_{\rm JC} \tag{1}$$

$$V_{\rm JC} = V_{\rm EIS-843} - 0.08 \times (B - V)_{\rm JC} \tag{2}$$

where $B_{\rm EIS-842}$ and $V_{\rm EIS-843}$ are in the EIS magnitude system, and the numbers correspond to ESO's filter identification number. The extinction coefficients for each passband were computed from the mean extinction curve for La Silla and the response of the WFI filters used yielding: $K_B = 0.235$ and $K_V = 0.135$.

The instrumental PSF magnitudes were converted into aperture magnitudes, assuming that $m_{\rm ap} = m_{\rm PSF}$ + constant (Stetson 1987), where the constant is the aperture correction. This was obtained for each image from the analysis of the growth curves of bright isolated stars identified on each frame. Typical values for the aperture correction are in the range 0.15–0.3 mag. In the case of crowded regions, like the SMC fields, aperture corrections were calculated after subtracting all stars around the measured bright objects.

As an example of the application of the above procedure, Fig. 7 shows the color-magnitude diagram obtained for the SHALLOW (top panel) and the DEEP (bottom panel) color catalogs. Note that the color-magnitude diagram derived from the SHALLOW catalog extends from V 10 to $V \sim 20$, while that derived from the DEEP catalog covers the magnitude interval $14 \lesssim V \lesssim 23$. The color-magnitude diagram of the final merged catalog covers an impressive 13 mag interval, as shown in Figs. 9 and 10.

The number of objects given in the final BV color catalog for each field is listed in Table 3. The table gives: in Col. (1) the name of the primary target; in Col. (2) the EIS identification name; and (3) the total number of sources.

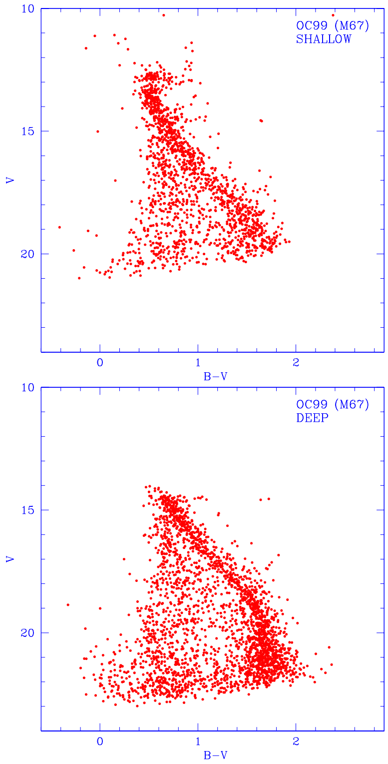

Fig. 7. The M 67 (OC99) color-magnitude diagram obtained from the final combination of the SHALLOW and DEEP data.

5.3. Comparison with other authors

As a check of the photometric catalogs being produced, these are compared to the data from Montgomery et al. (1993) for M 67 (OC99) and Vallenari et al. (1994) for NGC 330 (SMC5). The results of these comparisons are shown in Fig. 8. The two sets of panels refer to M 67 and NGC 330, respectively. In these plots the differences in the $(B-V)$ color (upper plot) and in the V magnitude (lower plot) are displayed as a function of the EIS V Johnson-Cousins magnitude. In these plots all stars in common are included.

For M 67 one finds a mean offset in the photometric zero-point of 0.068 mag and an rms of 0.064 mag in the magnitude interval $10 < V < 20$. For the $(B-V)$ color one finds a mean offset of -0.017 mag and an rms of 0.11 mag. In the case of NGC 330, one finds a mean value of magnitude differences of 0.050 mag, similar to the one mentioned above, and an rms of 0.18 mag, while the mean offset in $(B-V)$ is 0.053 mag with an rms of 0.15 mag, in the same magnitude interval as for M 67. Together, these results show that the measured colors are in excellent agreement

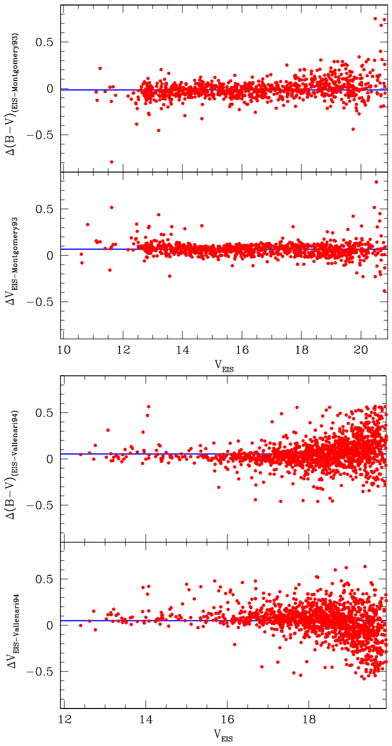

Fig. 8. Magnitude and color comparison of the EIS catalog with other authors. The *upper panel* shows a comparison of the EIS photometry of the M 67 (OC 99) field with that of Montgomery et al. (1993). The $(B-V)$ and V residuals are plotted against EIS V calibrated magnitudes. The *lower panel* shows a similar comparison but for NGC 330 (SMC 5) with the Vallenari et al. (1994). In these plots the horizontal lines indicate the median value of the differences.

with those measured by other authors despite of the large color term involved in the correction of the WFI instrumental magnitudes to the Johnson-Cousins system. The results also show that the present data may have a systematic error of $\lesssim$0.07 mag in the zero-point, which should be further investigated. More importantly, if one assumes that the random errors for EIS and the Montgomery et al. data are comparable, then the measured rms of the magnitude differences for M 67 implies an error of $\sim$0.04 mag at $V \sim 20$ in the EIS catalogs. This value is consistent with the internal estimates and the original requirements for the PF survey. The larger scatter measured from the comparison of NGC 330 may be due to the larger uncertainties in the magnitudes due de-blending problems in such very dense system.

6. Survey products

The images already released include the combined deep B and V exposures of each field, with all images normalized to 1 s exposure, and are presented in the TAN projection. In the data release the science images have been combined with their corresponding weight-maps into a single fits file containing two image extensions.

In addition to the pixel maps, for each of the six observed fields discussed in this paper, the following catalogs are also available:

1. Three instrumental photometric catalogs for each passband: the SHALLOW, the DEEP and the combined catalog, all in ASCII format. The following naming convention is adopted

   FIELD_FX_N_YYYY-MM-DDTHH:MM:SS.asc

   where FIELD is EIS target name, FX is the passband, N varies from 1 to 3 and corresponds to the SHALLOW, DEEP and COMBINED catalogs, respectively. The remaining characters refer to the date and time of the catalog production.
2. A calibrated BV color catalog available in three different formats for the convenience of the interested user: a FLAMES input file `.fld`, a SKYCAT input file `.scat`, and a normal ASCII file `.asc`. The name of each file follows the convention described above.

An example of the FLAMES input `.fld` file is shown in Table 4. The first four rows of the file are part of a header which includes: a LABEL with the name of the field; the UTDATE of the observations (this have to be changed according to the needs of the user); the CENTER of the field in RA and Dec coordinates; the EQUINOX of the coordinates (in this case, J2000.0). The targets following the header have the following fields: in Col. (1) the identification sequential number; in Cols. (2)–(4) the RA of the object in hours; in Cols. (5)–(7) the declination of the object in degrees; in Col. (8) one letter specifying the kind of fibers to be used among the different types available (e.g. FLAMES in MEDUSA mode is be identified with the "P" letter); in Col. (9) observation priority of the objects (highest 1; lowest 9), in this example, 1 is given for all the object; in Col. (10) measured V magnitude of the object; in Col. (11) another identification code (0 in this example); and in Col. (12) a comment field, which in this example lists the $(B-V)$ color.

7. Discussion

7.1. Color-magnitude diagrams

In order to illustrate the results obtained from the photometric data presented here, Figs. 9 and 10 show the color-magnitude diagram (CMD) for each of the observed fields. For most fields the CMDs were obtained using the catalog within the entire area covered by WFI. However, and in order to minimize foreground/background contamination, for the open clusters Berkeley 20 and NGC 2506,

Table 4. An example of a FLAMES operating system input file (.fld).

Header	LABEL EIS PF FIELD OC99								
	UTDATE 2001 07 01								
	CENTER 08 51 23.073 11 50 7.83								
	*EQUINOX J2000.0								
Targets	OC99_000001	08 50 26.850	11 33 43.03	P	1	16.620	0	1.663	
	OC99_000002	08 52 04.271	11 33 49.17	P	1	18.292	0	1.509	
	OC99_000003	08 51 01.327	11 33 50.11	P	1	19.078	0	0.829	
	OC99_000004	08 51 10.555	11 33 53.43	P	1	17.743	0	1.219	
	OC99_000005	08 51 40.304	11 33 55.29	P	1	17.299	0	0.885	
	OC99_000006	08 50 19.500	11 33 58.38	P	1	19.069	0	1.460	
	OC99_000007	08 50 26.126	11 33 59.22	P	1	18.705	0	1.049	
	OC99_000008	08 50 28.017	11 34 01.92	P	1	20.661	0	1.506	
	OC99_000009	08 52 05.010	11 34 08.15	P	1	18.423	0	1.515	

the CMDs shown correspond to a circular region around the nominal cluster center of 3 and 5 arcmin in radius, respectively.

Even though still a small sample, the examples presented here show the large variety of stellar systems being observed by the PF survey in terms of age, metallicity, size, distance and environment. The wide-area and the extended magnitude coverage ($\sim$13 mag) down to $V \sim 23$ provide an invaluable data set to extract samples suitable for the scientific drivers of FLAMES which include, among others, studies of: chemical abundances of stars in clusters and selected galactic regions (Bulge, Disk, and Halo); stellar kinematics and structure of stellar clusters; chemical composition and dynamics of nearby dwarf spheroidal galaxies; circumstellar activity in young stellar objects; very low mass stars and brown dwarfs in star forming regions.

From Figs. 9 and 10 one can see systems with well-defined main-sequences (MS), probable binary sequences, blue straggler populations, red clump stars, potential white dwarf candidates, very red objects and systems with composite stellar populations including very young stellar associations, and additional information about the galactic structure. These points are briefly discussed on an individual basis below.

7.2. Comments on individual systems

7.2.1. M 67

The close location to the Sun ($(m - M_V) = 9.59$), the low reddening, ($E_{B-V} = 0.05$; Montgomery et al. 1993), the rich population (800 $M_\odot$; Mathieu 1985; Montgomery et al. 1993) and the minimum contamination by foreground/background stars make M 67 one of the best studied open clusters. By fitting theoretical isochrones to the observed MS, Dinescu et al. (1995) derived an age of 4.0 ± 0.5 Gyr. Tautvaisiene et al. (2000) estimated a mean metallicity of $[\mathrm{Fe/H}] = -0.03 \pm 0.03$. This system is also of great interest because of its rich population of blue-stragglers, X-ray sources and white dwarfs. In many ways, M 67 is an ideal case for studies of the structure and evolution of Population I stars and thus a prime target for a spectroscopic follow-up with FLAMES. Moreover, and thanks to the precise proper-motions study of 663 stars by Girard et al. (1989), M 67 has been used as a test case for the astrometric calibration procedures adopted in the reduction of the PF data (Sect. 4).

From the CMD shown in Fig. 9, the MS is clearly discernible from the cluster turnoff (TO) at $V \simeq 12.8$ down to $V \simeq 22$. At $V \sim 18.5$ the MS shows an abrupt change in slope. At fainter magnitudes the $(B - V)$ is almost constant ($\simeq$1.8) due to the saturation of this color for very cool stars, corresponding to $M \sim 0.5\ M_\odot$. This may be also caused by a strong contamination by background stars and galaxies at the very faint end of the MS. The large magnitude baseline of the CMD allows allows one to probe the red giant branch up to $V \sim 10.0$. One can also see several blue stragglers at magnitudes brighter than $V = 12.5$ and in the color interval $-0.6 < (B - V) < 0.8$.

Close inspection of the CMD suggests the presence of a sparse, redder sequence running parallel to the cluster main sequence, as seen by Montgomery et al. using BVI data (see also Sect. 7.3). This has been interpreted as due to binary systems, estimated to constitute 38% of the cluster population. Furthermore, Pasquini & Belloni (1998), based on photometric and high-resolution spectroscopic studies of ROSAT sources, concluded that most of the detected X-ray sources are binaries. These ROSAT sources have peculiar locations in the cluster CMD consistent with the above interpretation.

Finally, several blue objects ($(B-V) < 0.4$) are visible fainter than $V \simeq 19$. These objects could be the brightest members of the white dwarf (WD) cooling sequence found by Richer et al. (1998), in the absolute magnitude interval of $M_V = 10{-}14.6$.

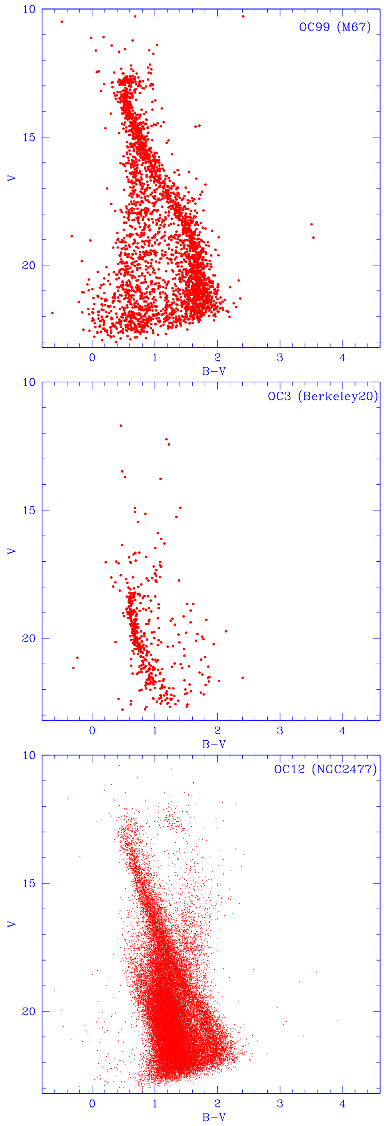

Fig. 9. The CMD for M 67, Berkeley 20 and NGC 2477, obtained from the combination of the catalogs extracted from the SHALLOW and DEEP images, as described in the text. To minimize foreground contamination the CMDs of Berkeley 20 corresponds to circular regions of 3 arcmin in radius around the nominal center of the cluster.

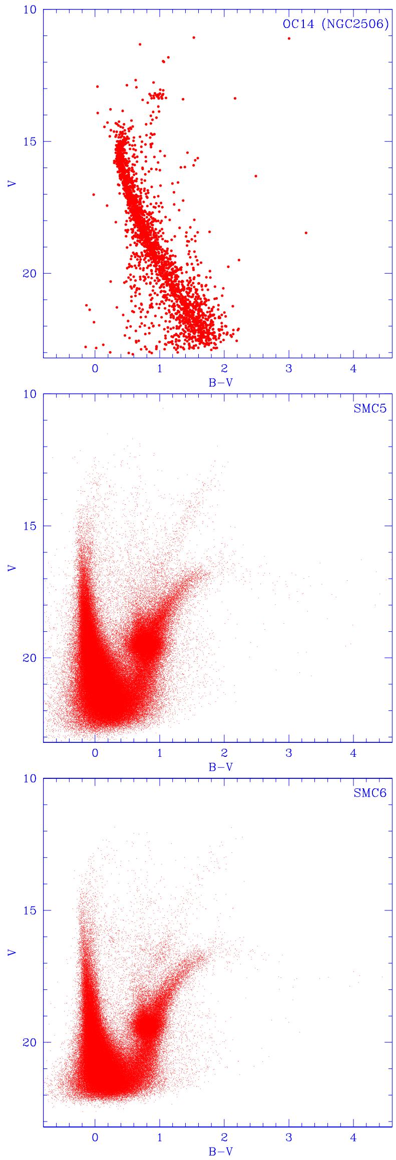

Fig. 10. The CMD for NGC 2506, SMC 5 and SMC 6, obtained from the combination of the catalogs extracted from the SHALLOW and DEEP images, as described in the text. To minimize foreground contamination the CMDs of NGC 2506 corresponds to circular regions of 5 arcmin in radius around the nominal center of the cluster.

7.2.2. Berkeley 20

From the study of several stellar systems carried out by Phelps et al. (1994), Berkeley 20 is ranked as one of the oldest open clusters, with an age comparable to that of M 67. From an analysis of the $V-(V-I)$ CMD

MacMinn et al. (1994) estimate a mean age of 6 Gyr and a metallicity of [Fe/H] $\simeq -0.23$. However, the system is further away, with a distance modulus of $(m-M)_V \simeq 15.0$ mag. It is also located in a direction of higher extinction, estimated to be $E_{V-I} \simeq 0.16$ mag. Moreover, it is very close to HD 64503, a bright star with $V \sim 4.5$. This explains some of the stray light seen over the images available for this field. Nevertheless, both the galactocentric distance and distance from the plane (MacMinn et al. 1994) make Berkeley 20 the most distant known open cluster, and a better determination of its metallicity and age would help trace the formation and evolution of the galactic disk.

Due to the cluster distance, the field covered by WFI leads to a high foreground contamination. In order to minimize this effect the CMD shown in Fig. 9 includes only objects within a circular region with 3 arcmin radius around the nominal center of this open cluster. Within this region, the CMD shows a well-defined turnoff at $V \simeq 18.25$ and $B-V \simeq 0.6$. There are also a number of blue-straggler candidates. However, no red clump is visible in the CMD shown in Fig. 9. On the other hand, if one inspects the CMD obtained using a larger radius ($\sim$10 arcmin) a small and isolated number of stars are found around $V \simeq 16.30$ and $(B-V) \simeq 1.1$. While at such distance from the cluster center it is difficult to discriminate cluster members from field stars, it is interesting to note that the location of this concentration would coincide with the red clump of M 67 (applying the appropriate scaling for the cluster distance). This result is consistent with the conclusions of MacMinn et al. that the general features of Berkeley 20 CMD are similar to those of M 67, even though no red clump was identified in their data. This shows the great value of the wide-area coverage of the PF data. Follow-up observations with FLAMES could settle this question.

7.2.3. NGC 2477

In contrast to the previous systems, NGC 2477 is a relatively young cluster ($1^{+0.3}_{-0.2}$ Gyr) located at a distance of $(m-M)_0 = 10.61$ (Kassis et al. 1997). Unfortunately, as shown by Kassis et al. and Majewski et al. (2000), NGC 2477 suffers from differential reddening, and both groups adopted a reddening range $E_{B-V} = 0.2 - 0.4$ determined by Hartwick et al. (1972). Friel & Janes (1993) determined a metal abundance of [Fe/H]$= -0.5 \pm 0.11$ using moderate resolution spectroscopy of seven cluster giants.

The CMD of NGC 2477 shows that the MS of the cluster is well-defined from $V \simeq 12.7$ to $V \simeq 22$. The TO of the cluster is located around $(B-V) \simeq 0.50$, at about the same magnitude of the red clump ($V \simeq 12.75$) seen at $(B-V) \sim 1.2$. The effect of the differential reddening is evident at the TO magnitude, which widens the MS near the TO. Finally, some blue-stragglers candidates are found at $(B-V) \simeq 0.2$ and $V \lesssim 12$.

A population of blue objects ($(B-V) \lesssim 0.6$) is present at $V \gtrsim 18$. However, the density of points in this region is far less than that seen in the CMD presented by Kassis et al. (1997) over a smaller area (15×15 square arcmin). A smaller density is also found by Majewski et al. (2000), even though in a different magnitude system. Furthermore, the blue population of Kassis et al. is spread over a large range of colors and does not seem to define any clear sequence which could reflect the WD cooling sequence. While the blue population observed with the present data may be associated with white dwarfs, as hinted by the presence of few faint stars around $V \sim 20$ and $(B-V) \simeq 0.2$, the Kassis et al. seem to considerably overestimate the density of these objects. The reasons for that are at the present time not clear.

One prominent feature of the NGC 2477 CMD is the substantial contribution of background field stars, which is independent of the region around the cluster considered. Fortunately, the contamination is concentrated in a well-defined color range ($0.8 < (B-V) < 1.6$) at magnitudes $V \gtrsim 18.0$, not severely affecting the MS of the cluster, except where it intersects the cluster MS around $V \sim 18$. The effect of the contamination, by field giant stars, is also seen at brighter magnitudes and redder colors, almost overlapping the cluster's red clump.

7.2.4. NGC 2506

This cluster has been studied by McClure et al. (1981) over a 10 arcmin diameter field of view, using photoelectric photometry, and by Marconi et al. (1997), who obtained CCD photometry of an area of 6×6 arcmin. The present data reach almost four magnitudes deeper than any previous study of this system, covering at the same time a much larger area, at least 10 times the size. NGC 2506 is a relatively old open cluster but its exact age is very uncertain, varying from 1.5–3.4 Gyr. Marconi et al. estimate 1.5–1.7 Gyr, in reasonable agreement with the value of 1.9 Gyr found by Carraro & Chiosi (1994), while McClure et al. (1981) estimate an age of 3.4 Gyr.

For this cluster Fig. 10 shows only objects within a circular region 5 arcmin in radius. The CMD of this region shows a well-defined MS closely resembling that presented by Marconi et al. In this case, differential reddening may be important. Schlegel et al. (1998) estimate $E_{B-V} = 0.087$ mag. Contamination of the MS by field stars is seen primarily as a vertical sequence around $(B-V) \simeq 0.6$. However, the group of stars bluer than $(B-V) \simeq 0.4$ and fainter than $V \sim 21$ can conceivably be the tip of the white dwarf cooling sequence associated with the cluster. These stars are particularly interesting for follow-up observations with FLAMES. At magnitudes brighter than the TO ($V = 14.7$), a small number of blue-straggler candidates are also seen. More candidates can be found if one considers a larger area than the one shown in Fig. 10.

Several issues related to this cluster could be addressed with FLAMES. In particular, a better and direct determination of its metallicity. Friel & Janes (1993) measured [Fe/H]$= -0.52 \pm 0.07$ from medium-resolution spectroscopy of five cluster members, while Marconi et al. using different stellar evolutionary models can fit the observed data either with values of metallicity consistent with that determined spectroscopically or with solar values.

7.2.5. Small Magellanic Cloud fields

The Magellanic Clouds are ideal targets for the study of galaxy formation and evolution. Their proximity has enabled ground-based observations to unveil their oldest populations and resolve them into individual stars. Moreover, both the LMC and SMC contain young, rich cluster systems that span a wide range of ages and metallicities, evidence of their extended star formation history. The young clusters offer a unique opportunity to study the properties of massive stars and to compare them with predictions of stellar evolutionary models. Such studies might provide insight into the physical processes responsible for their evolution, such as the treatment of mixing.

This PF release includes two adjacent fields in the SMC. The combined V image produced by the stacking of the two DEEP exposures of one of the SMC fields (SMC 5) is shown in Fig. 1. The image shows a uniformly distributed population of SMC "field stars", presumably the old population, and a considerable number of young star clusters. In SMC 5 the following clusters can be identified: NGC 346, NGC 330, IC 1611, NGC 306, NGC 299, OGLE 109, OGLE 119, OGLE 99. From an inspection of a similar image for SMC 6 one finds the clusters: OGLE 124, IC 1624, OGLE 129, K 50, OGLE 134, K 54. These images show the great contribution of a wide-field imager to the study of such nearby systems. The two fields of SMC being released provide a large survey of OB associations which can be immediately observed with FLAMES. One of the fields (SMC 5) includes the brightest HII region (NGC 346) of the SMC. Massey et al. (1989) confirm the presence of 33 O stars, 11 of which are of type O6.5 or earlier. Six stars were found in the mass range 40−80 $M_\odot$. They also identified few red supergiants of considerably lower mass (15 $M_\odot$) concentrated in a spatially distinct subgroup. From a close inspection of the image shown Fig. 1 the existence of this distinct subgroup is confirmed at $\alpha = 00^{\rm h}59^{\rm m}05.2^{\rm s}$ and $\delta = -72°09^{\rm m}15.4^{\rm s}$.

The CMD of the two SMC fields show a number of populations with different ages and metallicities, ideal targets for FLAMES. Note that the CMD of SMC 5 reaches fainter magnitudes compared to that of SMC 6. This is because only one DEEP V image is available for SMC 6. The most prominent feature of both SMC CMDs is the MS centered around $(B-V) \simeq -0.2$, as expected from the low reddening towards the SMC ($E_{B-V} = 0.037$, Schlegel et al. 1998). The broadening of the MS at faint magnitudes ($V \lesssim 20$) can be due to several effects such as crowding and increasing photometric errors. For magnitudes $V \lesssim 17$ the broadening is mainly caused by blue supergiants. The MS terminates around $V \simeq 14.3$ while the blue supergiants extend up to $V \simeq 12.5$. At redder colors ($0.5 \lesssim (B-V) \lesssim 2.0$) there is another tilted sequence which corresponds to the red end of the blue loop (red supergiants). In between the blue and red-end of this loop, there is an almost vertical sequence starting at $V \simeq 19.5$, $(B-V) \simeq 0.7$, which extends at least to $V \simeq 13.5$. This population is the so-called "vertical clump" (Gallart et al. 1998) formed by young (few hundred Myr to 1 Gyr old), core He-burning and intermediate-mass stars. Note, however, that this sequence might suffer contamination by foreground stars and supergiants along the loop. At $(B-V) \sim 1.6$ and $V \sim 17$ one sees the tip of a broad red giant branch (RGB). The width of the RGB at the tip is ∼0.45 mag. This is probably due to the combined effects of age and metallicity. Finally, even though hard to identify, given the resolution of the Fig. 10, the red extension of the horizontal branch is visible at $V \sim 19.5$ in the color interval $0.4 \lesssim (B-V) \lesssim 0.6$. However, one finds no evidence of a blue horizontal branch.

The CMD shown in Fig. 10 reflects primarily the properties of the SMC field star population. However, as mentioned above the two SMC fields observed so far contain at least 14 stellar systems, whose CMDs can also be extracted from the same data. Despite possible contamination problems, such analysis is of great interest to study the star formation history of both cluster and field populations.

7.3. Future work

As discussed above, the data presented here provides not only the means for producing target lists for FLAMES but also a wealth of information about a variety of stellar systems. Furthermore, the data from the survey can be combined to other data sets which can greatly enhance the scientific value of the survey.

As an example, for all the observed fields the final color catalogs were associated with those being produced by the 2MASS survey. Combined EIS and 2MASS data will provide a six passband multi-color data sets. As an illustration the upper panel of Fig. 11 shows the optical/infrared $V, (B-K)$ CMD obtained for M 67. Among many interesting features, it is worth noticing how the MS of M 67 (Fig. 9) is resolved into two well-defined parallel sequences, much more clearly than using the optical alone. The binary sequence is clearly visible in the magnitude interval $14.5 \lesssim V \lesssim 18$. Moreover, and in addition to the well-known gap at $V \sim 13$, the diagram shows clear evidence of another gap at $V \sim 16.15$ and $(B-K) \sim 3.35$. The lower panel of Fig. 11 shows the $K, (B-K)$ CMD for SMC 5. In contrast to the optical CMD, the optical/infrared provides a clear view of the lower temperature stars, while the hot MS and blue supergiants essentially disappear. In this diagram both the red supergiant and the red giant

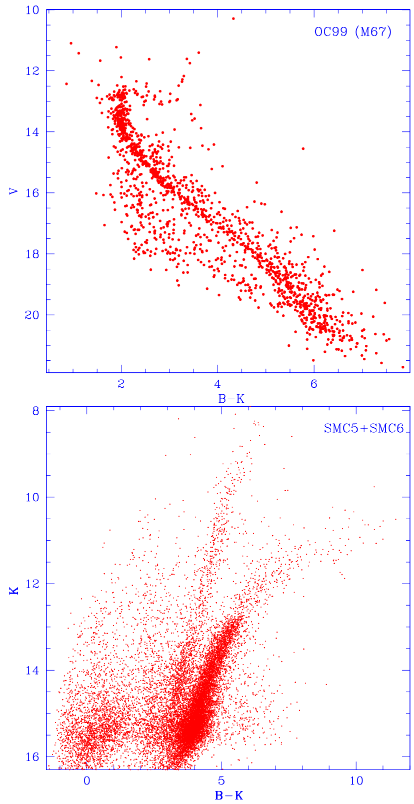

Fig. 11. The optical/infrared color-magnitude diagram obtained for M 67 combining EIS and 2MASS data.

sequences are clearly visible and more easily distinguishable. Also note the asymptotic giant branch (AGB) stars ($K \lesssim 12.5$) starting from $(B-K) \gtrsim 5.5$ and extending to extremely red colors ($(B-K) \sim 11.2$). Stars found in this region resemble those found by Nikolaev & Weinberg (2000), studying the 2MASS diagram of the LMC, and interpreted as Carbon-rich Thermally-Pulsating AGB and long period variables. In the blue part of the diagram some MS and blue supergiants are still present, and seem to be separated. In addition, there is a hint of a population along the blue loop ($K \sim 15.5$ and $0.5 < (B-K) < 2.5$). Thus, the color baseline provided by the combination of optical and infrared data, is a powerful tool in separating the different populations of composite systems.

Lastly, combining the optical and infrared data may also allow for the spectral classification of objects by matching the photometric measurements against template spectra (Hatziminaoglou et al. 2001). This may help further disentangle different populations and search for particular types of stars. Results from such an analysis will be presented in a subsequent paper of this series.

8. Summary

This paper presents the first set of fully-calibrated images and catalogs of the PF survey. The data presented here have been used to evaluate the observing strategy, data reduction, catalog production and preparation of target lists for feeding the FLAMES fiber positioner. Particular emphasis has been given to the accuracy of the astrometric calibration. The analysis presented in this paper has shown the need for some improvement in the software, currently underway, in order to efficiently cope with the large amount of data already available. From a comparison of the results obtained using different reference catalogs, one finds that while the USNO 2.0 provides adequate astrometric solutions, with accuracy within the requirements of FLAMES, future reductions should be done with the recently released GSC 2.2 catalog. The latter proved to be far superior with less systematics and smaller uncertainties.

The color catalogs produced have been used to derive color-magnitude diagrams for all the fields considered. The CMDs span 13 mag in V which ensures a better selection of both bright and faint targets for FLAMES. A comparison of the CMDs with those of other authors show good agreement over the magnitude range in common. However, the PF data are far superior given their extended magnitude and area coverage. Furthermore, combining these data with ongoing surveys in other wavelengths gives additional leverage for the identification of different stellar populations, of key importance for the envisioned FLAMES programs.

All the specific software developed to deal with the PF survey data is currently being incorporated into the EIS survey system framework. This should allow the efficient reduction of all of the remaining data gathered by this survey. The fully calibrated images and catalogs presented in this paper will be used in the commissioning phase of FLAMES and can be requested from the URL "`http://www.eso.org/eis`".

Acknowledgements. We thank L. Pasquini for having promoted the Pre-FLAMES survey and for his constant encouragement. We also thank A. Renzini for his continuing support of the EIS project. F. Comeron, V. Hill, and F. Primas are thanked for their support in the preparation of the original proposal. We would also like to acknowledge F. Ferraro, V. Hill, J. Krautter, J. Mermillod, B. Nordström, S. Ortolani, G. Piotto, F. Primas, S. Randich and E. Tolstoy for their suggestions in the initial phase of selection of the Pre-FLAMES targets. Y.M. thanks the Università di Padova, E. V. Held, G. Piotto & S. Ortolani. S.Z., thanks the Osservatorio di Trieste. We also thank M. Zoccali for careful reading of the paper, and L. Rizzi for useful discussions on WFI calibration. The Guide Star Catalogue-II is produced by the Space Telescope Science Institute in collaboration with the Osservatorio Astronomico di Torino. Space Telescope Science Institute is operated by the Association of the Universities for Research in Astronomy, for the National Aeronautics and Space Administration under contract NAS5-26555. Additional support is provided by the Association of Universities for Research in Astronomy, the

Italian Council for Research in Astronomy, European Southern Observatory, Space Telescope European Coordinating Facility, the International GEMINI project and the European Space Agency Astrophysics Division. This publication makes use of data products from the Two Micron All Sky Survey, which is a joint project of the University of Massachusetts and the Infrared Processing and Analysis Center/California Institute of Technology, funded by the National Aeronautics and Space Administration and the National Science Foundation. This research has made use of the SIMBAD database, operated at CDS, Strasbourg, France.

References

Arnouts, S., Vandame, B., Benoist, C., et al. 2001, A&A, 379, 740
Carraro, G., & Chiosi, C. 1994, A&A, 288, 751
Dinescu, D. I., Demarque, P., Guenther, D. B., & Pinsonneault, M. H. 1995, AJ, 109, 2090
Friel, E. D., & Janes, K. A. 1993, A&AS, 267, 75
Gallart, C. 1998, ApJL, 495, L43
Girard, T. M., Grundy, W. M., Lopez, C. E., & van Altena, W. F. 1989, AJ, 98, 227
Hartwick, F. D. A., Hesser, J. E., & McClure, R. D. 1972, ApJ, 174, 557
Hatziminaoglou, E., et al. 2001, A&A, submitted
Kassis, M., Janes, K. A., Friel, E. D., & Phelps, R. L. 1997, AJ, 113, 1723
Landolt, A. U. 1992, AJ, 104, 340
MacMinn, D., Phelps, R. L., Janes, K. A., & Friel, E. D. 1994, AJ, 107, 1806
Majewski, S. R., Ostheimer, J. C., Kunkel, W. E., & Patterson, R. J. 2000, AJ, 120, 2550
Marconi, G., Hamilton, D., Tosi, M., & Bragaglia, A. 1997, MNRAS, 291, 763
Massey, P., Parker, J. W., & Garmany, C. D. 1989, AJ, 98, 1305
Mathieu, R. D. 1985, in Proc. IAU Symp. 113, Dynamics of Star Clusters, ed. J. Goodman, & P. Hut (Dordrecht: Reidel), 427
McClure, R. D., Twarog, B. A., & Forrester, W. T. 1981, ApJ, 243, 841
McLean, B., Greene, G., Lattanzi, M., & Pirenne, B. 2000, Astronomical Data Analysis Software and Systems IX, ed. N. Manset, C. Veillet, & D. Crabtree, ASP Conf. Proc., 216, 145
Montgomery, K. A., Marschall, L. A., & Janes, K. A. 1993, AJ, 106, 181
Nikolaev, S., & Weinberg, M. D. 2000, ApJ, 542, 804
Pasquini, L., & Belloni, T. 1998, A&A, 336, 902
Pasquini, L., et al. 2000, SPIE, 4008, 129
Phelps, R. L., Janes, K. A., & Montgomery, K. A. 1994, AJ, 107, 1079
Renzini, A., & da Costa, L. N. 1997, The Messenger, 87, 23
Richer, H. B., Fahlman, G. G., Rosvick, J., & Ibata, R. 1998, ApJL, 504, L91
Schlegel, D. J., Finkbeiner, D. P., & Davis, M. 1998, ApJ, 500, 525
Stetson, P. B. 1987, PASP, 99, 191
Tautvaisiene, G., Edvardsson, B., Tuominen, I., & Ilyin, I. 2000, A&A, 360, 499
Vallenari, A., Ortolani, S., & Chiosi, C. 1994, A&AS, 108, 571
Vandame, B., Olsen, L. F., Jorgensen, H. E., et al. 2001, A&A, submitted

Appendix D

XML comfiguration for the generic instrument

This appendix describes how to configure or update a generic instrument described for the EIS/MVM pipeline. First of all, all the settings are identified under an unique instrument-name, which is used by the user to indicate to the pipeline which instrument is being considered. Currently, the already defined instrument are: SOFI, WFI and ISAAC (short wavelength mode).

The goal of the pipeline is to handle different instruments, single or multi-chips with complex electronic design. A skeleton of options is defined offering flexible tunings to handle a variety of instruments. The actual settings are organized in 7 parts:

1. Telescope location. Location of the telescope on earth. This information is used to compute the airmass and hour angle of an image.
2. Instrument properties. Main characteristics of the instrument (gain, read out noise, pixel size ...).
3. Chip Geometry. Description of chip layout for multi-chip instruments.
4. Quadrant Geometry. Description of the different kinds of electronic quadrants chip by chip. (over-scan areas, good pixel areas).
5. FITS raw keywords. Name and unit conventions of the raw FITS keywords.
6. FITS alias keywords. Name and unit conventions for the filtered/rewritten keywords.
7. Calibration images recognition. Object-name pattern recognition to identify calibration images (bias, dark, flat-sky, flat-dome).

Each of the 7 parts is described in XML node, set in a root node named *observatory*.

XML option name	*description*
/mvm-stack/observatory	XML path for the following relative options.
./telescope	Telescope information.
./instrument	Instrument name, with main characteristics.
./chip-geometry	Chip location within the instrument.
./quadrant-geometry	Internal chips structure.
./keyword-fits-raw	FITS keyword convention for the raw images.
./keyword-fits-alias	FITS keyword convention for the filtered images.
./calib-recognition	Object-name criteria to recognize calibration images.

D.1 Telescope information: *<telescope>*

XML options

The telescope is described by a name, and its location on earth:

XML option name	*description*
/mvm-stack/observatory/telescope	XML path for the following relative options.
./name	Telescope name.
./latitude	Latitude of the telescope in degrees (North positive).
./longitude	Longitude of the telescope in degrees (East positive).

Example

Sub-node for the ESO-2.2 telescope located in La Silla observatory:

```
<observatory>
      <telescope>
            <name>ESO-2.2</name>
            <latitude>-29.2543</latitude>
            <longitude>-70.7346</longitude>
      </telescope>
      ...
</observatory>
```

D.2 Instrument main description: *<instrument>*

XML options

The instrument is characterized by: the pixel size formed on the sky, the orientation, and by the main electronic parameters. The pixel size and orientation are defined by a 2×2 matrix following the World Coordinate System (WCS) convention (complete information can be found at `http://tdc-www.harvard.edu/software/wcstools/wcstools.wcs.html`).

XML option name	*description*
/mvm-stack/observatory/instrument	XML path for the following relative options.
./name	Instrument name, with working mode.
./cd1_1	WCS Matrix element (unit deg/pixel).
./cd1_2	
./cd2_1	
./cd2_2	
./gain	Default gain for all the chips. (unit e-/ADU)
./read-out-noise	Default read out noise of the chips. (unit e-)
./nb-hdu	Number of FITS extension of the raw images.

Example

Sub-node *instrument* set for the ISAAC instrument mounted on a VLT telescope. The instrument described is ISAAC in Short Wave (sw) working-mode.

```
<observatory>
    <instrument>
        <name>isaac-sw</name>
        <cd1_1>0.00004122</cd1_1>
        <cd1_2>0.0</cd1_2>
        <cd2_1>0.0</cd2_1>
        <cd2_2>-0.00004122</cd2_2>
        <gain>4.5</gain>
        <read-out-noise>11</read-out-noise>
        <nb-hdu>1<nb-hdu>
    </instrument>
    ...
</observatory>
```

Notes

- The instrument name defined for the framework must be expanded with the working-mode. Some instruments has more than one working-mode. The framework considers another working-mode as a new instrument. The name of the instrument is a key element for the pipeline, and to avoid confusions, one instrument with different working modes has to be clearly defined as different instruments. In the previous example, the instrument is named isaac-sw because the ISAAC instrument has two working mode (short and large wavelenght).
- The instrument is supposed to have always the same orientation in the sky, and the same pixel size. In other word the WCS matrix elements (CDx_x) must be constant. This strict assumption is flexible enough to deal with most of ground-based instruments.
- The electronic gain is assumed constant on all chips. This is not exactly true because each electronic converter associated to a chip has its own mean gain. Nevertheless a step of reduction will harmonize the mean gain for all chips, thus leading to a constant gain for all chips. The gain quoted for the instrument, should be the gain of the electronic converter used as reference for the gain harmonization procedure.

D.3 Chip arrangement within the instrument: *<chip-geometry>*

Description

The framework handles single or multi-chip instruments. The chips are assumed to be arranged in a matrix. Each one is referenced with an identifier (from 1 to the number of chips), located within the matrix of CCDs, and located within a large pixel grid containing the whole instrument. Figure D.1 illustrates the chip layout of the instrument WFI.

XML options

XML option name	*description*
/mvm-stack/observatory/chip-geometry	XML path for the following relative options.
./nb-chip-x	Number of chips in x axis.
./nb-chip-y	Number of chips in y axis.
./chip	Sub-node describing one chip. This node appears *nb-chip-x* * *nb-chip-y* times to describe all the chips of the instrument.
./chip/id	Id for the chip (from 1 to *nb-chip-x* * *nb-chip-y*)
./chip./x	X location of the chip in the matrix of CCDs (from 1 to *nb-chip-x*).
./chip/y	Y location of the chip in the matrix of CCDs (from 1 to *nb-chip-y*).

./chip/naxis1	Chip size in pixels x axis.
./chip/naxis2	Chip size in pixels y axis.
./chip/geometry-x	X, Y pixel coordinate of the bottom-right pixel of the chip within the full grid.
./chip/geometry-y	

Example

Sub-node *chip-geometry* for the Wield Field Imager (WFI). (partial example).

```
<observatory>
      <instrument>
            <name>wfi</name>
            ...
      </instrument>
       ...
      <chip-geometry>
            <nb-chip-x>4</nb-chip-x>
            <nb-chip-y>2</nb-chip-y>
            <chip>
                  <id>1</id>
                  <x>1</x>
                  <y>2</y>
                  <naxis1>2142</naxis1>
                  <naxis2>4128</naxis2>
                  <geometry-x>1</geometry-x>
                  <geometry-y>4130</geometry-y>
            </chip>
            <chip>
                  <id>2</id>
                  <x>2</x>
                  <y>2</y>
                  <naxis1>2142</naxis1>
                  <naxis2>4128</naxis2>
                  <geometry-x>2150</geometry-x>
                  <geometry-y>4130</geometry-y>
            </chip>
            <chip>
                  <id>3</id>
                  <x>3</x>
                  <y>2</y>
                  <naxis1>2142</naxis1>
                  <naxis2>4128</naxis2>
                  <geometry-x>4300</geometry-x>
                  <geometry-y>4130</geometry-y>
            </chip>
            ....
```

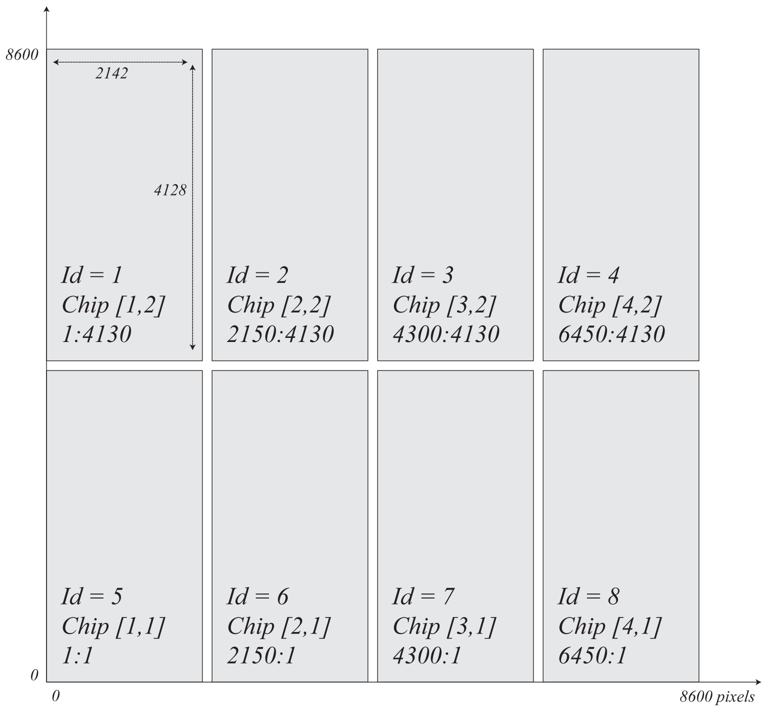

Figure D.1: Chip layout for the WFI instrument. The 8 chips are located in 2 ways. First: within the matrix of chips. Second: within a large pixel grid containing all the instrument. For instance the chip Id 3 is located in the cell [3,2] of the matrix of chips, and within the large pixel grid at the location 4300:4130.

```
        </chip-geometry>
    </observatory>
```

Notes

- The coordinates of the chip within the matrix, and the pixel coordinates of the chip within the full grid, start from 1 with a right-bottom origin.

- The *geometry-x* and *geometry-y* options are used to physically locate the chip within a grid of pixels containing all the CCDs. This information is useful to compute the typical size of the inter-chip gaps.

- The settings handles only instruments with CCDs of same size, arranged into a matrix. Other chips layout cannot yet be reduced by this pipeline.

D.4 Internal chip description: *<quadrant-geometry>*

Description

The actual framework handles complex electronic layouts defined chip by chip. Two types of areas are defined to characterize the electronic converters:

- Over scan area. A special region called over-scan area is dedicated to store the bias level. It consists of several columns constantly read during the exposure time. It is used to compute the variations of the electronic bias. An electronic converter may have zero or several over-scan areas.
- Quadrants used to read pixels. Some CCDs are read by several electronic converters. Each converter is reading a portion of the chip. This layout speeds up the read-out time by a factor of the number of electronic converters. Several steps of the reduction need this geometric definition.

In the framework, the over-scan areas are referenced as the *quadrant-test* areas. The quadrants used to read pixels are named: *quadrant-apply*. One chip has at least one *quadrant-apply* area, and may have no *quadrant-test* areas. The framework can handle complex electronic design with lots of quadrants. Figure D.2 illustrates the 4 electronic converters of the FORS1 instrument mounted on an ESO-VLT telescope.

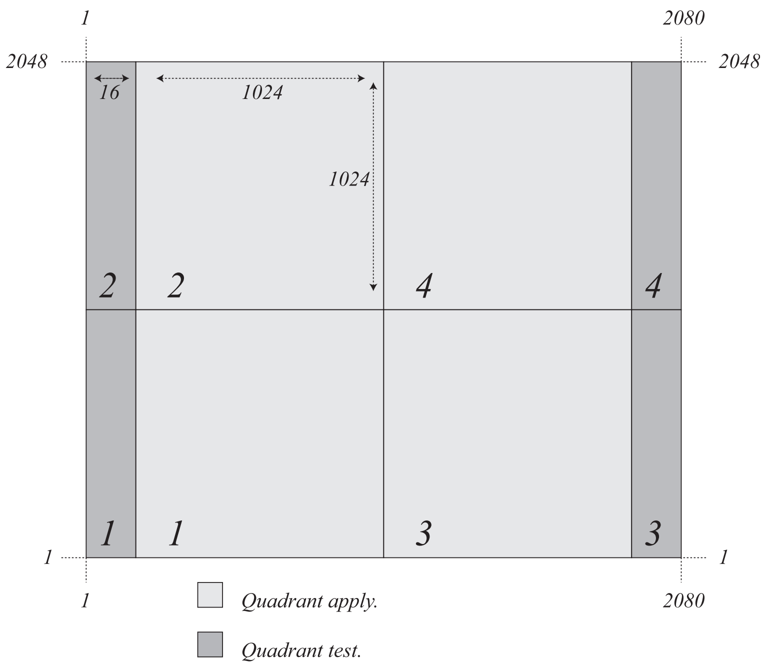

Figure D.2: Detail of the FORS1 instrument. This 2k by 2k CCD is read by 4 electronic converters each reading a quarter of the camera. Each one of the 4 quadrant-apply is associated to one quadrant-test (or over-scan area).

XML options

The node *quadrant-geometry* contains the descriptions for the 2 kinds of quadrants. Several chips may have the same internal electronic layout, information can be shared from one chip to another.

XML option name	*description*
/mvm-stack/observatory/	XML path for the following relative options.
./quadrant-chip	Description of all quadrants for one chip.
./quadrant-chip/pattern-chip-id	Specify which chips are concerned by this description.
./quadrant-chip/quadrant-test	Sub-node describing the *quadrant-test*.
./quadrant-chip/quadrant-apply	Sub-node describing the *quadrant-apply*.

A sub-node *quadrant-test* or *quadrant-apply* is organized as follows:

XML option name	*description*
./nb-quadrant	Number of quadrant within this
./quadrant	This node appears *nb-quadrant* times.
./quadrant/pattern-quadrant-id	Which quadrant is concerned.
./quadrant/x-init	Start of quadrant in x axis within the chip (unit: pixel, starting from 1).
./quadrant/y-init	Start of quadrant in y axis within the chip.
./quadrant/x-length	Size of quadrant in x axis (unit pixel).
./quadrant/y-length	Size of quadrant in y axis.

Example

Sub-node *quadrant-geometry* for the FORS1 instrument.

```
<observatory>
      <instrument>
            <name>fors1</name>
            ...
      </instrument>
       ...
      <quadrant-geometry>
            <quadrant-chip>
                  <pattern-chip-id>1</pattern-chip-id>
                  <quadrant-apply>
                        <nb-quadrant>4</nb-quadrant>
                        <quadrant>
```

```
            <pattern-quadrant-id>1</pattern-quadrant-id>
            <x-init>21</x-init>
            <y-init>5</y-init>
            <x-length>1020</x-length>
            <y-length>1020</y-length>
        </quadrant>
        <quadrant>
            <pattern-quadrant-id>2</pattern-quadrant-id>
            <x-init>21</x-init>
            <y-init>1025</y-init>
            <x-length>1020</x-length>
            <y-length>1020</y-length>
        </quadrant>
        <quadrant>
            <pattern-quadrant-id>3</pattern-quadrant-id>
            <x-init>1041</x-init>
            <y-init>5</y-init>
            <x-length>1020</x-length>
            <y-length>1020</y-length>
        </quadrant>
        <quadrant>
            <pattern-quadrant-id>4</pattern-quadrant-id>
            <x-init>1041</x-init>
            <y-init>1025</y-init>
            <x-length>1020</x-length>
            <y-length>1020</y-length>
        </quadrant>
    </quadrant-apply>
    <quadrant-test>
        <nb-quadrant>4</nb-quadrant>
        <quadrant>
            <pattern-quadrant-id>1</pattern-quadrant-id>
            <x-init>1</x-init>
            <y-init>1</y-init>
            <x-length>16</x-length>
            <y-length>1024</y-length>
        </quadrant>
        <quadrant>
            <pattern-quadrant-id>2</pattern-quadrant-id>
            <x-init>1</x-init>
            <y-init>1025</y-init>
            <x-length>16</x-length>
            <y-length>1024</y-length>
        </quadrant>
        <quadrant>
            <pattern-quadrant-id>3</pattern-quadrant-id>
            <x-init>2065</x-init>
            <y-init>1</y-init>
            <x-length>16</x-length>
            <y-length>1024</y-length>
        </quadrant>
        <quadrant>
            <pattern-quadrant-id>4</pattern-quadrant-id>
```

```
                        <x-init>2065</x-init>
                        <y-init>1025</y-init>
                        <x-length>16</x-length>
                        <y-length>1024</y-length>
                    </quadrant>
                </quadrant-test>
            </quadrant-chip>
        </quadrant-geometry>
        ...
    </observatory>
```

Notes

- One chip must have at least one *quadrant-apply* and may have no *quadrant-test*.

- Quadrant-tests are used to compute the electronic bias correction of the nearest quadrant-apply. During the reduction the associations of quadrant-test versus quadrant-apply are done automatically. More than one quadrant-tests may indicate the bias correction of one quadrant-apply.

- Quadrants may be smaller than the chip itself. For instance some portions of the over-scan areas are rejected because of electronic instabilities. Also the *quadrant-apply* may be smaller than the chip in order to remove some parts where for instance the vignetting is too strong.
  Figure D.3 shows the chip 4 of the WFI. It is made of 3 over-scan areas. The bottom one is not used because it suffers from lots of parasites (blooming from the image, hot columns). The 2 other ones are used partially to keep only the part where the electronic bias is constant. The *quadrant-apply* is defined smaller than the effective quadrant to mask out the strong vignetting at the border of the instrument. Figure D.3 shows the 2 *quadrant-tests* and the *quadrant-apply* defined for chip 4 of the WFI instrument.

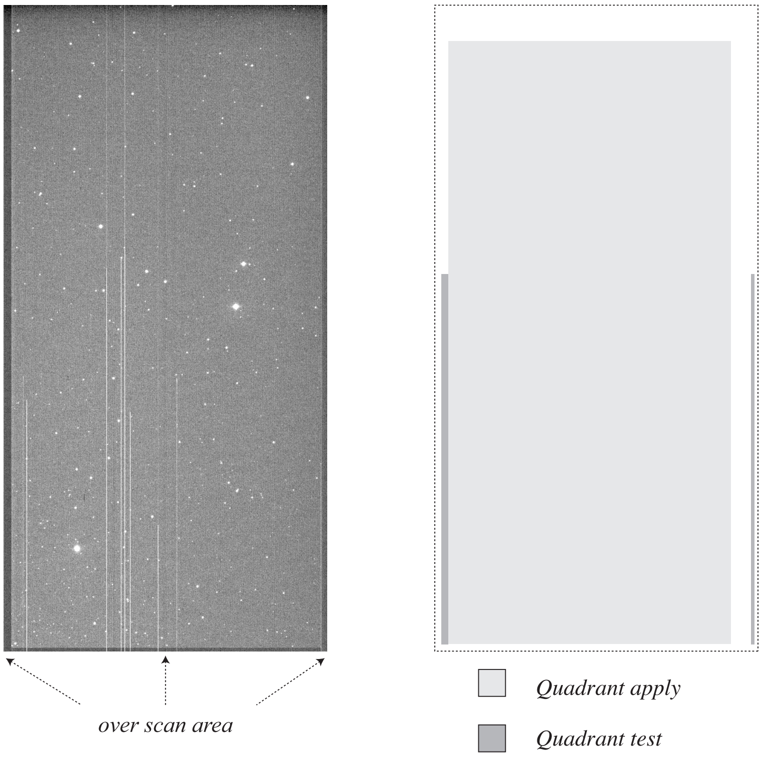

Figure D.3: Details of electronic layout defined for the WFI instrument. LEFT: electronic layout with 3 over-scan areas and one quadrant. RIGHT: Electronic layout defined for the pipeline: *quadrant-tests* and *quadrant-apply*. One over-scan area (the bottom one) is not used because it is affected by lots of hot columns. Only 2 *quadrant-tests* are defined and cover a smaller area than the original over-scans. The electronic bias is not constant in the rejected upper parts. The *quadrant-apply* is defined smaller than the CCD in order to remove the strong vignetting at the border of the instrument.

D.5 Raw FITS keyword convention: <*keyword-fits-raw*>

Description

The raw images have their own FITS header convention because there are no standards for keyword names and units. The framework needs to retrieve information from the images. It assumes the convention of keyword names and units to be constant in time, or at least during the run being reduced. Only 9 critical keywords are read from each raw image. Other information are either constants of the instrument (gain, RON, pixel size) or computed from other keywords (airmass).

Pipeline Keyword needed

The following table lists all the informations needed by the framework and the corresponding unit used. The first block of the table gives the 9 keywords that must be found in the header of all raw images.

needed informations	description	Unit	Location
filter-name	Name of the filter used for the image.	*string*	Fits header
object-name	Name of the pointing.	*string*	Fits header
exposure-time	Exposure time for the image.	*second*	Fits header
number-sub-image	Number of sub integration.	$sub - image$	Fits header or set to 1
julian-day	True Julian day of the exposure.	*day*	Fits header
crval1	Right ascension of the pointing.	*degree*	Fits header
crval2	Declination of the pointing.	*degree*	Fits header
crpix1	Reference pixel x axis.	*pixel*	Fits header
crpix2	Reference pixel y axis.	*pixel*	Fits header
total-exposure-time	Total exposure time for the raw image.	*second*	Computed
total-stack-image	Number of stacked images.	*image*	Set to 1
background-value	Background value of the deflated image	$\frac{ADU}{deg^2}$	Computed
airmass	Airmass of the observation.	arccos $(1/dz)$	Computed
cd1_1	WCS matrix element.	$deg/pixel$	Instrument options
cd1_2	”		
cd2_1	”		
cd2_2	”		
ctype1	Type of projection.	*string*	set to RA—TAN
ctype2	”		set to DEC–TAN
gain	Instrumental gain.	$e - /adu$	Instrument options
read-out-noise	Instrumental read out noise.	$e-$	Instrument options
instrument-name	Name of the instrument.	*string*	User specified

- Some instruments or archives provide raw images that are already the combination of several observations named *sub-images*. This occurs especially in IR where exposure times are short. This pre-stacking decreases the number of images to be archived. This notion must be carried out by the framework to update critical informations (exposure time, gain).
- *Number-sub-image* indicates how many sub-images are combined. The sub-images are assumed to have all the same exposure time indicated by the exposure-time.

XML options

XML option name	*description*
/mvm-stack/observatory[instrument /name="select"] /keyword-fits-raw	XML path for the following relative options.
./filter	Name of the raw keyword to get the filter name.
./archive-name	Archive name of the image. Will be used in future version.
./object-name	Raw keyword name of the object-name.
./exposure-time	Raw keyword name for exposure time.
./number-sub-image	Keyword name to indicate the number of observed images already combine in one raw image.
./julian-day	Keyword name to indicate the True Julian date.
./crval1	Keyword name for the Right Assencion of the image.
./crval2	Keyword name for the Declination of the image.
./crpix1	CRPIX1 keyword
./crpix2	CRPIX2 keyword
./delete	Raw keyword to be deleted

The Node *keyword-fits-raw* contains the description of the 9 critical keywords that must be found in each header of the raw image. The information *archive-name* is not yet used, but must be defined. The *delete* information indicates which raw keywords can be removed (see the following example sub-section: D.5). Each of the raw keyword described in the previous table is defined by a keyword name and a unit in a dedicated XML node.

XML option name	*description*
/mvm-stack/observatory[instrument /name="select"]/keyword-fits-raw	XML path for the following relative options.
./information-name/name	Name of the raw FITS keyword to be read.
./information-name/unit	Unit of the keyword.

Example

keyword-fits-raw XML node for the WFI instrument:

```
<observatory>
      <instrument>
```

```
            <name>wfi</name>
            ...
      </instrument>
       ...
      <keyword-fits-raw>
            <filter>
                  <name>HIERARCH ESO INS FILT NAME</name>
                  <unit>none</unit>
            </filter>
            <archive-name>
                  <name>ARCFILE</name>
                  <unit>none</unit>
            </archive-name>
            <object-name>
                  <name>OBJECT</name>
                  <unit>none</unit>
            </object-name>
            <number-sub-image>
                  <name>none</name>
                  <unit>none</unit>
            </number-sub-image>
            <julian-day>
                  <name>MJD-OBS</name>
                  <unit>mjd</unit>
            </julian-day>
            <crval1>
                  <name>RA</name>
                  <unit>none</unit>
            </crval1>
            <crval2>
                  <name>DEC</name>
                  <unit>none</unit>
            </crval2>
            <crpix1>
                  <name>CRPIX1</name>
                  <unit>none</unit>
            </crpix1>
            <crpix2>
                  <name>CRPIX2</name>
                  <unit>none</unit>
            </crpix2>
            <delete>
                  <name>HIERARCH ESO DET (IRACE|VOLT)|CROTA|CDELT</name>
                  <unit>none</unit>
            </delete>
      </keyword-fits-raw>
      ...
</observatory>
```

Each sub-node must contain a name and a unit. If no unit conversion is needed, then the unit is set to *none*. The available units are: *mjd, hour, min, deghour* with the follwing conversion:

Unit name	*Conversion applied on the read value*
mjd	+ 2400000.5
hour	* 3600
min	* 60
deghour	* 15

The sub-node *delete* indicates which raw keywords will be removed. Some images have very long headers that describe "irrelevant" informations for the data reduction. The delete node indicates in a Perl-like pattern matching convention, which keywords should be deleted. In the example, all keywords matching "ESO DET VOLT" or "ESO DET IRACE" or CROTA or CDELT are removed.

D.6 Pipeline internal FITS keyword convention: *<keyword-fits-alias>*

Description

Each original image is associated with information coming either from the raw FITS keywords or from the instrument settings. These informations are then rewritten to the raw images following an homogeneous convention. The output FITS keywords are set by the user in the XML node *./observatory/keyword-fits-alias.*

XML options

XML option names	Defaults	Unit	*Description*
/mvm-stack/observatory [instrument/name="select"] /keyword-fits-alias			XML path for the following relative options.
./filter	FILTER	String	Raw keyword name of the filter-name.
./archive-name	ARCNAME	String	Archive name of the image. Will be used in future version.
./object-name	OBJECT	String	Raw keyword name of the object-name.
./exposure-time	EXPTIME	Second	Raw keyword name of the exposure time.
./number-sub-image	IMG-SUB	sub-image	Raw keyword name to indicate the number of sub-images already combine in one raw image.
./julian-day	JULIAN	Day	Raw keyword name to indicate the True Julian date.

./crval1	CRVAL1	degree	Raw keyword name of the Right Assencion of the pointing.
./crval2	CRVAL2	degree	Raw keyword name of the Declination of the pointing.
./crpix1	CRPIX1	pixel	CRPIX1 keyword
./crpix2	CRPIX2	pixel	CRPIX2 keyword
./nb-tot-image	TOT-IMAG	images	Number of total combined images (always 1 for original images)
./tot-exptime	TOT-EXPT	second	Total exposure time
./airmass	AIRMASS	cos(1/dz)	Airmass of the pointing.
./background-value	BACK-VAL	$\frac{ADU}{deg^2}$	Sky background value.
./instrument	INSTRUME	String	Name of the selected instrument.

Example

The following example is set for all instrument supported by the pipeline. Even if those settings could be specific to one instrument.

```
<observatory>
      <instrument>
            <name>”All instrument supported”</name>
            ...
      </instrument>
       ...
      <keyword-fits-alias>
            <filter>FILTER</filter>
            <archive-name>ARCNAME</archive-name>
            <object-name>OBJECT</object-name>
            <number-sub-image>IMG-SUB</number-sub-image>
            <julian-day>JDAY</julian-day>
            <crval1>CRVAL1</crval1>
            <crval2>CRVAL2</crval2>
            <crpix1>CRPIX1</crpix1>
            <crpix2>CRPIX2</crpix2>

            <total-nb-image>TOT-IMAG</total-nb-image>
            <total-exposure-time>TOT-EXPT</total-exposure-time>
            <airmass>AIRMASS</airmass>
            <background-value>BACK-VAL</background-value>
            <instrument-name>INSTRUME</instrument-name>
      </keyword-fits-alias>
      ...
</observatory>
```

Note

- The names of the rewritten keywords are defined for all supported instruments, and should be defined similarly to have common keyword names and units.

D.7 Calibration images recognition: <*calib-recognition*>

Description

The pipeline distinguishes 4 kinds of calibration images:

- FLAT-SKY: Flat observations made on the sky during twilight.
- FLAT-DOME: Flat observations made on a screen set in the dome of the telescope.
- BIAS: Image with 0 second integration time, observed to calibrate the electronic bias level.
- DARK: Image observed with the shutter closed with non-zero integration time. It is used to calibrate the thermal noise of the CCD.

The calibration images are recognized with their *object-name* using Perl-like pattern recognitions. During the preparation part, the object-name of the recognized calibration images are rewritten as one of the 4 defined type (flat-sky, flat-dome, bias, or dark).

XML options

XML option name	*description*
/mvm-stack/observatory [instrument/name="select"] /calib-recognition	XML path for the following relative options.
./flat-sky	Recognition of flat-sky object-name.
./flat-dome	Recognition of flat-dome object-name.
./bias	Recognition of bias object-name.
./dark	Recognition of dark object-name.
./reject	Recognition of object-name rewritten as reject.

The *reject* sub-node specifies the image that must be rejected according to the object-name. For instance test or focus images are never used and can be set as rejected.

Example

The following XML nodes are set for the WFI instrument:

```
<observatory>
      <instrument>
            <name>wfi</name>
            ...
      </instrument>
       ...
      <calib-recognition>
            <flat-sky>^fs|^ff|^flat_|skyff</flat-sky>
            <flat-dome>^fd</flat-dome>
            <bias>bias</bias>
            <dark>dark</dark>
            <reject>test|focus|beta-light</reject>
      </calib-recognition>
      ...
</observatory>
```

All *object-name* keywords starting by: *fs* or *ff* or *flat_* or containing *skyff*, are rewritten as *flat-sky*. All *object-name* containing: *test* or *focus* or *beta-light* are recognized as rejected images.

Bibliography

Abell, G. O., Corwin, H. G., and Olowin, R. P. (1989). A catalog of rich clusters of galaxies. ApJS, 70:1–138.

Alcock, C., Allsman, R. A., Alves, D., Axelrod, T. S., Becker, A. C., Bennett, D. P., Cook, K. H., Freeman, K. C., Griest, K., Guern, J., Lehner, M. J., Marshall, S. L., Peterson, B. A., Pratt, M. R., Quinn, P. J., Rodgers, A. W., Stubbs, C. W., Sutherland, W., Welch, D. L., and The MACHO Collaboration (1997). The MACHO Project Large Magellanic Cloud Microlensing Results from the First Two Years and the Nature of the Galactic Dark Halo. ApJ, 486:697–+.

Andersen, M. I., Freyhammer, L., and Storm, J. (1995). Gain calibration of array detectors by shifted and rotated exposures. In *Calibrating and Understanding HST and ESO Instruments*, pages 87–+.

Arnouts, S., Vandame, B., Benoist, C., Groenewegen, M. A. T., da Costa, L., Schirmer, M., Mignani, R. P., Slijkhuis, R., Hatziminaoglou, E., Hook, R., Madejsky, R., Rité, C., and Wicenec, A. (2001). ESO imaging survey. Deep public survey: Multi-color optical data for the Chandra Deep Field South. A&A, 379:740–754.

Aubourg, E., Bareyre, P., Brehin, S., Gros, M., de Kat, J., Lachieze-Rey, M., Laurent, B., Lesquoy, E., Magneville, C., Milsztajn, A., Moscoso, L., Queinnec, F., Renault, C., Rich, J., Spiro, M., Vigroux, L., Zylberajch, S., Ansari, R., Cavalier, F., Moniez, M., Beaulieu, J.-P., Ferlet, R., Grison, P., Vidal-Madjar, A., Guibert, J., Moreau, O., Tajahmady, F., Maurice, E., Prevot, L., and Gry, C. (1995). Search for very low-mass objects in the Galactic Halo. A&A, 301:1–+.

Banse, K., Crane, P., Grosbol, P., Middleburg, F., Ounnas, C., Ponz, D., and Waldthausen, H. (1983). MIDAS - ESO's new image processing system. *The Messenger*, 31:26–28.

Bertin, E. (2001). *EyE (Enhance Your Extraction) v1.1.* http://terapix.iap.fr/cplt/oldSite/soft/eye/.

Bertin, E. (2002). *SWarp User Guide v1.34.* http://terapix.iap.fr/fsoft/swarp/.

Bertin, E. (2003). *SExtractor User Guide v2.3.* http://terapix.iap.fr/IMG/ps/sextractor.ps.

Bertin, E. and Arnouts, S. (1996). SExtractor: Software for source extraction. A&AS, 117:393–404.

Bucciarelli, B., García Yus, J., Casalegno, R., Postman, M., Lasker, B. M., Sturch, C., Lattanzi, M. G., McLean, B. J., Costa, E., Falasca, A., Le Poole, R., Massone, G., Potter, M., Rosenberg, A., Borgman, T., Doggett, J., Morrison, J., Pizzuti, A., Pompei, E., Rehner, D., Siciliano, L., and Wolfe, D. (2001). An all-sky set of (B)-V-R photometric calibrators for Schmidt surveys. GSPC2.1: First release. A&A, 368:335–346.

Corwin, H. G., de Vaucouleurs, A., and de Vaucouleurs, G. (1985). *Southern galaxy catalogue. A catalogue of 5481 galaxies south of declination -17 grad. found on 1.2m UK Schmidt IIIa J plates.* University of Texas Monographs in Astronomy, Austin: University of Texas, 1985.

Cuillandre, J.-C. (1999). *FITS Large Images Pre-processing Software.* http://www.cfht.hawaii.edu/ jcc/Flips/flips.html.

da Costa, L., Rite, C., and Slijkhuis, R. G. (2004). The ESO Imaging Survey Project: Building a Survey Software System. In *ASP Conf. Ser. 314: Astronomical Data Analysis Software and Systems (ADASS) XIII*, pages 3–+.

Deul, E. (1990). *Leiden Data Analasis Center software.* http://ftp.strw.leidenuniv.nl/pub/ldac/software.

Deul, E. R., Holl, A., Guglielmo, F., Borsenberger, J., deBatz, B., Bertin, E., Copet, E., Epchtein, N., Fouque, P., Lacombe, F., LeBertre, T., Rouan, D., Ruphy, S., Tiphene, D., Kimeswenger, S., Kienel, C., Hron, J., and Forveille, T. (1995). Data processing for the DENIS project. *Memorie della Societa Astronomica Italiana*, 66:549–+.

Devillard, N. (1997). *Eclipse, ESO C library for an Image Processing Softwa.* http://www.astro.psu.edu/ users/cwc/ufoered/calib.html.

Devillard, N. (2001). ESO C Library for an Image Processing Software Environment (eclipse). In *ASP Conf. Ser. 238: Astronomical Data Analysis Software and Systems X*, pages 525–+.

Djandji, J., Bijaoui, A., and Mamère, R. (1993). Geometrical Registration of images. The multiresolution approach. *Photogrammetric Engineering and Remote Sensing*, (59):645–653.

Efstathiou, G., Ellis, R. S., and Peterson, B. A. (1988). Analysis of a complete galaxy redshift survey. II - The field-galaxy luminosity function. MNRAS, 232:431–461.

Eisenhardt, P., Dickinson, M., .A., S. S., Ward, J., and Valdes, F. (1999). *DIMSUM, Deep Infrared Mosaicing Softaware, V2.* http://star-www.rl.ac.uk/iraf/ftp/iraf/contrib/dimsumV2/dimsum.readme.

Epchtein, N., de Batz, B., Capoani, L., Chevallier, L., Copet, E., Fouque, P., Lacombe, F., Le Bertre, T., Pau, S., Rouan, D., Ruphy, S., Simon, G., Tiphene, D., Burton, W. B., Bertin, E., Deul, E., Habing, H., Borsenberger, J., Dennefeld, M., Guglielmo, F., Loup, C., Mamon, G., Ng, Y., Omont, A., Provost, L., Renault, J.-C., Tanguy, F., Kimeswenger, S., Kienel, C., Garzon, F., Persi, P., Ferrari-Toniolo, M., Robin, A., Paturel, G., Vauglin, I., Forveille, T., Delfosse, X., Hron, J., Schultheis, M., Appenzeller, I., Wagner, S., Balazs, L., Holl, A., Lepine, J., Boscolo, P., Picazzio, E., Duc, P.-A., and Mennessier, M.-O. (1997). The Deep Near-Infrared Southern Sky Survey (DENIS). *The Messenger*, 87:27–34.

Epchtein, N., de Batz, B., Copet, E., Fouque, P., Lacombe, F., Le Bertre, T., Mamon, G., Rouan, D., Tiphene, D., Burton, W. B., Deul, E., Habing, H., Boersenberger, J., Dennefeld, M., Omont, A., Renault, J. C., Rocca-Volmerange, B., Kimeswenger, S., Appenzeller, I., Bender, R., Forveille, T., Garzon, F., Hron, J., Persi, P., Ferrari-Toniolo, M., and Vauglin, I. (1994). DENIS: A Deep Near-Infrared Survey of the southern sky. Ap&SS, 217:3–9.

Fruchter, A. S. and Hook, R. N. (2002). Drizzle: A Method for the Linear Reconstruction of Undersampled Images. PASP, 114:144–152.

Górski, K. M., Banday, A. J., Hivon, E., and Wandelt, B. D. (2002). HEALPix — a Framework for High Resolution, Fast Analysis on the Sphere. In *ASP Conf. Ser. 281: Astronomical Data Analysis Software and Systems XI*, pages 107–+.

Górski, K. M. and et al. (1999). Analysis issues for large CMB data sets. In *Evolution of Large Scale Structure : From Recombination to Garching*, pages 37–+.

Hodapp, K., Hora, J., Graves, E., Irwin, E. M., Yamada, H., Douglass, J. W., Young, T. T., and Robertson, L. (2000). Gemini near-infrared imager (NIRI). In *Proc. SPIE Vol. 4008, p. 1334-1341, Optical and IR Telescope Instrumentation and Detectors, Masanori Iye; Alan F. Moorwood; Eds.*, pages 1334–1341.

Hough (1962).

Landsman, W. B. (1995). The IDL Astronomy User's Library. In *ASP Conf. Ser. 77: Astronomical Data Analysis Software and Systems IV*, pages 437–+.

Lewis, J. (2003). *CIRDR Documentation Homepage.* http://www.ast.cam.ac.uk/ jrl/cirdr/.

Lewis, J. (2004). *Overview of the Gemini IRAF Package.* http://www.gemini.edu/sciops/data/dataSoftware.html.

Lewis, J. and Irwin, M. (1999). *Wide Field Survey - Pipeline Processing.* http://www.ast.cam.ac.uk/ wfcsur/pipeline.php.

Maddox, S. J., Efstathiou, G., Sutherland, W. J., and Loveday, J. (1990). Galaxy correlations on large scales. MNRAS, 242:43P–47P.

Magnier, E. and Cuillandre, J.-C. (1997). *The Elixir System.* http://www.cfht.hawaii.edu/Instruments/Elixir/home.html.

Mallat, S. (1989). A Theory for Multiresolution Signal Decomposition the wavelet representation. *IEEE*, 11(7):674–693.

Mallat, S. G. (1989). A theory for multiresolution signal decomposition - The wavelet representation. *IEEE Transactions on Pattern Analysis and Machine Intelligence*, 11:674–693.

Manfroid, J. (1996). On CCD standard stars and flat-field calibration. A&A, 118:391–395.

Manfroid, J. and Selman, F. (2001). Achieving 1% photometric accuracy with the ESO Wide Field Imager. *The Messenger*, 104:16–+.

McMahon, R. G., Walton, N. A., Irwin, M. J., Lewis, J. R., Bunclark, P. S., and Jones, D. H. (2001). The INT wide field imaging survey (WFS). *New Astronomy Review*, 45:97–104.

Momany, Y., Vandame, B., Zaggia, S., Mignani, R. P., da Costa, L., Arnouts, S., Groenewegen, M. A. T., Hatziminaoglou, E., Madejsky, R., Rité, C., Schirmer, M., and Slijkhuis, R. (2001). ESO imaging survey. Pre-FLAMES survey: Observations of selected stellar fields. A&A, 379:436–452.

Monet, D. B. A., Canzian, B., Dahn, C., Guetter, H., Harris, H., Henden, A., Levine, S., Luginbuhl, C., Monet, A. K. B., Rhodes, A., Riepe, B., Sell, S., Stone, R., Vrba, F., and Walker, R. (1998). The USNO-A2.0 Catalogue (Monet+ 1998). *VizieR Online Data Catalog*, 1252:0–+.

NTT Team, T. (1997). *SOFI Flat Fielding Imagery.* http://www.ls.eso.org/lasilla/Telescopes/NEWNTT/sofi/reduction/flat_fielding.html.

O'Mullane, W., Banday, A. J., Górski, K. M., Kunszt, P., and Szalay, A. S. (2001). Splitting the Sky - HTM and HEALPix. In *Mining the Sky*, pages 638–+.

Radovich, M. (2002). *Astrometrix, Astrometry of wide-field images.* http://www.na.astro.it/ radovich/wifix.htm.

Research Systems Inc (2004). *IDL: The Interactive Data Language.* http://www.rsinc.com/idl/.

Sabbey, C. N., McMahon, R. G., Lewis, J. R., and Irwin, M. J. (2001). Infrared Imaging Data Reduction Software and Techniques. In *ASP Conf. Ser. 238: Astronomical Data Analysis Software and Systems X*, pages 317–+.

Shane, C. D. and Wirtanen, C. A. (1954). The distribution of extragalactic nebulae. AJ, 59:285–+.

Skrutskie, M. F., Schneider, S. E., Stiening, R., Strom, S. E., Weinberg, M. D., Beichman, C., Chester, T., Cutri, R., Lonsdale, C., Elias, J., Elston, R., Capps, R., Carpenter, J., Huchra, J., Liebert, J., Monet, D., Price, S., and Seitzer, P. (1997). The Two Micron All Sky Survey (2MASS): Overview and Status. In *ASSL Vol. 210: The Impact of Large Scale Near-IR Sky Surveys*, pages 25–+.

Tody, D. (1986). The IRAF Data Reduction and Analysis System. In *Instrumentation in astronomy VI; Proceedings of the Meeting, Tucson, AZ, Mar. 4-8, 1986. Part 2 (A87-36376 15-35). Bellingham, WA, Society of Photo-Optical Instrumentation Engineers, 1986, p. 733.*, pages 733–+.

Udalski, A., Szymanski, M., Kaluzny, J., Kubiak, M., and Mateo, M. (1992). The Optical Gravitational Lensing Experiment. *Acta Astronomica*, 42:253–284.

Vandame, B. (2001). Fast Hough Transform for Robust Detection of Satellite Tracks. In *Mining the Sky*, pages 595–+.

Vandame, B. (2004). *Alambic, the EIS/MVM pipeline.* http://www.eso.org/science/eis/survey_release.html.

World Wide Web consortium (1999). *XML Path Language (XPath) Version 1.0.* http://www.w3.org/TR/xpath.

World Wide Web consortium (2001). *XML Inclusions (XInclude) Version 1.0.* http://www.w3.org/TR/xinclude.

World Wide Web consortium (2004). *The XML C parser and toolkit of Gnome.* http://www.xmlsoft.org/index.html.

Zacharias, N., Urban, S. E., Zacharias, M. I., Hall, D. M., Wycoff, G. L., Rafferty, T. J., Germain, M. E., Holdenried, E. R., Pohlman, J. W., Gauss, F. S., Monet, D. G., and Winter, L. (2000). The First US Naval Observatory CCD Astrograph Catalog. AJ, 120:2131–2147.

Zwicky, F., Herzog, E., and Wild, P. (1968). *Catalogue of galaxies and of clusters of galaxies.* Pasadena: California Institute of Technology (CIT), 1961-1968.